Development of an Aircraft Noise Emission Model Accounting for Flight Parameters

vorgelegt von
Dipl.-Ing.
Christoph Zellmann
geb. in Berlin

von der Fakultät V – Verkehrs- und Maschinensysteme
der Technischen Universität Berlin
zur Erlangung des akademischen Grades

Doktor der Ingenieurwissenschaften
– Dr.-Ing –

genehmigte Dissertation

Promotionsausschuss:

Vorsitzender:	Prof. Dr.-Ing. Ennes Sarradj
Gutachter:	Prof. Dr.-Ing. Christian Oliver Paschereit
Gutachter:	Prof. Dr.-Ing. Eike Stumpf

Tag der wissenschaftlichen Aussprache: 15. Dezember 2017

Berlin 2018

Impressum

Umschlagfotografie: Stefan Plüss

Umschlaggestaltung: Christoph Zellmann

Teile der Dissertation wurden im Voraus veröffentlicht:

Zellmann C., Schäffer B., Wunderli J.M., Isermann U., Paschereit C.O. (2017), “An Aircraft Noise Emission Model Accounting for Aircraft Flight Parameters", *Journal of Aircraft*, accessed September 09, 2017. doi: https://arc.aiaa.org/doi/abs/10.2514/1.C034275

Zellmann C., Wunderli J.M., Paschereit C.O. (2016) , “The sonAIR sound source model: spectral three-dimensional directivity patterns in dependency of the flight condition", *INTER-NOISE 2016 - 45th International Congress on Noise Control Engineering: Towards a Quieter Future; Hamburg*, p. 786-94.

Zellmann C., Wunderli J.M. (2014), “Influence of the atmospheric stratification on the sound propagation of single flights", *INTER-NOISE 2014 - 43rd International Congress on Noise Control Engineering: Improving the World Through Noise Control; Melbourne.*

Zellmann C., Wunderli J.M., Schäffer B. (2013), “SonAIR - Data acquisition for a next generation aircraft noise simulation model", *INTER-NOISE 2013 - 42nd International Congress and Exposition on Noise Control Engineering: Noise Control for Quality of Life; Innsbruck*, p. 842-50.

Vorwort

Die vorliegende Arbeit ist für mich persönlich ein wichtiger Lebensabschnitt, der meinen neuen Lebensmittelpunkt in der Schweiz und meine deutsche Heimat miteinander verbindet. Während dieser Zeit hatte ich an beiden Orten eine großartige fachliche und persönliche Unterstützung, für die ich mich bei all jenen bedanken möchte, die dazu beigetragen haben.

Zuerst möchte ich Herrn Prof. Paschereit für seine fachliche und administrative Unterstützung aus Berlin danken. Bei Herrn Prof. Stumpf möchte ich mich für seine spontane Einwilligung, als externer Gutachter tätig zu werden, bedanken. Weiterhin möchte ich Ullrich Isermann vom DLR Göttingen danken, der – obwohl ich nicht bei ihm promoviert habe – immer ein offenes Ohr, kritische Anmerkungen und motivierende Worte für mich hatte. Ich habe mich mit dir und deinem Team immer gerne ausgetauscht.

In der Schweiz möchte ich mich vor allem bei Kurt Eggenschwiler, Jean Marc Wunderli und Beat Schäffer bedanken. Ihr habt mich an der Empa seit Beginn herzlich aufgenommen, mich unterstützt, motiviert und fachlich voran gebracht. Dank euch auch für eure vielen, wertvollen Korrekturen zu meinen Publikationen. Mein Dank gilt auch den vielen Partner des Projekts sonAIR und den damit verbunden Personen, die das Projekt finanziell, organisatorisch und mit wertvollen Daten unterstützten: Das Bundesamt für Zivilluftfahrt, das Bundesamt für Umwelt, der Kanton Zürich, die Empa, die Flughäfen Zürich und Genf, Swiss International Air Lines, skyguide, SciTrackS, BeSB GmbH Berlin und n-Sphere.

Während meiner Zeit an der Empa gab es natürlich viele Kollegen, denen ich allen für die gute Zeit danke und doch einige speziell nennen möchte. Markus Studer, es war mir eine Ehre deine letzte große Messkampagne an der Empa mitzuerleben, die du sehr gewissenhaft vorbereitet hast und einwandfrei abgelaufen ist. Meritxell, Danke für die detaillierten Diskussionen zur Datenauswertung und deinen Beitrag zur Einzelflugsimulation. Meine Zimmergenossen Janni und später Olivier haben immer für eine lockere Stimmung im Büro gesorgt und mich aufgebaut wenn nötig. Nicht zu vergessen auch die fleissigen Praktikantinnen Flurina und Monica, die Tausende von Lärmereignissen manuell überprüfen mussten. Ohne „Computer says no“, Autounfälle und zerstörte Festplatten wäre die Zeit wohl nur halb so spannend gewesen.

Ganz besonders möchte ich mich bei meiner Familie, meiner Freundin Bettina und ihrer Familie bedanken – ihr alle habt mich sehr unterstützt. Und an alle meine Freunde in Berlin, Zürich und wo ihr euch sonst so herumtreibt: Ihr seid die Besten!

Zürich im Januar 2018 Christoph Zellmann

Zusammenfassung

Heutige Berechnungsmodelle für Fluglärm sind nur teilweise zur Bewertung und Optimierung von lärmarmen Flugverfahren geeignet. Die Modelle sind entweder zu stark vereinfacht, basieren auf semiempirischen Modellen, die anspruchsvolle Flugparameter erfordern, oder sind nicht öffentlich zugänglich.

In dieser Arbeit wurde ein akustisches Emissionsmodell für Flugzeuge mit Strahltriebwerken in Abhängigkeit von Flugparametern (Leistungsstufe, Fluggeschwindigkeit und Konfiguration) entwickelt. Antriebs- und Umströmungslärm wurden dabei separat anhand weniger Modellparameter modelliert. Der Modellansatz ist universell und lässt sich auf verschiedene Flugzeugtypen anwenden.

Um eine Datengrundlage möglichst vieler Flugparameter zu erstellen, wurden umfassende akustische Messungen des Flugbetriebs am Flughafen Zürich durchgeführt. Anschließend wurden die akustischen Messungen mithilfe von Flugdaten, Flugbahnen und meteorologischen Profilen zur Quelle zurück gerechnet. Auf dieser Datengrundlage und multipler linearer Regression wurden drei Modellvarianten von unterschiedlichem Detaillierungsgrad entwickelt: Ein detailliertes Modell mit dreidimensionaler Richtwirkung (3D) und zwei reduzierte Modelle ohne Berücksichtigung der Konfiguration. Die reduzierten Modelle, die auch ohne Flugschreiberdaten verwendet werden können, sind entweder mit dreidimensionaler (3Dred) oder zweidimensionaler Richtwirkung (2Dred) modelliert.

Insgesamt wurden 19 akustische Emissionsmodelle für verschiedene Kombinationen von Flugzeug- und Triebwerkstypen erstellt. Für das Antriebslärmmodell ist die Drehzahl der Niederdruckwelle der wichtigste Modellparameter, mit dem sich auch die Richtwirkung verändert. Für das Umströmungslärmmodell ist die Machzahl der massgebende Modellparameter. Allerdings können auch die Fahrwerke den Gesamtschallpegel bei der Landung je nach Flugzeugtyp bis zu 5 dB erhöhen, besonders wenn sie frühzeitig, d.h. bei höheren Machzahlen, ausgefahren werden. Solch ein lokal wichtiger Einfluss wird durch das 3D-Modell berücksichtigt.

Unter Anwendung eines Zeitschrittverfahrens und eines detaillierten Ausbreitungsmodells wurden 10 524 Flugereignisse simuliert, die bereits für die Entwicklung der Modelle verwendet wurden. Ein Vergleich des 3D-Modells mit den Messungen ergab für die simulierten Ereignispegel im Mittel eine Überschätzung von 0.1 dB bei einer Standardabweichung von 0.9 dB. Der simulierte Maximalschallpegel wurde im Mittel leicht unterschätzt bei größerer Standardabweichung. Das reduzierte Modell 3Dred zeigte ähnliche Ergebnisse, da der Einfluss der fehlenden Konfiguration bei Landungen mit der Machzahl skaliert. Die Vereinfachung auf eine zweidimensionale Richtwirkung (2Dred) hingegen zeigte eine größere Standardabweichung.

Anhand physikalischer und empirischer Kenntnisse der Schallentstehung wurden adäquate Modellparameter gewählt und linearisiert, wodurch ein physikalisches Verhalten des statistischen Modells erreicht wurde. Es konnte gezeigt werden, dass die Emissionsmodelle die akustischen Messungen mit hoher Genauigkeit reproduzieren. Allerdings muss eine Extrapolation der Modelle außerhalb der bekannten Parameterbereiche noch durch eine Validierung mit unabhängigen Daten geprüft werden. Die Ergebnisse der Dissertation zeigen bereits das große Potential des Modells auf, lärmarme Flugverfahren präzise bewerten und optimieren zu können.

Abstract

Existing aircraft noise models are only partly suited for the assessment and optimization of noise abatement flight procedures. Either the models are too simplified, or are based on semi-empirical models which require ambitious flight parameters, or are not publicly available. In this thesis, an aircraft noise emission model for turbofan-powered aircraft was developed with the capability to take the flight configuration (thrust rating, airspeed, and aeroplane configuration) into account. Engine and airframe noise were modeled separately with a small number of model parameters. The approach is universal and thus applicable on many aircraft types.

To establish a data basis for different flight configurations under regular air traffic, extensive acoustical measurements around Zurich airport were realized. The acoustical data were processed with the help of flight data, flight paths, and meteorological data to obtain direction-dependent sound emission levels at the source. By means of this data base and multiple linear regression, three model variants with different level of detail were developed: an advanced model with three-dimensional directivity (3D) and two reduced models without aeroplane configuration. The reduced models, which can be applied if no flight data records are available, are modeled either with a three-dimensional directivity (3Dred) or a two-dimensional directivity (2Dred).

In total, 19 aircraft noise emission models for combinations of engine type and aircraft type were established. The main parameter for the engine noise model is the rotational speed of the engines, which also influences the directivity of the model. For airframe noise, the aircraft Mach number is the main parameter. However, also the landing gear is an important sound source of the airframe. If deployed early during approach and thus at high aircraft Mach numbers, it raises the total sound emission level up to 5 dB. Such local influence of the aeroplane configuration is represented by the 3D model.

A time-step method and a detailed propagation model were applied to simulate 10 524 flight events that were used for the development of the models. A comparison between 3D model and measurement resulted in a slight overestimation of the simulated sound exposure level of 0.1 dB with a standard deviation of 0.9 dB. In comparison, the simulated maximum sound pressure level was slightly underestimated and showed larger variations. The model variant 3Dred showed similar results, because the aeroplane configuration during approach is related to the aircraft Mach number. In contrast, the reduction to a two-dimensional directivity (2Dred) resulted in larger standard deviations.

Based on physical and empirical knowledge about sound generation, appropriate model parameters were chosen and linearized, whereby a physical behavior of the statistical model could be achieved. It was shown that the aircraft noise emission models are capable to reproduce the acoustical measurements with high accuracy. However, extrapolations to unknown flight configurations require validation with independent data in the future. The results of the thesis indicate the model's great potential for the assessment and optimization of noise abatement flight procedures.

Contents

List of Figures

List of Tables

List of abbreviations

2D	two-dimensional
3D	three-dimensional
A	approach
AIC	Akaike information criterion
ATOM	actual take-off mass
BIC	Bayesian information criterion
BPF	blade passing frequency
D	departure
CDA	Continuous Descent Approach
COSMO	Consortium for Small-Scale Modeling
CR	close range
EASA	European Aviation Safety Agency
EFB	electronic flight bag
EPR	engine pressure ratio
FDR	flight data recorder
FFT	fast Fourier transform
FR	far range
GIS	geographical information system
GUM	Guide to the expression of uncertainty in measurement
ICAO	International Civil Aviation Organization
IQR	interquartile range
LDLP	Low Drag Low Power
MLAT	multilateration
NADP	noise abatement departure procedure
NPD	noise-power-distance
OLS	ordinary least squares
RPK	revenue passenger kilometer
SD	standard deviation
TCDS	type certification data sheet
VIF	variance inflation factor
WLS	weighted least squares

Glossary

Latin symbols

Symbol	Unit	Description
A	dB	attenuation
$\mathbf{b}$	–	estimated coefficient vector
c	$^{m}/_{s}$	speed of sound
D	–	directivity
DF	–	Doppler factor
$\mathbf{E}$	–	residual error vector
f	Hz	frequency
i	–	number integer band-shifts
I	$^{W}/_{m^2}$	sound intensity
K	–	coherence loss
L	dB	sound level
m	–	number of model parameters
Ma	–	aircraft Mach number
n	–	number of observations
$N1$	%	relative rotational speed of the low pressure compressor
p	Pa	pressure
q	–	ratio of engine to total sound emission
$\mathbf{r}$	–	position vector
R	$^{J}/_{kgK}$	specific gas constant
RC	–	time constant for the exponential weighting of the sound pressure (slow: 1 s, fast: 0.125 s)
RD	–	robust estimate of Mahalanobis distance
RH	–	relative humidity
t	s	time
t_r	s	time at receiver
t_{10}	s	time in which $L(t)$ is not smaller than $L_{max} - 10\,\mathrm{dB}$
$\mathbf{T}$	–	transformation matrix
T	°C	air temperature outside
U	$^{m}/_{s}$	mean flow speed
u	dB	standard uncertainty
V	$^{m}/_{s}$	velocity
$\mathbf{W}$	–	weight matrix
W	W	sound power
w	–	weighting factor
$\mathbf{X}$	–	design matrix
x	–	longitudinal axis
$\mathbf{Y}$	–	response vector
y	–	lateral axis
Z	–	number of blades
z	–	vertical axis

Greek symbols

Symbol	Unit	Description
α	$^\circ$	angle of attack
α_{atm}	$^{\mathrm{dB}}/_{\mathrm{m}}$	absorption coefficient
β	–	sideslip angle
$\boldsymbol{\beta}$	–	vector with regression parameters
γ	$^\circ$	climb angle
Γ	m	characteristic dimension
$\boldsymbol{\epsilon}$	–	vector of independent normal random variables with expectation
θ	$^\circ$	polar angle of the directivity
ϑ	s	integration time
κ	$^1/_{\mathrm{m}}$	curvature of the flight track
κ	–	adiabatic index
μ	–	bypass ratio
ρ	$^{\mathrm{kg}}/_{\mathrm{m}^3}$	ambient air density
σ	–	standard deviation, error mean square
τ	s	retarded time
φ	$^\circ$	azimuth angle of the directivity
ϕ	$^\circ$	bank angle
χ	$^\circ$	flight path azimuth
ω	rpm	rotational speed of the low pressure compressor

Subscripts

Symbol	Description	linked to
0	reference	sound pressure, sound power
A	A-weighting	acoustic metrics
afm	airframe	airframe noise model
atm	atmospheric absorption	propagation effects
av	average	uncertainty
$basic$	basic module	direct calculation of the propagation
cal, ref	calibration, reference	uncertainty
cal, op	calibration, operational	uncertainty
div	divergence	propagation effects
E	exposure	sound exposure level
E	error	regression model
em	emission	sound emission level (arithmetic mean)
$\overline{em}$	corrected emission	sound emission level (energy mean)
eng	engine	engine noise model
eq	equivalent	equivalent sound pressure level
FE	flight effect	moving source
f	body axis	coordinate systems
fil	filter	uncertainty
fol	foliage	propagation effects
$ForestCliff$	forest, cliff module	calculation of reflections at cliffs and forests
g	earth axis	coordinate systems
gr/bar	ground effect, barriers	propagation effects
$inst$	instrument	uncertainty of the measurement system
j	index	integration of discrete values
k	flight path axis	coordinate systems
lin	level linearity	uncertainty
m	mid	mid frequency
$Meteo$	meteo module	calculation of additional meteorological propagation effects
mic	microphone	uncertainty, coordinate systems
max	maximum	$N1$ determination
$peak$	peak	$N1$ determination
r	receiver	simulation
$Reflect$	reflection module	calculation of diffuse and specular reflections at buildings
s	source	simulation
S	slow	time constant (1 s)
U	voltage supply	uncertainty

Superscripts

Symbol	Description	linked to
i	initial	data separation

1 Introduction

Aircraft noise is a significant environmental problem around airports, affecting millions of people in Europe. According to a study considering five European airports (Heathrow, Gatwick, Stansted, Schiphol and Maastricht), the resulting yearly airport-specific noise costs add up from 1.3 to 179.5 million euros [65]. In addition, many socio-acoustical and epidemiological studies identified negative impacts of aircraft noise on health [7; 8; 16; 18].

Currently, there is an open discussion on whether the population became more sensitive over the years, however, there seems to be a growing concern about aircraft noise [5; 17; 41]. An explanation for the increased concerns and annoyance could be the rapid growth of aircraft operations [37]. From 2010 to 2015, the world's revenue passenger kilometer (RPK) increased between 5 and 8 % each year [15]. For the development between 2015 and 2035, the Boeing Market Outlook [15] predicts a mean growth rate of 4.8 % RPK and a doubling of the number of aircraft in service. Whether the sensitivity of the people, number of aircraft or other influencing factors increased the annoyance, the public pressure on policy-makers is rising. A tendency for more restrictive noise legislation represent one of the major operational limitations for airports nowadays as reported by [3; 35].

Mitigation measures are needed to tackle the aircraft noise problem and to prevent operational and thus economic limitations. The Balanced Approach to aircraft noise [47] of the International Civil Aviation Organization (ICAO) proposes four elements how authorities and airports can take action. The first element of the Balanced Approach aims to reduce noise at the source, which is realized by the industry and enforced by noise limits for certification. New technologies can be very effective to achieve a noise reduction at the source; however, they are long-term measures due to development and implementation times.

Land-use planning and management is addressed as the second element, including medium- to long-term actions. As affected areas of aircraft noise are large, authorities use calculations to maintain the noise exposure. For that purpose, best practice programs such as ICAO Doc. 9911 [48] or ECAC Doc. 29 [31], national guidance as AzB [4; 53] in Germany, and FLULA2 [74; 61] in Switzerland are in use (see [20; 21; 50]). Based on these calculations and depending on the political framework, mitigation measures, and zoning are mainly applied. In reality, however, these measures are not successful in reducing the population density around airports. In fact, the population near Zurich

airport, as an example, rose above average in the last decade, because other advantages such as the infrastructure were prioritized [83].

The third element covers noise abatement procedures to reduce or redistribute noise. Three main categories listed in [46] represent possible measures: flight procedures, spatial optimization, and ground management. These possibilities were investigated in several studies, which showed local noise reduction potentials from 3 to 12 dB on approach and 2 to 9 dB on departure [46].

The fourth element proposes operational restrictions if all other elements were exploited. Operational restrictions result in severe economic and capacitive constraints. Therefore, noise abatement procedures have the highest potential for short-term to medium-term noise relief with manageable economic and capacitive constraints.

1.1 Problem and research question

The introduction of new noise abatement procedures is complicated because of many requirements such as safety, capacity, and aircraft equipment [46]. In addition, new procedures need to be certified, and pilots and air traffic controllers need to accept and train them. The introduction following the principal of trial and error is time-consuming and costly. Moreover, the effect on the sound exposure can only be determined afterward. It is therefore essential to perform a comprehensive noise study in advance, showing the potential of new procedures and discuss the trade off between noise and emissions (fuel burn).

Best practice programs for the calculation of aircraft noise such as Doc. 9911 or Doc. 29 are designed to calculate yearly air traffic [84]. Effects of spatial modifications such as changes in track dispersion or the introduction of preferred routes can be reliably calculated. However, effects of changes in the vertical flight profile are limited to a simplified acoustical description of the source. The main drawback of the noise-power-distance (NPD) data is the lack of airframe noise parameters like airspeed or aeroplane configuration to account for source effects at approach. Therefore, the best practice programs are currently of limited use for the assessment of vertical noise abatement procedures for approach.

Scientific programs such as ANOPP2 [60], SIMUL [54] or PANAM [9; 11] are able to accurately calculate new flight procedures as they combine semi-empirical models for engine noise sources (e.g. [42; 94]) and airframe noise sources (e.g. [30; 76; 80]) to represent the sound sources of the aircraft. However, they require very detailed input data of the physical flight parameters (e.g. primary jet speed or airflow mass) as well as of the geometry of the sources (e.g. landing gear dimensions) for accurate predictions. Moreover, they provide a very limited data base of aircraft types [10], as the aerodynamic

source models have to be calibrated for each type with wind tunnel experiments. Another drawback is the limited accessibility of these programs to other users.

To date, no appropriate calculation program allows optimizing and assessing departure and approach flight procedures for a wide range of aircraft. The predicted increase of movements and population, as well as the high costs to introduce new procedures, create a demand for a reliable and precise aircraft noise prediction model. The challenge for this new model is to find a compromise between the necessary level of detail and complexity.

1.2 Research objectives

The present work aims for a new aircraft noise emission model for aircraft which eliminates the limitations of current models. The goal of this thesis is to achieve the following requirements:

1. explicit separation of source and propagation phenomena
2. separation of airframe and engine noise
3. description of the source mechanisms with physical parameters
4. acoustical description as spectral directivity patterns
5. compromise between the degree of detail and number of required flight parameters
6. general approach which can be transferred to other aircraft types

The model development focuses on turbofan-powered narrow- and wide-body aircraft. Those contribute most to the aircraft noise today due to many movements, each emitting a high sound energy. Depending on the fuselage design, number of engines, and aerodynamic behavior, the same noise abatement procedure can have different effects. Therefore, it is the objective to include the most important flight parameters for airframe and engine noise and to identify their individual contributions to the total noise.

The latter goal requires to gather a huge amount of data. This includes acoustical measurements, the acquisition of the flight paths, and access to flight parameters. Several aircraft types need to be measured in the regular air traffic under almost all relevant flight configurations, i.e. flight parameters and aeroplane configuration [48].

An overall objective is the integration of the aircraft noise emission model into a simulation tool, to calculate the received sound exposure at the ground. To reproduce level-time histories the time-step method is an approved technique, which requires a source description based on directivity patterns. If the aircraft noise emission model is separated from sound propagation, no limitations on the atmospheric conditions and considered effects apply for the simulation.

1.3 Overview of the thesis

In the following, the research project and the structure of the thesis are briefly summarized. The research project sonAIR, in which the thesis was conducted in, was funded by the Federal Office of Civil Aviation, Empa, skyguide, Canton of Zurich, and Zurich and Geneva airport. The goal of sonAIR was the development of a new aircraft noise simulation tool with the following challenges: develop an aircraft noise emission model in dependency of the flight configuration, implement the sophisticated propagation model sonX with manageable calculation time, and to build and integrate a simulation tool into a geographical information system (GIS)-environment.

While the the author was focused on the data acquisition, data analysis, and model development of the aircraft noise emission model, all topics of the project interfered. For instance, the propagation model sonX, which was already developed at Empa for other noise sources, was used to calculate the sound emissions at the source as input data for the model development. In this context, some necessary modifications were found to adapt sonX to high and large broadband noise sources.

To be able to simulate the sound exposure at the ground, two simulation tools were developed in the framework of the project. One simulation tool was established in Matlab as a test environment for the aircraft noise emission model and to verify the model. In addition, the partner company n-sphere who integrated sonAIR into the GIS-environment, implemented a simulation tool in C#.

Data acquisition and processing

Acoustical measurements (Sec. 3.1) of the regular air traffic were carried out around Zurich airport. To cover a wide range of flight configurations, measurements in the close range (CR) – distance below 2.5 km to the airport – and far range (FR) – distances up to 20 km – were conducted in 2013 and 2014. In total, 3 200 flights were measured in the close range and approximately 11 000 flights in the far range. In addition to the flyover measurements, measurement data of a static run-up test of an A330-300 were analyzed to determine the relation between the sound power level and the (relative) rotational speed of the engine ($N1$).

Besides the flyover measurements, many other data sources were needed. Meteorological data as described in Sec. 3.2 were used to account for the atmospheric effects on the sound propagation through the air. Flight paths of the measured flight events were collected from radar, multilateration (MLAT), and optical data (Sec. 3.3) and supplemented with meta data from the flight plan. Essential flight parameters (Sec. 3.4) for the development of the aircraft noise emission model were provided for the Swiss and Edelweiss aircraft fleet. For aircraft types without flight data recorder (FDR) data, $N1$ was determined

from the spectrogram of the audio signal. During the thesis many data sources were used, which were provided from different partners:

1. Meteorological data: MeteoSwiss and Empa
2. Optical tracking data: SciTracks
3. MLAT data: skyguide (Swiss air navigation)
4. Radar data: skyguide and Zurich airport
5. Movement lists: Zurich airport
6. FDR data: Swiss International Air Lines
7. $N1$ analysis: BeSB GmbH Berlin
8. Run-up test: Swiss International Air Lines and Zurich airport
9. Simulator data: Swiss Aviation Training

For the items 1 to 7 the comprehensive data processing is described in Sec. 3.5. Item 8 is used to support the model development and item 9 is used in Chap. 7, where an example is presented how data from a full flight simulator can be used as input to the aircraft noise emission model for noise predictions.

Model development

The aircraft noise emission model is based on multiple linear regression as introduced in the theoretical background (Sec. 2.3). Based on the resulting data sets (Sec. 4.1), a data exploration in Sec. 4.2 was executed to reveal the most influential parameters as well as their relationships to the sound emission level. The flight parameters $N1$, aircraft Mach number, air density as well as the aeroplane configuration (landing gear, high-lift devices, speedbrakes) are discussed.

In Sec. 4.3 the methodical procedure of the model development is described. Subsequently, the final regression models for airframe and engine noise and reduced model variants are presented (Sec. 4.4). To account for the energy mean of normal distributed sound levels, a theoretically based correction is introduced. Along with the regression models, a new technique is presented to separate the data set of the total aircraft sound emission into their contributions of airframe and engine noise (Sec. 4.5).

Results

In the results (Chap. 5) the grouping of aircraft types is explained and a list of 19 established aircraft noise emission models is presented. Further results focus on the aircraft noise emission models of the six aircraft types where FDR data were available.

Based on these types, the influence of different model variants on the results can be compared.

Sec. 5.2 presents the model performance of the regression models of the 24 frequency bands. Furthermore, some examples of the directivity and spectra are presented to show the potential of the models (Sec. 5.3). In Sec. 5.4, the effects of the model parameters on the sound emission level at the source and on the sound pressure level at a receiver are demonstrated. This section probably provides the most practical results and targets at aircraft noise experts, who intend to explain variations in measurements and between measurements and calculations caused by the sound source.

When applying the aircraft noise emission models, it is also essential to know the parameter range the aircraft were operated in during measurements. So far, only inside of this parameter range the models are verified. A potential noise modeler may also be interested to define plausible default flight parameters for each aircraft type, if no other data are available. Therefore, some mean flight parameters are presented for approach and departure in Sec. 5.5. An additional analysis of the influence of the runway length at Zurich airport is presented to indicate the complexity of flight operations.

Verification

As background for the verification in Chap. 6, also example level-time histories from the simulation tool (Sec. 2.4) are presented. With the verification the different variants of the aircraft noise emission model are compared among each other as well as to measurements. Based on the $L_{AE,t10}$ and $L_{AS,max}$, about 10 500 events for aircraft types with FDR data and 5 300 events for other aircraft types are compared to the measurements. In this way, the model is tested on its reproducibility over the known parameter range.

The comparisons between the model variants quantify the influence on the simulation results if the flight configuration or the lateral directivity is not considered for. These results are of interest for aircraft types where no FDR data are available, because in this case the aeroplane configuration is unknown. Furthermore, the theoretical approach of the correction to the energy mean is supported by the verification in Sec. 6.3.

Application

Finally, Chap. 7 completes the thesis showing the first application examples with the model implemented in a GIS-environment and an interface to a full flight simulator. In addition, the comparison of two approach procedures shows the capabilities of the model to assess and optimize noise abatement procedures.

2 Theoretical background

The theoretical background focuses on the main physics and equations related to this work. However, only a brief summary and reference to the applied methods and nomenclature is provided. A deeper understanding of the field or additional literature is required to follow the technical details. In the beginning of each section the author provides helpful references.

2.1 Coordinate system

The coordinate systems used in this thesis stem from the classical definitions of flight mechanics [55] under the assumption of no wind. Fig. 2.1 depicts three of the main aircraft-carried coordinate systems, which are all right-handed:

- Earth axis (g): the x-axis $\mathbf{x}_g$ is oriented to true north and the z-axis $\mathbf{z}_g$ is perpendicular to the earths tangent plane, pointing towards it.
- Flight path axis (k): the x-axis is tangential to the flight path, with $\mathbf{x}_k$ indicating the flight direction and $\mathbf{z}_k$ pointing towards the earth. The vertical plane (Fig. 2.1a) is rotated by the climb angle γ, the horizontal plane (Fig. 2.1b) by the flight path azimuth χ.

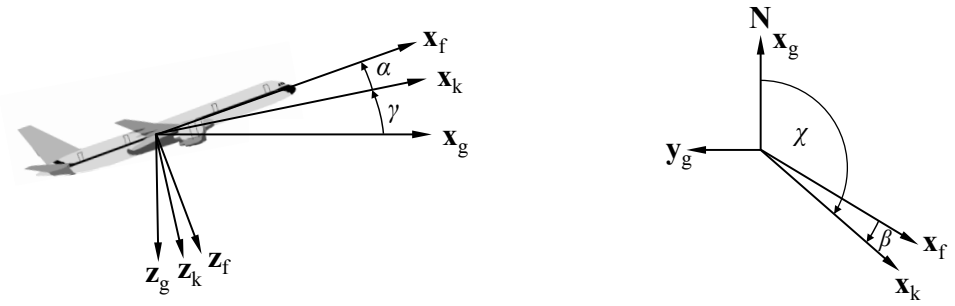

(a) Vertical plane (b) Horizontal plane

Figure 2.1: Definition of the different aircraft-carried axis systems and the angles between them. Wind is neglected and all x-axis are located in the vertical (a) or horizontal (b) plane.

- Body axis (f): the x-axis is the longitudinal axis of the aircraft, the axis of symmetry of the aircraft defines the vertical plane. The main difference to the flight path axis is an additional rotation in the vertical plane by the angle of attack α to produce the required lift force. The sideslip angle β in the horizontal plane can be neglected, especially under the assumption of no wind.

The flight path axis system is used as main reference system in this thesis (Fig. 2.2). It is aircraft-carried and its origin is located at the center of the aircraft as provided from the flight path (Sec. 3.3). It was decided to use the flight path axis instead of the body axis, as the flight path is always available, e.g. for calculations with radar data. In addition, for the acoustical description the differences are negligible (in contrast to flight mechanics), as α typically varies between $\pm 10°$ and β is mainly zero for modern turbofan aircraft.

From the acoustical perspective, the aircraft is simplified to a point source at the origin of the flight path axis with a three-dimensional (3D) directivity. The directivity is described in spherical coordinates by the polar angle θ and azimuth angle φ as depicted in Fig. 2.2. Both radiation angles are calculated with the law of cosine.

$$\theta = \arccos\left(\frac{\mathbf{r}_{k,mic} \cdot \mathbf{x}_k}{|\mathbf{r}_{k,mic}| \cdot |\mathbf{x}_k|}\right) \tag{2.1}$$

$$\varphi = -\mathrm{sgn}(\mathbf{y}_k) \cdot \arccos\left(\frac{\mathbf{r}_{k,mic,yz} \cdot \mathbf{z}_k}{|\mathbf{r}_{k,mic,yz}| \cdot |\mathbf{z}_k|}\right) - \Phi \tag{2.2}$$

The angles are defined from $0° \leq \theta \leq 180°$ and $0° \leq \varphi \leq 180°$ under the assumption of symmetry of φ in the vertical plane. The symmetry is implemented with the signum-function of y_k. To obtain $\mathbf{r}_{k,mic}$, the following transformation from the earth axis system to the flight path axis system is necessary.

$$\mathbf{r}_{k,mic} = \mathbf{T}_{kg}(\chi, \gamma) \cdot \mathbf{r}_{g,mic} \tag{2.3}$$

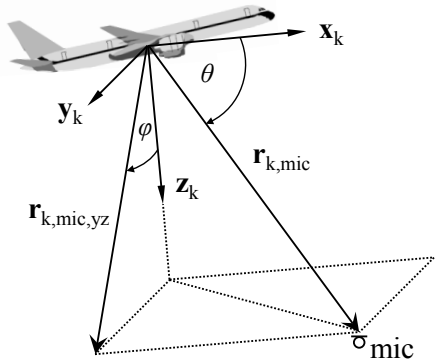

Figure 2.2: Flight path axis system (index k) with polar angle θ and azimuth φ.

The transformation matrix $\mathbf{T}_{kg}(\chi, \gamma)$ [55] is based on two rotations, one over the flight path azimuth χ and one over the climb angle γ as depicted in Fig. 2.1. The vector $\mathbf{r}_{g,mic}$ can be derived by subtracting the microphone position from the flight path, which both are typically available in Swiss coordinates (CH1903).

While the error on θ (Eq. 2.1) is small using the flight path axis instead of the body axis, the error on φ can get significant for the curved flight. Therefore, φ (Eq. 2.2) is corrected with the bank angle Φ, which describes the rotation of the aircraft around the longitudinal axis.

$$\tan \Phi = \frac{\kappa \cdot V_k^2 \cdot \cos \gamma}{g} \tag{2.4}$$

Under the assumption of no acceleration, the bank angle depends on the curvature of the flight path κ, the flight path velocity V_k, the climb angle γ, and the gravity g. All values can be derived from the flight path. For instance, the curvature is calculated with Eq. 2.5, where $\dot{x}, \dot{y}$ are time derivatives of the track coordinates.

$$\kappa = \frac{\dot{x}\ddot{y} - \dot{y}\ddot{x}}{(\dot{x}^2 + \dot{y}^2)^{\frac{3}{2}}} \tag{2.5}$$

2.2 Acoustics

Basic knowledge about acoustics is imparted in the textbooks [59; 66; 69]. Specific background on the sound sources of aircraft is described in [52; 81; 91]. In the connection with sound generated by aircraft the term *noise* is commonly used, also in this thesis. The meaning refers to the technical understanding of a sound rather than to an annoying noise as used in common speech [20].

2.2.1 Acoustic quantities

The sound pressure fluctuation $p(t)$ can be measured with a calibrated free-field microphone and is the basis for the acoustical signal analysis. A common signal attribute is the momentary sound pressure level $L_p(t)$ in Eq. 2.6. $L_p(t)$ is calculated with a moving average of the normalized $p(\vartheta)^2$ applying an exponential time weighting (time constant RC). The most common time weightings are the slow weighting (RC=1 s) and fast weighting (RC=0.125 s).

$$L_p(t) = 10 \log \left(\frac{1}{RC} \int_{-\infty}^{t} \frac{p^2(\vartheta)}{p_0^2} e^{\frac{\vartheta - t}{RC}} \mathrm{d}\vartheta \right) \tag{2.6}$$

Another signal attribute is the sound exposure level L_E. It represents the integral of $p(t)^2$ over the event length t_e (Eq. 2.7).

$$L_E = 10 \log \left(\frac{1}{1\ \mathrm{s}} \int_0^{t_e} \frac{p^2(\vartheta)}{p_0^2} \mathrm{d}\vartheta \right) \tag{2.7}$$

In many cases not only the total L_p is of interest, but also the contribution of the pressure signal in the frequency domain. The signal is then filtered with band-filters from IEC 61260-1 [49]. In acoustics, usually octave or one-third-octave bands (1/3-octave bands) are considered with mid-frequencies from Eq. 2.8 as defined in ISO 9613-1 [56]. The frequency range considered in this work ranges from 25 Hz to 5 kHz.

$$f_m = 1000 \cdot 10^{0.1 \cdot k}, k = -16...7 \tag{2.8}$$

Acoustic metrics are commonly frequency weighted as specified in [28, Annex E]. In the field of environmental noise the A-weighting (Eq. 2.9) is the most common weighting curve, as it accounts for the sound perceived by the human ear: low frequencies are perceived less intense than frequencies around 1 kHz. The A-weighting as depicted in Fig. 2.3 corresponds to an equal-loudness contour that was determined in a listening test. The figure shows, that frequencies below 100 Hz are strongly attenuated for more than 20 dB, thus their contribution vanish for an A-weighted total sound level. Further information about the A-weighting can be found in [69].

$$A_{filter}(f) = 10 \log_{10} \left(\frac{12194^2 f^4}{(f^2 + 20.60^2)(f^2 + 107.7^2)^{0.5}} \cdots \right. \tag{2.9}$$
$$\left. \frac{}{(f^2 + 737.9^2)^{0.5}(f^2 + 12194^2)} \right)^2 - 2\,\mathrm{dB}$$

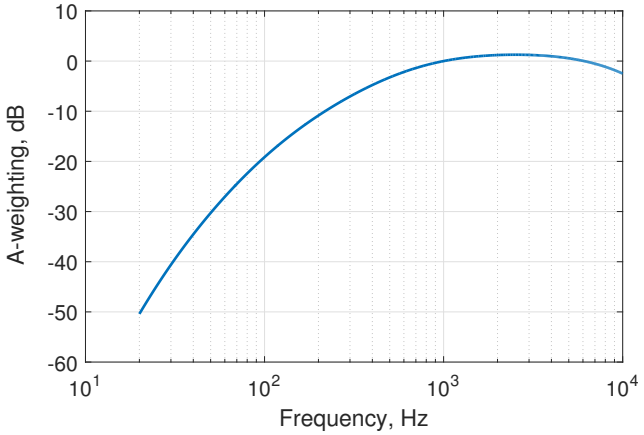

Figure 2.3: A-weighting versus frequency.

For the measurement of a source at a receiver, the sound needs a certain time $^{d}/_{c}$ to travel through the atmosphere along distance d. To calculate the time delay, the speed of sound c is required. Under the assumption that the air behave like an ideal gas (p=ρRT) in the troposphere, Eq. 2.10 is used.

$$c^2 = \kappa \frac{p}{\rho} = \kappa RT \tag{2.10}$$

The air is described by the adiabatic index κ≈1.4 and the specific gas constant R=287 $^{\mathrm{J}}/_{\mathrm{kgK}}$. A received sound pressure signal at a microphone contains these time delays due to the time the sound needed to travel through the atmosphere. The retarded time τ is used to evaluate the original source position when the sound was emitted.

$$\tau = t - \frac{d}{c} \tag{2.11}$$

2.2.2 Uncertainty of measurement

The standard literature on this topic is the Guide to the expression of uncertainty in measurement (GUM) [58]. For specific details to uncertainties in aircraft noise measurement and modeling [19; 85; 97; 98] are highly recommended. The calculation of the measurement uncertainty follows DIN45643 [27, B.2.2.3], which describes the uncertainty for measurement and assessment of aircraft sound.

$$u_{instr} = (u_{mic}^2 + u_{lin}^2 + u_A^2 + u_U^2 + u_p^2 + u_T^2 + u_{RH}^2 + u_{cal,ref}^2 + u_{cal,op}^2)^{1/2} \tag{2.12}$$

In Eq. 2.12 the uncertainty of a measurement system u_{instr} mainly consists of the uncertainty of the directivity of the microphone u_{mic}, the uncertainty of the level linearity u_{lin} and uncertainty of the A-weighting u_A. Additional effects are due to deviations in the voltage supply u_U, atmospheric variations u_p, u_T, u_{RH}, and calibration under reference $u_{cal,ref}$ and operational conditions $u_{cal,op}$. With the provided uncertainties from DIN45643 u_{instr} sums up to 0.86 dB for incidence angles below 90° and to 0.74 dB for incidence angles below 30°.

2.2.3 Sound propagation

A commonly used and appropriate approach for the calculation of the sound pressure level at a particular distance from a point source is defined in Eq. 2.13. The frequency dependent sound pressure $L_p(f)$ at a particular receiver is the sum of the sound power

$L_W(f)$ of the source, a directivity of the source $D(f, \theta, \varphi)$, and the attenuation terms due to the sound propagation $\sum A(f)$.

$$L_p(f) = L_W(f) + D(f, \theta, \varphi) - \sum A(f) \tag{2.13}$$

In this work, the propagation model sonX [33] is used to calculate the attenuation terms. The different methods applied in sonX are summarized below. The model distinguishes between different modules as shown in Eq. 2.14. The modules *Basic* and *Meteo* were used in this thesis, as the measurement points were chosen in such a way that reflections at buildings, forest or cliffs can be neglected.

$$\sum A(f) = A_{Basic}(f) + A_{Meteo}(f) + A_{Reflect}(f) + A_{ForestCliff}(f) \tag{2.14}$$

The basic attenuation $A_{Basic}(f)$ is calculated for a homogenous atmosphere and accounts for geometrical divergence A_{div}, atmospheric absorption A_{atm}, ground reflections and barriers $A_{gr/bar}$, and foliage attenuation A_{fol}. In line with the definition of the sound power level, the geometrical divergence A_{div} includes the conversion constant $\log_{10}(4\pi)$.

$$A_{Basic}(f) = A_{div} + A_{atm}(f) + A_{gr/bar}(f) + A_{fol}(f) \tag{2.15}$$

The geometrical divergence is calculated according to ISO 9613-2 [57]. The atmospheric absorption coefficient $\alpha_{atm}(f)$ is calculated according to ISO 9613-1 [56]. However, the ISO standard with A_{atm}=$\alpha_{atm}(f)r$ is defined for pure tones. To account for broadband aircraft noise and large distances between receiver and source, a correction for broadband noise as proposed in Defrance et al. [25] is applied in sonX[1].

$$A_{atm}(f) = \alpha_{atm}(f)r \cdot (1.0053255 - 0.00122622 \cdot \alpha_{atm}(f)r)^{1.6} \tag{2.16}$$

For the calculation of ground reflections $A_{gr/bar}$, an analytical solution for spherical waves is used, which is extended to uneven terrain and varying ground properties using a Fresnel-zone-approach [23]. Additionally, the ground reflection model accounts for the coherence loss K (Eq. 2.17) between direct and reflected sound in dependence of frequency f and propagation distance r'_{dir} [43].

The parameters γ_0 and γ_1 were derived based on the work of Parkin and Scholes [71] and Daigle et al. [24].

$$K = e^{-(\gamma_0 + \gamma_1 f^2 r'_{dir} + \gamma_2 f^2 d_s)} \tag{2.17}$$

Parkin and Scholes [71] used a single mounted jet engine, which is not fully applicable to the whole aircraft as the sound is stemming from two or more engines and other source

[1] Eq. 2.16 yields decreasing values with increasing distance for air absorptions greater than approximately 250 dB. The term $\alpha_{atm}(f)r$ in the bracket is therefore limited to 200 dB.

locations. The sound sources can be separated in some cases by substantial distances of up to 50 m. To account for this effect, the approach for the coherence loss according to [43] was extended with $\gamma_2 f^2 d_s$ as given in Eq. 2.17. The newly introduced parameter γ_2 was derived in comparison with measurements of Airbus A340 and Fokker 100, the first having wing-mounted engines with large spacing in between them, the latter having body-mounted engines with small spacing. For large aircraft, a standard setting of the source distance d_s of 50 m is recommended.

Barriers are calculated according to the approach of Pierce [72]. Foliage attenuation is implemented according to the annex of ISO 9613-2 [57].

The meteorological attenuation $A_{Meteo}(f)$ is described as deviations from the homogenous atmosphere (Eq. 2.18) which occur due to vertical profiles of temperature, pressure, relative humidity, and wind. First, the local temperature and humidity change the atmospheric absorption. Second, the gradients of wind and temperature bend the sound rays which may result in shadow zones, change the barrier effect, and change the foliage attenuation. Shadow zones and barrier effects are combined in D_{met}. These effects can play an important role in the sound propagation.

$$\begin{aligned} A_{Meteo}(f) &= (A_{atm,Meteo}(f) - A_{atm,Basic}(f)) \\ &\quad +(A_{fol,Meteo}(f) - A_{fol,Basic}(f)) - D_{met} \end{aligned} \tag{2.18}$$

2.2.4 Moving sound source

A moving sound source changes the received sound pressure signal. The sound wave crests are compressed in the direction of motion and stretched to the opposite direction. Consequently, the received frequency spectrum is shifted towards higher or lower frequencies, which is referred to as Doppler shift. In addition, also the sound intensity at the receiver increases or decreases because the number of arriving crests per time interval changes. This effect is called the kinematic effect in [94]. Both effects scale with the Doppler factor DF, which is defined in dependency to the relative Mach number of the source towards the receiver.

$$DF = 1 - Ma \cdot \cos\theta \tag{2.19}$$

The frequency at the receiver f_{Rec} is shifted with the ratio DF^{-1} with respect to the frequency at the source f_{Src}.

$$f_{Rec} = DF^{-1} \cdot f_{Src} \tag{2.20}$$

In the same manner the change of the sound pressure due to motion of the source can be described. For a pressure point source at subsonic speeds, $p(t) \propto DF^{-1}$ [44, p. 49],

which is known as the kinematic effect of a sound source in motion. Not only the kinematic effect is accounted for, but also the dynamic effect of noise sources that move with the aircraft as classified by Stone [94]. The dynamic effect accounts for the motion of the source relative to the propagation medium, which is dependent on the type of source, e.g. monopole, dipole or quadrupole ([77; 94]). For a volume monopole or force dipole, $p(t) \propto DF^{-2}$ [44, p. 50].

Combing both effects leads to the following general level amplification for aircraft noise, which was experimentally supported by [68]. Eq. 2.21 describes the flight effects for the calculation from the source to a receiver.

$$\Delta L_{FE} = 40 \cdot \log_{10}(DF^{-1}) \tag{2.21}$$

The frequency shift as well as the flight effect occur at the source which is in motion. Thus, in a simulation (Sec. 2.4) both effects are applied before the attenuations due to propagation are added to the sound power level of the source. For a calculation from the source to the receiver (Sec. 3.5), first the sound propagation is reversed before the inverse Doppler shift and flight effect are applied.

As mentioned in Sec. 2.2, acoustic signals are often analyzed within frequency bands. In this case, the implementation of the Doppler shift in Eq. 2.20 is not straight forward. The energy of a single tone with high amplitude may lie in the middle or at the border of a band but is now distributed over the whole bandwidth. To apply Doppler effect on frequency bands, an assumption has to be made for the distribution of the energy in each frequency band. Therefore, a method is introduced in this work, which assumes equally distributed energy over each frequency band. The method is used to remove the measured Doppler shift from a sound power spectra as well as to apply the Doppler shift on a predicted sound power spectra for a simulation.

At first, a ratio q_{DF} is determined, which defines how much sound power of each band is shifted. Fig. 2.4 depicts how the ratio is defined in dependency of DF=0.7 in relation to the nearest integer band-shifts (DF_{lim}). The difference of DF to the lower limit (ΔDF) over the width (ΔDF_{lim}) of the two surrounding limits leads to the ratio searched for:

$$q_{DF} = \frac{\Delta DF}{\Delta DF_{lim}} = \frac{DF^{-1} - DF_{lim,i_n-1}}{DF_{lim,i_n} - DF_{lim,i_n-1}}. \tag{2.22}$$

The limits DF_{lim} of integer 1/3-octave band shifts i are calculated with Eq. 2.23, which is derived from Eq. 2.8. An i of 0 corresponds to no shift (θ=90° or Ma=0), an i

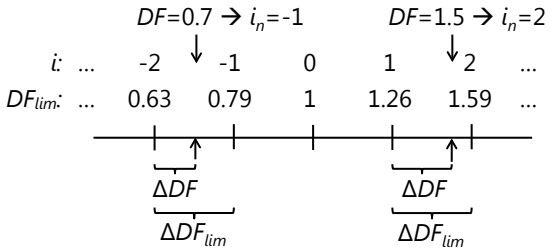

Figure 2.4: Scheme for the application of the Doppler shift to 1/3-octave bands. Two examples are shown on the an axis with DF_{lim}.

of -1 corresponds to a shift of one entire band to lower frequencies and an i of $+1$ to a shift of one entire band to higher frequencies.

$$DF_{lim} = 10^{0.1 \cdot i}, i = -10... + 10 \tag{2.23}$$

The actual index i_n used in Eq. 2.22 for a given flight configuration corresponds to the subsequent DF_{lim} higher than DF. In the examples of Fig. 2.4 the subsequent i_n would be -1 for DF=0.7 and 2 for DF=1.5.

Finally, the shifted sound power $W_{shifted,k}$ is calculated for each frequency band k with Eq. 2.24. It consists of the sound power of the two bands $k - i_n$ and $k - i_n + 1$ with the proportions defined by the ratio q_{DF}. In the example for the negative frequency shift (DF=0.7), each frequency band would be composed of the energy of parts of the two subsequent higher bands.

$$W_{shifted,k} = W_{k-i_n} \cdot q_{DF} + W_{k-i_n+1} \cdot (1 - q_{DF}) \tag{2.24}$$

$$L_{W,k} = 10 \log_{10} \left(\frac{W_{shifted,k}}{W_0} \right) \tag{2.25}$$

Remark: Under the assumption of equally distributed energy over a band, the spectrum is smoothed when shifting it with the proposed method. Thus, applying this algorithm back and forth on a spectrum does not lead to the original spectrum.

2.3 Multiple linear regression

Helpful textbooks on linear regression models are Neter et al. [70] and Zuur et al. [108]. The classical approach for multiple linear regression in matrix notation from [70, p. 222] is given in Eq. 2.26. It represents the formal statement of the model.

$$\mathbf{Y} = \mathbf{X}\boldsymbol{\beta} + \boldsymbol{\epsilon} \tag{2.26}$$

In the response vector $\mathbf{Y}$ all n observations of an experiment or measurement are included. All m explanatory variables build the columns of the design matrix $\mathbf{X}$ with corresponding n rows for each observation. $\boldsymbol{\beta}$ is a vector with regression parameters, $\boldsymbol{\epsilon}$ represents the vector of independent normal random variables with expectation.

2.3.1 Model assumptions and model checks

The following assumptions are made by applying the ordinary least squares (OLS) algorithm to estimate the coefficients of the model:

- **Normal distribution:** The errors are normal distributed, $\epsilon_i = N(0, \sigma_\epsilon^2)$. The assumption is checked visually with normal plots (Q-Q plots) of the residuals.
- **Expectation value:** The expectation of the error is zero, $E[\epsilon_i] = 0$. This means, the relations between the explanatory variables and dependent variable are linear. The assumption is checked with scatterplots of the residuals against the explanatory variables and against the fitted values. The smoother (moving average) should not systematically deviate from zero.
- **Constant variance:** Constant variance of the error term, $\mathrm{Var}(\epsilon_i) = \sigma_\epsilon^2$. The assumption is checked with scatterplots of the residuals against the explanatory variables and against the fitted values. The variance should be constant along the x-axis.
- **Independent observations:** No correlations between the errors of the different instances, $\mathrm{Cov}(\epsilon_i, \epsilon_j) = 0$ for all $i \neq j$. Scatterplot of residuals, see above.

2.3.2 Weighted least squares

To introduce weights on the observations, the classical OLS can be extended by a diagonal weight matrix $\mathbf{W}$. Consequently, with weighted least squares (WLS) the predicted error mean square $\widehat{\sigma}_E^2$ is to be minimized numerically to estimate the regression coefficients $\mathbf{b}_w$.

$$(\mathbf{X'WX})\mathbf{b}_w = \mathbf{X'WY} \tag{2.27}$$

The coefficient of determination R^2 and the error mean square $\widehat{\sigma}_E^2$ [70, p. 424] are also weighted with the corresponding weighting factor w_i for each of n observations.

$$R^2 = 1 - \frac{\sum_{i=1}^{n} w_i \left(y_i - \widehat{y}_i\right)^2}{\sum_{i=1}^{n} w_i \left(y_i - \overline{y}\right)^2} \tag{2.28}$$

$$\widehat{\sigma}_E^2 = \frac{1}{n - (m+1)} \sum_{i=1}^{n} w_i \left(y_i - \widehat{y}_i\right)^2 \tag{2.29}$$

The fitted values are calculated with $\widehat{\mathbf{Y}} = \mathbf{X}\mathbf{b}_w$ and the error vector $\boldsymbol{E}$ of the residual terms with $E_i = y_i - \widehat{y}_i$. All models of the present thesis were fit with the help of the Statistical Toolbox of Matlab 2014b. The fit of the models with WLS was carried out by *fitlm*.

2.3.3 Outlier detection

Outliers are removed before estimating the coefficients by an adaptive outlier detection method of Filzmoser [34]. This method uses the robust Mahalanobis distance RD (for multiple parameters) to automatically detect at which quantile the tails of the RD^2 distribution deviate from the ideal χ^2 distribution. Filzmoser outlines that an often used fixed threshold (e.g. $\chi^2_{p,0.98}$) is inadequate because (extracted from [34, p. 582])

1. If the data should indeed come from a single multivariate normal distribution, the threshold would be infinity because there are no observations from a different distribution (only extremes);
2. There is no reason why this fixed threshold should be appropriate for every data set; and
3. The threshold has to be adjusted to the sample size

The advantages of the method are that the threshold is adjusted to the sample size and therefore only detects reasonable outliers. It is thus possible that no outliers are detected in contrast to a outlier detection based on a fixed threshold.

2.3.4 Model selection

Zuur [108, p. 541] lists three options how to generally select model parameters:

1. Drop individual explanatory variables one by one based on hypothesis testing procedures.
2. Drop individual explanatory variables one by one (and each time refit the model) and use a model selection criteria like the Akaike information criterion (AIC) or Bayesian information criterion (BIC) to decide on the optimal model.
3. Specify a priori chosen models, and compare these models with each other.

In this work R^2 and the root-mean-square error $\widehat{\sigma}_E$ are used to compare the model approaches. The criteria AIC [2] and BIC [89] are two popular measures which were used in addition. They both provide penalties for adding more explanatory variables to the model.

In general, each explanatory variable that is included into the model must show a linear behavior in respect to the dependent variable. This implies a careful data exploration and

the use of physical relations. To establish a linear behavior variable transformations are applied, such as the logarithm or quadratic transformations of the explanatory variable.

It is also important not to include explanatory variables that are correlated to other explanatory variables (multicollinearity). First, this would have strong effects on the estimates of the regression coefficients and brings the risk of overfitting. To prevent for multicollinearity, a correlation matrix (Eq. 2.30) and the variance inflation factor (VIF) (Eq. 2.31) are used.

$$\rho_{i,j} = \frac{\mathrm{Cov}(X_i, X_j)}{\sqrt{\mathrm{Var}(X_i) \cdot \mathrm{Var}(X_j)}} \tag{2.30}$$

The VIF is calculated with m-times of multiple linear regression, where each explanatory variable is used as dependent variable to the other explanatory variables (see [70, p. 408]). In this way, the coefficient of determination R_m^2 results the degree of correlation to all other model parameters.

$$VIF_m = \frac{1}{1 - R_m^2} \tag{2.31}$$

2.3.5 Energy correction

The result of the multiple linear regression with WLS is a model that represents the arithmetic mean value $\widehat{L}$ of the underlying data in dependency of its explanatory variables. While statistically correct, the logarithmically scaled sound levels have to be averaged energetically, which is the arithmetic mean of the sound power. Assuming that the sound power levels are normally distributed, which is one of the mandatory requirements for the linear regression, an analytical correction can be applied [6, p. A.38] and [31, p. 50].

$$L = \widehat{L} + 0.115 \cdot \sigma^2 \tag{2.32}$$

For multiple linear regression the expectation of the error mean square corresponds to the variance σ^2 [70, p. 225], hence $\widehat{\sigma}_E^2$ is an unbiased estimator of σ^2 [70, p. 25].

$$E\left(\widehat{\sigma}_E^2\right) = \sigma^2 \tag{2.33}$$

2.4 Simulation

2.4.1 Time-step method

In this section the calculation of a level-time history $L(t)$ based on discrete source positions is derived. Such method is necessary to compare simulations to measurements over time on the basis of single events. A time-step procedure with j discrete source

positions is used to calculate the discrete sound pressure levels $L_{r,j}(f)$ at a receiver r with Eq. 2.34.

$$L_{r,j}(f) = \underbrace{\widehat{L}_{\overline{em},total,j}(f)}_{Eq.\ 4.19} + \underbrace{\Delta L_{FE,j}}_{Eq.\ 2.21} - \underbrace{\sum A_j(f)}_{Eq.\ 2.14} \tag{2.34}$$

$L_{r,j}(f)$ is the sum of the predicted and Doppler shifted sound emission level $\widehat{L}_{\overline{em},total,j}(f)$, of the flight effect $\Delta L_{FE,j}$, and of the attenuations $\sum A_j(f)$. It is particularly important to correct for the same flight effect as applied to the back propagation (Sec. 3.5) to avoid systematic errors. Fig. 2.5 depicts how sensitive the flight effect changes the directivity already at relatively low Mach numbers at departure.

The energy sum over all frequencies results in the total $L_{r,j}$ (Eq. 2.35). The commonly used A-weighting can be introduced in this equation by adding a $A_{filter}(f)$ as described in Sec. 2.2.

$$L_{r,j} = 10\log_{10}\sum_{f=1}^{24} 10^{0.1(L_{r,j}(f)+A_{filter}(f))} \tag{2.35}$$

Fig. 2.6 depicts a scheme with j generated sound emission levels at their emission time τ_j (Sec. 2.2.1) and irregular time-bins which represent the time period, where $L_{r,j}$ is assumed to be constant. These time-bins are defined over the interval $[t_{r,j}; t_{r,j+1}]$ around the time instant $\tau_j + {}^{x_j}/_{c}$, which is the time at which the noise generated at τ_j reaches the receiver. The time intervals are calculated as follows.

$$t_{r,j} = \begin{cases} \frac{3}{2}\left(\tau_j + \frac{x_j}{c_j}\right) - \frac{1}{2}\left(\tau_{j+1} + \frac{x_{j+1}}{c_{j+1}}\right) & \text{for } j = 1; \\ \frac{1}{2}\left(\tau_j + \frac{x_j}{c_j} + \tau_{j-1} + \frac{x_{j-1}}{c_{j-1}}\right) & \text{for } j = 2...T. \end{cases} \tag{2.36}$$

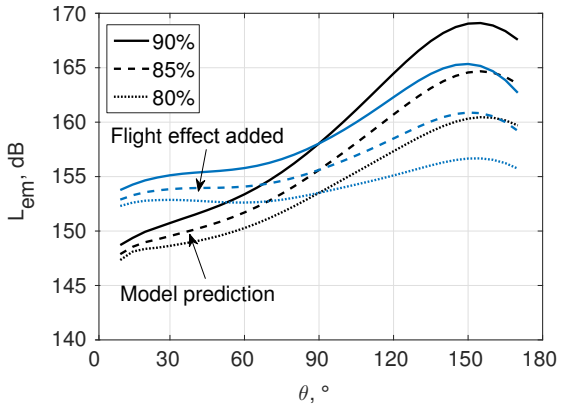

Figure 2.5: Comparison of the influence of the flight effect with Ma=0.26 for typical departure settings of $N1$. (Aircraft type: A330-300 with TRENT7)

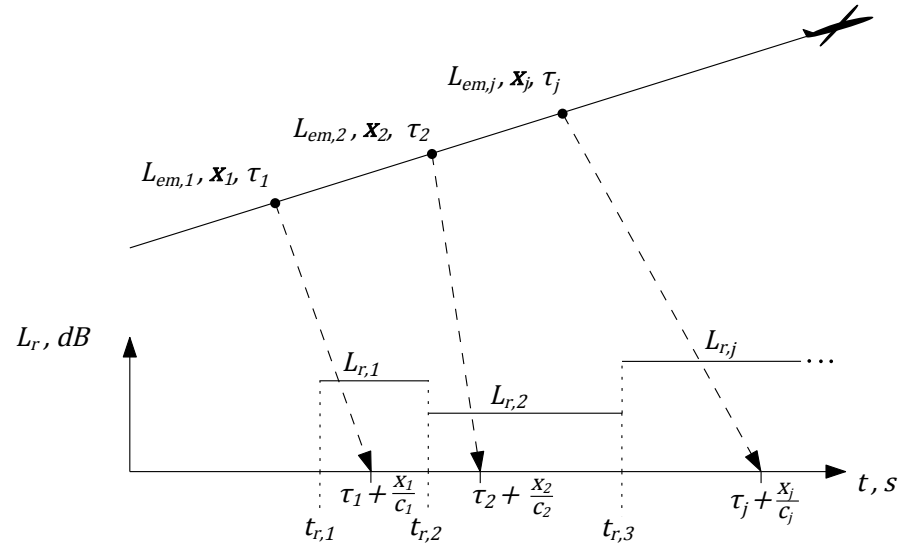

Figure 2.6: Geometry of the time-step simulation with irregular time-bins of constant sound pressure levels L_r at the receiver.

The time resolution of the flight path is free of choice and could also be unevenly spaced. For each position vector $\mathbf{x_j}$ of the aircraft with respect to the receiver the attenuations and the time delay are calculated with sonX. More specifically, the vertical stratification of the atmosphere is taken into account for the air absorption but also for the speed of sound.

Each of the time intervals was related to a constant $L_{r,j}$. Likewise, a constant sound pressure p_j can be expressed for each time-bin (Eq. 2.37). The sound pressure is the basis for the signal analysis of a measured (analog) signal and therefore helps to derive the equations for an equivalent signal analysis for the simulation results.

$$p_j^2 = p_0^2 \cdot 10^{0.1 L_{r,j}} \tag{2.37}$$

The momentary sound pressure level $L_p(t)$ for an analog signal can be calculated with Eq. 2.6. Identically, the step function of constant p_j can be integrated with a moving average from $-\infty$ to any t. The time constant RC of exponential weight function defines the part of the sound pressure signal which is accounted for. Thus, in the case of simulation, the Eq. 2.6 is rewritten to Eq. 2.38 for constant sound pressure values in each time interval.

$$L_p(t) = \begin{cases} 10\log_{10}\left(\frac{p_1^2}{RC \cdot p_0^2} \int_{t_{r,1}}^{t} e^{\frac{\vartheta - t}{RC}} d\vartheta\right) & \text{for } t_{r,1} < t < t_{r,2} \\ 10\log_{10}\left(\frac{1}{RC \cdot p_0^2}\left(\sum_{j=1}^{K-1} p_j^2 \int_{t_{r,j}}^{t_{r,j+1}} e^{\frac{\vartheta - t}{RC}} d\vartheta \right.\right. & \text{for } t > t_{r,2} \\ \left.\left. + p_K^2 \int_{t_{r,K}}^{t} e^{\frac{\vartheta - t}{RC}} d\vartheta\right)\right) & \end{cases} \tag{2.38}$$

K is the integer that holds $t_{r,K} < t < t_{r,K+1}$ for each value of t. The only restriction for Eq. 2.38 is a time step of τ smaller than RC, in this work the time step is 50 or 100 ms. In this way, for instance the L_{AS} can be calculated on an equidistant time axis, which is necessary to compare level-time histories of a simulation to a measurement on the basis of L_{AS}. With Eq. 2.37 and solving the integrals, the momentary sound pressure level can also directly be calculated from the discrete $L_{r,j}$.

$$L_p(t) = \begin{cases} 10\log_{10}\left(10^{0.1L_{r,1}}\left(1 - e^{\frac{t_{r,1}-t}{RC}}\right)\right) & \text{for } t_{r,1} < t < t_{r,2} \\ 10\log_{10}\left(\sum_{i=1}^{K-1} 10^{0.1L_{r,j}}\left(e^{\frac{t_{r,j+1}-t}{RC}} - e^{\frac{t_{r,j}-t}{RC}}\right)\right. & \text{for } t > t_{r,2} \\ \qquad \left. +10^{0.1L_{r,K}}\left(1 - e^{\frac{t_{r,K}-t}{RC}}\right)\right) & \end{cases} \tag{2.39}$$

2.4.2 Metrics

From the momentary sound pressure level in Eq. 2.39 the maximum sound pressure level L_{max} and the sound exposure level L_E can be derived. The former metric could also be derived with a simple integral of the sound pressure level based on the retarded time. However, the level-time histories are used to compare single event for an entire overflight as well as to determine the time-weighted $L_{AS,max}$. The maximum sound pressure level can be directly determined for the chosen time constant RC. The sound exposure level is calculated on the same basis as above, with the sum of constant sound pressure or L_r, respectively (Eq. 2.40).

$$L_E = 10\log_{10}\frac{\sum_{j=1}^{T} p_j^2(t_{r,j+1} - t_{r,j})}{p_0^2 \cdot 1\,\mathrm{s}} \tag{2.40}$$

$$L_E = 10\log_{10}\sum_{j=1}^{T}\frac{(t_{r,j+1} - t_{r,j})}{1\,\mathrm{s}} \cdot 10^{0.1L_{r,j}} \tag{2.41}$$

2.4.3 Process of verification

A verification of the aircraft noise emission models was conducted by simulating all flight events which were also used to create the model (Chap. 6). The term verification is used instead of validation because the measurements were used to build the model and are thus not independent. The comparison to the measured input data should therefore verify that the regression equations are correct, i.e. that the model approach is able to reproduce the measurements. Further explanation and a discussion on the use of k-fold cross validation is given in Sec. 4.1.

For a comparison with measurements $L_{AS,max}$ is determined from the A-weighted $L(t)$ with the time constant slow. The L_{AE} is calculated over the same time period as the measurements. Determining the L_{AE} could lead to an overestimation of the

measurements due to background noise. The $L_{AE,t10}$ is used in this work to guarantee an adequate comparison between measurement and simulation.

The $L_{AE,t10}$ is defined in SAE1845 [82, App. B] and represents the sound energy of the time interval where the momentary sound pressure level is less than 10 dB below the $L_{AS,max}$ (Fig. 2.7a). This time limitation leads to an underestimation of the L_{AE}, which is normally not greater than 0.5 dB. $L_{AE,t10}$ of the simulation is calculated with Eq. 2.41, based on L_r. On the contrary, $L_{AE,t10}$ of the measurements is calculated with Eq. 2.42, based on the time-weighted momentary level L_{AS}.

This difference of the methodology is necessary, as the sound pressure signal of the simulation is much smoother than the one from the measurement (Fig. 2.7b). A sound pressure peak of about 3 dB as shown in the example Fig. 2.7b, can lead to a shifted interval of the t10-time and would underestimate the $L_{AE,t10}$ compared to L_{AS}-based version in Fig. 2.7a. Therefore, the $L_{AE,t10}$ based on the L_{AS} is a good solution for a comparison of measurement and simulation. As the time-weighting is energy-neutral, this makes almost no difference to the L_{AE}.

$$L_{AE,t10} = 10 \log_{10} \sum_{j=t_1}^{t_2} \Delta t_j \cdot 10^{0.1 L_{AS,j}} \tag{2.42}$$

The statistics for the verification are based on the differences of simulation minus measurement.

$$\Delta L_{AE,t10} = L_{AE,t10,sim} - L_{AE,t10,meas} \tag{2.43}$$

$$\Delta L_{AS,max} = L_{AS,max,sim} - L_{AS,max,meas} \tag{2.44}$$

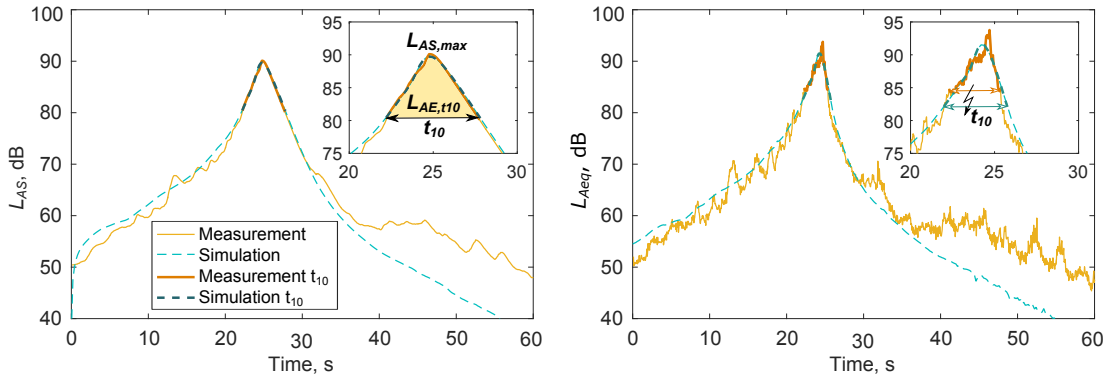

(a) L_{AS}-time history (b) L_{Aeq}-time history

Figure 2.7: Differences in the level metrics between simulation and measurement. The determination of $L_{AE,t10}$ is based on the the L_{AS} (a), as the fluctuations of the measured short L_{Aeq} (50 ms) in (b) lead to systematic errors.

In this way, not only the differences of the aircraft noise emission models but also errors in the propagation model are included in such a comparison. In addition, background noise sources might still be included in the measurements, which influence the statistical results. To account for the latter, all level differences between calculation and measurements with $|\Delta L_{AS,max}| \geq 5\,\mathrm{dB}$ or $|\Delta L_{AE,t10}| \geq 5\,\mathrm{dB}$ or $|\Delta t_{10}| \geq 10\,\mathrm{s}$ were checked and events with strong background noise were discarded.

Typical plots used in the verification section for the high number of flights are scatter plots and box-and-whisker plots. The latter is explained in Fig. 2.8 in comparison to the probability density function of a normal distribution. The thick line represents the median of the distribution, the box represents the interquartile range (IQR) which is the range from the first to the third quartile. The whiskers extend each end of the box to 1.5 times of the IQR. Outliers (∘) are defined to be inside of 3 times the IQR, values above are declared as extrema (⋆).

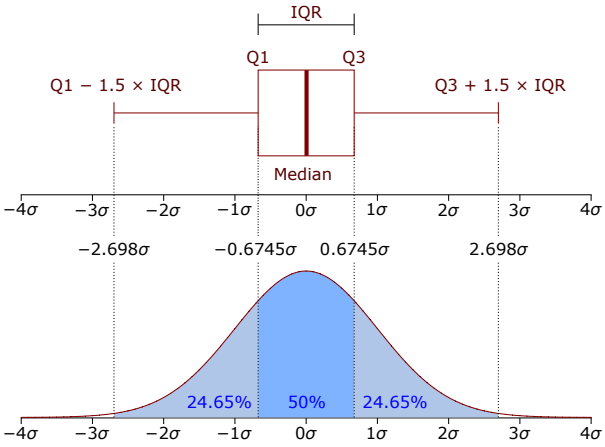

Figure 2.8: Definition of the box-and-whisker plot compared to the probability density function of a normal distribution. Image: Jhguch at en.wikipedia, CC BY-SA 2.5, https://commons.wikimedia.org/w/index.php?curid=14524285

3 Data acquisition and processing

In this chapter, the data basis of the thesis is introduced. The acoustical measurements in the close range and far range at Zurich airport are described. Due to different runway lengths, operational concepts and destinations at this airport, a large variety of flight configurations could be gathered for the development of the aircraft noise emission model. Additional data such as the flight paths, flight parameters, and meteorological data are presented. Finally, the data processing and the resulting data set are shown. Parts of this chapter are revised and extended versions of [104], [105], and [107].

3.1 Acoustical measurements

Acoustical measurements have been carried out at Zurich airport under regular air traffic to collect the dominant commercial aircraft types operating on Swiss airports. The measurements covered different routes on approach (A) and departure (D) in the close and far range of Zurich airport.

The scope of the acoustical measurements was to cover a frequency range from 25 Hz to 5 kHz. This frequency range was chosen to cover the characteristics of aircraft noise which contains high acoustic energy in the low frequency range from the jet. Frequencies above 5 kHz are quickly attenuated due to the normally relatively large distances between aircraft and receiver and can thus only be measured close to the source.

3.1.1 Directivity patterns in the close range

In close vicinity of the airport, data for 3D directivity patterns were collected. It was necessary to measure in close distance to the aircraft because only there it is possible to gain measurements for large lateral radiation angles φ. Also a wide range of polar angles θ can be covered for very small and large angles (radiation to the aircraft nose and rear).

The measurement layout is depicted in Fig. 3.1. For each runway seven to eight microphones were used to cover a wide range of radiation angles. On runway 14 all types of aircraft land during daytime (Fig. 3.1a). During daytime, the major number of departures of narrow-body aircraft can be collected on runway 28 (Fig. 3.1b). Wide-body aircraft such as the A330 or A380 normally take-off to the south from the longest runway 16.

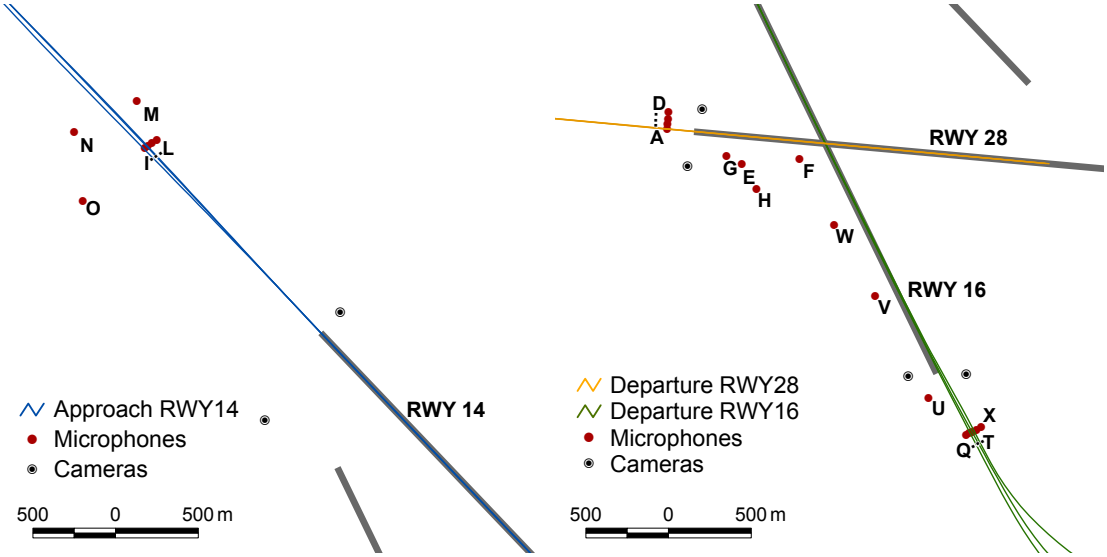

(a) Approach 14 (b) Departure 28 and 16

Figure 3.1: Measurement setup in the close range of Zurich airport with example flight tracks

To define the locations of the microphones, a Matlab program was used to obtain an optimal measurement layout. As the take-off positions are very variable, flight paths derived from radar data of different aircraft types with an early and a late take-off point per type were used as input data for the prediction tool. For landing aircraft the flight path is well defined by the glide path.

Fig. 3.2 shows example results of the prediction tool. For a flight path with a short take-off, almost all microphones showed a good coverage in θ (Fig. 3.2 left) because of their location in front of the take-off point. The data are expected to be limited to angles of θ between 15 and 170 °. However, this range is sufficient whilst smaller and larger angles are negligible with respect to their sound contribution. Further, the variation of the flight paths of a statistically adequate number of events will provide data for large areas of the sphere, as shown in Fig. 3.2 right. Within the marked surfaces for two example microphone positions, good data coverage can be predicted.

The data coverage depends on the microphone positions as well as on the take-off points. For the same aircraft type, the take-off points vary up to 500 m while they vary up to 1 500 m between different aircraft types due to different take-off weights and thrust levels. Therefore, the microphones are located not only at the end of the runways, but also alongside the runways to catch early take-offs. In addition, the final layout also depends on various other boundary conditions such as safety restrictions at the airport, inaccessibility of some areas and acoustically disadvantageous locations with reflections or high background noise.

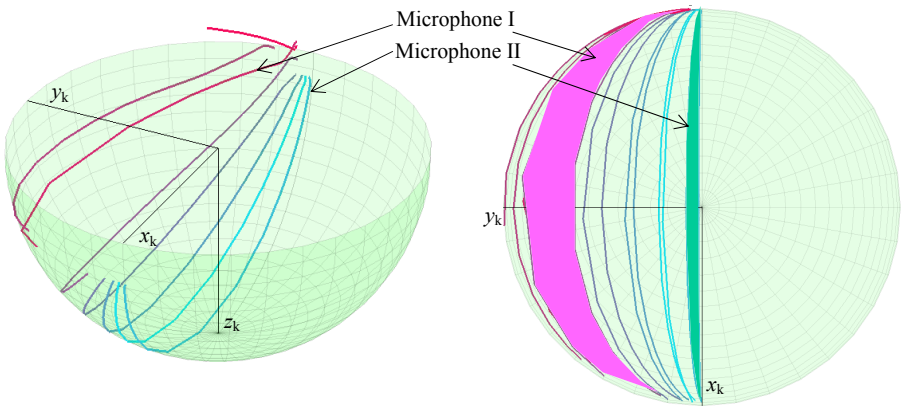

Figure 3.2: Angle coverage by a given measurement setup for a short take-off (left) and two flights of the A320 with different take-off points (right). As a result of the variation in the flight paths, a wide range of angles can be measured with one microphone.

This concept to design the measurement layout as presented in [105], was verified again after the measurements. Fig. 3.3a shows departures from runway 28 for all measured flights of the A320. The coverage of the directivity is almost complete, taking into account that the lateral directivity is assumed to be symmetrical to the y_k-z_k-layer ($|\varphi|$ is plotted). Only very high lateral angles to the side $\varphi > 80°$ are not covered. Also the distribution for approaches in Fig. 3.3b confirms that the measurement layout was well chosen. Due to the identical flight path for each final approach, the variation and coverage for each microphone is much smaller than for the departure. The directivity pattern is not covered for all angle-combinations, but the missing regions can be interpolated as the microphones are evenly distributed over φ. Hence, the placing and distribution of the microphones with the help of the prediction tool was successful.

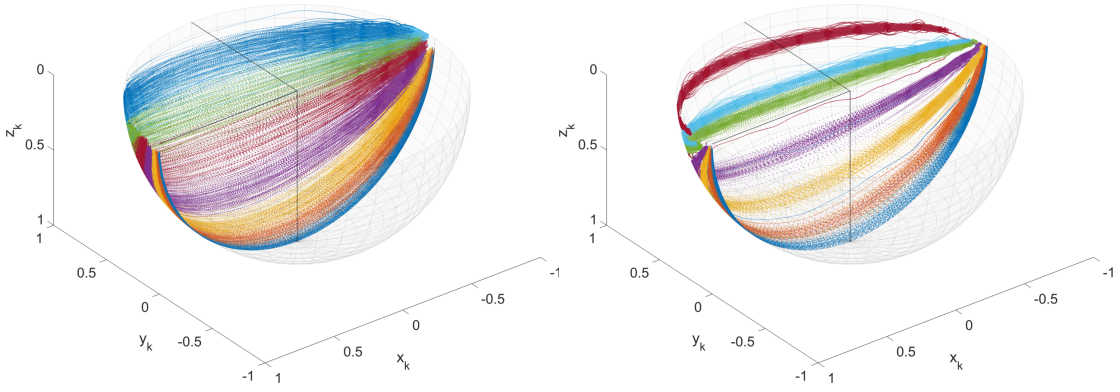

(a) Departure 28 (b) Approach 14

Figure 3.3: Angle coverage of measurements in the close range

Approaches on runway 14 were measured during final approach with a minimum distance of 85 m above microphone I. Departures are measured in the phase of initial climb, after the lift-off. The mean distances to the microphones variate between 85 and 260 m, depending on aircraft type and runway.

3.1.2 Additional flight configurations in the far range

Additional flight configurations were measured at ten autonomous measurement stations, which were placed in the far range of the airport with distances up to 20 km (Fig. 3.4). The figure depicts three example flight tracks for each runway to show the nominal routes. Departures were measured on the same runways as in the close range to cover narrow and wide-body aircraft. Approaches were measured on the glide path of runway 34. Due to the bundling of the aircraft the range of the lateral radiation angles is very limited. However, for departures the dispersion of the tracks is much wider which also allows collecting a certain range of lateral radiation angles in the far range.

Departures at Zurich airport follow the noise abatement departure procedure (NADP) NADP1 [45], conducting the cutback at approximately 460 m and climbing at maximum rate until 1070 m above runway [1]. The flight configurations before cutback are covered by the microphones in the close range. The flight configurations after cutback are measured at the measurement points 5 for D28 and 8 for D16 during climb with constant

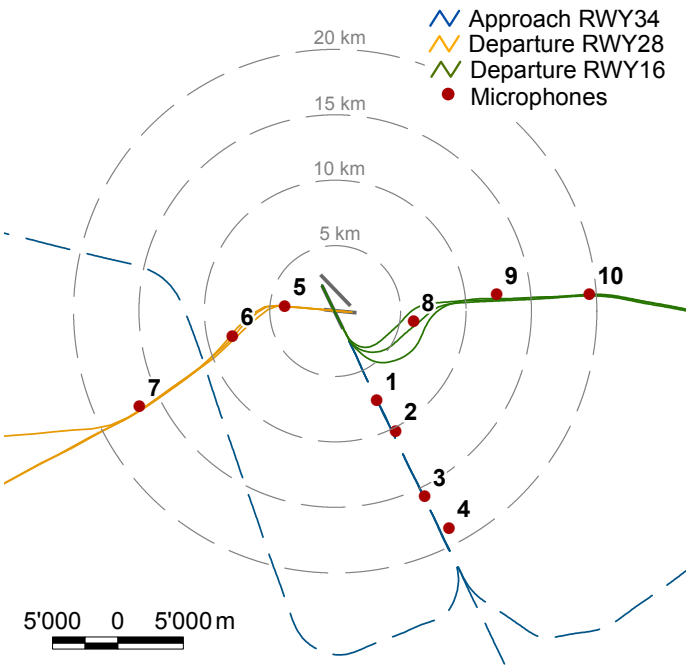

Figure 3.4: Measurement setup in the far range of Zurich airport with example flight tracks

speed and thrust. Measurement points 6 (D28) and 9 (D16) are located in the phase of acceleration where the flaps and slats are retracted. Finally the aircraft continue to climb in clean configuration which is measured at 7 (D28) and 10 (D16).

Approaches are measured along the glide path. On the glide path the scope of the pilot is to reduce the speed of the aircraft to landing speed, which can only be achieved by increasing lift and drag. Thus, the aeroplane configuration (high-lift devices, landing gear) is changed stepwise until the final approach configuration is set. Measurement point 4 is the first point where the aircraft are bundled (Fig. 3.4). Ahead of this position, the flight tracks are curved and gather from every direction, thus no optimal measurement location can be set further away. At 4 the aircraft are expected to arrive in almost clean configuration, i.e. flap-position 1 or 2 is set (see Sec. 3.4.1), and the landing gear is retracted. Measurement points 2 and 3 cover further configuration steps with different speeds, flap-settings and the deployed of the gears. Finally, the aircraft is measured in final approach condition at measurement point 1. In contrast to the measurements in the close range this point is still approximately 4 km further ahead and measures slightly higher speeds and more variations in thrust.

The measurement points on D28 and D16 had to be designed differently for narrow-body and wide-body aircraft because of the different climb power of the aircraft types. Especially for aircraft with two engines, the minimum distances to the measurement points increase fast (Table 3.1). For the A320 the distances at 5 are 650 m and 1440 m at 7. This influences the availability of high frequency bands which are highly attenuated with larger distances. The layout for D16 was optimized for wide-body aircraft, thus the A320 is probably not always in the intended flight configuration as for D28. Nevertheless these measurement points can still be evaluated and deliver an even wider range of flight parameters. In contrast, the distances of the A343 are only 430 m at 5 or 970 m at 10.

Table 3.1: Mean minimum 3D distances to the measurement points in m per type and flight configuration. The minimum 3D distance also depends on the horizontal distance of the flight path to the receiver. In particular for MP 8 a high variance of the tracks was found.

		Cutback		Acceleration		Cont. Climb	
Type	# Eng.	5 (D28)	8 (D16)	6 (D28)	9 (D16)	7 (D28)	10 (D16)
A320	2	650	1000	1200	1270	1440	1645
A333	2	600	850	1090	1180	1370	1290
A343	4	430	1150	1010	1015	–	970
RJ1H	4	380	650	980	1170	1230	1300

3.1.3 Static engine run-up test

A static run-up test was conducted for the A330-300 with its TRENT7 engines in the free field on runway 16 of Zurich airport. The primary scope of the measurement was to identify the sound insulation of the new noise protection hangar at Zurich airport by comparing the spectral sound power of the aircraft outside with the aircraft inside the hangar at similar measurement points [32]. The run-up test was executed by Swiss International Air Lines and the measurements were conducted by Empa and Zurich airport. With the permission of all parties, the data from [32] were reanalyzed in this work to find the functional relation of the sound pressure level (L_p) and the rotational speed of the low pressure shaft ($N1$). The stationary aircraft excludes all airframe noise sources and flight effects from the measurements.

Fig. 3.5 depicts the measurement setup with five microphone locations at a radius of 170 m for radiation angles of $15°, 50°, 90°, 120°$, and $155°$. The right engine was driven from idle to the highest thrust setting possible on ground up and down in six steps (Fig. 3.6). The whole cycle was repeated once to maintain a higher number of samples, i.e. each thrust level was established two to four times. The left engine acted as balance engine for the highest thrust setting to reduce the effective torque on the aircraft. This may have led to additional noise, but the left engine was shielded with the fuselage and thus the influence can be neglected. To process the data, time intervals of constant $N1$ were selected (see orange markers) and mean $L_{p,<N1>}(f)$ were analyzed on the basis of 1/3-octave bands.

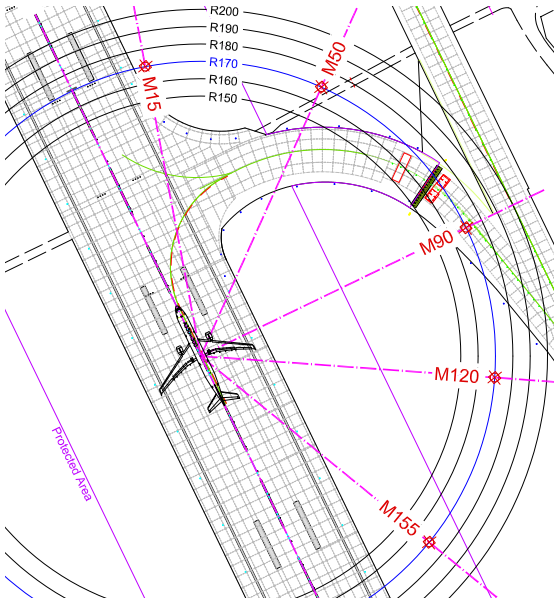

Figure 3.5: Engine run-up test of an A330-300 on runway 34-16 at Zurich airport. From Zurich Airport [32] with permission.

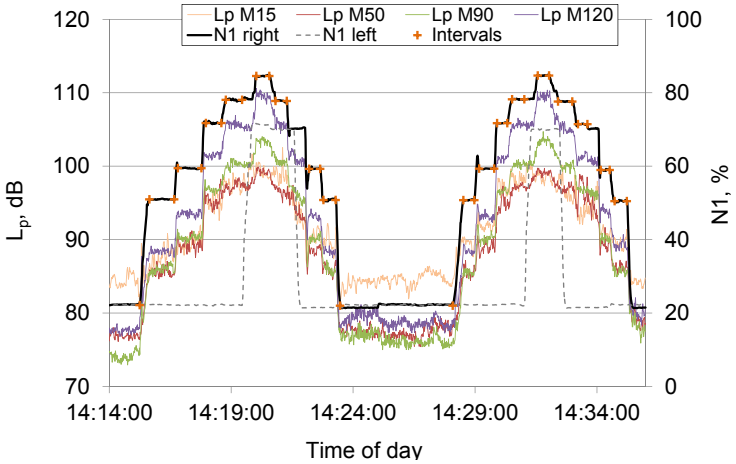

Figure 3.6: Acoustical measurement and rotational speed $N1$ of the run-up test of the A330-300. Two cycles were driven on the right engine with totally six thrust levels. Presentation with permission of Zurich Airport.

The measurements were conducted on March 12, 2014 from 2 p.m. to 3 p.m. with the following atmospheric conditions: $T = 13.5\,°\mathrm{C}, RH = 40.9\,\%, p = 977.4\,\mathrm{hPa}$. The stratification was unstable (no inversion) and only minor wind speed below $2\,\mathrm{m/s}$ from north-west were measured.

3.1.4 Instrumentation and measurement uncertainty

For the measurements in the close and far range the following uncertainty estimation is conducted. The measurements of the static run-up are only used qualitatively and therefore no uncertainty is shown.

The measurement system was either a sound level meter (Brüel & Kjær 2238) or an impedance converter, both conform to DIN EN 61672-1, Class 1 [28], which worked as the preamplifier for the omnidirectional condenser microphones. In the close range and far range the received voltage signal was saved in high quality on a sound device in the wave format (44.1 kHz, 16 bit). The calibration and signal processing was performed with the signal processing toolbox FAMOS[1]. The following calculation of the measurement uncertainty is based on Sec. 2.2.2. The total uncertainty $u_{L_p}(f)$ is defined in Eq. 3.1 and evaluated in Table 3.2.

$$u_{L_p}(f) = (u^2_{mic,dir}(f) + u^2_{lin} + u^2_U + u^2_p + u^2_T + u^2_{RH} + u^2_{fil} + u^2_{cal})^{1/2} \tag{3.1}$$

The uncertainty of the sound pressure level depends on the microphone tolerance and its error in directivity $u_{mic,dir}$, which is dependent on the angle of incidence θ_{mic} and

[1] imc FAMOS: `http://www.imcadd.ch/produkte/messtechnik-software/imc-famos/`

Table 3.2: Uncertainty $u_{L_p}(f)$ of the measured sound pressure level in dependency of the frequency. Uncertainties in dB.

Frequency range	$\theta_{mic} < 30°$	$\theta_{mic} < 90°$
250 Hz – 1 kHz	0.78	0.89
> 1 kHz – 2 kHz	0.78	1.03
> 2 kHz – 4 kHz	0.89	1.69
5 kHz	1.18	2.80

frequency f. This is important, as the data processing and the model are based on 1/3-octave bands. From DIN45643 Annex B [27], the following uncertainties are adopted: the uncertainty of level linearity with $u_{lin} = 0.31\,\text{dB}$, the fluctuations in the voltage supply with $u_U = 0.04\,\text{dB}$, and the fluctuations of the atmosphere from the reference conditions (Sec. 2.2.2) with $u_p = 0.16\,\text{dB}$ and $u_T = u_{RH} = 0.19\,\text{dB}$.

Afterward, the recorded signal is calibrated and processed applying a 1/3-octave filter bank (Sec. 2.2) to divide the time signal into 24 fractional bands from 25 Hz to 5 kHz and converted to the decibel scale to a frequency dependent sound pressure level $L_p(f)$. The uncertainty u_{fil} of filter class 0 is 0.21 dB [101].

For the calibration, a Bruel & Kjær sound calibrator type 4231 was used to generate the calibration tone at 1 kHz with 94 dB in far range or 114 dB in close range. According to DIN EN 60942 [26] the tolerance limits for a class 1 calibrator are 0.4 dB for reference and for working conditions, which leads to a standard uncertainty of

$$u_{cal,ref} = u_{cal,op} = 0.16\,\text{dB}. \tag{3.2}$$

The calibration factor is recorded in the same way as the measurement signal, but some modifications are needed to obtain Eq. 3.3. First, the uncertainty of the directivity is not needed as the calibrator tone is generated directly at the microphone. Second, the influence of the atmospheric conditions during the measurement can be neglected. They are accounted for by the working condition of the calibrator. The recorded calibration signal is then averaged over a period of minimum 20 s [26], which adds $u_{av} = 0.13\,\text{dB}$ for the uncertainty of the RMS value.

$$u_{cal} = (u_{mic}^2 + u_{lin}^2 + u_U^2 + u_{fil}^2 + u_{av}^2 + u_{cal,ref}^2 + u_{cal,op}^2)^{1/2} = 0.47\,\text{dB} \tag{3.3}$$

The acoustic data of this thesis (measurements in close and far range) underlie a measurement uncertainty as shown in Table 3.2. For most 1/3-octave bands smaller or equal 2 kHz, the uncertainty is 1 dB or below, which is a common value. For higher frequency bands the uncertainty increases. However, the highest uncertainties (1.7 to 2.8 dB) apply only for $\theta_{mic} > 30°$.

3.2 Meteorological data

Meteorological data were provided by MeteoSwiss from several ground measurement stations and from a numerical weather prediction model. The model was developed under the Consortium for Small-Scale Modeling (COSMO) of the national weather services of Germany, Greece, Italy, Poland, Romania, Russia, and Switzerland[2]. The data provided by MeteoSwiss are based on the model COSMO-2 with a grid spacing of 2.2 km including the Alpine arc [102]. The numerical model assimilates atmospheric observation data from radiosonde, aircraft, wind profiler, and surface-level data. It is usually used for predictions for one to five days in advance. The provided hourly profiles represent the as-is state and include temperature, humidity, wind speed, and wind direction for heights of approximately 10 to 4 900 m above ground.

Fig. 3.7 depicts three different profiles from 9:30 a.m. to 12:00 p.m. for temperature and humidity at a day in September from the measurement in the close range. The COSMO-2 data are compared to idealized profiles which were classified to the unstable stratification with a radiation balance and adjusted to the absolute values at the ground

[2]Consortium for Small-scale Modeling, `http://cosmo-model.org/`

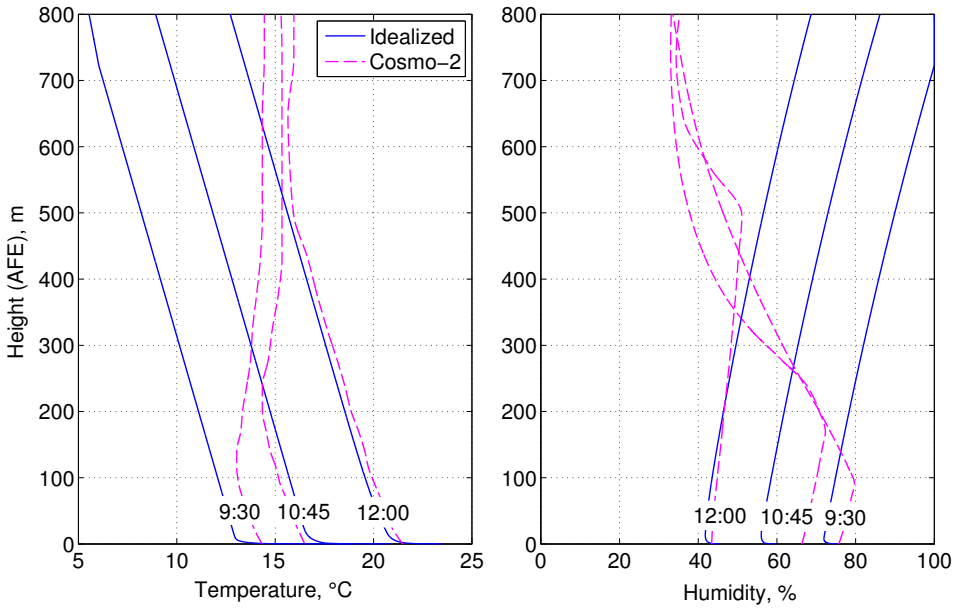

Figure 3.7: Selected temperature and humidity profiles for an example day between 9 a.m. and 12 noon in September 2013 at Zurich airport. The numerical model COSMO-2 (magenta dashed line) indicates that the stratification from a stable boundary layer at night to a typically unstable layer at a sunny day is still ongoing until noon. The use of idealized profiles (blue solid line) would lead to significant deviations.

station (see [104]). In comparison to the COSMO-2 profiles large errors in temperature and humidity can occur above 100 m using idealized profiles. The transformation of the stratification of the atmosphere to an unstable layer up to 500 m endured until noon for this sunny and clear day. It was found, that such influence of the atmospheric stratification can lead to systematic errors up to −3.6 dB for high frequency bands [104]. Therefore, the COSMO-2 profiles were chosen as input for the back propagation of each single flight in the close and far range.

The data at the ground stations were also used for documentation and automatic rejection of events in the far range. For each measurement campaign with three to four microphones with distances up to 20 km from the airport, the two closest weather stations were chosen to obtain temperature, wind, and precipitation. All data were available in a resolution of 10 minutes as actual or average values. With the help of such data from both ground stations, events with strong wind ($> 4\,\mathrm{m/s}$) or rain were discarded. Table 3.3 shows the range of atmospheric conditions at ground of Zurich airport during the different measurement periods (weather station Kloten). The data include only conditions with considered events in the data processing.

Table 3.3: Weather conditions for the measurement periods at close range (CR) and far range (FR). Minimum and maximum temperature and rel. humidity at 2 m above ground at Kloten.

Period	Runway	CR/FR	T in °C	RH in %
2013-08-19 to 2013-08-28	A14	CR	11 – 27 °C	40 – 92 %
2013-08-21 and 2013-08-23	D34	CR	16 – 20 °C	61 – 70 %
2013-09-02 to 2013-09-13	D28	CR	11 – 29 °C	24 – 85 %
2014-03-07 to 2014-04-14	A34	FR	−3 – 16 °C	30 – 100 %
2014-05-05 to 2014-05-16	D16	CR	9 – 27 °C	24 – 90 %
2014-06-20 to 2014-07-21	D28	FR	9 – 32 °C	22 – 100 %
2014-07-24 to 2014-08-24	D16	FR	12 – 27 °C	30 – 100 %

3.3 Flight paths

With the measurements in the close and far range of Zurich airport, different requirements to the flight path accuracy in time and space apply. In addition, some systems such as radar data are not sufficient in accuracy and coverage close to the airport. Therefore, different tracking systems were used to determine the path of the aircraft. In general, all flight path data were smoothed with B-Spline algorithm based on the Generalized Cross-Validation and Mean-Squared Prediction Error Criteria as in [22].

In the close range the flight paths were mainly measured by an optical tracking system. This system was developed within the sonAIR project.[3] It works with two cameras, which detect and track the aircraft automatically when installed and calibrated for a certain runway. During post processing, the images were reanalyzed to find the center of area of the aircraft in each image with high accuracy. Then, the data of both cameras were combined and the three-dimensional position (reference: aircraft center) was estimated by a Kalman-filter. In addition, a precise GPS-satellite clock synchronized the acoustical system and the tracking system.

This system was optimized for the measurements on runway 14 and 28 in the close range. For take-offs from runway 16 both the size and speed of the aircraft were too large in comparison to the available lateral distance of the cameras to the runway. Thus, the cameras had problems to keep track of the aircraft. In addition, the departure procedure dictates an early left turn which the system was not developed for to follow. As a consequence, a large part of the flight paths was not available or not of sufficient quality. Fig. 3.8 shows an example of an optical flight path which is limited due to the left turn compared to FDR data showing the true flight path. Although the height profile seems to be good, the airspeed deviates significantly from the FDR data.

As a substitute, MLAT data from skyguide, the Swiss air navigation service, were used on runway 16. The provided data are highly accurate in time as well in space close to the airport. In comparison to the FDR data (Fig. 3.8), the MLAT flight path is suitable for the range of interest. However, the corrected flight paths from the FDR data

[3]Hardware and software solution by SciTracks, www.scitracks.com

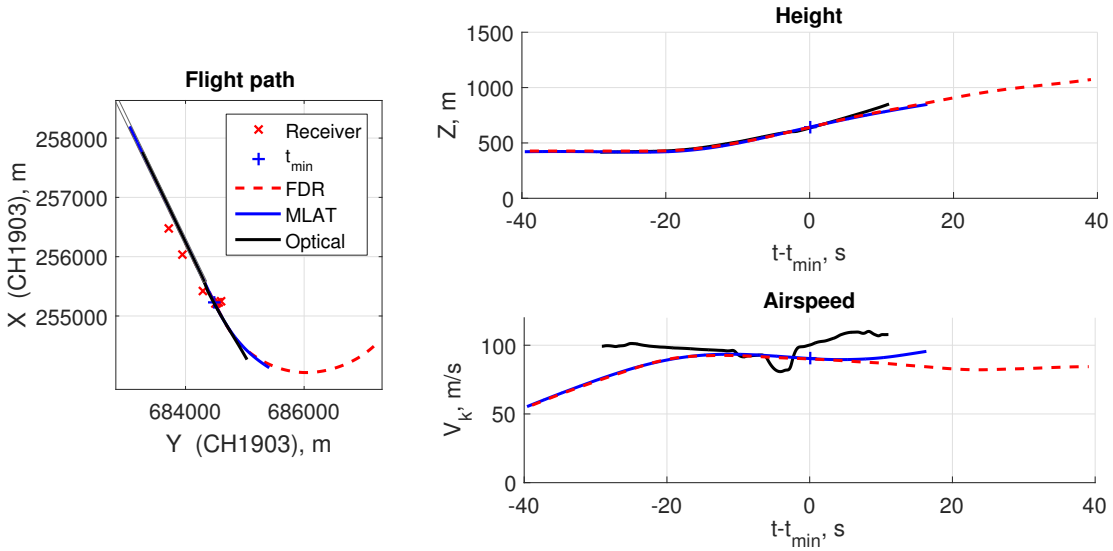

Figure 3.8: Flight path for a take-off from runway 16, tracked by three different tracking systems.

(see Sec. 3.4.1) was preferred when available because the uncertainty of the MLAT data increases outside of the airport area. The corrected flight paths are based on smoothed trajectories from two GPS signals combined with the best available altitude sensor. The main issue with FDR data is time synchronization. Therefore, flight paths from FDR data were synchronized with MLAT data, using the time at closest 3D distance to the receiver.

In the far range the corrected FDR flight paths were again used as the best available information. For other types only radar data were available. Radar data were also used to synchronize the FDR data in time. The accuracy of radar data is certainly of minor quality than for the other systems used, but also the requirements in the position and time accuracy are lower.

3.4 Flight parameters

3.4.1 FDR data

Flight parameters were provided by Swiss International Air Lines for 2 840 flights in total. Flights for the close range and far range are available for each of the seven aircraft types of the Swiss and Edelweiss fleet in 2013 and 2014. The fleet consisted of four narrow-body aircraft, the A319, A320, A321, and the RJ1H. Three wide-body aircraft are used for international flights, the A332, A333, and the A343. Each type is equipped with only one main engine option.

A data set for a specific flight event consists of 42 parameters from different sensors with a resolution of one second. The parameters contain atmospheric information, different altitudes and airspeeds, the position and orientation of the aircraft, engine parameters, and aeroplane configuration. A full description of the parameters is provided in the Appendix A.2 at Table A.2. All parameters were delivered for all aircraft type, except for the flap handle position which is not recorded for the RJ1H.

The parameters were provided on segments of 80 s in the close range and 240 s in the far range around a reference microphone. The time signal is composed of the time at the shortest three-dimensional distance and the relative time vector.

The time reference may differ strongly with ±80 s. One reason is, that the provided time signal of the RJ1H is set manually. This must also be the case for parts of the A320-family which were expected to be synchronized with a GPS clock, as all three types showed similar high deviations. In contrast, the time deviations of the wide-body aircraft are within ±3 s and thus much more accurate. Nevertheless, all flight parameters of all types were synchronized with the help of the time at the shortest distance from the chosen flight paths (MLAT, optical or radar data) in Sec. 3.3.

3.4.2 N1 determination

The determination of $N1$ from the acoustic signal was developed in cooperation of BeSB GmbH Berlin and TU Berlin [86; 87]. The comparisons to FDR data were done by the author to validate the method. A summary of the applied algorithms is presented here, as the results of the $N1$ determination were used in this thesis for all aircraft types without FDR data available.

The starting point is the acoustic signal in the time domain with a high resolution of 44.1 kHz and 16 bit. In preparation to the fast Fourier transform (FFT), the sample-rate of the acoustic signal is decimated to 22.05 kHz, divided into blocks of 4 096 samples, and a Hanning window with 75 % overlap is applied. With the decimation of the sample-rate, a frequency resolution of 5.4 Hz can be achieved and the frequency range is limited to 11 kHz, which reduces needless data. Afterward, the signal is transformed to the frequency domain by applying the FFT algorithm.

A 4th order high-pass filter is applied on each spectrum of the FFT to compensate the effects of air attenuation for high frequencies. In addition, a low- and high-pass filter is applied to the spectra to improve the automatic peak detection in the relevant region (Fig. 3.9a). Therefore, the cut-off frequencies of the filters are in function of the estimated $N1$ and the engines parameters. Fig. 3.9b shows the resulting spectrogram for an example approach condition.

The detected peaks are further processed to filter only the relevant peaks using a noise suppression and a selection criterion only allowing small changes of f_{peak} between two

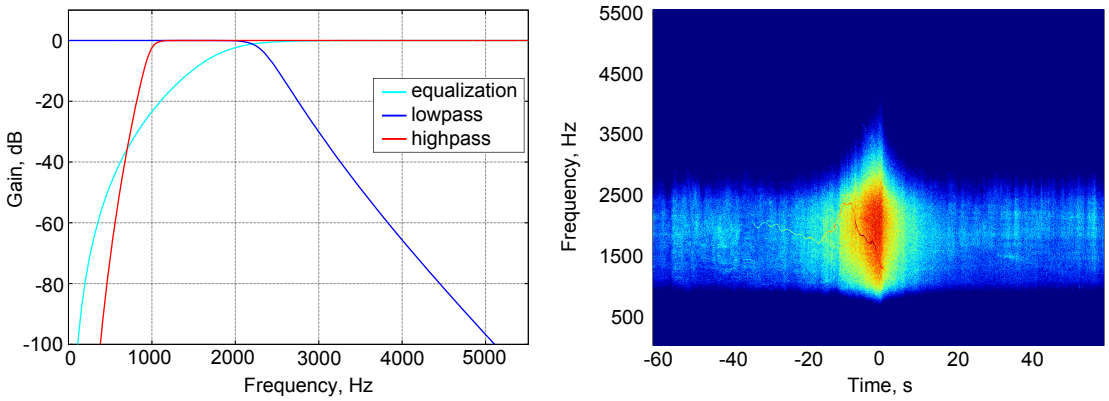

(a) Applied filters on the FFT

(b) Filtered spectrogram

Figure 3.9: Applied filters and the filtered narrow-band spectrogram with visible BPF. From [86], BeSB GmbH Berlin with permission.

neighboring points. Then, the Doppler frequency shift is corrected using the relative velocity of the flight path to the microphone position v_{rel} in Eq. 3.4.

$$BPF = f_{peak} \cdot \left(1 - \frac{v_{rel}}{c}\right) \tag{3.4}$$

The rotational speed of the low pressure shaft ω can be calculated on the basis of the BPF and the number of blades of the fan Z_{Fan}.

$$\omega = \frac{BPF \cdot 60}{Z_{Fan}} \tag{3.5}$$

Each turbofan engine is limited to a maximum rotational speed ω_{max} associated to a $N1_{max}$, which are both provided in the TCDS[4] of the European Aviation Safety Agency (EASA). For the CFM56-5B the following values are given: $\omega_{max} = 5\,200\,\text{rpm}$ at $N1_{max} = 104\,\%$. See Table A.1 in the Appendix for further data (also Z_{Fan}) of the engine types used in this work. $N1$ is calculated according to Eq. 3.6.

$$N1 = N1_{max} \cdot \frac{\omega}{\omega_{max}} \tag{3.6}$$

A quality flag was introduced to discard events with an insufficient quality. This quality flag consists of four steps (very good, good, partly good and bad) and was determined visually, looking at the smoothness of $N1$ over time and the number of detected peaks. Fig. 3.10a shows a good example of the determined $N1$ for an approach in the close range with a small mean error in comparison to $N1$ from FDR data. A second example in Fig. 3.10b shows a less accurate example with a mean error which is still acceptable. It also shows that an inaccurate synchronization in time causes errors. The quality flags,

[4] `https://www.easa.europa.eu/document-library/type-certificates`

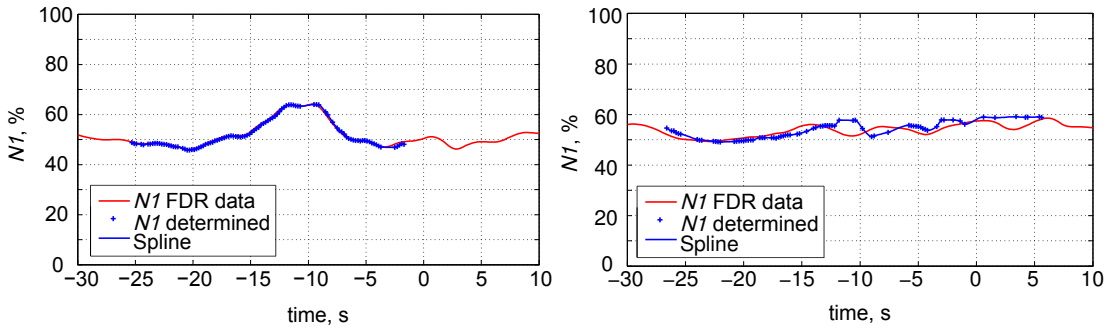

(a) Example 1, mean error 0.36%

(b) Example 2, mean error 1.75%

Figure 3.10: Validation of the $N1$-determination for two examples at approach in comparison to FDR data.

which were set without the knowledge of the FDR data, are in line with the comparisons with FDR data. All events which were classified as bad were discarded. In the close range 18 % of the departures on D28 and D16 and 40 % of the approaches on A14 were discarded.

In the far range of the airport the number of discarded events is substantially larger than for the close range. The main problem for the determination of $N1$ is the need of a prominent fan tone. This tone is mainly prominent to the front of the aircraft, but not to the rear. At departures in the far range, the higher distance to the source attenuates the higher frequencies and only a small time interval is available for a $N1$ determination. Therefore the number of discarded events depends on the measurement point: 1 % and 31 % at measurement point 8 and 10 for D16 as well as 8 % and 42 % at measurement point 5 and 7 for D28, respectively.

To benefit of the different segments of $N1$ on the same flight path in the far range, all segments were used to interpolate missing data. Fig. 3.11 depicts an A320 departing on D28. Measurement point 5 and 6 provide useful data points of $N1$, while 7 was not used as the quality is bad. A robust interpolation algorithm was applied to extend $N1$ between two measurement points, if they provide data that are at least of partly good quality. It is robust, as the linear interpolation between two measurement points align to the mean value of the last and first 20 % of the $N1$ values. Finally, a B-Spline is used to smooth the extended $N1$-data, which reduces the influence of outliers (no outliers occurred in the presented example).

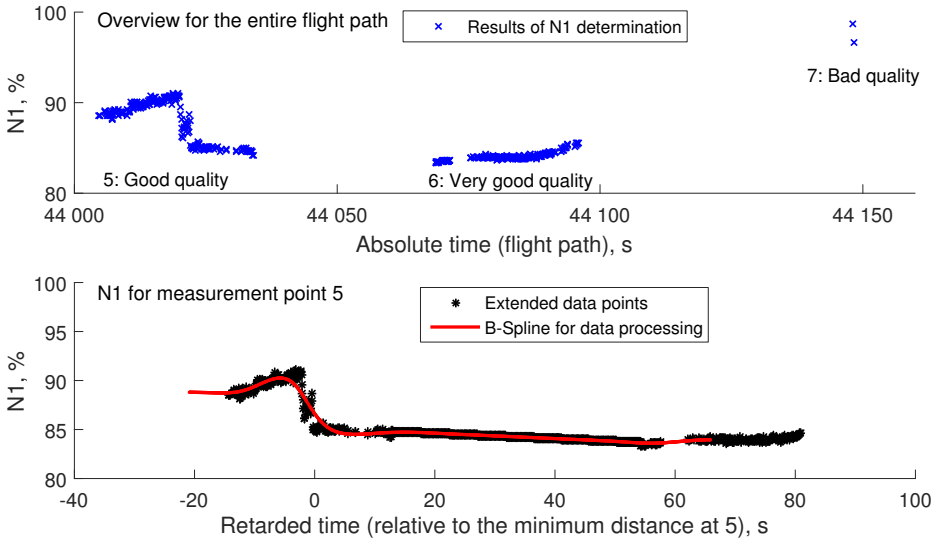

Figure 3.11: Example of $N1$ in the far range for an A320 (D28). Top: Data points (blue circles) represent the results from the $N1$ determination, which are extended with linear interpolation (black stars). Bottom: The extended data points are splined to smooth the curve and to prevent outliers.

For approach almost no data were detectable, as the lower amplitude and lower frequency of the fan tone make it difficult to detect the BPF. In addition, tones from the airframe overlap the fan tone, which leads to mistakes. Instead, $N1$ was set to idle (30 %) for measurement point 2 to 4, and measurement point 1 was completely discarded for the model development, as the FDR data showed that $N1$ has the highest variations at this location.

3.5 Data processing

Fig. 3.12 depicts the data processing applied to back propagate measured sound pressure levels. The flight paths, flight parameters and meteorological data as described above constitute the input data. The acoustic wave files from the measurements in the close and far range were calibrated and filtered to 1/3-octaves with 24 mid-frequencies from 25 Hz to 5 kHz. For each event a 120 s time-window was cut out from the wave file.

A moving average with a constant time interval of 50 ms was used to obtain the sound pressure levels $L_p(f)$ for each 1/3-octave band (Fig. 3.13). In addition, the L_p were smoothed with a moving average over 0.125 s to obtain smooth level-time-histories L_{smooth}. The L_{smooth} were used to determine individual time intervals that only correspond to the sound exposure of the aircraft. To that aim, an automatic algorithm selected the time interval, where the L_{smooth} was at least 6 dB above the minimum level inside the analyzed time window of 120 s. Starting at the maximum L_{smooth}, the algorithm searched along both directions and stopped the first time when the level was below the criterion. In that way, the background noise could be separated from the actual aircraft noise event for each frequency band as shown in Fig. 3.13.

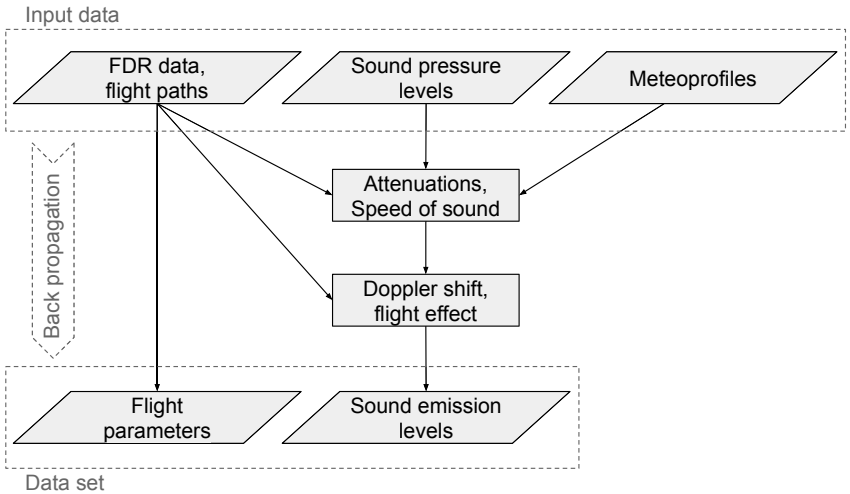

Figure 3.12: Flowchart of the data processing

In addition, the L_{AS} is calculated and checked for noise of other sources, as follows. From $L_{AS,max}$ the slopes on both sides are checked for level rise of more than 4 dB, which is the case for the two peaks on the right in Fig. 3.13. In case that the level rises again it is assumed to be non-aircraft noise contamination and the time intervals for all bands are terminated.

In the next step of Fig. 3.12, the sound propagation model sonX [100; 103] was used to calculate the corresponding attenuations and the speed of sound for each source-receiver combination. In this step, the assumption of a point source is made. The source location refers to the center of the aircraft. In sonX, the geometrical divergence, atmospheric attenuation, ground effect, foliage attenuation, as well as the influence of vertical gradients of wind, temperature, and relative humidity are accounted for (Sec. 2.2.3). For each flight, individual meteorological profiles from COSMO-2 (Sec. 3.2) were used to reproduce the real atmospheric conditions as precisely as possible.

The meteorological profiles are implemented in sonX to calculate the air attenuation per meter and time delay per meter as depicted in Fig. 3.14. The resolution of the meteorological profiles is fine below 100 m (1, 3, 6, 12, 25, 50, and 100 m) and continues with a fixed step of 100 m above. Each propagation path is calculated by integrating the air attenuation and speed of sound per meter distance for the corresponding altitude. The example in Fig. 3.14 shows the correlation of the time delay with the air temperature whilst the atmospheric attenuation is highly influenced by relative humidity and temperature. For the chosen condition the time delay varies between 0.29 to 0.31 $^{s}/_{100\,m}$ and the attenuation between 0 to 9 $^{dB}/_{100\,m}$, strongly depending on the frequency band. Air absorption becomes relevant for high frequencies (> 1 kHz).

Source positions, flight parameters and attenuations were corrected for the time delay of the sound traveled through the atmosphere to meet the equidistant resolution of the acoustical data. Each parameter is re-sampled to the time axis of the calculated $L_{p,50ms}$. The time delay of the sound between the source-receiver points was calculated

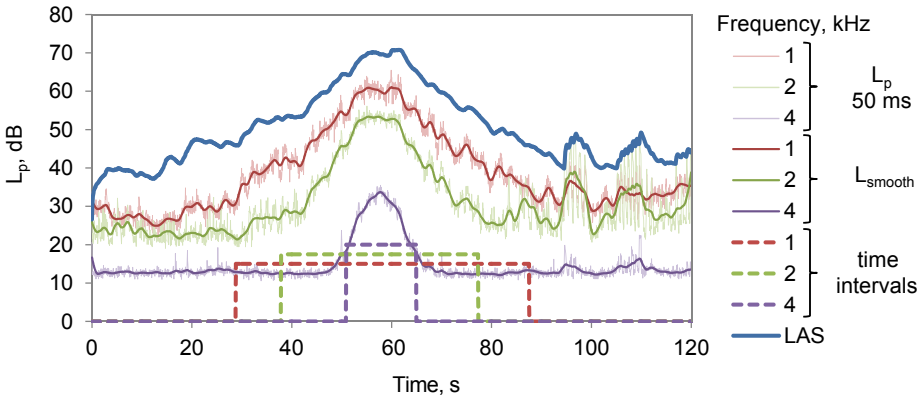

Figure 3.13: Time intervals, 50 ms-L_p and L_{smooth} for example frequency bands.

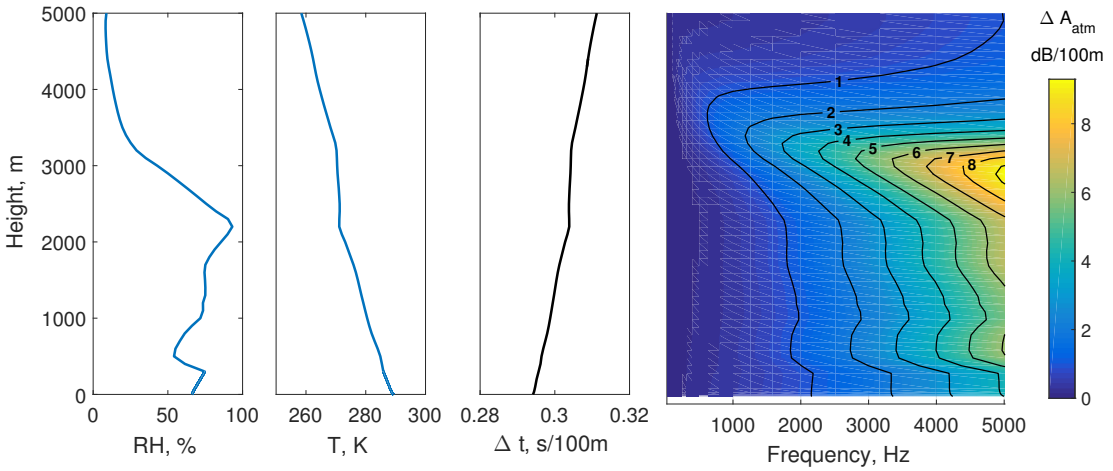

Figure 3.14: Calculation of time delay (Δt) and atmospheric attenuation (ΔA_{atm}) versus height above ground under consideration of the atmospheric profiles of relative humidity (RH) and temperature (T). The contour lines (right) show equal steps of 1 dB.

in the former step. Now, each source position is associated with the corrected time for a receiver which generates a deformed flight path or parameter to the retarded time vector. Finally the true position and flight parameters for each $L_{p,50ms}$ are interpolated on the original time axis. For this step, the flight path and the flight parameters were recalculated with a B-Spline algorithm based on the Generalized Cross-Validation and Mean-Squared Prediction Error Criteria with [22].

In this work, the sound emission level $L_{em}(f, \theta, \varphi)$ is equivalent to a sound power level L_W which already contains the directivity D (Eq. 3.7). This aggregation is unavoidable, as the directivity cannot be separated because it is dependent on the flight parameters which can change during a flight segment. With the classical equation of sound propagation outdoors (Eq. 2.13), Eq. 3.8 is obtained which summarizes the back propagation procedure to obtain the sound emission levels L_{em} for each 1/3-octave band.

$$L_{em}(f, \theta, \varphi) = L_W(f) + D(f, \theta, \varphi) - \Delta L_{FE} \tag{3.7}$$

$$\Rightarrow L_{em}(f, \theta, \varphi) = L_{p,50ms}(f) + \sum A(f) - \Delta L_{FE} \tag{3.8}$$

The back propagation from the receiver to the source is performed based on short term sound pressure levels $L_{p,50ms}$ for all receivers (microphone locations) which are corrected for the propagation attenuation $\sum A$ according to Sec. 2.2.3 and the flight effect ΔL_{FE} from Sec. 2.2.4. In line with the definition of the sound power level, the geometrical divergence includes the conversion constant $\log_{10}(4\pi)$. Finally, the frequency shift is applied for 1/3-octave bands (Sec. 2.2.4) after performing the back propagation to the point source according to Eq. 3.8.

4 Model development

For departures, the sound of a civil aircraft is dominated by engine noise, while for approach with engines running in idle also airframe noise may dominate to the total sound emission [51]. In Fig. 4.1 the interaction between pilot, flight configuration and the most important parameters for aircraft noise are shown. The pilot mainly performs a flight procedure by controlling the airspeed, altitude, and orientation of the aircraft. These parameters are summarized on the primary flight display in the cockpit. The main control elements to change those parameters are the elevator, the thrust setting, and also the aeroplane configuration to guarantee sufficient lift or drag during departure and approach.

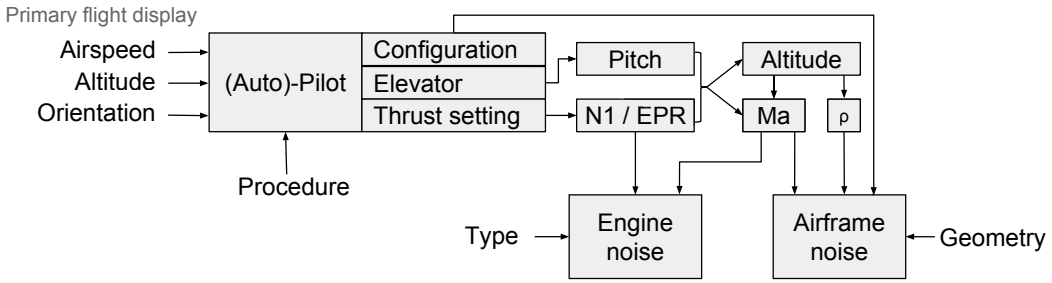

Figure 4.1: Block diagram of the most important parameters for aircraft noise.

The control elements directly or indirectly influence the generation of airframe noise and engine noise. Engine noise is mainly dominated by the thrust setting, which is based for many engine types on the rotational speed of the fan spool ($N1$) or on the engine pressure ratio (EPR). Depending on the thrust setting, the mass flow and the jet exhaust velocity are changed which influence the generation of broadband jet noise and broadband fan noise.

The pitch angle of the aircraft is used to define the climb rate and acceleration of the aircraft. In this way, the aircraft Mach number (Ma) as well as the altitude can be changed by the pilot. Since the engines are operating in the surrounding airflow, the aircraft Mach number influences the emitted sound energy. Airframe noise is mainly generated at the landing gear, flaps, slats, and speedbrakes. The sound generation is dependent on their geometry and scales with the local flow velocity (similar to Ma),

based on the aeroacoustic theory. This theory also implies that the outside air density ρ, which changes with altitude and weather, influences the sound emission of the airframe.

It is beneficial to model engine and airframe noise sources separately for three reasons. First, with the separation each noise source can be described more precise on the basis of individual parameters. Second, the influence of parameters such as Ma can be modeled with different relations for each source. Finally, the separation of the noise sources makes it possible to combine existing airframes to different engines, which might be interesting for forecasts or if measurements of a certain airframe and engine combination are missing.

The models presented in this section were established by means of multiple linear regression. This method allows for identifying effects of different influential parameters and their interactions in great detail. In a first step, the data set is introduced in Sec. 4.1. In Sec. 4.2, the parameters for the models are selected and their relations to the sound emission level are revealed. The model approach and its validity is discussed in Sec. 4.3. Finally, the regression models are presented in Sec. 4.4 and the process to separate the data set to airframe and engine noise is described in Sec. 4.5.

Data processing, data analysis, and fitting of the aircraft noise emission models were conducted with Matlab 2014b. The models were fitted with the Statistical Toolbox via the command *fitlm*, which uses an ordinary least squares fit and allows for individual weighting of the data points.

4.1 Data set

A data set is prepared for all events of each available combination of aircraft type and engine type as basis for the model development. It was decided to use the whole data set to estimate the model parameters, instead of applying a (k-fold) cross validation data structure with a subdivision of the data into training, test, and validation sets [70]. First, the expenses to gather enough data over a large range of flight parameters are high and the parameter estimates become imprecise if the original data sets were divided [70]. Second, the measured events are not independent from each other as they were measured at the same airport, with the same set-up, and in a particular season. In the future, the model should rather be validated with external and independent measurements.

The level of detail for the classification is limited to general types, thus no distinction is made for optional equipment such as winglets or dual annular combustors. For instance, the A320 family is divided to its types A319, A320, and A321 which mainly differ in length and maximum take-off weight. For every type of this family, different engine options are available, the CFM56 or V2500, which implies six possible data sets if all combinations are measured.

Each data set consists of 24 subsets for the evaluated 1/3-octave bands with mid-frequencies from 25 Hz to 5 kHz. A subset includes the corresponding emission levels L_{em} in dB from Eq. 3.8, calculated radiation angles θ, φ in degree, flight parameters such as the rotational speed of the engines $N1$ in %, aircraft Mach number Ma, and the atmospheric parameters pressure p in Pa, temperature T in °C, density ρ in kg/m^3, and speed of sound c in m/s. If FDR data are available, also the angle of attack α, the sideslip angle β, and the aeroplane configuration are available. The Mach number could have been related to the true airspeed (in respect to the moving air) of the aircraft for FDR data, but for consistency it is related to the flight path velocity V_k (in respect of the ground) for all aircraft.

In addition, identification numbers for the events and microphones are appended to each data point (line) for traceability during model development. An event with a flight segment of 60 s adds 1 200 data points per microphone to the data set. For all flights and measurement locations this may add up to one to two million data points per subset, i.e. per 1/3-octave band.

Table 4.1 shows the list of aircraft types with FDR data and the number of measured flights for each measurement period. In the close range up to eight and in the far range up to four microphone recordings are available for each flight (Sec. 3.1). The total number of recordings depends on the number of discarded events due to weather conditions or noise from other sources. In Table 4.2 types without FDR data are listed likewise. For these types only events at a receiver with a sufficient quality of $N1$ ('partly good' or better, Sec. 3.4.2) are included into the data set.

Table 4.1: Measured aircraft and engine types with FDR data.

		Close range				Far range			Sum		
Aircraft	Engine	A14	D16	D28	D34	A34	D16	D28	D	A	Total
A319	CFM56-5B	17	1	18		24	1	100	120	41	161
A320	CFM56-5B	178	24	153		71	48	199	424	249	673
A321	CFM56-5B	83	44	26		43	92	138	300	126	426
A332	PW4168	4					9	1	10	4	14
A333	TRENT7	61	102	3		75	130	14	249	136	385
A343	CFM56-5C	34	36	4	10	86	94	22	166	120	286
RJ1H	LF507	125		115		77	2	207	324	202	526

Table 4.2: Measured aircraft and engine types without available FDR data.

		Close range			Far range			Sum		
Aircraft	Engine	A14	D16	D28	A34	D16	D28	D	A	Total
A318	CFM56-5B				4		80	80	4	84
A319	CFM56-5B	64	1	39	19		180	220	83	303
A319	V2500	4	1	30	12		94	125	16	141
A319	CFM56-5A	4		1	2		18	19	6	25
A320	CFM56-5B	177	4	48	84	9	157	218	261	479
A320	V2500	2		8	8	7	25	40	10	50
A320	CFM56-5A	7	1	10	2		27	38	9	47
A321	CFM56-5B	15	1	2	1	2	25	30	16	46
A321	V2500	3		5	4	2	26	33	7	40
A332	PW4168			2	3	1	16	19	3	22
A332	TRENT7			2	9	4	5	11	9	20
A333	TRENT7		10		91	17	5	32	91	123
A346	TRENT5		8		25	22	1	31	25	56
A388	TRENT9	6	11		14	27		38	20	58
A388	GP7270	0	7		2	19		26	2	28
B733	CFM56-3	17		11	6	1	17	29	23	52
B734	CFM56-3		2		2	6	2	10	2	12
B735	CFM56-3	11		6	3	1	38	45	14	59
B736	CFM56-7B	5		6			1	7	5	12
B737	CFM56-7B	14		11	5		93	104	19	123
B738	CFM56-7B	6		12	7	8	164	184	13	197
B739	CFM56-7B					1	1	2	0	2
B762	CF6-80C2		8		15			8	15	23
B763	PW4060	11	2		23	2	5	9	34	43
B763	CF6-80C2	1	7		20		2	9	21	30
B764	CF6-80C2		1		21	1		2	21	23
CRJ9	CF34-8C5	10		4	12		67	71	22	93
E170	CF34-8E	23		14	4		48	62	27	89
E170	CF34-3	1					1	1	1	2
E190	CF34-10E	20		42	29		201	243	49	292
F100	TAY 650-15	11		31	50	11	192	234	61	295
F100	TAY 620-15	1		1				1	1	2
FA7X	PW307	5		5	5		12	17	10	27
GLF5	BR700-710A	5		4	1		7	11	6	17
RJ1H	LF507	49		8	20	1		9	69	78
RJ1H	LF502	1			2				3	3

4.2 Data exploration

4.2.1 Outlier detection

Since the data processing of the measurements is performed highly automated, which was necessary due to the high amount of data, it must be assumed that outliers remain in the regression data set. Primary background noise and errors of the back propagation over large distances are potential sources for outliers. Outliers are removed by an adaptive outlier detection method of Filzmoser [34] for multivariate data (Sec. 2.3.3).

Especially the third point in Sec. 2.3.3 becomes important in this context, which stated that the threshold to detect outliers need to be adjusted to the sample size. This is the case for the regression data set, where each 1/3-octave band has a very different size due to the individual event intervals above background level (Sec. 3.5).

In this work RD^2 was only calculated for L_{em} and radiation angles (θ, φ). Otherwise, seldom observations of L_{em} such as large aircraft Mach numbers were detected as outliers. In addition, the 3D distance d between source and receiver was accounted for to detect unusual far distances. This approach was chosen due to the unbalanced data and automatic data processing. Fig. 4.2 shows an example outlier for the A333 (TRENT7) at 1 kHz with a 1.82 % detected outliers. The χ^2_4-distribution has a degree of freedom of 4, accounting for the variables RD is based on (L_{em}, θ, φ and d_{3D}).

4.2.2 Multicollinearity

Multicollinearity exists if explanatory variables correlate with each other, which is expected e.g. for the atmospheric parameters p, T, and ρ, which are physically connected by the ideal gas law. Multicollinearity can have strong effects on the estimates of the

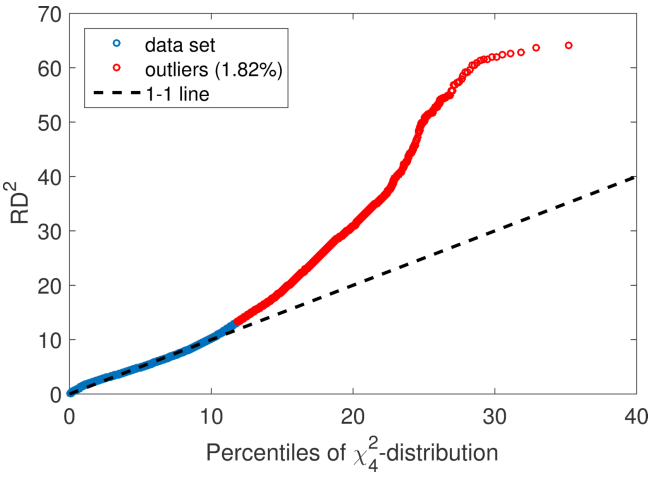

Figure 4.2: Outlier detection with squared robust distance versus χ^2-distribution. Example for the A333 (TRENT7) at 1 kHz with 1.82 % detected outliers.

Table 4.3: Pearson's correlation matrix for all regression parameters of the A320.

	θ	φ	$N1$	Ma	ρ	p	T	c	α	β	L_{em}
θ	1										
φ	0.1	1									
$N1$	0.1	−0.1	1								
Ma	0.0	−0.2	0.3	1							
ρ	0.0	0.2	−0.3	**−0.8**	1						
p	0.0	0.2	−0.2	**−0.9**	**0.9**	1					
T	0.0	0.2	0.1	−0.4	0.2	0.5	1				
c	0.0	0.2	0.1	−0.4	0.2	0.5	**1**	1			
α	−0.1	0.1	0.2	−0.5	0.3	0.4	0.3	0.3	1		
β	−0.1	0.0	−0.5	−0.2	0.2	0.1	−0.1	−0.1	0.0	1	
L_{em}	0.2	−0.1	0.6	0.4	−0.3	−0.3	−0.1	−0.1	0.0	-0.3	1

regression coefficients and brings the risk of overfitting. Even if the model equation may still be useful in its known intervals, the individual effects of the parameters may be poorly estimated and would lead to wrong interpretation [70, p. 283].

To check for multicollinearity the correlation coefficient and the variance inflation factor (VIF) will be used [70, p. 408]. The correlation coefficient (Table 4.3) gives already a good hint on correlated parameters. It turns out that ρ and p highly correlate as expected by the ideal gas law $p = \rho RT$. Both also correlate with Ma. In contrary, the temperature is uncorrelated to p and ρ as its gradient depends on radiation and convection. A correlation coefficient of 1 can be found for T and c which can be explained by the definition of the speed of sound with $c^2 = \kappa RT$ (Sec. 2.2). To prevent multicollinearity, the VIF is used to reject the correlated parameters with the highest VIF step by step.

Table 4.4 shows all parameters of the regression data set and their VIF values. If the VIF equals 1, no correlation exists while considerably large values indicate multicollinearity [70, p. 409]. Not surprisingly the VIF value for T and c are very large. Therefore, the parameter with the largest value (T) is rejected and the VIFs are calculated again in the next column. The VIF value of c is considerably reduced but still too large. Nevertheless, the largest value applies for p that is rejected in the next step. After this, no VIF is too large anymore and the mean VIF is 2.7. Thus, multicollinearity is no problem when using the reduced data set without p, T (4th column of Table 4.4).

4.2.3 Relationships

Before the relationships of the explanatory variables can be revealed, the dependent variable needs to be determined. It was found, that the back propagated (directivity-dependent) sound power of the engine is not normally distributed. Thus, the sound

Table 4.4: VIF for all parameters of the regression data set of the A320. Each column is reduced for the parameter with the largest VIF to prevent for multicollinearity.

Step:	all	$-T$	$-p$
θ	1.1	1.1	1.1
φ	1.1	1.1	1.1
$N1$	3.8	3.7	3.7
Ma	5.9	5.8	5.3
ρ	3 894.8	3 590.9	3.9
p	5 170.6	4 781.7	–
T	34 071.5	–	–
c	32 194.9	596.8	2.0
α	1.6	1.6	1.6
β	1.4	1.4	1.4
FH	4.6	4.6	4.5
LG	3.8	3.8	3.7
SB	1.2	1.2	1.2
$\overline{\text{VIF}}$	5 796.6	749.5	2.7

power is no option as dependent variable for a multiple linear regression. But the base-10 logarithm of the sound power, denoted as sound emission level $L_{em}(f, \theta, \varphi)$, is normally distributed. Therefore, the scope in this section is to find the relations of the explanatory variables to the back propagated $L_{em}(f, \theta, \varphi)$.

Rotational speed of the compressor

For many engines, $N1$ is the control parameter of the power setting. In contrast to the thrust or jet velocity of the engine, it is a directly measurable parameter. The jet velocity, which is the main physical parameter for jet noise, see e.g. Lighthill [63] or Stone et al. [95], correlates with $N1$. Thus, for frequencies below 1 kHz where jet mixing noise is dominant [38; 93], $N1$ can be used as a substitute for the jet velocity.

The BPF as well as the broadband noise with a center frequency of 2.5 times the BPF [42] are directly connected to $N1$. Heidmann [42] also revealed that the fan noise mainly scales with the total temperature rise over the fan stage as well as the mass flow (cmp. [9]). Both parameters increase with a rise in $N1$. Simons et al. [90] also suggested to incorporate $N1$ into aircraft noise models as the parameter explains large parts of the variations of aircraft noise measurements at final approach. For most engine types, the BPF and thus also the broadband noise can be found above 1 kHz. Hence, $N1$ is a reasonable explanatory variable for jet and fan noise covering the whole engine spectra.

To answer the question how to model the sound emission in relation to $N1$, an engine run-up test of an A330-300 with the TRENT7 was evaluated. In Fig. 4.3 the example results are depicted for four 1/3-octave bands. An engine run-up test of an A330-300

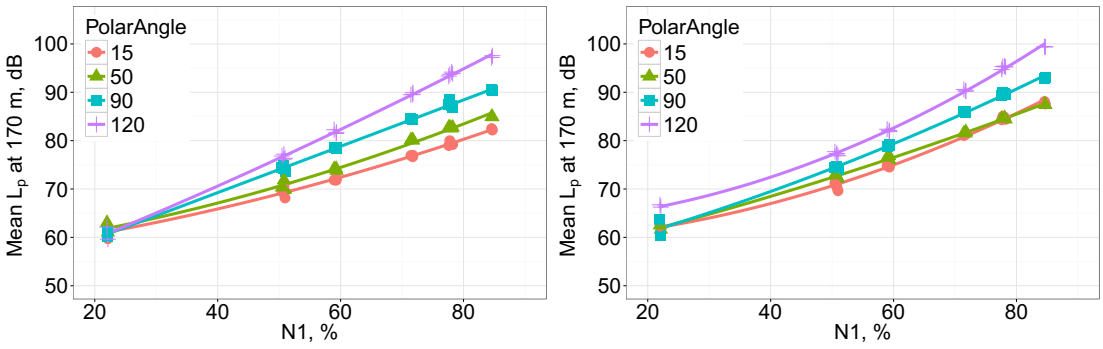

(a) 31.5 Hz (b) 125 Hz

Figure 4.3: Engine run-up test results of the A330-300 (TRENT7) for low 1/3-octave bands

with the TRENT772B (Sec. 3.1.3) was evaluated to establish the functional relation between sound pressure level and $N1$ for each 1/3-octave band, as no such relation was known to the author. In Fig. 4.3 the example results are depicted for four 1/3-octave bands. The mean sound pressure levels for six steps of constant $N1$ are grouped by the polar angle (microphone position, aircraft nose represents 0°). A simple regression model was fitted for each polar angle with a second order polynomial fit for $N1$.

According to Fig. 4.3 and Fig. 4.4, the second order fit is reasonable for all 1/3-octave bands and is therefore chosen for the regression model established below. However, the functional relation is changing with frequency and polar angle. For 31.5 Hz in Fig. 4.3a the quadratic fits are slightly parabolic to the front and almost linear to the rear of the aircraft. In addition, the slope increases to the rear. For 125 Hz (Fig. 4.3b) and 500 Hz (Fig. 4.4a) the curvature of the quadratic fits are negative for all polar angles. For frequencies above 630 Hz, e.g. 2 kHz in Fig. 4.4b, the curvature of the quadratic

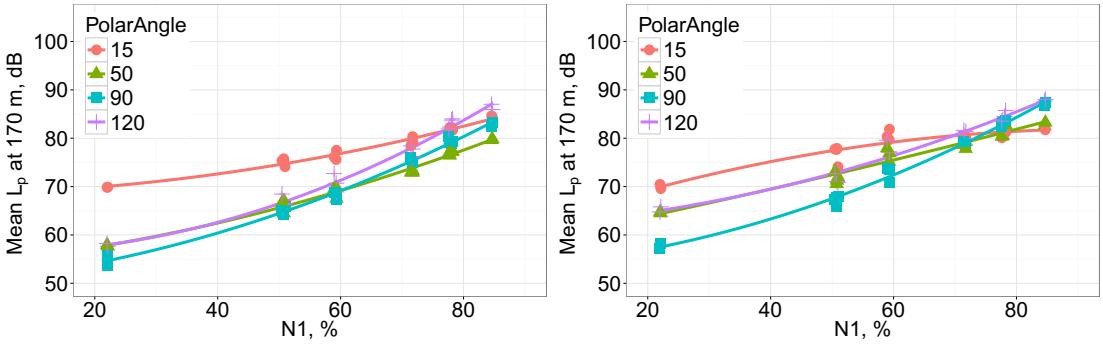

(a) 500 Hz (b) 2 kHz

Figure 4.4: Engine run-up test results of the A330-300 (TRENT7) for mid and high 1/3-octave bands

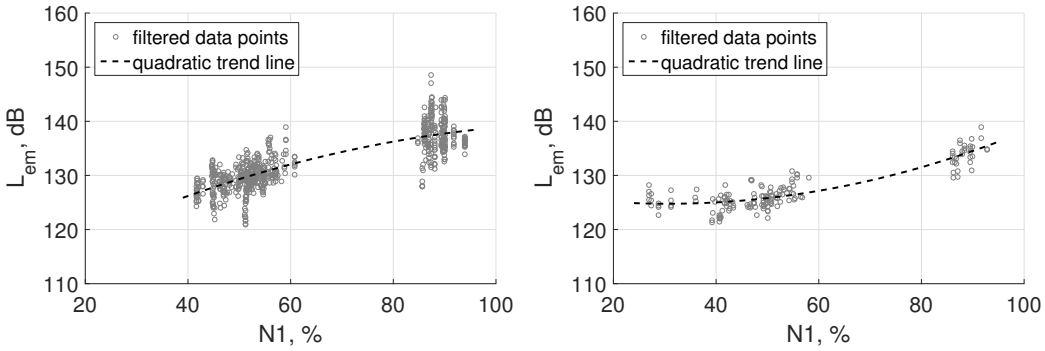

(a) $N1$-behavior at θ=25° (b) $N1$-behavior at θ=100°

Figure 4.5: Influence of $N1$ on the sound emission level of the A320 with CFM56-5B for 2 kHz.

fits are negative (50 to 120°) as well as positive (15°). Thus, a second order polynomial approach in dependency of the polar angle θ adequately represents the relation between L_p and $N1$ for each 1/3-octave band.

In general, the turbofan engines of today's civil aircraft are very similar and the mechanisms of sound generation are the same. Therefore, it is assumed that the second order polynomial approach is also valid for other turbofan engines. This assumption was confirmed with the back propagated data set at 2 kHz for the CFM56-5B of the A320 (Fig. 4.5) and the CF34-8E of the E170 (Fig. 4.6), which show the same trends for the L_{em} (negative as well as positive curvature).

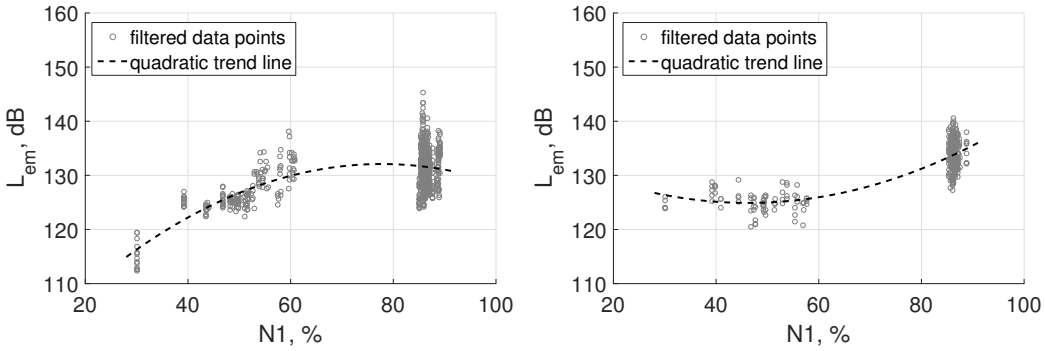

(a) $N1$-behavior at θ=30° (b) $N1$-behavior at θ=100°

Figure 4.6: Influence of $N1$ on the sound emission level of the E170 with CF34-8E for 2 kHz.

Aircraft Mach number

The aircraft Mach number Ma is chosen to take the speed dependent sound sources into account. It is an aerodynamic characteristic that is interpreted as compressible flow condition and therefore ensures comparable flow phenomena.

The dependency of the sound emission of airframe noise sources to Ma is provided by the aeroacoustic analogy of Lighthill [63]. The generation of sound from the fluctuating fluid is described by the classical wave equation, which is extended by three basic source terms: monopole, dipole, and quadrupole. The theoretical free-field solutions in Eq. 4.1 from Ribner [77] reveal that the sound power W is proportional to the air density ρ, a characteristic dimension of the source Γ, the mean flow speed U, and the Mach number Ma. The exponent l depends on the source term (monopole l=1, dipole l=3, quadrupole l=5).

$$W \propto \rho \Gamma^2 U^3 Ma^l \tag{4.1}$$

This physical relation is used to derive the relationship of L_{em} to Ma. By applying the base-10 logarithm, Eq. 4.2 results. To account for the logarithm, the units were normalized by the reference quantities ρ_0, Γ_0, and V_0.

$$L_W \propto 10 \log_{10}\left(\frac{\rho}{\rho_0} \cdot \frac{\Gamma^2}{\Gamma_0^2}\right) + 10 \log_{10}\left(\frac{V_k^3}{V_0^3}\right) + 10 \log_{10}(Ma^l) \tag{4.2}$$

For the application on all airframe noise sources of the aircraft the mean local flow speed U, which can be different for each source of the aircraft, is simplified to the flight track velocity V_k of the aircraft. This is a practical solution, as V_k can always be derived from the flight path. For an airframe model which represents all sources at once, it represents a good approximation of the mean airflow. Correspondingly, Ma represents the ratio of V_k to the local speed of sound c in a single, dimensionless variable.

The dependencies of Eq. 4.2 are transferred to the L_{em} which is proportional to L_W as defined in Eq. 3.8. In a regression model, the implementation of V_k and Ma is problematic as these parameters are highly correlated (multicollinearity). In order to prevent for multicollinearity, only $\log_{10}(Ma)$ instead of $\log_{10}(V_k)$ is accounted for. Thereby, the regression coefficient represents the power l of Ma at which the total airframe noise scales.

Also engine noise is affected by the aircraft Mach number. Fan noise directly depends on the airflow mass [42], which increases with the incoming airspeed. Jet noise reduces with the incoming airspeed due to the reduced relative jet speed. For instance during take-off ground roll, which is the flight segment of acceleration on the runway, a linearly decreasing relation to the speed of the surrounding airflow was found by [75]. The sound

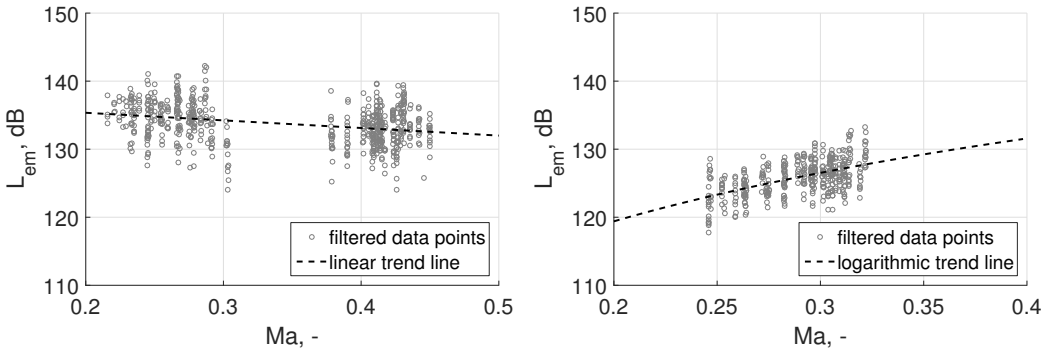

(a) Departure θ=90°

(b) Approach θ=60°

Figure 4.7: Influence of Ma on the sound emission level of the A320 at departure (a) and approach (b) for 250 Hz.

pressure level of the jet in the far field decreases with increasing flow speed U, which was confirmed experimentally by [36].

Fig. 4.7 shows the dependency of L_{em} on Ma for 250 Hz for typical flight configurations at departure with high thrust in Fig. 4.7a and approach with idle thrust in Fig. 4.7b. Engine noise is expected to be dominating in Fig. 4.7a and a linear regression seems to be reasonable to extrapolate L_{em} against Ma. In contrast, airframe noise is likely to be dominant for approaches [51] as shown in Fig. 4.7b, where the logarithmic relation applies.

A characteristic noise generation was found for the A320 family at the 500 Hz and 630 Hz bands. Two prominent cavity tones from the lower surface of the wings dominate the sound emission spectrum at approach. These tones have been measured before [76] and vortex generators were developed to suppress them. Swiss International Air Lines assembled the generators to the whole A320 family after the measurements from Sec. 3.1. Therefore, the characteristic tones were considered in the model development but need to be corrected for in the future if the vortex generators are installed.

Fig. 4.8 shows the data set of the A320 at 500 Hz, separated to approach with engines at idle (blue dots) and to departures (magenta dots). The slope of L_{em} versus Ma is steep for the approach, as the tone of a Helmholtz resonator scales with the flow speed at the cavity. The figure also shows that the cavity tone is prominent at approach but not for departure. An explanation for such characteristic might be a different local flow condition below the wing, as the lift force is much higher for departures and higher angles of attacks are needed.

The sound power of a cavity tone theoretically scales with $\log_{10}(Ma^{10})$ [96]. A logarithmic fit to the data in Fig. 4.8 revealed $L_{em} \propto log_{10}(Ma^{9.4})$, which is in line with the theoretical approach and empirical data of [96]. Therefore, the linear relation to Ma

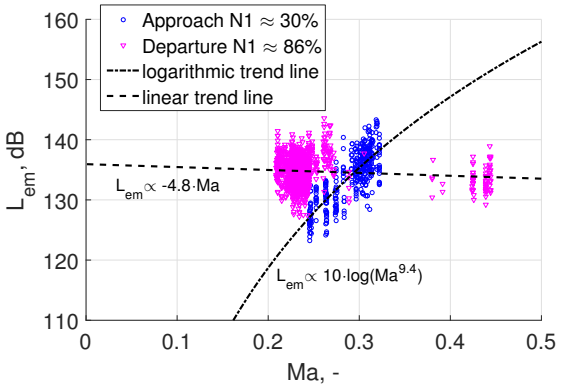

Figure 4.8: Different behavior of L_{em} with Ma for approach and departure of the A320. At 500 Hz a cavity tone is very prominent for approach but seems not to scale in the same way for departures.

for engine noise and the logarithmic relation on Ma for airframe noise as selected before are also valid for the noise generation of the cavity tone.

Air density

In the same manner as for Ma the effect of the air density is accounted for in the airframe model with the base-10 logarithm to be in line with the aeroacoustic theory (Eq. 4.2). All other atmospheric parameters have been rejected due to multicollinearity (Sec. 4.2.2).

Radiations angles

The sound emission of an aircraft has a directivity that is best described with spherical coordinates. Particularly the longitudinal radiation, represented by the polar angle θ, strongly changes with the aircraft type, frequency band, and $N1$ as shown in Fig. 4.3. The lateral radiation, represented by the azimuth angle φ, is also taken into account in dependency of aircraft type, frequency band, and $N1$. In [62] it was shown, that the lateral directivity can lead to level differences up to 3 dB over φ. Additionally, the lateral directivity in [62] showed significant discrepancies to the generalized corrections proposed in Doc. 29 [31], which only distinguishes between wing and fuselage-mounted engines.

A Fourier series of second order was chosen to describe the longitudinal directivity. It is a simple mathematical approach that can be implemented to the regression model and to reproduce different directivity patterns. Other possible approaches such as spherical hemispheres are also possible descriptions for the directivity, but they are less straightforward to implement in the regression model. During the model development, a higher order Fourier series was also tested but resulted in problematic slopes at the borders, where less data are available. Particular for conditions far away from the

receivers the directivity at high frequencies was critical. The lateral directivity is modeled with a half range Fourier series (2nd order) to simplify the number of terms and also to prevent problematic slopes in areas with low data coverage.

Aeroplane configuration

The aeroplane configuration is modeled with three variables: The position of the landing gear (retracted: 0, deployed: 1), the position of the high-lift devices (fix combinations of slat and flap deflection, equivalent to flap handle position 0 to 4), and the deployment of the speedbrakes (inactive: 0, active: 1). These parameters are available from FDR data.

Due to the measurement of regular air traffic the data are naturally not balanced and it was not possible to gain data for all combinations of the aeroplane configuration. Furthermore, the flap handle positions highly correlate to different intervals of Mach numbers due to the procedures and structural limits as shown in Fig. 4.9 (underlying data in the Appendix, Table A.20). In particular for approach, the empirical data is limited to very narrow ranges of Mach number and angles of attack (see next page), which must be taken into account when applying the model to different flight configurations. Despite these constraints, the influence of the flap handle position is of interest and is therefore accounted for as described in Sec. 4.4.1.

Fig. 4.10 shows the effect of the landing gear on the sound emission of the A320. The shown data points are measurements for approach conditions with deployed and retracted landing gear. Each data set is fitted with a simple logarithmic regression to show the influence of the landing gear. In a), a slightly larger slope of the regression

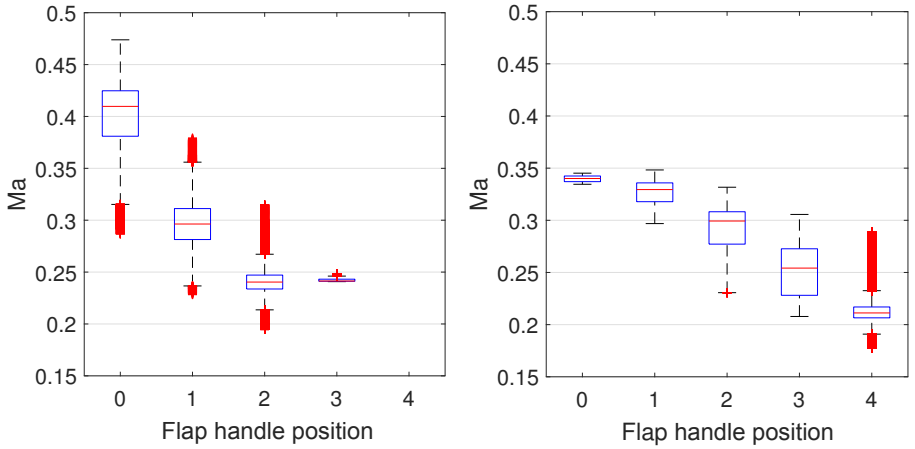

(a) Departure (b) Approach

Figure 4.9: Distribution of measured flap handle positions of the A320 in dependency of the Ma-Number. In contrast to approach, the flap handle position 1 refers to a different deflection angle of flaps at departure (1+F).

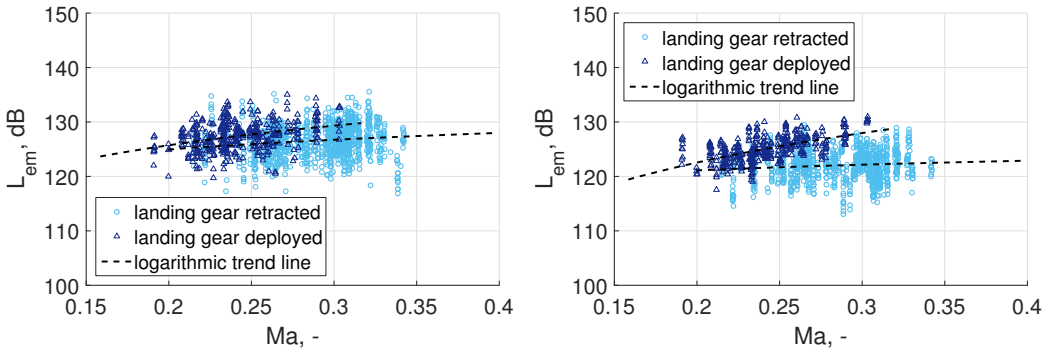

(a) Approach 250 Hz (b) Approach 2 kHz

Figure 4.10: Influence of the landing gear on the sound emission level of the A320 at approach in idle for 250 Hz in (a) and 2 kHz in (b). Measured data and the trend lines show a clear effect on the sound emission level.

with deployed landing gear can be found. For low Ma the emission levels are similar, but for high Ma of 0.3 the level difference is 2.6 dB. At 2 kHz in b) the effect of the landing gear on the Ma-dependency of the sound generation is much stronger. At Ma=0.3 the difference is already 6 dB.

Other variables

Further variables have been considered but rejected during the model development due to insignificance or practical reasons. For instance, no important correlations to the emission level could be found for the angle of attack and sideslip angle. Besides, these angles are often not available for predictions.

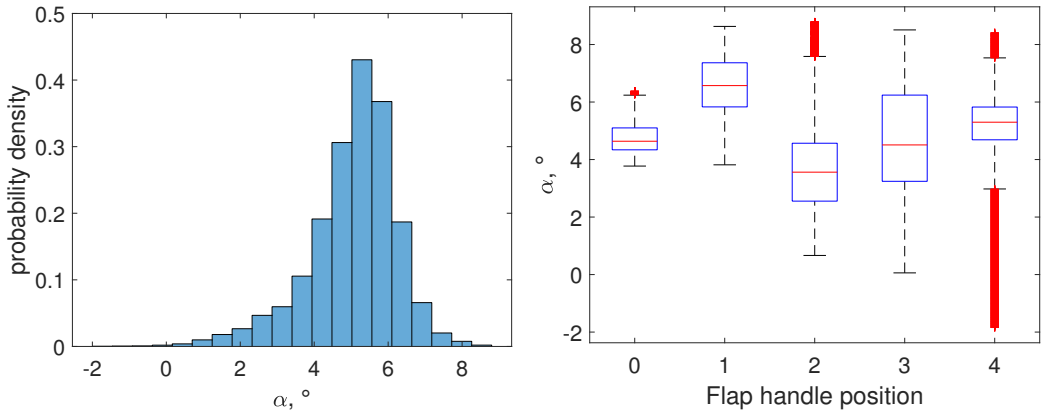

(a) Probability density function (b) Box plot grouped by flap handle position

Figure 4.11: Observed range of angle of attack α for approach of the A320.

Although the angle of attack was found to show large influence on the sound level above 12° [29], such influence can be neglected for typical angles of attack during approach. An analysis of the FDR data for approach of the A320 revealed that the angle of attack was mainly used between 3° and 7° (Fig. 4.11a). In addition, the each flap handle position showed an specific range of α and therefore covers a possible influence already (Fig. 4.11b). The measured angles of attack for each flap handle position of aircraft types with available FDR data are listed in the Appendix, Table A.20.

For the speed of sound c no relation to L_{em} was found, too. Furthermore, c is already used within $Ma = V_k/c$ and also correlated to ρ via the ideal gas law ($c^2 = \kappa \cdot p/\rho$). The parameter was tested during the model development but did not improve the model.

4.3 Modeling approach

The regression models in Sec. 4.4 combine continuous explanatory variables, categorical variables with a certain number of levels, and interactions to predict the dependent variable L_{em}. Interactions are deviations from the additive model describing how the effect of one variable depends on the levels of another variable, e.g. the dependency of the noise emitted by the landing gear on the aircraft Mach number.

4.3.1 Variables and transformations

For the airframe noise model, two transformations are introduced, applying the base-10 logarithm to the aircraft Mach number (lMa) and to the air density ($l\rho$), to fulfill the requirement of a linear relation between the continuous variables and L_{em} (Sec. 4.2.3).

$$lMa = \log_{10}(Ma) \tag{4.3}$$

$$l\rho = \log_{10}\left(\frac{\rho}{\rho_0}\right) \tag{4.4}$$

The air density is normalized by the density at mean sea level as defined by the International Standard Atmosphere (ρ_0=1.225 kg/m^3). For zero airspeed the transformation tends towards minus infinity which is physically reasonable. In practice, Ma is set to 10^{-3} to obtain a real value. In addition, the landing gear position (LG), the flap handle position (FH), the speedbrakes (SB), and the procedure ($Proc$) are categorical variables of the airframe noise model. The engine noise model only consists of continuous variables and their interactions, namely Ma, $N1$, $N1^2$, θ, and φ.

4.3.2 Model selection

The general structures of the regression models were developed based on the A320 data set, which provides FDR data and a large number of flights. Preliminary models were

developed and tested on parts of the data set, e.g. only departures and only approaches. In addition, example frequency bands for low, mid, and high frequencies were used to test different model approaches. With the first experiences and results the models were fitted on the entire data set and all frequency bands.

In a next step, the data sets were separated to airframe and engine noise (Sec. 4.5), which allowed to develop two independent models for each source characteristic. Furthermore, the models were tested and improved on the five other aircraft types with FDR data to confirm that the models are applicable to different aircraft and engine types. The scope was to select a general model, which can be applied on all 1/3-octave bands and on other turbofan-powered aircraft types.

The parameter selection is based on the Sec. 4.2. From the statistical point of view, this approach equals the forward selection with the scope to only include the relevant parameters for both sources. Each model with a new parameter or interaction was compared by the coefficient of determination R^2, the mean squared error $\widehat{\sigma}_E^2$, and Akaike information criterion (AIC) [2]. All criteria were compared over all frequencies to find a global optimum (minimize AIC, $\widehat{\sigma}_E^2$; maximize R^2).

In addition, both the airframe and engine noise model were checked at each frequency band for the model assumptions from Sec. 2.3. Fig. 4.12 shows an example check for normal distribution of L_{em} via a histogram and Q-Q-plot. They show that the

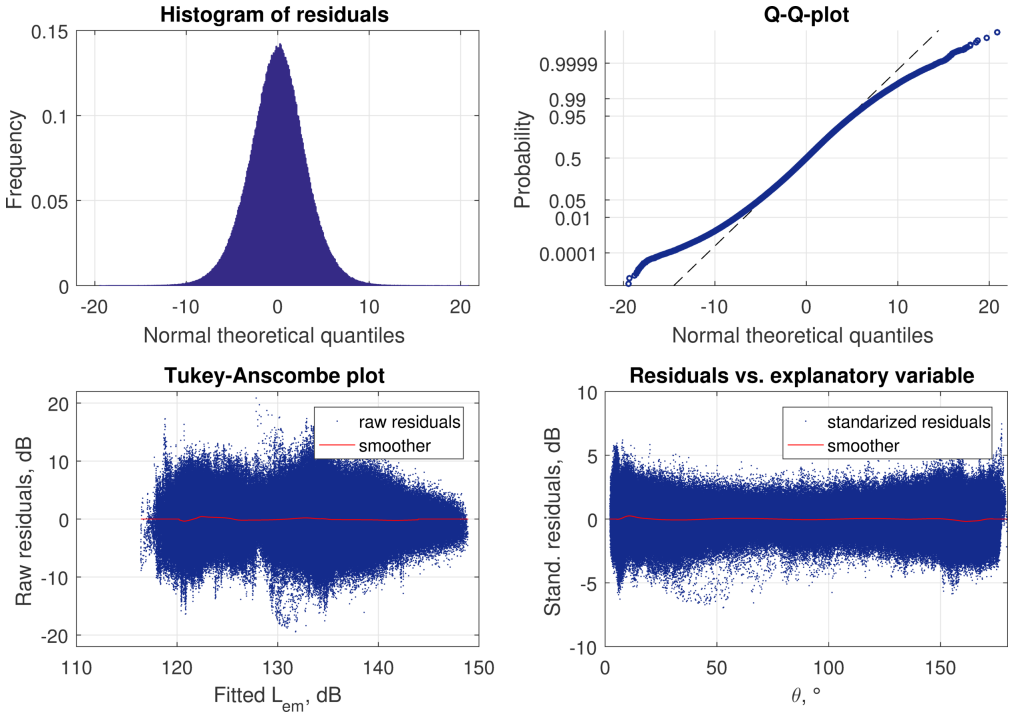

Figure 4.12: Example model validation for 631 Hz for the A333 (TRENT7). Residuals for n=1.24 million are depicted.

distribution is normal but slightly short-tailed. Though the Q-Q-plot shows tails, most of the 1.24 million residuals are on the 1:1 line while only data points outside 1 to 99 % are deviating. In addition, the zero error assumption and constant error variance is tested with scatterplots. The raw residuals are plotted against the fitted L_{em} and each explanatory variable, as shown for polar angle θ. No systematic deviations from zero were found for the smoothed red line. Overall, the results of the tested assumptions were satisfactory for each aircraft type and frequency band.

4.3.3 Weighting

During measurements, the polar angle θ changes slowly when the aircraft is far away, but quickly while the aircraft overflies the microphone. Consequently, only few data points of the equally spaced acoustical samples are available in the most relevant range of θ and vice versa. When establishing the model coefficients, the weighting reduces the influence of the inhomogeneous distribution of data points over θ. This distribution is inversely proportional to the time derivative $\dot{\theta} = \mathrm{d}\theta/\mathrm{d}t$. Analogous to OLS in linear regression, the models were therefore fitted with the WLS algorithm (Sec. 2.3).

As each flight and receiver combination has a different geometry, $\dot{\theta}$ was standardized by the maximum value per event and receiver, denoted as $w_{0,i}$ in Eq. 4.5. The standardization prevents a higher weight of measured levels for an aircraft close to the receiver than far away, where $\dot{\theta}$ is generally lower. The weights were then normalized by their mean value $\overline{w}_0$ to ensure that the sum of all weights w_i, which are used for the WLS algorithm, matches the number of observations n used in the analysis (Eq. 4.6).

$$w_{0,i} = \dot{\theta}_i / \max\left(\dot{\theta}\right)_{event,receiver} \tag{4.5}$$

$$w_i = \frac{w_{0,i}}{\overline{w}_0} \Rightarrow \sum_1^n w_i = n \tag{4.6}$$

4.4 Regression models

This section presents the regression models for airframe and engine noise, established with multiple linear regression analysis. Apart from the advanced models, which were developed on aircraft with FDR data (Table 4.1), also reduced models with fewer parameters are presented. Each model approach is at first summarized by its main model parameters to provide an overview of the dependencies. Subsequently, the whole model equation is given with all coefficients for the model parameters and their interactions. Major parts of this section have been submitted in similar form for publication in [107].

4.4.1 Advanced models

Airframe noise

The sound emission level of the airframe $\widehat{L}_{em,afm}(f)$ is modeled as the sum of the source terms and the radiation angle terms as summarized in Eq. 4.7.

$$\widehat{L}_{em,afm}(f) = \underbrace{\widehat{L}_{0,afm}(lMa, l\rho, FH, LG, SB, Proc)}_{\text{source term}} + \underbrace{\Delta\widehat{L}_{\theta,afm}(\theta)}_{\text{radiation angle term}} \tag{4.7}$$

The dependency on the frequency f indicates that all coefficients of the source and radiation angle terms are fitted for all 1/3-octave bands, even if not further denoted below for readability. Eq. 4.8 represents the source terms of the airframe model.

$$\begin{aligned} \widehat{L}_{0,afm} \quad = \quad & L_{a0} + a_{a1} \cdot lMa + Proc \cdot (a_{a2} + a_{a3} \cdot lMa) + b_{a1} \cdot l\rho \\ & + LG \cdot (c_{a1} + c_{a2} \cdot Proc + c_{a3} \cdot lMa) \\ & + \sum_{j=1}^{4} FH_j \cdot (d_{a1j} \ + d_{a2j} \cdot LG + d_{a3j} \cdot Proc) \\ & + SB \cdot (e_{a1} + e_{a2} \cdot LG + e_{a3} \cdot lMa) \end{aligned} \tag{4.8}$$

L_{a0} is the intercept and a_{a1} to e_{a3} are the frequency dependent coefficients of all model variables. The continuous variables are the logarithmic transformations lMa and $l\rho$, which represent the aeroacoustic sound generation in line with other semi-empirical models [12; 76]. In addition, each aeroplane configuration change of LG, FH or SB is modeled with additive level changes.

For FH and SB, interactions with the LG are considered to account for the changes in their effect when the sound emission level is raised by the deployed landing gear. Further, interactions between lMa and LG as well as SB are considered to account for the speed dependent sound generation. For the FH, the interaction with lMa is neglected as each flap handle position is only used for a certain small range of aircraft Mach numbers (Fig. 4.9) and an interaction with lMa can thus not be determined without high uncertainty.

Nevertheless, the varying combinations of flap handle position and aircraft Mach number range for approach and departure of Fig. 4.9 need to be considered in the model in one way or another. Further, the different deflection angles of the flap handle position 1 of the A320 family for departures and approaches need to be taken into account. Finally, the observation of the A320-family that 1/3-octave bands with cavity tones can have a strong increase in level with increasing Ma for approaches but not for departures, need to be considered. It is assumed that the local flow field is different for approach and departure due to different angle of attack and flap handle positions. To account for these

differences, an additional categorical variable, the flight procedure *Proc* (departure: 1, approach: 0) was introduced.

The directivity of the airframe model (Eq. 4.9) is expressed as an axially symmetric radiation along the longitudinal axis.

$$\Delta\widehat{L}_{\theta,afm} = k_a \cdot \cos\theta + l_a \cdot \cos 2\theta + m_a \cdot \sin\theta + n_a \cdot \sin 2\theta \tag{4.9}$$

The polar angle θ is taken into account with a second order Fourier series to model the longitudinal directivity. The coefficients for the airframe directivity are k_a to n_a. No interactions are included, i.e. the shape of the emission directivity is the same for all flight configurations. This simplification is justified as the data set was already corrected for the flight effect (Eq. 3.8).

Engine noise

The sound emission level of the engine noise $\widehat{L}_{em,eng}(f)$ is modeled by the sum of source terms and a more detailed approach for the radiation angle terms as summarized in Eq. 4.10.

$$\widehat{L}_{em,eng}(f) = \underbrace{\widehat{L}_{0,eng}(Ma, N1, N1^2)}_{\text{source term}} + \underbrace{\Delta\widehat{L}_{\theta,eng}(\theta, N1, N1^2) + \Delta\widehat{L}_{\varphi,eng}(\varphi, N1)}_{\text{radiation angle term}} \tag{4.10}$$

Source terms for engine noise (Eq. 4.11) include the intercept L_{e0} and three variables with their coefficients a_{e1}, b_{e1}, and b_{e2}. The first source term of engine noise is $N1$. The quadratic approach for $N1$ represents the jet as well as the fan noise as observed in Sec. 4.2.3. In addition, the aircraft Mach number Ma accounts for the source strength variation of the jet mixture with the surrounding flow (Sec. 4.2.3).

$$\widehat{L}_{0,eng} = L_{e0} + a_{e1} \cdot Ma + b_{e1} \cdot N_1 + b_{e2} \cdot N_1^2 \tag{4.11}$$

As the relation of L_{em} to $N1$ strongly depends on the polar angle θ (Sec. 4.2.3), the Fourier terms of the longitudinal directivity $\Delta\widehat{L}_{e\theta,eng}$ interact with $N1$ as well as $N1^2$ (Eq. 4.12). The corresponding model coefficients are $k_{e,j}$ to $n_{e,j}$ with index j for each interaction. The lateral directivity (Eq. 4.13), which represents the installation effect, is included as a half range Fourier series of second order, i.e. with only sine terms of φ. Similar to the longitudinal directivity, each term has an interaction with $N1$

with coefficients $o_{e,j}, p_{e,j}$. Also an interaction with $N1^2$ was tested but not found to significantly improve the results.

$$\begin{aligned} \Delta\widehat{L}_{\theta,eng} &= (k_{e,j} \cdot \cos\theta + l_{e,j} \cdot \cos 2\theta + m_{e,j} \cdot \sin\theta + n_{e,j} \cdot \sin 2\theta) \\ &\quad \cdot(1 + N1 + N1^2) \end{aligned} \tag{4.12}$$

$$\Delta\widehat{L}_{\varphi,eng} = (o_{e,j} \cdot \sin\varphi + p_{e,j} \cdot \sin 2\varphi) \cdot (1 + N1) \tag{4.13}$$

With Eq. 4.12 and Eq. 4.13, the shape of the 3D directivity for each frequency band is allowed to change with $N1$. Thus, also the spectral content of the total directivity varies with $N1$.

4.4.2 Reduced models

For aircraft without available FDR data, regression models with a reduced set of parameters can be derived. Namely, the aeroplane configuration of the aircraft is unknown without FDR data. Another reason to reduce the parameters of the model could be measurements with insufficient coverage of the lateral angle. In this case the directivity can be reduced to a two-dimensional (2D) model.

These reduced models can also be established for aircraft with FDR data to determine the influence of the aeroplane configuration or lateral directivity on the results. Within this thesis, the following model variants were established:

- **3D:** Advanced model with a 3D directivity and the influence of the aeroplane configuration. It is the standard model for aircraft types with available FDR data.
- **3Dred:** Model with a 3D directivity but without aeroplane configuration effects. It is the standard model for types with $N1$-determination based on acoustic signal analysis (Sec. 3.4.2).
- **2Dred:** Model with a 2D directivity and without aeroplane configuration effects.

Effects of the aeroplane configuration are accounted for in the airframe model. Therefore, for 3Dred only the airframe model changes compared to 3D. LG, FH, SB, and their interactions are removed from the model.

$$\widehat{L}_{em,afm}(f) = \underbrace{\widehat{L}_{0,afm}(lMa, l\rho, Proc)}_{\text{source terms}} + \underbrace{\Delta\widehat{L}_{\theta,afm}(\theta)}_{\text{radiation angle terms}} \tag{4.14}$$

$$\widehat{L}_{0,afm} = L_{a0} + a_{a1} \cdot lMa + Proc \cdot (a_{a2} + a_{a3} \cdot lMa) + b_{a1} \cdot l\rho \tag{4.15}$$

For 2Dred both the airframe and engine noise model need to be modified compared to the advanced model to establish a two-dimensional model without aeroplane configuration. In addition to the changes above (Eq. 4.15), the directivity of the engine model is reduced

to 2D by omitting $\widehat{L}_{\varphi,eng}(\varphi, N1)$ in Eq. 4.10. The directivity of the airframe model is already two-dimensional.

$$\widehat{L}_{em,eng}(f) = \underbrace{\widehat{L}_{0,eng}(Ma, N1, N1^2)}_{\text{source terms}} + \underbrace{\Delta\widehat{L}_{\theta,eng}(\theta, N1, N1^2)}_{\text{radiation angle terms}} \tag{4.16}$$

For each model variant all parameters of the engine as well as the airframe noise model were established with an individual multiple linear regression. Even if only the aeroplane configuration is reduced in the airframe model, the iterative process to separate the data to airframe and engine noise (cf. Sec. 4.5) will lead to slightly different coefficients of the engine model in comparison to the advanced model.

4.4.3 Energy correction

As a consequence of the minimization of $\widehat{\sigma_E}$ with the WLS algorithm, the model coefficients are fitted to the arithmetic mean of L_{em}. Therefore, a correction is needed to predict the energy mean, denoted as energy correction. The energy mean is equal to the arithmetic mean of the sound power instead to the arithmetic mean of the logarithmic quantity. As the L_{em} is normal distributed, which was the requirement for a linear regression, the energy correction can be determined analytically by $0.115 \cdot \sigma^2$ [6; 31] as shown in Sec. 2.3.5.

For the variance σ^2 a suitable choice has to be taken. In case of the statistical model in this thesis, the error mean square $\widehat{\sigma}_E^2$ may be a good substitute: it represents the unexplained variation between model and data. Fig. 4.13 shows that $\widehat{\sigma}_E^2$ is is much larger for microphones in the far range compared to the close range. It is assumed that propagation effects and thus uncertainty of the back propagation cause the higher

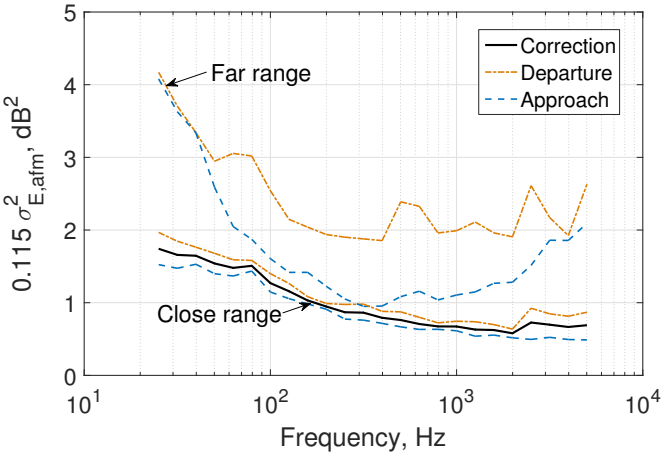

Figure 4.13: Correction term for energy mean versus frequency for the A320 (CFM56-5B) from the airframe noise model (similar for engine noise model).

variance in the far range, where the distances between receiver and source are considerably higher.

It was decided not to consider these variations as they do not represent the underlying level variations of the source. Indeed, the energy correction of the regression models should only account for the variations of the source and not for the unexplained variations due to the back propagation. Therefore, $\widehat{\sigma}_{E,CR}(f)$ of the data in the close range (combined error of approach and departure) was used for the corrections in Eq. 4.17 and Eq. 4.18.

$$\widehat{L}_{\overline{em},afm}(f) = \widehat{L}_{em,afm}(f) + 0.115 \cdot \widehat{\sigma}^2_{E,afm,CR}(f) \quad (4.17)$$

$$\widehat{L}_{\overline{em},eng}(f) = \widehat{L}_{em,eng}(f) + 0.115 \cdot \widehat{\sigma}^2_{E,eng,CR}(f) \quad (4.18)$$

The energetic sum of the fitted final models for airframe (Eq. 4.17) and engine noise (Eq. 4.18) yields the total predicted emission level $\widehat{L}_{\overline{em},total}(f)$, corrected for the energy mean.

$$\text{Energy mean: } \widehat{L}_{\overline{em},total}(f) = \widehat{L}_{\overline{em},afm}(f) \oplus \widehat{L}_{\overline{em},eng}(f) \quad (4.19)$$

For the comparison with mean measured data (Chap. 5) and a simulation without correction (Sec. 6.3), also the arithmetic mean sound emission level $\widehat{L}_{em,total}(f)$ of the models is used.

$$\text{Arithmetic mean: } \widehat{L}_{em,total}(f) = \widehat{L}_{em,afm}(f) \oplus \widehat{L}_{em,eng}(f) \quad (4.20)$$

4.5 Data separation technique

In Fig. 4.14 the model development and the separation of the measured total emission levels from the regression data set to airframe and engine noise is shown. In step 1, the data set is separated into two subsets: subset one contains data for the engines running in idle i.e. only approach conditions, and subset two contains all other data from approach and departure with engines on load. It is assumed that airframe noise is dominating the total L_{em} for subset one, as supported by [51; 91].

The limit for the separation with $N1$=40 % was determined by engineering judgment and from data plots of L_{em} versus $N1$ (Fig. 4.15). With a higher limit (e.g. 50 %) the contribution of the engines increases, and more likely results in overestimating the contribution of airframe noise. With a lower limit (e.g. 30 %) the number of observations would substantially decrease and would prevent from establishing reliable model coefficients. While the separation limit thus seems feasible, the iterative process of the data separation further refines the initial ratio (step 3) between airframe and engine noise.

In step 2, an initial airframe and an initial engine models (simplified versions of the models in Sec. 4.4, see Appendix A.1) are fitted on their corresponding subsets to determine the main effects for each sound source. Only 6 % to 8 % of the total data set is used to fit the initial airframe model (all data with $N1 < 40\,\%$), and for high frequencies the fraction even decreases. Likewise the engine model is fitted on all other data with $N1 \geq 40\,\%$ that includes all phases of the departure and the final approach.

With the aid of the predicted airframe and engine sound emission levels, a source ratio can be calculated for each data point in the original data set (step 3). On the basis of sound emission, the ratio q^i (Eq. 4.21) is defined as the predicted sound emission of the engine divided by the total sound emission.

$$q^i(f) = \frac{10^{0.1\widehat{L}^i_{em,eng}(f)}}{10^{0.1\widehat{L}^i_{em,eng}(f)} + 10^{0.1\widehat{L}^i_{em,afm}(f)}} \tag{4.21}$$

A ratio of zero indicates that only airframe noise contributes to the total sound emission and a ratio of one corresponds to engine sound emission only. Note that all predictions from these models are marked by a hat to distinguish from input data; the superscript i indicates that the initial models are used.

The method requires the initial models to be extrapolated. For example, the initial airframe model was based on approaches with Mach numbers smaller 0.35, while depar-

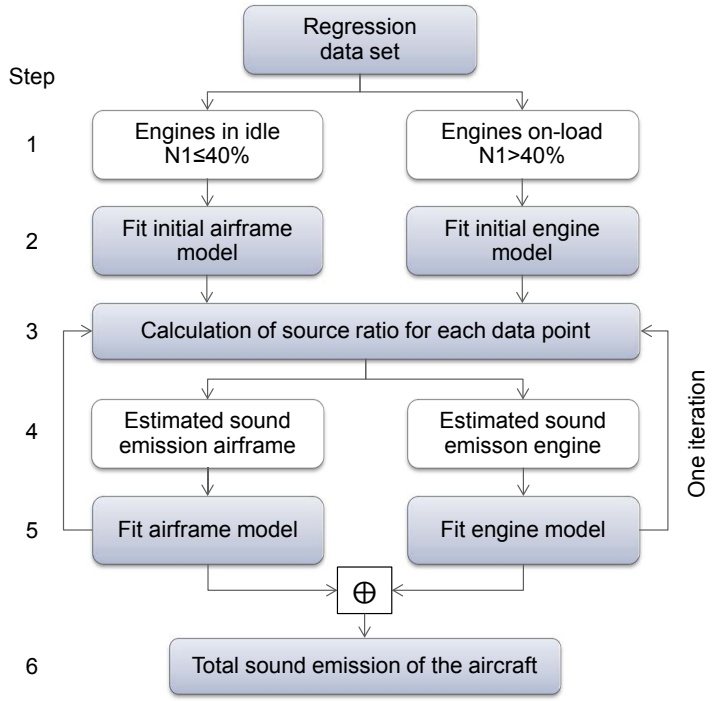

Figure 4.14: Process of model development and data separation

tures with up to Mach numbers of 0.45 were measured. As a consequence, to predict $\widehat{L}^i_{em,afm}$ for each data point on the whole data set, extrapolations become necessary. Nevertheless, the extrapolation for the Mach number is based on physical knowledge (Sec. 4.2.3), thus allowing for a plausible first estimation of airframe and engine noise for the whole data set.

Based on the ratio q^i two separated data sets, both including all measurements for approach and departure, were created for each 1/3-octave band (step 4). One represents the sound emission of the engines $L^i_{em,eng}$ and the other the sound emission level of the airframe $L^i_{em,afm}$.

$$L^i_{em,eng}(f) = L_{em}(f) + 10\log_{10}\left(q^i(f)\right) \tag{4.22}$$

$$L^i_{em,afm}(f) = L_{em}(f) + 10\log_{10}\left(1 - q^i(f)\right) \tag{4.23}$$

Fig. 4.15 compares both data sets to the original L_{em}. The airframe levels are dominating for $N1 < 40\%$, which is the implication of the assumption in step 1, while they are approximately 20 dB lower than the total levels for departures. In contrast, the engine levels (bottom right) are dominant for departures and lose influence at lower $N1$.

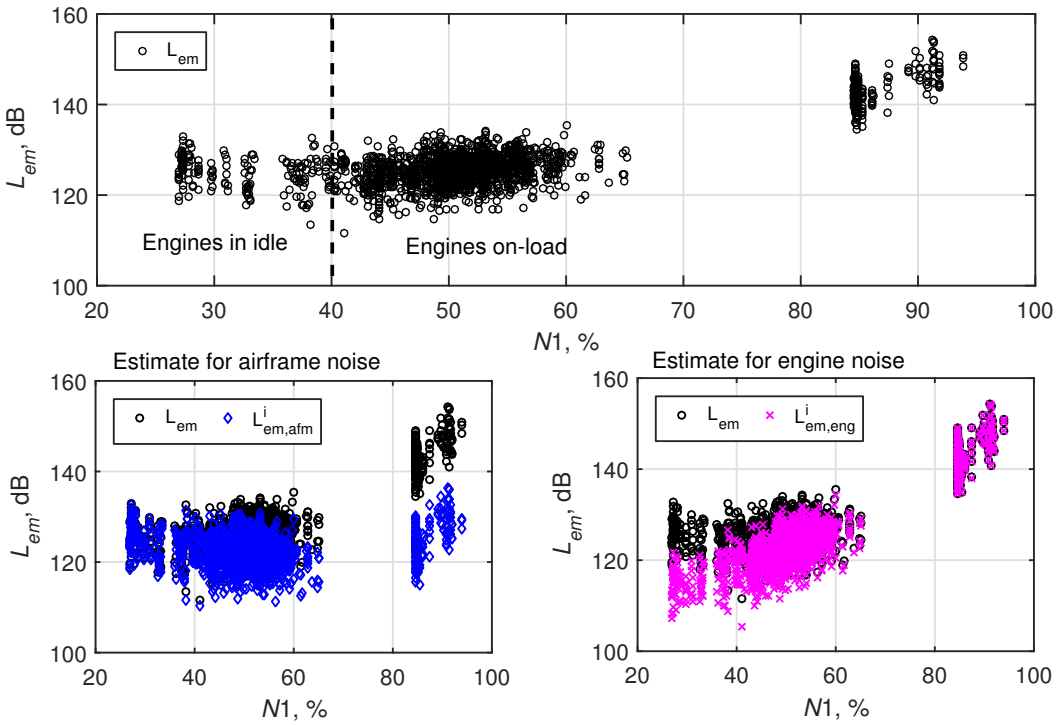

Figure 4.15: Data separation example for the A320 at 100 Hz. The back propagated data on the top are separated to estimates of the sound emission related to airframe (bottom left) and engine noise (bottom right).

In total, by adding the individual levels of both data sets energetically, the original data set can be reconstructed.

In step 5 of Fig. 4.14, the final models for airframe and engine noise (Sec. 4.4) are fitted on these data sets. Steps 3 to 5 are repeated once to improve the estimation of the ratio between airframe and engine noise. In the second run, the ratio is based on the models that are fitted on the whole data set in contrast to the initial models. Finally, the energetic sum of the airframe and engine model adds up to the predicted total $\widehat{L}_{em}$ (Sec. 4.4.3). The entire process of data separation and model fitting is performed 24 times to establish models for each 1/3-octave band.

5 Results

5.1 Established aircraft types

Based on the measurements around Zurich airport, 43 different combinations of aircraft and engine type were measured (Sec. 4.1). For types with FDR data, advanced models (3D) for each combinations of aircraft and engine type were established. Only the A332 had too few data (14 in total) to establish a model. In particular approaches in the far range were missing for this type, which are mandatory for the separation of airframe and engine noise. For a comparison of the different models, also the reduced models 3Dred and 2Dred were established.

The designations of the 19 aircraft noise emission models in Table 5.1 are composed by the aircraft type and engine type, divided by an underscore (e.g. A333_TRENT7). As an example, the model parameter estimates for the A333_TRENT7 are listed in Sec. A.3 of the Appendix. These model parameters were established on the specific data set of

Table 5.1: Aircraft noise emission models and their data basis: input data (from FDR or $N1$ determination), model variant (Adv.=Advanced, Red.=reduced) and number of flights for departure and approach.

Model name	Description	Input	Model	D	A	Total
A319_CFM56-5B	Airbus A319-100, CFM56-5B	FDR	Adv.	120	41	161
A320_CFM56-5B	Airbus A320-200, CFM56-5B	FDR	Adv.	424	249	673
A321_CFM56-5B	Airbus A321-200, CFM56-5B	FDR	Adv.	300	126	426
A32X_CFM56-5A	Airbus A320-Family, CFM56-5A	N1	Red.	57	15	72
A32X_V2500	Airbus A320-Family, V2500	N1	Red.	198	33	231
A333_TRENT7	Airbus A330-300, TRENT7	FDR	Adv.	249	136	385
A343_CFM56-5C	Airbus A340-300, CFM56-5C	FDR	Adv.	166	120	286
A388_GP7270	Airbus A380-800, GP7270	N1	Red.	26	2	28
A388_TRENT9	Airbus A380-800, TRENT9	N1	Red.	38	20	58
B737_CFM56-3	Boeing B737 Classic (-300 to -500)	N1	Red.	84	39	123
B737_CFM56-7B	Boeing B737 NG (-600 to -900)	N1	Red.	297	37	334
B763_PW4060	Boeing 767-300, PW4060	N1	Red.	9	34	43
B76X_CF6-80C2	Boeing 767-Family (-200 to -400)	N1	Red.	19	57	76
CRJ9_CF34-8C5	Bombardier Regional Jet CRJ-900	N1	Red.	71	22	93
E170_CF34-8E	Embraer ERJ 170	N1	Red.	62	27	89
E190_CF34-10E	Embraer ERJ 190	N1	Red.	243	49	292
F100_TAY650-15	Fokker 100	N1	Red.	234	61	295
FA7X_PW307	Dassault Falcon 7X	N1	Red.	17	10	27
RJ1H_LF507	BAE SYSTEMS AVRO RJ-100	FDR	Adv.	324	202	526

the aircraft type. Even if the model approach uses physical relations for the parameters, extrapolation of a linear regression model is precarious. See Appendix A.4 for the flight parameter range each aircraft noise emission model is based on. Table A.19 concentrates on the continuous parameters available for the advanced and reduced models. Table A.20 and Table A.21 provide a more detailed insight to the Mach number range for each combination of the categorical variables (FH and LG as well as SB and LG).

For aircraft types without FDR data the reduced models (3Dred) were established if a sufficient number of flights for departures and approaches in the close and far range was available. In case of a low number of movements or missing procedures, similar aircraft subtypes with the same engine type were grouped. For instance, the B736 and B739 are grouped with the B737 and B738 due their low number of flights (below 13, cmp. Table 4.2). Thus, the Boeing 737 New Generation, equipped with the CFM56-7B, were grouped to establish one combined aircraft noise emission model, which is then based on 334 flights. A grouping over different engines was not done, as the engine is the dominant source, and different engines have different noise characteristics.

Fig. 5.1 illustrates that the grouping strategy works well for different aircraft types with the same engine. It shows that the engine parameters $N1$ and Ma are used at different parameter settings to generate sufficient thrust and lift for departures. This fact makes it beneficial to group the aircraft types of a family with the same engine type, because a larger data range (e.g. for $N1$) improves the fit of the model. Systematic differences that would indicate a different acoustical behavior between aircraft subtypes could not be found. Further, the main airframe noise sources of an aircraft family are identical, only the length of the fuselage is changed. Therefore, also for airframe noise no severe differences between subtypes are expected.

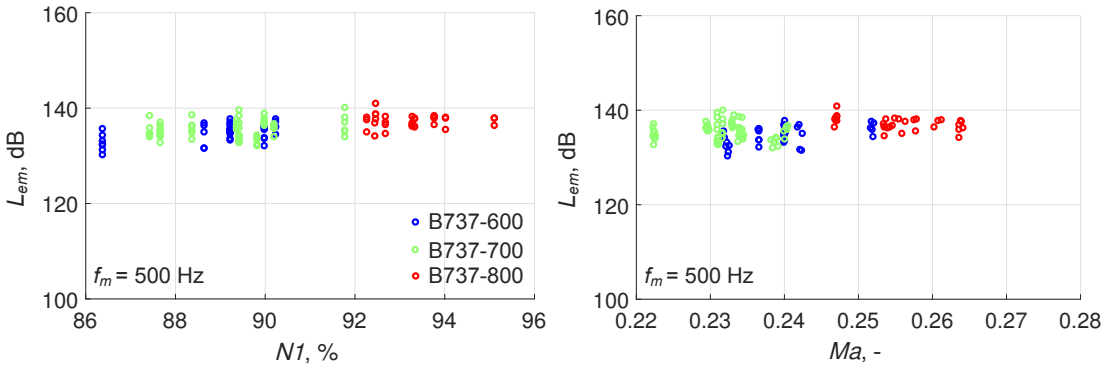

(a) L_{em} versus $N1$ (b) L_{em} versus Ma

Figure 5.1: Grouping of the B737 New Generation family equipped with the CFM56-7B. The plots illustrate that each subtype uses a different range of $N1$ and Ma for departure, thus supporting the grouping strategy.

5.2 Model performance

The model performance is assessed with the coefficient of determination R^2 and the root-mean-square error $\widehat{\sigma}_E$ (Sec. 2.3). R^2 gives a dimensionless measure to assess the variance explained by the selected parameters in each frequency band. $\widehat{\sigma}_E$ assesses the unexplained variations on the basis of the same unit as the sound emission level (dB).

The best expressiveness is found in R^2_{total}, which is represented by the sum of the predicted values (Eq. 4.19) with respect to the original set of back propagated data L_{em}. R^2_{afm} and R^2_{eng} are helpful for qualitative considerations. They have to be regarded with care as they are calculated with respect of the separated data set which was separated by those models.

Fig. 5.2a shows the results for the model performance of the A320_CFM56-5B. The R^2_{total} lies between 0.7 and 0.8. The engine model R^2_{eng} shows values slightly higher than 0.8 for most frequency bands. In contrast, R^2_{afm} is between 0.2 and 0.6 with much more variation between the different frequency bands. The value of R^2 depends on the frequency range in which the sound sources radiate. For instance, R^2_{eng} of the A320 is high between 50 to 400 Hz where the jet noise is dominant. This is in line with [14]. Similar, R^2_{eng} is high at 2 to 3 kHz, the bands which contain the blade passing frequency (BPF) of the A320 at departure.

Airframe sound sources can be identified in the same manner. In accordance to measurements on an A320 full scale wing in the large low-speed facility of the German-Dutch Wind Tunnels (DNW-LLF), the slats (included by the parameter *Flaps*) considerably radiate sound between 100 and 300 Hz [76]. Further, a prominent cavity tone in the wing can be found at 500 and 630 Hz. Finally, excess noise of the flap side edge is

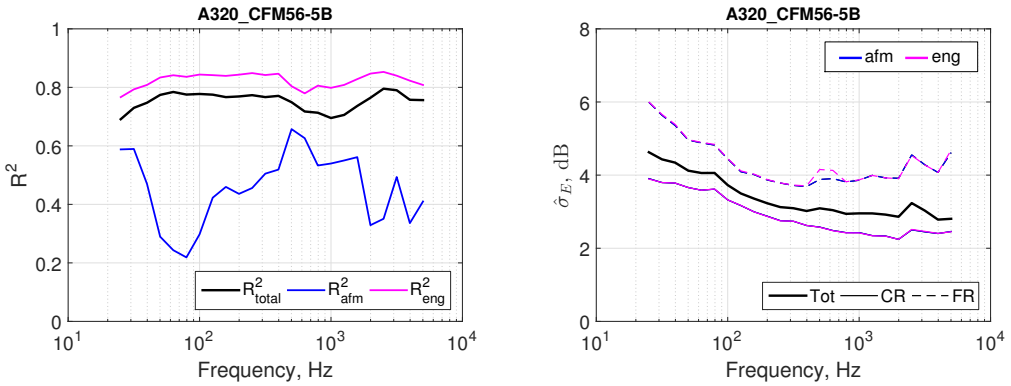

(a) Coefficient of determination (3D)

(b) Root-mean-square error (3D)

Figure 5.2: Coefficient of determination (a) and $\widehat{\sigma}_E$ (b) versus frequency for airframe, engine, and total model of the A320_CFM56-5B. $\widehat{\sigma}_E$ is divided into far range (FR) and close range (CR).

prominent between 1 and 1.6 kHz. In those frequency ranges, the R^2_{afm} shows local maxima. In contrast, there are no explicit sound sources for 50 to 100 Hz and above 1.6 kHz, consequently R^2_{afm} is low.

Fig. 5.2b depicts the unexplained variations each frequency band. It shows the total $\widehat{\sigma}_E$ and also the division into airframe and engine model, which shows no significant differences. However, a partition into close range and far range provides additional information. In the close range $\widehat{\sigma}_E$ is 1 to 2 dB smaller than in the far range. The total $\widehat{\sigma}_E$ lies in between with over 4 dB for low frequencies and around 3 dB for mid and high frequencies. This error is partly explained by the uncertainties of the measurement and back calculation (Sec. 2.2.2). The larger error in the far range can therefore be explained with a higher uncertainty due to the larger propagation distances. In addition, lower noise levels are susceptible to be influenced by noise from other sources.

The model performance (R^2 and $\widehat{\sigma}_E$) does not significantly change for the reduced model variant 3Dred (see Fig. 5.3a and Appendix A.5). Only the R^2_{afm} shows pronounced differences if the aeroplane configuration is dominant in a certain frequency range as shown for the RJ1H. Around 100 Hz the R^2_{afm} is clearly higher in 3D compared to 3Dred, which can be explained by a tone which is only accounted for by the aeroplane configuration. For 500 Hz to 1 kHz and around 3 kHz a noise generation from the aeroplane configuration can be assumed, as the 3D model is improved compared to the 3Dred model. The $\widehat{\sigma}_E$ for the total model is therefore also very similar (Fig. 5.4a), but slightly larger values are found below 125 Hz.

The comparison of the RJ1H between 3D and 2Dred in Fig. 5.3b shows larger differences for R^2_{afm} as wells as for R^2_{eng} and R^2_{total}. In Fig. 5.4b also $\widehat{\sigma}_E$ has larger values of up to 0.3 dB over the whole frequency range. Therefore, the model performance indicates that 2Dred is a less accurate model while 3D and 3Dred are comparable.

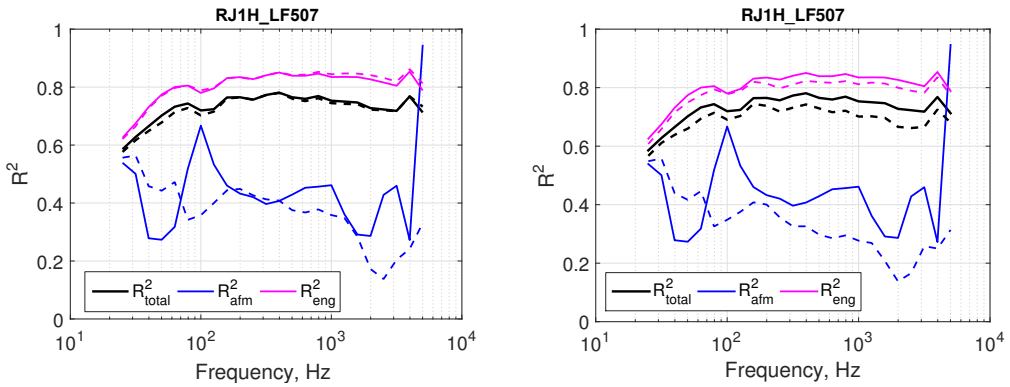

(a) 3D (solid) versus 3Dred (dashed)

(b) 3D (solid) versus 2Dred (dashed)

Figure 5.3: Influence of the model variants on R^2 for the RJ1H_LF507.

At 5 kHz the 3D model seems to be overfitted, which is also observed for the A319 and A343 for every model variant (see Appendix A.5). For these two types $\widehat{\sigma}_E$ also increases which supports the assumption of overfitting. Especially $\widehat{\sigma}_E$ of the A343 increases around 1 dB in total and almost 2 dB in the far range. Due to the high value and uncertainty of the air absorption the model for this frequency band seems to be less confidential. For the A319 $\widehat{\sigma}_E$ rises only slightly but is similar to the A343. The RJ1H actually has a decrease in $\widehat{\sigma}_E$ and is therefore more trustful. In addition, 3Dred and 2Dred do not show this effect.

The model performance showed a consistent behavior for almost all FDR types. Only the A319 has a bit lower R^2 and higher $\widehat{\sigma}_E$. This type is also based on the lowest number of flights (161) compared to the the next lowest number for the A343 (286) or the most available A320 (673). Overall, the R^2_{eng} is mainly very high around 0.8 and the shape of R^2_{tot} is very similar but on a slightly lower level, as the total noise is dominated by the engine in most of the flight configurations. R^2_{afm} is generally on a lower level between 0.2 and 0.6 with high values only in bands where airframe noise is dominant. $\widehat{\sigma}_E$ is very consistent in shape and value for all FDR types and varies between 5 dB (low frequencies) to a minimum of 3 dB at high frequencies. Regarding R^2 and $\widehat{\sigma}_E$ together, these results already testify a good modeling approach which works for different aircraft types and model variants. An exception is the 5 kHz band.

Types without FDR data (see Appendix A.6) show more differentiated results. R^2_{eng} in the most cases still exhibits values around 0.8. However R^2_{tot} does not always follow the trend of R^2_{eng} as it was the case for types with FDR data. For some type it does not follow the same shape as R^2_{eng} (e.g. A32X_V2500) or is much lower than it (e.g. B763_PW4060). One reason is the much lower number of flights the models are based on (27 to 334). A second reason is the higher uncertainty of the $N1$ which was determined

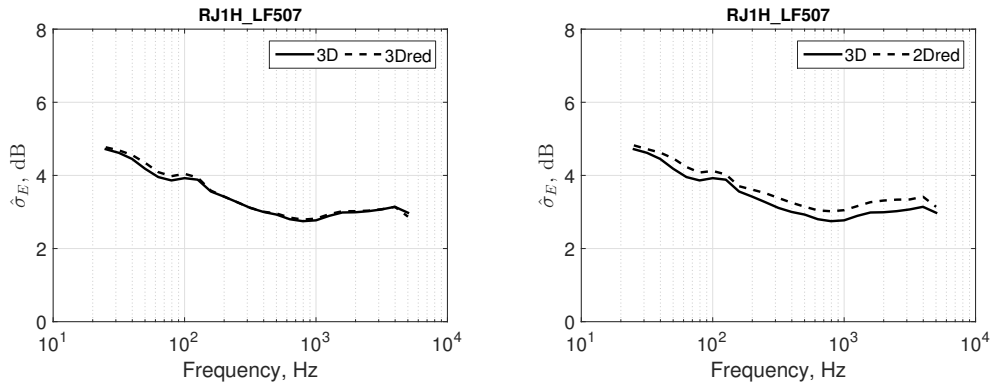

(a) 3D (solid) versus 3Dred (dashed)

(b) 3D (solid) versus 2Dred (dashed)

Figure 5.4: Influence of the model variants on $\widehat{\sigma}_E$ for the RJ1H_LF507.

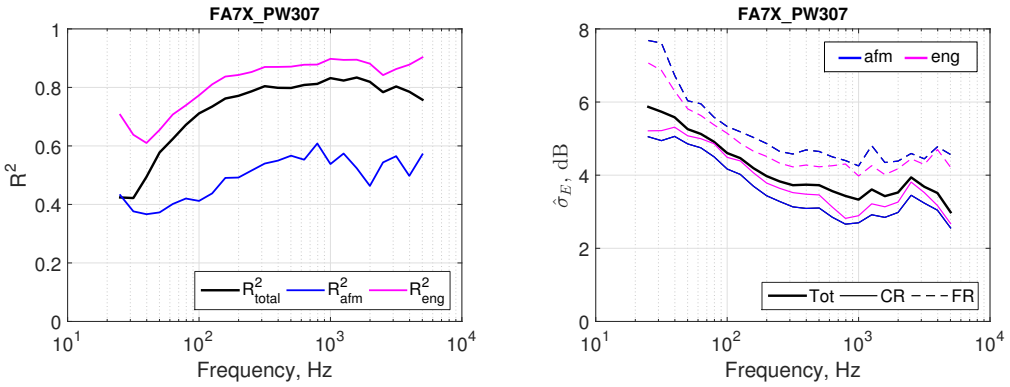

(a) Coefficient of determination (b) Root-mean-square error

Figure 5.5: Coefficient of determination (a) and $\widehat{\sigma}_E$ (b) versus frequency for airframe, engine, and total model of the FA7X_PW307. $\widehat{\sigma}_E$ is divided into far range (FR) and close range (CR).

from the acoustical measurements. R^2_{afm} varies between 0.2 and 0.6 and shows some regions with high impact, even as the aeroplane configuration is unknown for these types.

Nevertheless, $\widehat{\sigma}_E$ is very similar to the FDR types and normally varies between 5 dB (low frequencies) to a minimum of 3 dB (high frequencies). The FA7X_PW307 also shows very good results in R^2 (Fig. 5.5a). Only at low frequencies the values are low, which might be due to no noise generation at these bands. However, this example shows the importance to assess both R^2 and $\widehat{\sigma}_E$, as $\widehat{\sigma}_E$ shows high values between 3.5 and 6 dB (Fig. 5.5b). The FA7X_PW307 is the aircraft type with the lowest number of flights for the model development (27), which might be the explanation for the higher $\widehat{\sigma}_E$.

5.3 Directivity and spectra

In this section, example model predictions of spectra and directivity patterns are shown for various flight configurations and compared to measurements. For comparison of model predictions with the measured data, the data set is filtered as follows: flight parameters for the flight phase and a radiation angle of interest are chosen to predict the sound emission level. Then, the same parameters with a certain interval around each parameter are used to create a subset from the complete data set (φ=60° ± 5°, $N1$=93 % ± 2 % etc.). Finally, the arithmetic mean L_{em} is calculated and compared with the arithmetic mean of the predicted values $\widehat{L}_{em}$ (see Sec. 4.4.3). Hence, the large variations of the measured data in Sec. 4.2.3 are averaged for the comparison. This comparison allows assessing if the model approach is appropriate, even if it is not an independent comparison because the model was fitted on the same data set.

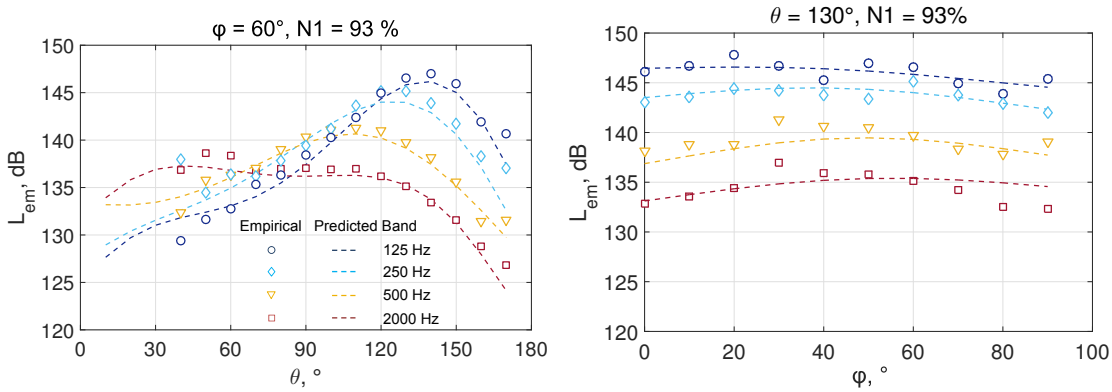

(a) Longitudinal directivity

(b) Lateral directivity

Figure 5.6: Spectral directivity patterns for departure of the A320_CFM56-5B with high thrust setting.

Spectral directivity patterns are predicted and compared to mean values of measured data with corresponding flight parameters. A departure of the A320 with a high thrust setting of $N1$=93 % is shown in Fig. 5.6. The longitudinal directivity in Fig. 5.6a is presented for an observer on the side at φ=60° for four representative 1/3-octave bands. The shape of the directivity of the low frequencies clearly follows the typical jet characteristic [88]. With increasing frequency, the maximum amplitude decreases and is shifted towards the front. At 2.5 kHz the shape shows two maxima which is typical for the sound emission of fan noise to the front as well as to the rear through the bypass. The model reproduces the measured data of the chosen flight configuration very good.

The lateral directivity in Fig. 5.6b is shown to the rear at θ=130°. The level variations are much smaller than for the longitudinal directivity. The maximum peak lies between 20 and 40° and not directly below the aircraft. The model generally follows the trend but is too simplified to reproduce the exact shape. In addition, the shape of the lateral directivity might slightly change with θ but this interaction is not included in the model. Thus the model represents the mean lateral directivity over all θ for the chosen $N1$. However, the simplified lateral directivity of the model is justified as all these effects are small. Further examples of the total directivity (longitudinal and lateral) in comparisons to measurements in dependence of $N1$ are presented in [106]. The comparisons resulted in good agreement with the mean values of the measurements.

In Fig. 5.7 spectra for typical flight configurations of the A320_CFM56-5B at take-off and final approach are depicted for θ=90° in Fig. 5.7a and θ=130° in Fig. 5.7b. For take-off, as seen in Fig. 5.6, each frequency band has its specific longitudinal directivity pattern. Thus, the spectra for take-off in Fig. 5.7a differs particularly below 400 Hz compared to Fig. 5.7b. Above, both spectra are similar, showing the BPF at 2.5 kHz.

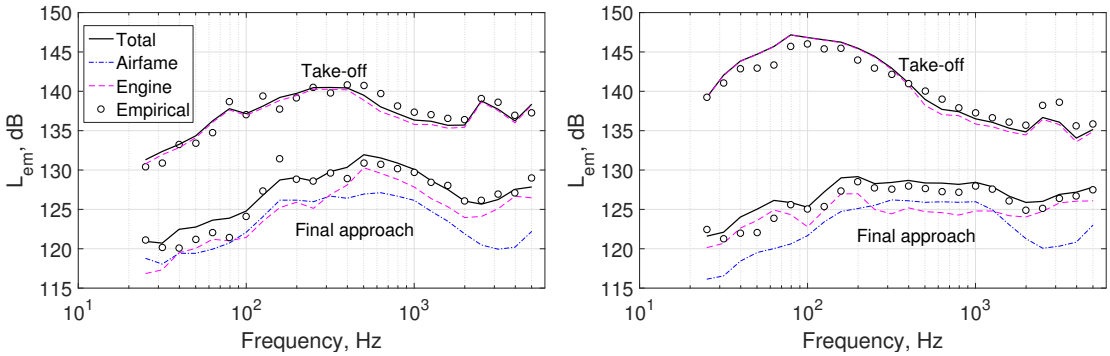

(a) Spectra below the aircraft at θ=90°, φ=30°

(b) Spectra in the rear at θ=130°, φ=30°

Figure 5.7: Spectra for final approach ($N1$=55 %) and take-off at high thrust setting ($N1$=93 %) for the A320_CFM56-5B. The airframe spectra is not shown for take-off to avoid an overlay with the spectra of final approach. The levels, however, are much lower than the engine noise levels.

The prediction shows that the $\widehat{L}_{em,total}$ is dominated by the engine model while the airframe model only slightly contributes in the bands between 400 Hz to 2 kHz.

At final approach, the model predicts a very similar contribution of airframe and engine noise to the total emission. In Fig. 5.7a engine noise dominates above 400 Hz. With $N1$=55 % the BPF is at 1.65 kHz and from [42] the fan broadband noise is expected to be distributed at 2.5 times the BPF (4.2 kHz). At this frequency the engine spectrum has a local maximum. In Fig. 5.7b the low frequencies ($<$ 200 Hz) and high frequencies ($>$ 1.25 kHz) are dominated by the engine noise. For mid frequencies the airframe noise dominates the spectra due to the deployed landing gear. The total levels are in good agreement with the mean measured data.

5.4 Effects of the model parameters

In this section, the regression models are evaluated for each flight parameters while all other parameters are kept constant. In this way, the effect of each model parameter can be shown individually for two different cases, namely at the source and at the receiver, which can yield helpful insights.

Fig. 5.8 depicts the directivity of a departing aircraft at the source (curve 1), which is the outcome of the regression models (Eq. 4.19) and corresponds to the energy mean of the sound emission level. Doppler shift and the flight effect are applied because both effect change the spectra and directivity at the source (curve 2). As an example, the A-weighting is added to the sound emission level to simulate the frequency response of the human ear (curve 3). As the A-weighting attenuates low frequencies, the total sound level is considerably reduced to the rear where jet-noise dominates ($\theta > 90°$). Finally,

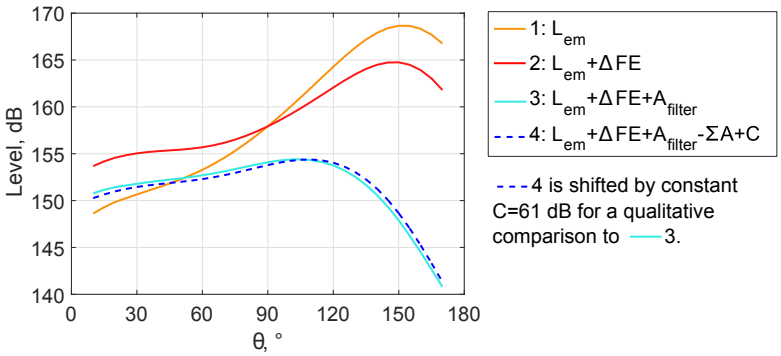

Figure 5.8: Pure sound emission level and the segregated influence of the flight effect, A-weighting, and sound propagation. Example prediction for the A333_TRENT7 with 3Dred at $N1$=90 %, φ=0°, Ma=0.26, ρ=1.15 kg/m³.

the sound propagation for a distance of 304.8 m is applied, which attenuates the sound dependent on the frequency spectra for each θ. A constant of 61 dB is added to show that there are almost no differences of the directivity between curve 4 at the receiver and at the A-weighted emission in curve 3. Thus, curve 2 represents the sound emission at the source and curve 4 the received sound exposure, which are two interesting viewpoints to study the effects of the model parameters.

The effects of the model parameters are therefore presented in the following figures (e.g. Fig. 5.9) for the total sound emission level $\widehat{L}_{\overline{em}}$ at the source applying the Doppler and flight effect (left side, in red) as well as for the total, A-weighted sound pressure level L_{pA} at a receiver (right side, in blue). L_{pA} represents the propagated sound at a receiver with a fixed propagation distance of 304.8 m (1000 ft). The direct sound propagation is based on the international standard atmosphere (T=15 °C, RH=70 %, p=1013.25 hPa).

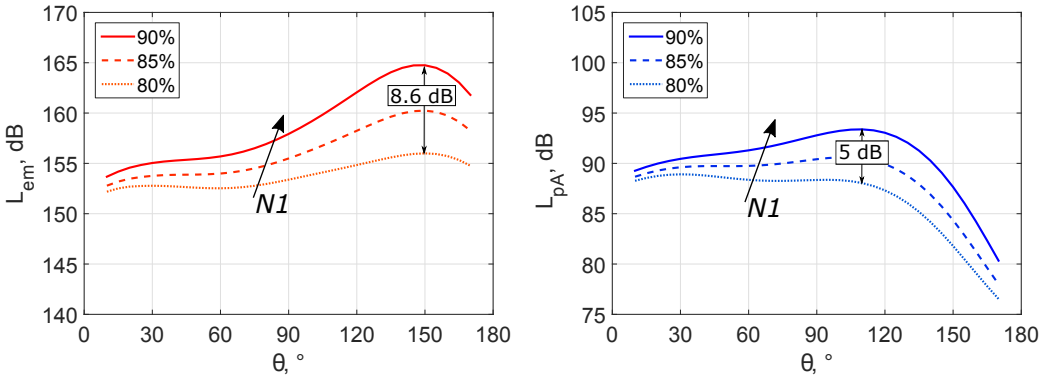

(a) Level at source (d=1 m)

(b) Level at receiver (d=304.8 m)

Figure 5.9: Relationship of (a) $\widehat{L}_{\overline{em}}$ and (b) L_{pA} to the polar angle for different $N1$ settings at take-off for the A333_TRENT7. Predicted with 3Dred model at φ=0°, Ma=0.26, ρ=1.15 kg/m³.

Fig. 5.9 depicts the longitudinal directivity pattern for three take-off settings for the A333 ranging from a high thrust setting to cutback thrust. The level maximum at the source (left) is at θ=150°. At this point the change of $N1$ from 80 % to 90 % leads to a maximum sound pressure level difference of 8.6 dB, which decreases to the front of the aircraft. The shape of the directivity changes with $N1$, due to the interaction of $N1$ and θ in the engine noise model. On the receiver side (right), the A-weighting strongly attenuates the (low-frequency) levels to the rear and bands above 1 kHz are substantially attenuated by atmospheric absorption. Compared to the source, the maximum sound pressure level shifts forwards to approximately 110°, thus, the maximum level difference between 80 % and 90 % reduces to 5 dB.

Fig. 5.10 shows the same situation over the lateral radiation angle at θ=90°, which represents the level at the shortest distance for an overfly of an A333. Each step of 5 % $N1$ leads to about 2 dB increase of the sound emission level and 2 dB(A) of the sound pressure level. The shape of the lateral directivity only slightly changes with $N1$ for the chosen take-off settings. While the longitudinal directivity is more pronounced, also the lateral directivity cannot be neglected, as the sound pressure level below the aircraft can be as much as 2.4 dB(A) smaller than the maximum radiation at an angle φ=40°. To the side, the level is up to 4 dB(A) smaller than the maximum. An even more pronounced lateral directivity was found for the RJ1H (Fig. 5.11), where the level decreases more than 5 dB to the side.

The above discussed figures already showed how $N1$ influences the sound emission level at departure. First, with increasing polar angle the influence of $N1$ on $\widehat{L}_{\overline{em}}$ rises. Second, $\widehat{L}_{\overline{em}}$ increases to the same extent for a given longitudinal angle (2 dB/5 % $N1$ at θ=90° in the case of Fig. 5.10). However, the change of $\widehat{L}_{\overline{em}}$ with $N1$ is not linear

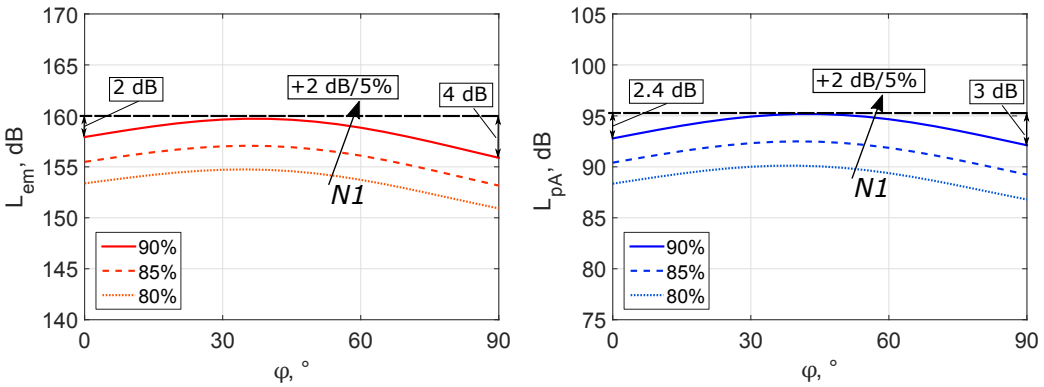

(a) Level at source (d=1 m) (b) Level at receiver (d=304.8 m)

Figure 5.10: Relationship of (a) $\widehat{L}_{\overline{em}}$ and (b) L_{pA} to the azimuth angle for different $N1$ settings at take-off for the A333_TRENT7. Predicted with 3Dred model at θ=90°, Ma=0.26, ρ=1.15 $^{kg}/_{m^3}$.

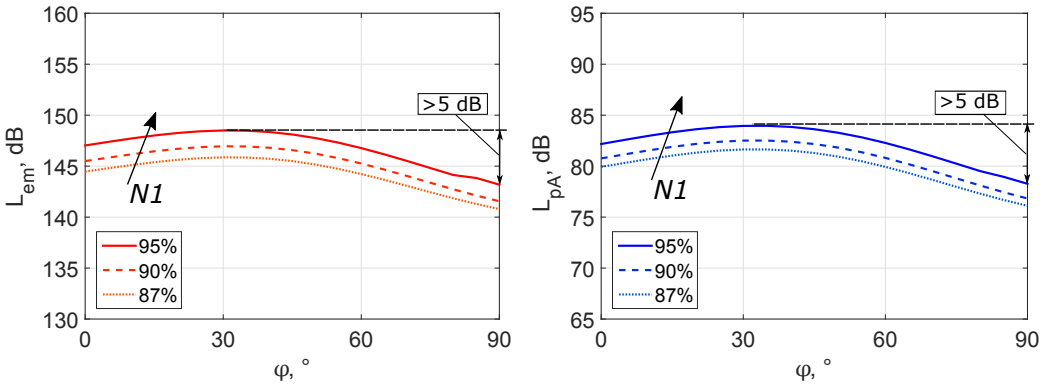

(a) Level at source (d=1 m) (b) Level at receiver (d=304.8 m)

Figure 5.11: Relationship of (a) $\widehat{L}_{\overline{em}}$ and (b) L_{pA} to the azimuth angle for different $N1$ settings at take-off for the RJ1H_LF507. Predicted with 3Dred model at θ=90°, Ma=0.22, ρ=1.15 kg/m³.

in respect to the full range of $N1$, as shown in Fig. 5.12. In addition, the relation of $N1$ on $\widehat{L}_{\overline{em}}$ and L_{pA} depends on the polar angle θ. In Fig. 5.12a the $N1$ dependency is stronger for larger θ while an opposite trend applies at the receiver for $N1 < 80\,\%$ in Fig. 5.12b. This change of the trend is explained by the A-weighting which attenuates the low frequencies.

The influence on the Mach number depends on the aircraft type. Wide-body aircraft as the A333 with strong jet noise show a decrease of the sound emission level with the Mach number (Fig. 5.13). The increasing speed of the surrounding flow lowers the jet noise, in particular to the rear (120°), where the jet is dominant. To high speeds

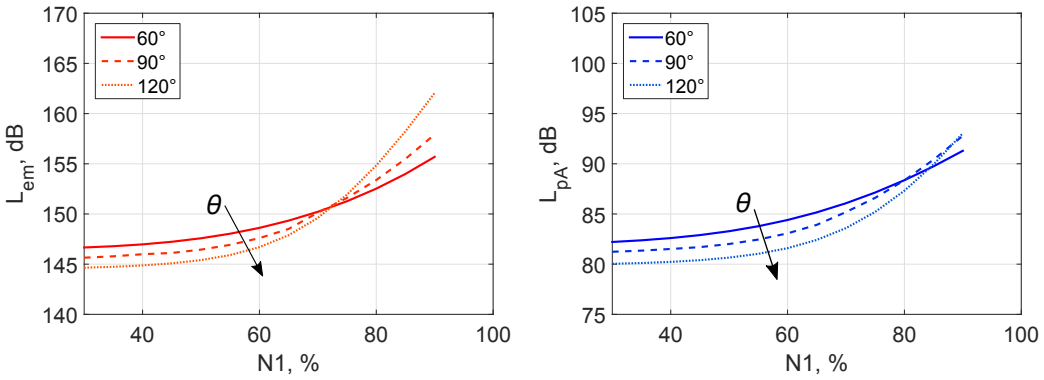

(a) Level at source (d=1 m) (b) Level at receiver (d=304.8 m)

Figure 5.12: Relationship of (a) $\widehat{L}_{\overline{em}}$ and (b) L_{pA} to $N1$ for different polar angles at departure for the A333_TRENT7. Predicted with 3Dred model at φ=0°, Ma=0.26, ρ=1.15 kg/m³.

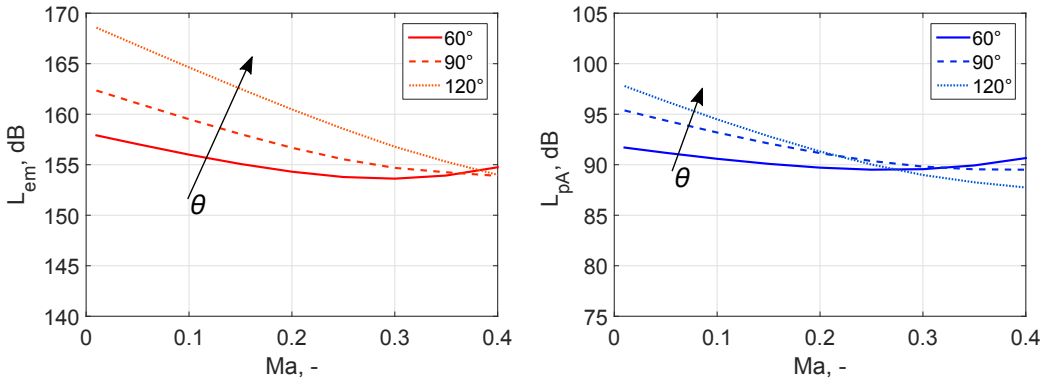

(a) Level at source (d=1 m) (b) Level at receiver (d=304.8 m)

Figure 5.13: Relationship of (a) $\widehat{L}_{\overline{em}}$ and (b) L_{pA} to the Mach number for different polar angles at departure for the A333_TRENT7. Predicted with 3Dred model at φ=0°, $N1$=85 %, ρ=1.1 kg/m³.

above Ma=0.3 the effect levels out with increasing influence of the flight effect and also because the airframe noise begins to contribute to the sound emission level. For the RJ1H, the influence of the Mach number on $\widehat{L}_{\overline{em}}$ is smaller, but shows the same trend with increasing Mach number (Fig. 5.14). At the receiver, mainly the A-weighting changes the influence versus Ma on the L_{pA}. The resulting level difference due to the surrounding flow at θ=90° between break release (Ma=0) and lift off speed (Ma≈0.25) is 5 dB for the A333 and 0 dB for the RJ1H (Ma≈0.22).

Fig. 5.15 shows an approach condition of the A333 with engines in idle. Effects of the Mach number as well as of FH and LG are predicted for the $\widehat{L}_{\overline{em}}$ and L_{pA}. The figure shows how dominant the landing gear is when deployed early, hence at high speeds. The

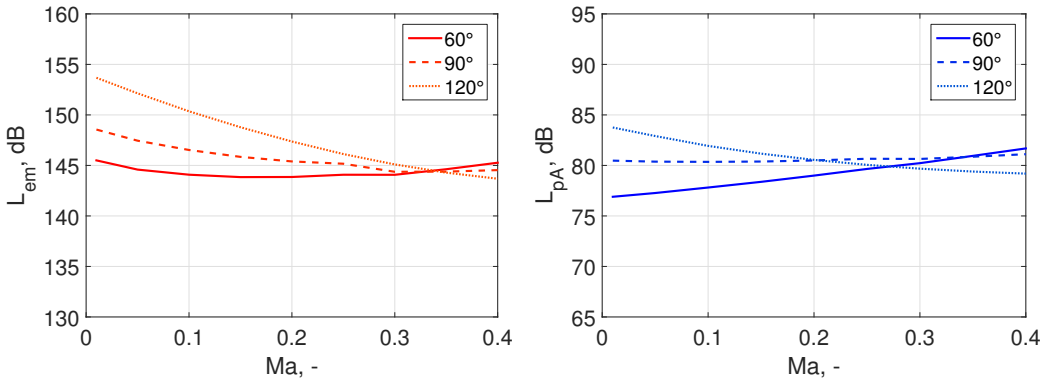

(a) Level at source (d=1 m) (b) Level at receiver (d=304.8 m)

Figure 5.14: Relationship of (a) $\widehat{L}_{\overline{em}}$ and (b) L_{pA} to the Mach number for different polar angles at departure for the RJ1H_LF507. Predicted with 3Dred model at φ=0°, $N1$=90 %, ρ=1.1 kg/m³.

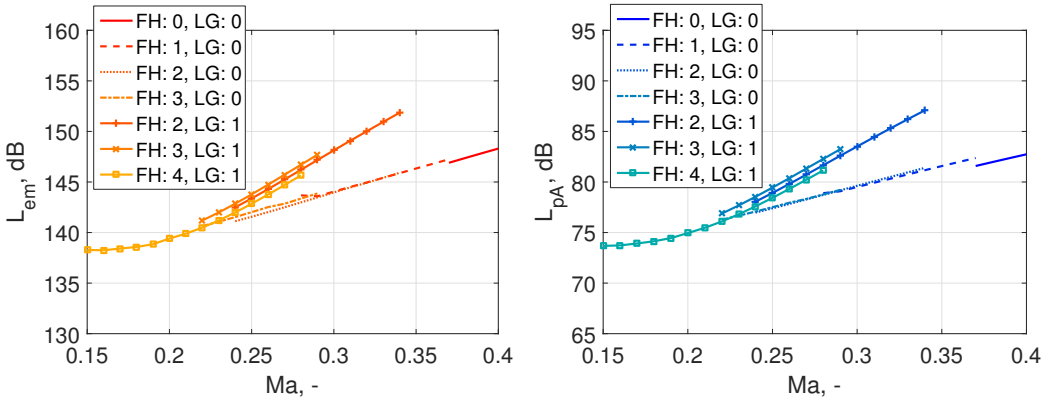

(a) Level at source (d=1 m) (b) Level at receiver (d=304.8 m)

Figure 5.15: Relationship of (a) $\widehat{L}_{\overline{em}}$ and (b) L_{pA} to the Mach number for different aeroplane configurations (FH: flap handle, LG: landing gear) at approach for the A333_TRENT7. Predicted with 3D model at θ=90°, φ=0°, $N1$=30 %, ρ=1.1 kg/m³. Each aeroplane configuration setting is depicted on the measured Mach-range.

speed-dependent noise generation of the landing gear is found at the source and at the receiver with differences of up to 5 dB. However, with decreasing speed of the aircraft the contribution of the landing gear to the $\widehat{L}_{\overline{em}}$ decreases. At landing speed ($Ma \approx 0.22$) no difference can be observed.

In contrast, no important effect could be found for the flap handle handle position. While the landing gear is retracted, the model predicts slight L_{em}-surcharges of 0.5 dB for a flap change from 0 to 1 and 2 to 3. With the landing gear deployed there is no consistent trend. While the effect of flaps is negligible, Fig. 5.16 reveals that speedbrakes affect the levels at the source and receiver. In particular at lower speeds with retracted landing gear, the effect can be as much as 2 dB. The effect on the total sound level is smaller when the landing gear is deployed due to the logarithmic behavior of the sound levels (interaction between LG and SB).

For the RJ1H no flaps positions were available from the FDR data. When opening or closing the gap between flaps and wing strong momentary tones are generated. However, momentary tones can not be represented by the aircraft noise emission model, they are incorporated into the mean effects of the known flight configurations. In Fig. 5.17 the effect of the Mach number and the aeroplane configuration (without flaps) of the RJ1H is shown for an approach condition with engines in idle. Again, the speedbrakes (up to 2 dB) as well as the landing gear (up to 5 dB) have a strong effect on the sound emission level, especially to higher Mach numbers.

At the receiver, the relations to L_{pA} are different than to $\widehat{L}_{\overline{em}}$ in case of the RJ1H_LF507. Mainly the A-weighting affects the frequency spectra which is found to have high contri-

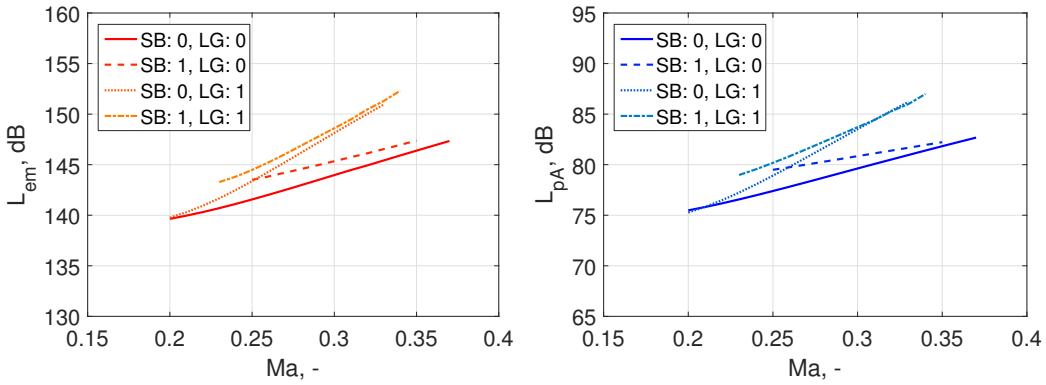

(a) Level at source (d=1 m) (b) Level at receiver (d=304.8 m)

Figure 5.16: Relationship of (a) $\widehat{L_{\overline{em}}}$ and (b) L_{pA} to the Mach number for different aeroplane configurations (SB: speedbrakes, LG: landing gear) at approach for the A333_TRENT7. Predicted with 3D model at θ=90°, φ=0°, $N1$=30 %, ρ=1.1 kg/m³, FH=2, SB=0. Each aeroplane configuration setting is depicted on the measured Mach-range.

butions at low frequency bands. With retracted landing gear a prominent tone at 100 Hz was found and is assumed to be generated by the first flap settings. Also the landing gear contributes a lot of energy to the low frequency bands. While the landing gear show almost no additional effect compared to the clean configuration in Fig. 5.17a towards landing speed of Ma=0.24, the effect at the receiver in Fig. 5.17b is 3 dB(A).

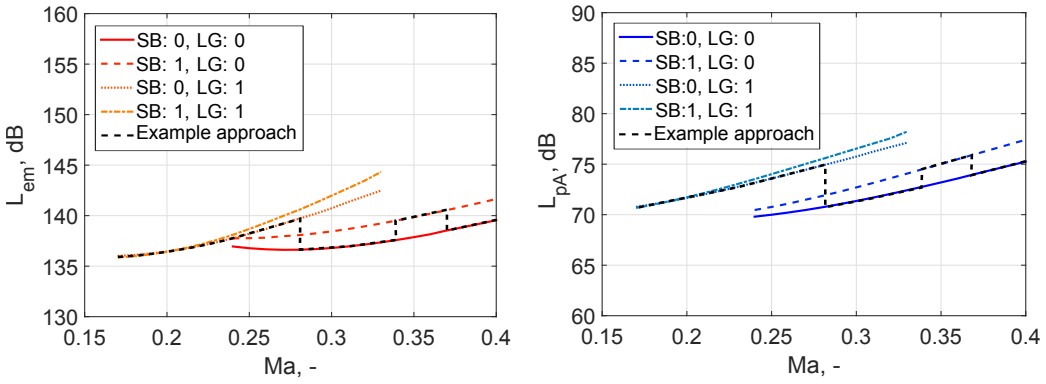

(a) Level at source (d=1 m) (b) Level at receiver (d=304.8 m)

Figure 5.17: Relationship of (a) $\widehat{L_{\overline{em}}}$ and (b) L_{pA} to the Mach number for different aeroplane configurations (SB: speedbrakes, LG: landing gear) at approach for the RJ1H_LF507. The dashed black line shows an example parameter setting during approach on the glide path. Predicted with 3D model at θ=90°, φ=0°, $N1$=30 %, ρ=1.1 kg/m³. FH was not available from FDR data. Each aeroplane configuration is depicted on the measured Ma range.

The dashed line in Fig. 5.17 shows how the sound emission could be predicted by the model for a typical approach. Ma is constantly reduced along the glide path and thus the source and receiver levels tend to decrease. With changes in the aeroplane configuration (deployed speedbrakes or landing gear) the levels increase. Additional diagrams for all types with FDR data can be found as additional material in Appendix A.7.

5.5 Mean flight parameters

The structure of the aircraft noise emission model demands knowledge of the flight parameters for each aircraft type. The most appropriate input data for the model would be FDR data, data from a flight simulator or from flight mechanical calculations. In case that no such data is available, this section provides mean flight parameters from the measurements (Sec. 3.1) for each aircraft type. In addition, the use of reduced take-off thrust is analyzed depending on actual take-off mass (ATOM) and runway length.

As shown in Fig. 5.1, $N1$ and Ma are used differently depending on the subtype of the B737_CFM56-7B. Therefore, the mean values and twice the standard deviation (SD) for $N1$ and Ma shortly after lift-off are depicted in Fig. 5.18 for each measured aircraft

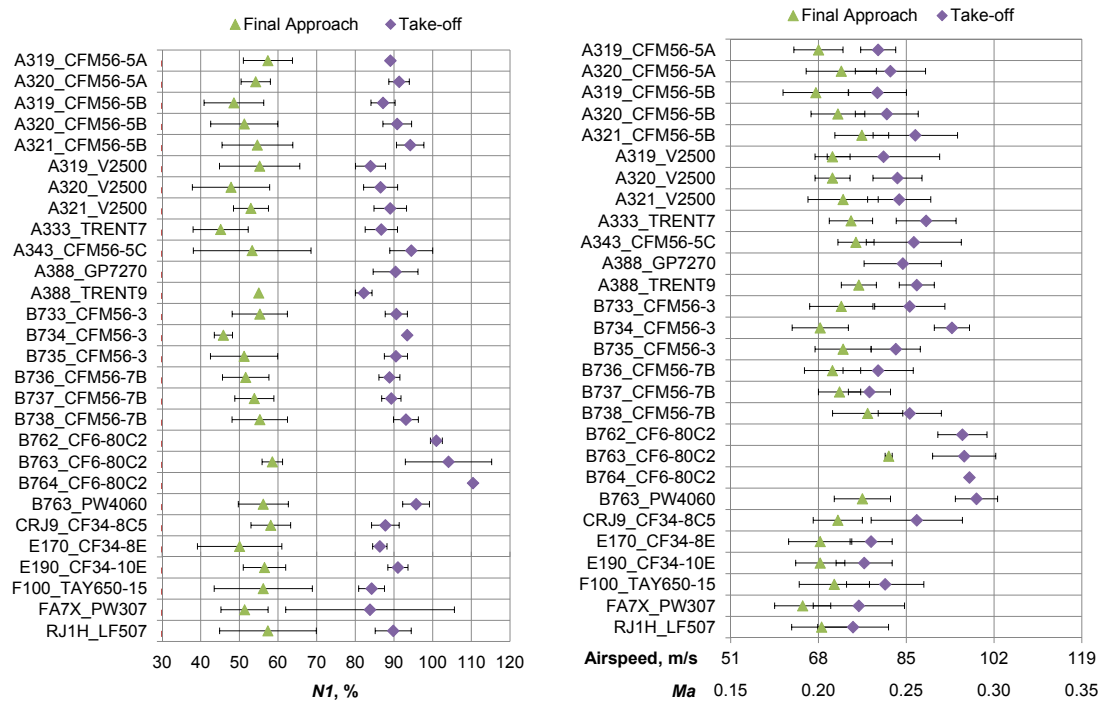

(a) Mean rotational speed $N1$

(b) Mean Ma-number

Figure 5.18: Mean parameter and 2σ for all measured subtypes at take-off and final approach. Airspeed is calculated for c=340 m/s.

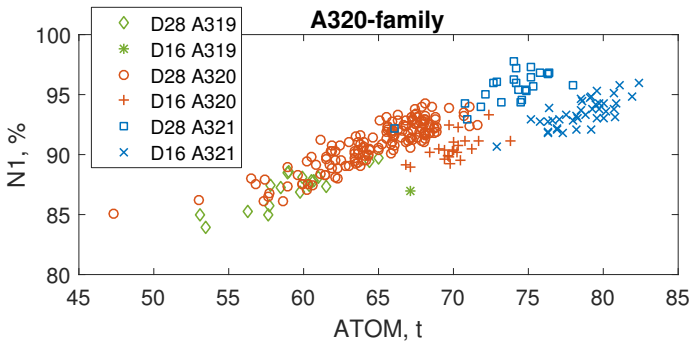

Figure 5.19: $N1$-setting at take-off as a function on ATOM and runway for the A320-family (CFM56-5B).

and engine combination. These parameters are only representative for the procedures of Zurich airport during the period of the measurements. Nevertheless, the parameter settings of each subtype provide good estimates for typical values. Aircraft types like the A388 are an exception, as the A388_TRENT9 only operates to the far destination Singapore and the A388_GP7270 to the nearby destination Dubai. A comparison of both types would thus not be fair.

In Table A.3 in the Appendix the mean parameters and SDs for take-offs and in Table A.4 for final approach are documented for each type and engine combination. The tables also provide the number of events the parameters are based on.

The thrust setting and thus $N1$ depends on many factors. For the final approach the thrust is used to compensate the drag force to keep the landing speed constant. In addition, the engines must ensure the possibility of a go around maneuver. For take-off, the thrust setting mainly depends on runway length and ATOM as airlines are highly motivated to reduce the thrust to extend maintenance intervals and save costs. Current practice at Swiss International Air Lines is a computer-aided calculation on the electronic flight bag (EFB), which provides a take-off performance software to calculate the needed thrust[1]. The main parameters used for this calculation are the ATOM, runway length, weather conditions, and obstacle clearance.

Fig. 5.19 shows a very good example for the variability of thrust setting for the mid-range A320-family. On runway 28, an almost linear dependency between ATOM and $N1$ is found. As all aircraft types in this plot are equipped with the same engine, no differences - except from the ATOM - are found. The residual variation can be dedicated to different weather conditions and to different safety margins.

In contrast, on runway 16 the ATOMs of all three subtypes are larger, but the $N1$-relation is shifted towards smaller $N1$-values. This runway is 1.2 km longer than runway 28, hence heavier aircraft can depart and less thrust is needed for a safe take-off. The

[1]Information from Manfred Bill, Senior Aircraft Performance Engineer at Swiss International Air Lines.

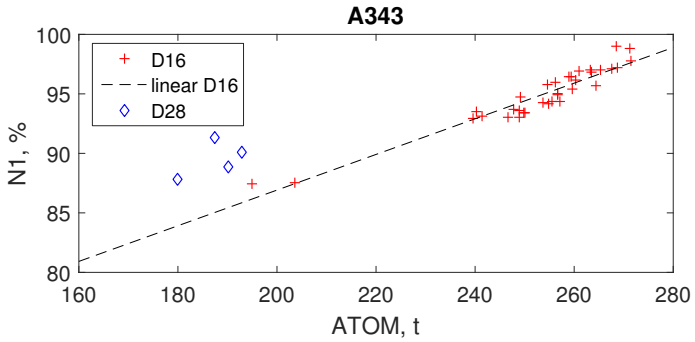

Figure 5.20: $N1$-setting at take-off as a function on ATOM and runway for the A340-300 (CFM56-5C).

behavior of the three aircraft types scatters more for runway 28. An explanation for this might be the use of different break-release points, as observed for narrow-body aircraft on runway 16 during the measurements.

As a second example, the $N1$-setting of the long-range aircraft A343 is depicted for both runways in Fig. 5.20. With two medium-range destinations very light A343s are able to take-off from runway 28 or 16. The $N1$-reduction for the two events on D16 fits very well to a linear behavior on the ATOM. However, the shorter length of runway 28 leads to an approximately 4 % higher $N1$-setting. Therefore, the mean value of 94.5 % (Fig. 5.18) represents runway 16 but not the setting for runway 28 with light take-offs.

To conclude, the mean $N1$ setting for take-off is to be considered carefully as it depends on many parameters. If the ATOM is available it should be taken into account for an improved estimation of the take-off setting. Further aircraft types are shown in Fig. A.1 to A.2 of Sec. A.2. For aircraft types without FDR data the ATOM are mostly not available, therefore only the information from Fig. 5.18 can be presented.

5.6 Level-time histories and spectrograms

For aircraft noise, the most common metrics L_{AE} and $L_{AS,max}$ are derived from level-time histories. It is therefore desirable that the model is able to accurately reproduce the measured level-time histories. In combination with a propagation model and the simulation method described in Sec. 2.4, level-time histories were therefore calculated and compared to measurements. Its basis, the A-weighted level L_{AS} is dominated by the mid-frequencies of the model or of the measurements.

Fig. 5.21 shows a departure passing by microphone 5 and 7 in the far range of the airport (see Fig. 3.4). In addition to the sound pressure level, the main model parameters are depicted. In Fig. 5.21a the aircraft remains at constant speed and performs a cutback of about 10 % $N1$ reduction. The level-time history agrees very well with the

measurement. While microphone 5 is relatively close to the airport, microphone 7 in Fig. 5.21b is further away with a larger propagation distance to the aircraft. The aircraft has increased its speed to $Ma \approx 0.4$ and is in clean configuration. Nevertheless, the measured and calculated level-time histories are still similar, although the simulation predicts a slightly larger maximum sound pressure level at an earlier time.

In Appendix A.8 the level-time histories of both microphones in Fig. 5.21 are also depicted for each frequency band. At low frequencies the ground effect from the sound propagation is very pronounced. In this example, the predicted ground effect fits very well with the measurements at microphone 5 (Fig. A.37a). At microphone 7, the predicted ground effect patterns deviate from the measured ones (Fig. A.37b). For mid frequencies, which are most important for an A-weighted level, the level-time histories agree very well. High frequency bands are also in very good agreement. At microphone 5 the level at 5 kHz is still measurable (Fig. A.42a), but at microphone 7 the measured and simulated levels are mostly below 20 dB (Fig. A.42b). Those low levels are one reason why the model performance showed bad results for this band.

Two simulations for an approach are shown in Fig. 5.22 and compared to measurements at microphone 3. In both examples the engines are in idle. The airspeed (Ma) is reduced after the landing gear is deployed. In Fig. 5.22a the 3D model agrees well with measurement. In contrast, the 3Dred model underestimates the level after the deployment of the landing gear by about 2 dB. However, this level difference assimilates

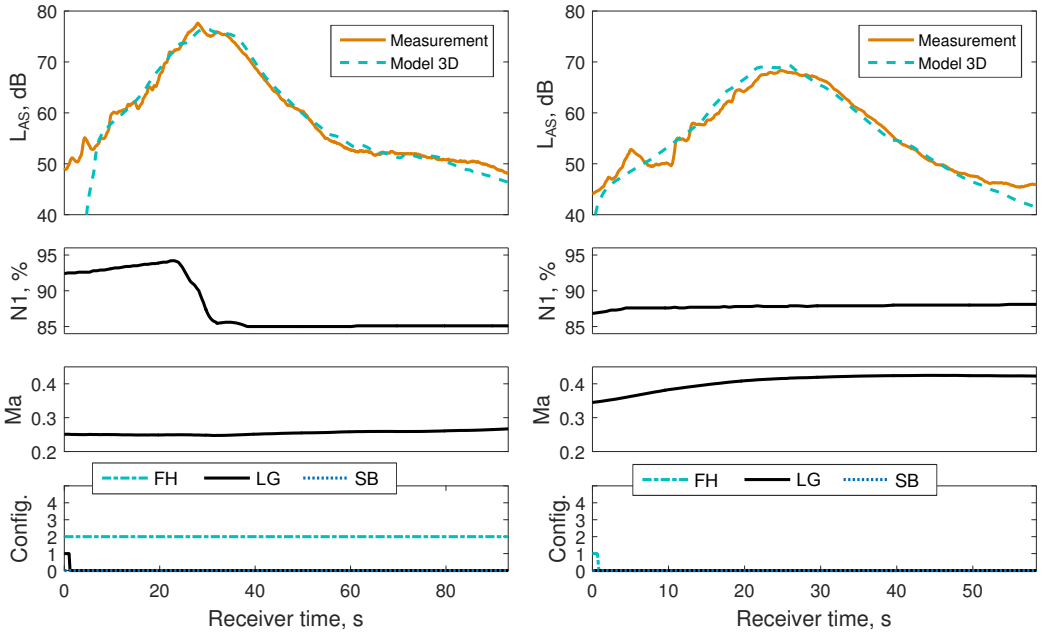

(a) Microphone 5: Cutback

(b) Microphone 7: Final climb

Figure 5.21: Simulation for a departing A320 at two different locations in the far range.

with the reducing Mach-number, because the 3Dred model includes the mean effect of the landing gear of all measurements. For low Ma-numbers the landing gear is statistically always deployed and the models predict the same level. In Fig. 5.22b the same effect is found, in this case the difference on the L_{AS} due to the landing gear is 1.7 dB. For both aircraft types the effects of the flaps and speedbrakes are small.

Instead of level-time histories for each band it is also possible to compare the events with a spectrogram in 1/3-octave bands. In Fig. 5.23 the spectrogram for the above presented approach of the A330_TRENT7 is depicted. A good agreement between simulation Fig. 5.23a and measurement Fig. 5.23b is found with a slight overestimation in the area of the figure marked with (A). The propagation effects (B, C) correlate with the measurement. The effect of the landing gear deployment at (D) is remarkable over the whole frequency range and shows the importance to include aeroplane configuration parameters in the airframe model.

Fig. 5.24 shows the simulated and measured spectrograms of the A320 from the previous Fig. 5.22b. The predicted and measured sound pressure levels over time agree well, although low frequencies are again overestimated at the rear (A). The air absorption of high frequency bands (B) and the ground effect (C) are well visible and correlate with the measurements. The deployment of the landing gear at (D) shows a slight increase in level in simulation and measurement. A specific cavity tone of the A320, which can

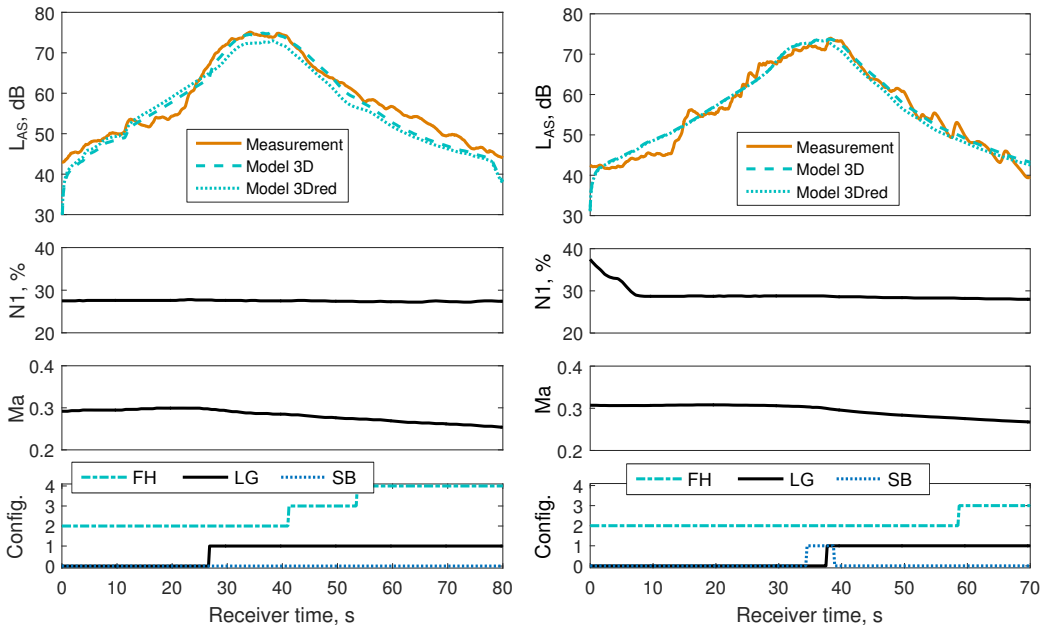

(a) A333_TRENT7 (b) A320_CFM56B

Figure 5.22: Level-time histories for approaches at receiver 3 in the far range. The landing gear is deployed in both examples.

be found at 800 Hz decreasing to 400 Hz due to the Doppler shift is well reproduced, although it smears over two frequency bands for the first 15 s (E) due to the modeling approach in 1/3-octave bands.

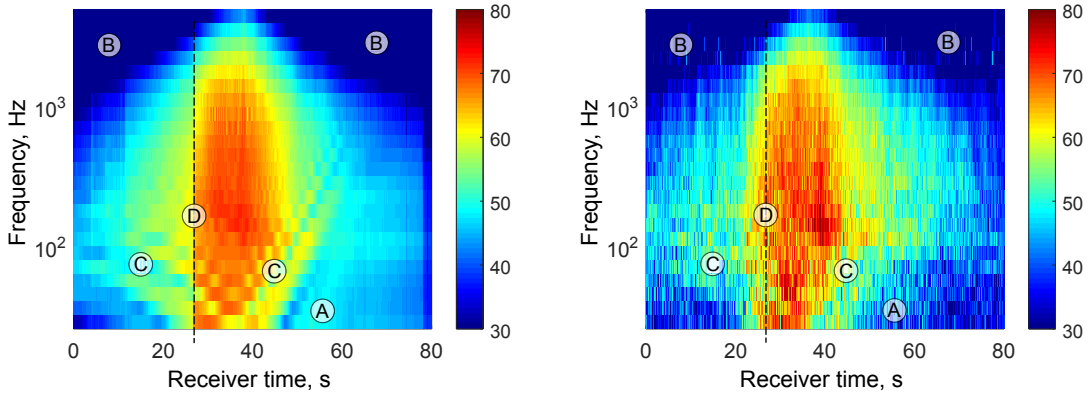

(a) Prediction (b) Measurement

Figure 5.23: Spectrogram in 1/3-octave bands of an A330_TRENT7 on approach. The landing gear is deployed at the dashed line (D).

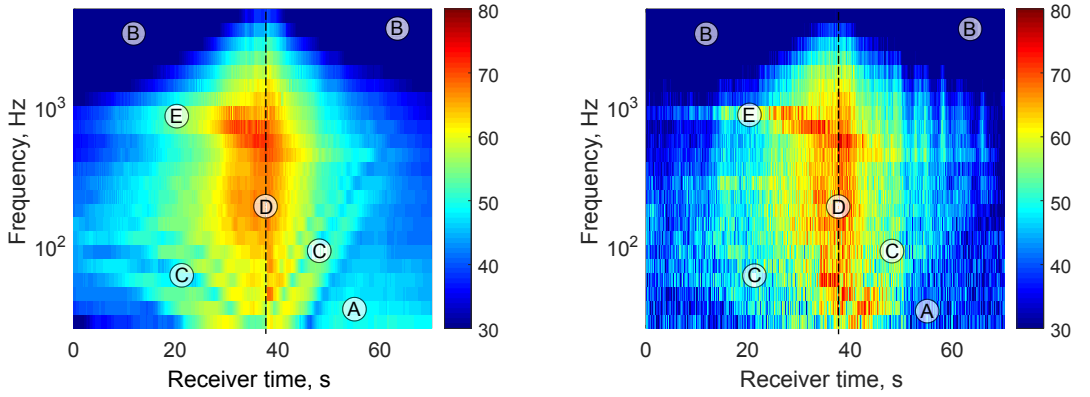

(a) Prediction (b) Measurement

Figure 5.24: Spectrogram in 1/3-octave bands of an A320_CFM56-5B on approach. The landing gear are deployed at the dashed line (D).

6 Verification

The verification is divided into three main parts. In the first part, only aircraft noise emission models based on FDR data are evaluated statistically in comparison to measurements. This also allows to identify the differences of the three model variants 3D, 3Dred and 2Dred (cf. Sec. 4.4). In the second part, aircraft noise emission models without FDR data are evaluated based on the 3Dred model. Finally, the energy correction (Sec. 4.4.3) is verified through a comparison with measurements. The simulation tool, the methodology of the verification and box-and-whisker plots are described in Sec. 2.4.

For each 1/3-octave band individual time intervals with sound exposure above background noise levels were selected within the data processing (Sec. 3.5). In addition, non-aircraft noise contamination was detected. To exclude events with non-aircraft noise contamination also for the verifications, level differences ($\Delta L_{AE,t10}$, $\Delta L_{AS,max}$) between calculation and measurements above 5 dB and $t10$-times above 10 s were checked (Sec. 2.4.3). For aircraft noise emission models with FDR data, in total 53 events were discarded due to significant contributions from other noise sources. For aircraft noise emission models without FDR data, 49 events were discarded. Afterward, 10 524 events of models with FDR data and 5 278 events of models without FDR data were available for the comparison between measurement and calculation.

6.1 Types with FDR data

6.1.1 Comparison of the model variants

Fig. 6.1a depicts a scatter plot of the simulation results between 3Dred and 3D, which shows that the influence of the aeroplane configuration on calculated $\Delta L_{AE,t10}$ is small for departures. The SD of the differences $\Delta L_{AE,t10}$ for departures is 0.1 dB (Table 6.1). For approaches, the SD reaches 0.5 dB, which can be explained with the aeroplane configuration that is important for approach at levels below 88 dB (Fig. 6.1a). For higher sound exposure levels up to 99 dB the variation is smaller than for departure and therefore hidden by data points of departure. These high levels correspond to measurements close to the runway at final approach, where the aeroplane configuration makes no difference anymore as the aircraft are in full configuration.

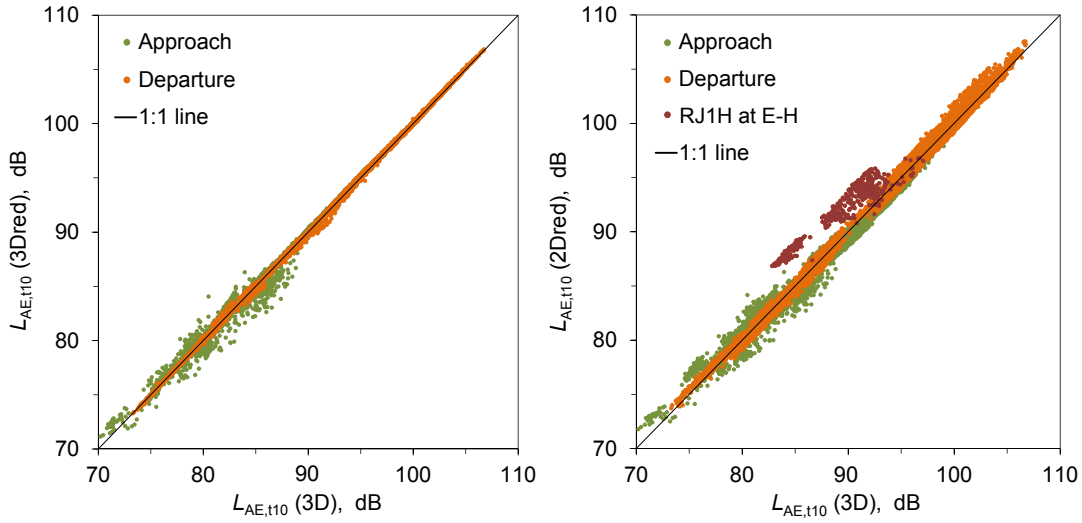

(a) 3Dred versus 3D

(b) 2Dred versus 3D

Figure 6.1: Scatter plot based on $L_{AE,t10}$ for all aircraft types with FDR data (10 524 events) comparing the model variants with each other.

In Fig. 6.1b the 2Dred model is compared to the 3D model. For departures, the simplification of a 2D directivity clearly increases the variation between the models over the whole level range (SD: 0.9 dB). The highest deviations are found for the RJ1H at the measurement point E to H (red dots), which mainly covered lateral angles above 50 ° for departures in the close range. The 2Dred model overestimates the sound exposure levels to the side with up to 4 dB. A similar trend was found in Fig. 5.11. The finding is further checked in the next section, where the models are compared to measurements.

For approach, the variation also increases (SD: 0.8 dB), in particular for high sound exposure levels over 88 dB. This is again the region of the final approach where the engines contribute significantly so that the directivity of the aircraft has a similar effect as for departures. The mean $\Delta L_{AE,t10}$ for all data is zero for 3Dred versus 3D. Comparing

Table 6.1: Level differences $\Delta L_{AE,t10}$ and $\Delta L_{AS,max}$ in dB of all types with FDR data for the comparisons between 3Dred−3D and 2Dred−3D. Mean values (with p-value) and standard deviations based on 10 524 events.

Comparison	Attribute	Mean	SD	Max.	Min.	p-value
3Dred−3D	$\Delta L_{AE,t10}$	0.0	0.3	3.5	−3.6	< 0.01
	$\Delta L_{AS,max}$	0.0	0.4	3.6	−4.1	0.25
2Dred−3D	$\Delta L_{AE,t10}$	0.1	0.9	4.2	−3.3	< 0.01
	$\Delta L_{AS,max}$	0.0	0.9	4.2	−3.8	< 0.01

2Dred versus 3D, the mean $\Delta L_{AE,t10}$ is 0.1 dB. The results of a comparison based on $L_{AS,max}$ are similar and not shown here, but can be found in Fig. A.44 of the Appendix.

6.1.2 Comparison of the models versus measurements

The scatter plot in Fig. 6.2a compares the simulated sound exposure levels of the 3D model with the measured sound exposure levels. In general the sound exposure levels correlate well with the measurements, scattering symmetrically along the 1:1 line. Between approach and departure no obvious differences in the variance or in the correlation with measurements are detected. The accuracy of the model is constant for small as well as high sound exposure levels. The result for the 3Dred model is very similar (cf. Fig. A.46 in the Appendix).

In Fig. 6.2b the model variant 2Dred is compared to the measurements. The variance increases in accordance to the comparison of 2Dred and 3D (Fig. 6.1b). However, there still is a good agreement with the measurements over the whole level range. Again, the RJ1H at measurement points E to H show the a clear overestimation for 2Dred but not for 3D. The 3D model clearly improves the predictive quality in comparison to the measurements.

In Table 6.2 the level differences are summarized with mean values and SD for three model variants. On average, all models adequately reproduce the measurements, although the mean differences are significantly different from 0. This is a consequence of the high

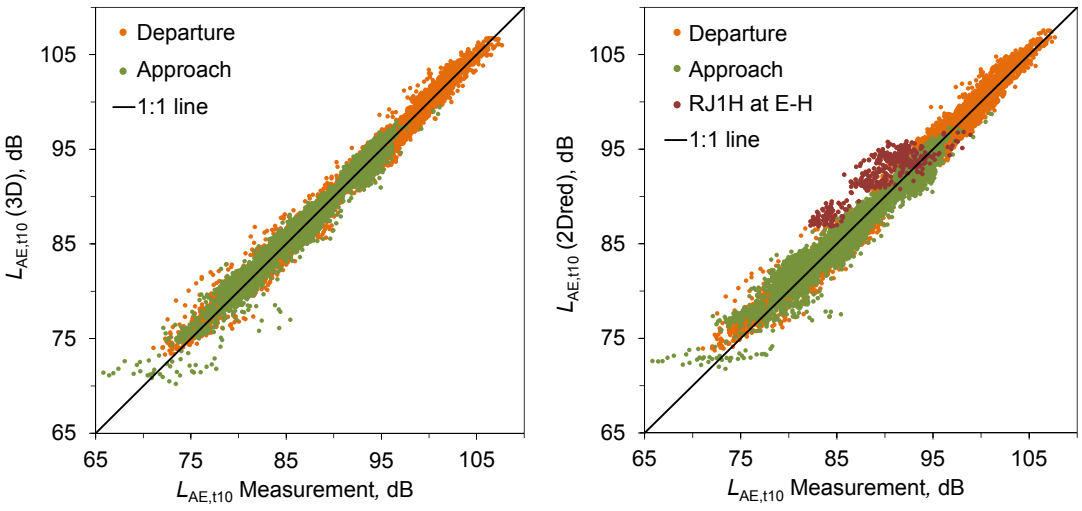

(a) 3D versus Measurements

(b) 2Dred versus Measurements

Figure 6.2: Comparison based on the $L_{AE,t10}$ results of the 3D and 2Dred variants with measurements for all aircraft types with FDR data (10 524 events).

Table 6.2: Level differences $\Delta L_{AE,t10}$ and $\Delta L_{AS,max}$ in dB (calculation minus measurement) of all types with FDR data for the model variants 3D, 3Dred, and 2Dred. Mean values (with p-value) and standard deviations based on 10 524 events.

Model	Attribute	Proc	Mean	SD	Max.	Min.	p-value
3D	$\Delta L_{AE,t10}$	all	0.1	0.9	5.6	−8.5	< 0.01
		departure	0.1	0.9	5.6	−4.2	< 0.01
		approach	0.2	1.0	5.6	−8.5	< 0.01
	$\Delta L_{AS,max}$	all	−0.2	1.3	6.1	−12.1	< 0.01
		departure	−0.3	1.2	6.1	−7.7	< 0.01
		approach	−0.1	1.5	5.4	−12.1	< 0.01
3Dred	$\Delta L_{AE,t10}$	all	0.1	1.0	6.3	−8.0	< 0.01
		departure	0.1	0.9	5.6	−4.2	< 0.01
		approach	0.1	1.1	6.3	−8.0	< 0.01
	$\Delta L_{AS,max}$	all	−0.2	1.3	6.1	−11.2	< 0.01
		departure	−0.3	1.2	5.9	−7.7	< 0.01
		approach	−0.1	1.5	6.1	−11.2	< 0.01
2Dred	$\Delta L_{AE,t10}$	all	0.2	1.3	6.8	−7.9	< 0.01
		departure	0.3	1.2	6.5	−4.0	< 0.01
		approach	0.0	1.3	6.8	−7.9	0.03
	$\Delta L_{AS,max}$	all	−0.2	1.6	6.7	−11.1	< 0.01
		departure	−0.1	1.5	6.7	−7.7	< 0.01
		approach	−0.3	1.6	6.6	−11.1	< 0.01

number (10 524) of compared events. For the SD similar results are found for 3D and 3Dred, but for 2Dred the SD is approximately 0.3 dB larger.

Table 6.2 also shows that $\Delta L_{AS,max}$ is slightly underestimated with -0.2 dB for all model variants. The reason are variations of the sound pressure level due to turbulence in the atmosphere which is not accounted for in the simulation. In addition, momentary tones as found for approaches of the RJ1H and A333 sometimes lead to large differences of the $L_{AS,max}$. Fig. A.45a of the Appendix shows 3Dred against the measured $L_{AS,max}$.

For two aircraft types, the narrow-body A320 and the wide-body A343, a closer look is taken in Fig. 6.3. For each model variant a box plot shows the differences $\Delta L_{AE,t10}$ (calculation minus measurements) for approach and departure, separately for close range (CR) and far range (FR). The results of the A320 are representative for the other narrow-body aircraft, and the A333 shows similar results as the A343.

The A320 in Fig. 6.3a shows good agreement with the measurements in the close range for all models. In the far range, the sound exposure levels are slightly overestimated on average but still show a good agreement and similar variance in comparison to the measurements. In general, 3D and 3Dred are very similar whereas 2Dred shows higher variations in the close range.

For the A343 in Fig. 6.3b, the median values in the close range are clearly overestimated for approach but also for departure with each model. The far range, in contrast, shows

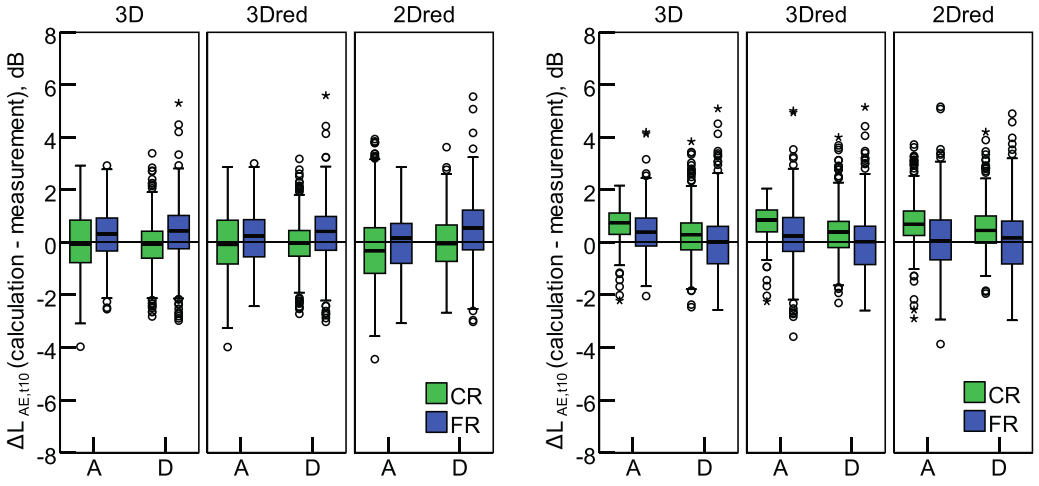

(a) A320_CFM56-5B (b) A343_CFM56-5C

Figure 6.3: Box-and-whisker plot of $\Delta L_{AE,t10}$ for the model variants 3D, 3Dred, and 2Dred, for approach (A) and departure (D) from measurements in the close range (CR) and far range (FR) of the airport.

only slight overestimation. A possible error in the close range could be the assumption of a point source. The assumption is possibly inappropriate for the A343 in the close range, as the closest distances to the microphones are at 100 m to 200 m only. Again, 3D and 3Dred yield to similar results while 2Dred shows larger variance.

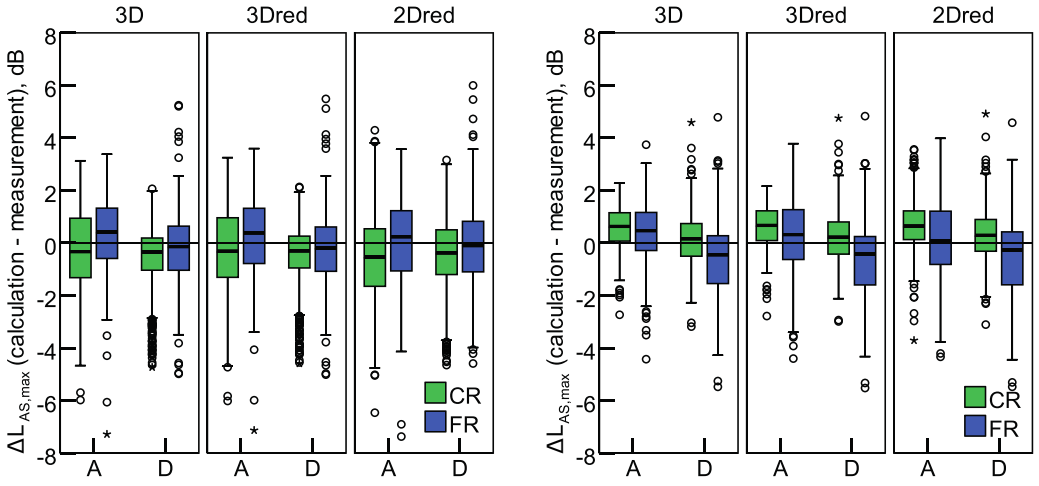

(a) A320_CFM56-5B (b) A343_CFM56-5C

Figure 6.4: Box-and-whisker plot of $\Delta L_{AS,max}$ for the model variants 3D, 3Dred, and 2Dred, for approach (A) and departure (D) from measurements in the close range(CR) and far range (FR) of the airport.

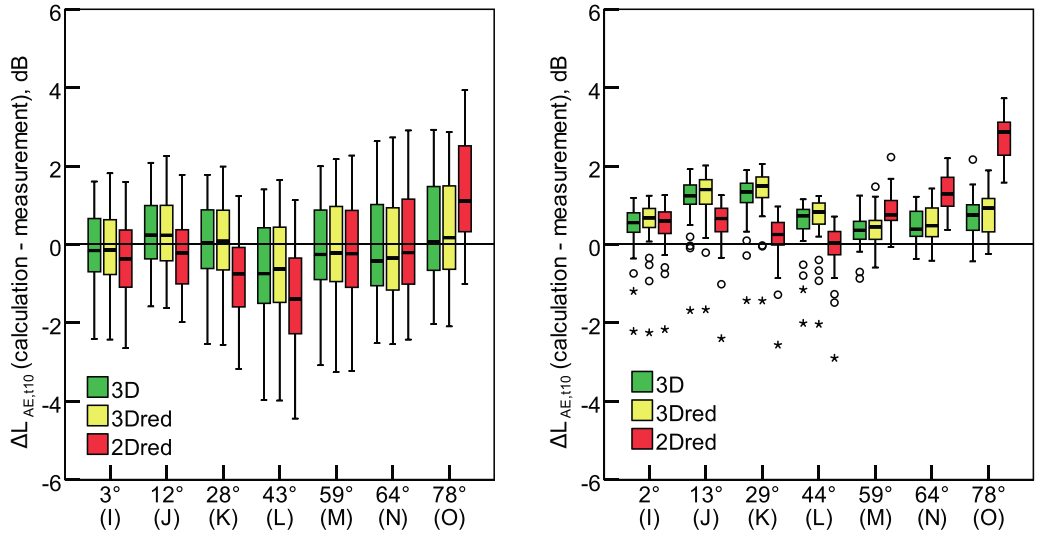

(a) A320_CFM56-5B

(b) A343_CFM56-5C

Figure 6.5: Box-and-whisker plots of $\Delta L_{AE,t10}$ at each measurement point (sorted by mean φ) for approach A14.

In Fig. 6.4 the comparison is repeated for the $\Delta L_{AS,max}$. The maximum sound pressure level of the A320 (Fig. 6.4a) is underestimated in the close range for all model variants. In the far range the median values are close to zero. For the A343 (Fig. 6.4b) all models overestimate the $L_{AS,max}$ in the close range. Departures in the far range are slightly underestimated, and vice versa for approaches. The mean differences $\Delta L_{AE,t10}$ and $\Delta L_{AS,max}$ for approach and departure of all models are listed in Table A.22 (3D, 3Dred) and Table A.23 (2Dred) in the Appendix.

The three different models can be compared in more detail by looking at the verification results of single microphone positions. Fig. 6.5 shows the final approach in the close range (A14) of the A320 and A343. For 3D and 3Dred of the A320 the medians scatter randomly around zero, while for 2Dred the measurement point K, L, and O differ considerably from zero (1 to 1.5 dB). For K and L ($\varphi \approx$ 25-45°) the levels are underestimated with a 2D directivity. For the measurement point O ($\varphi \approx$ 75-80°) at the sideline, the sound exposure levels are overestimated. For the A343 all measurement points are over estimated. 2Dred differs considerably from 3D/3Dred. Especially at O the difference of the median with 3 dB is very high.

Differences at the single measurement points for departures are shown in Fig. 6.6 for the A320 on D28 at for the A343 on D16. 3D and 3Dred again show mostly good results with variations around zero. Only at H a clear underestimation of $L_{AE,t10}$ can be found. With a taxi way in front of H a possible reason for this might be the underestimation of the ground effect. For 2Dred, $L_{AE,t10}$ under the aircraft ($\varphi < 15°$) are clearly overestimated

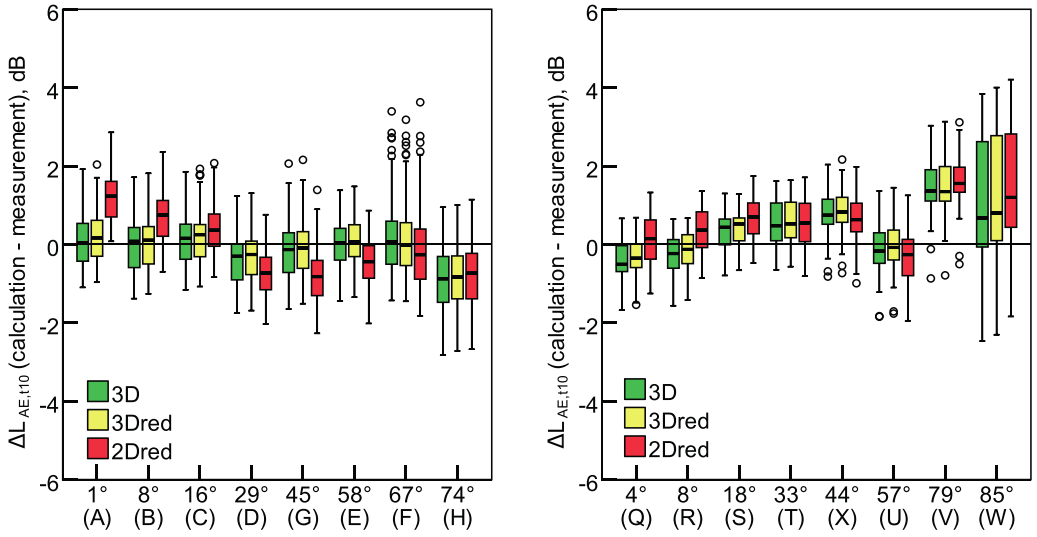

(a) A320_CFM56-5B (b) A343_CFM56-5C

Figure 6.6: Box-and-whisker plots of $\Delta L_{AE,t10}$ at each measurement point (sorted by mean φ) for departures D28 (a) and D16 (b).

(A, B). For lateral angles $\varphi > 25°$, the $L_{AE,t10}$ are underestimated by up to -1 dB. The A343 does not show big differences between the model variants. Large deviations occur for V and W which were close to the runway.

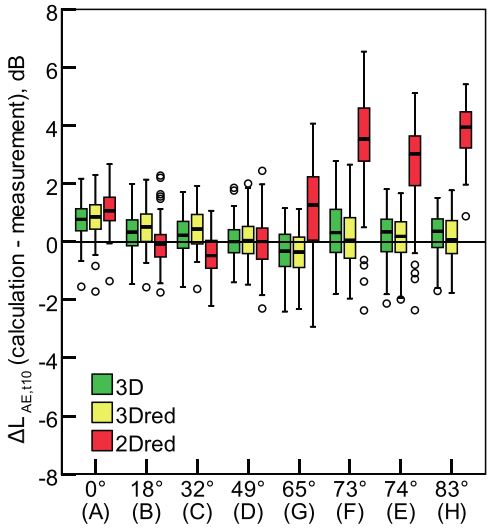

Figure 6.7: High deviations with 2Dred for departure D28 of the RJ1H_LF507 at measurement points E-H (sorted by mean φ), which corresponds to $\varphi \geq 65°$.

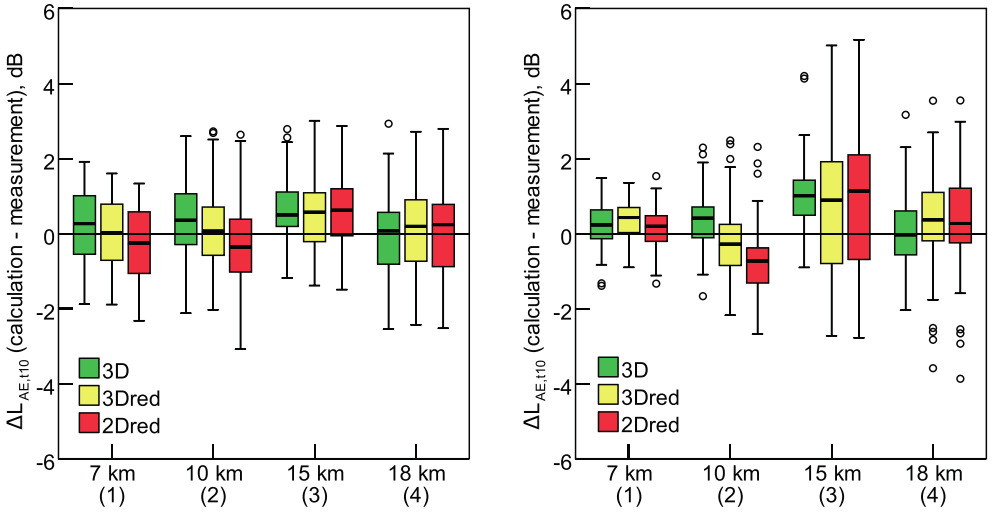

(a) A320_CFM56-5B

(b) A343_CFM56-5C

Figure 6.8: Box-and-whisker plots of $\Delta L_{AE,t10}$ at each measurement point (sorted by distance to runway) for approach A34.

In the scatter plot (Fig. 6.1b) the 2Dred model showed substantially higher sound exposure levels in comparison to 3D of the RJ1H. Fig. 6.7 therefore shows the departures in the close range also for the RJ1H. For A-D no significant differences can be found between the models. But 2Dred overestimates the measurements at E-H ($\varphi > 65°$) by 1.3 to 3.9 dB on average (see also Fig. 5.11).

Measurement points in the far range are compared in Fig. 6.8 for approaches. In Fig. 6.8a no distinct differences can be found between the three models. For the A343 Fig. 6.8b in particular measurement point 3 shows much higher variations for 3Dred and 2Dred. The landing gear is usually deployed in this area and thus the reduced models show a higher standard deviation. However, the median differences from zero are not different from 3D, and all models overestimate this measurement point for both aircraft types. At measurement point 2 and 4 the median of 3D is closer to zero than for 3Dred and 2Dred, which is due to the fact that the aeroplane configuration is considered.

6.2 Types without FDR data

In Fig. 6.1a overall 5 278 events of the 13 aircraft noise emission models without FDR data were simulated and compared to measurements. The sound exposure levels agree similarly well with the measurements for the whole level range as for the types with FDR data. The SD for approach is slightly larger than for departures, which is in line

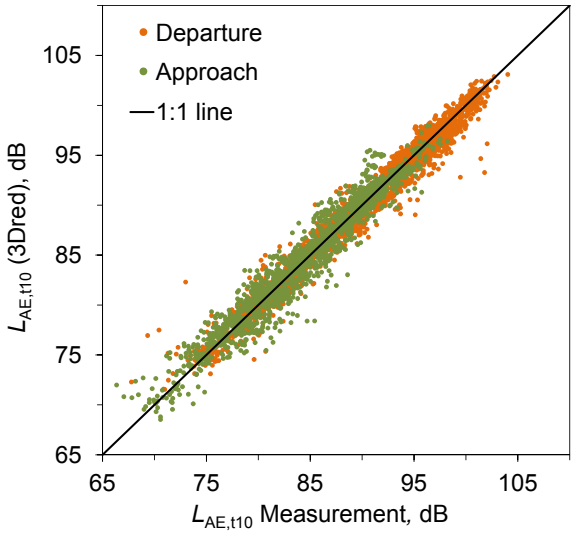

Figure 6.9: Comparison based on the $L_{AE,t10}$ of the 3Dred variant with measurements (5 278 events) for all aircraft types without FDR data.

with the findings in Sec. 6.1. Without any parameter of the aeroplane configuration in 3Dred, the prediction accuracy of approaches decreases.

In Fig. A.45b of the Appendix all flights are evaluated against the measured $L_{AS,max}$. The 3Dred model tends to underestimate the measurements, in particular for departures below 85 dB(A). Such trend supports the assumption that the atmospheric turbulence rises the maximum sound pressure level with increasing distance between source and receiver. For example, the distances between source and receiver at approach are relatively small and the mean deviation of −0.1 dB is also much smaller than −0.7 dB for departures with larger distances (Table 6.3).

The statistical analysis of all level differences in Table 6.3 yields that the mean of $\Delta L_{AE,t10}$ is not significantly different from zero. In contrast, the maximum sound pressure level of all events is significantly underestimated by −0.5 dB. Also the SD of

Table 6.3: Level differences $\Delta L_{AE,t10}$ and $\Delta L_{AS,max}$ in dB (calculation minus measurement) of all types without FDR data for 3Dred. Mean values (with p-values) and standard deviations based on 5 278 events.

Model	Attribute	Proc	Mean	SD	Max.	Min.	p-value
3Dred	$\Delta L_{AE,t10}$	all	0.0	1.2	9.3	−8.5	0.86
		departure	−0.1	1.1	9.3	−8.5	< 0.01
		approach	0.2	1.5	5.6	−7.0	< 0.01
	$\Delta L_{AS,max}$	all	−0.5	1.6	6.7	−11.4	< 0.01
		departure	−0.7	1.4	6.7	−11.4	< 0.01
		approach	−0.1	1.9	6.0	−8.7	0.21

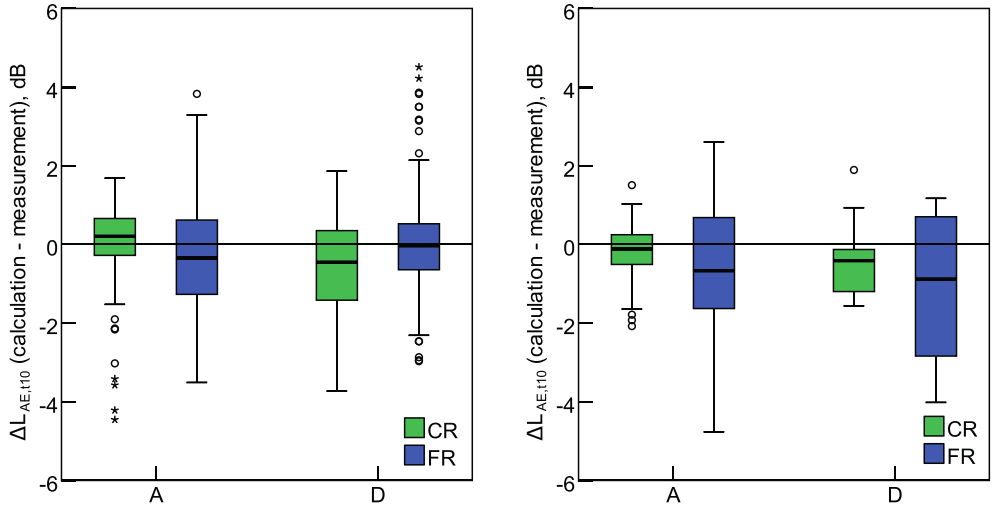

(a) B737_CFM56-7B (b) B763_PW4060

Figure 6.10: Box-and-whisker plot of $\Delta L_{AE,t10}$ with 3Dred, for approach (A) and departure (D) at measurements in the close range (CR) and far range (FR) of the airport.

$\Delta L_{AS,max}$ is larger as for $\Delta L_{AE,t10}$. Compared to the 3Dred model of the FDR types (Table 6.2), the variation of $\Delta L_{AE,t10}$ and $\Delta L_{AS,max}$ is approximately 0.3 dB larger. Three factors explain the larger SD: the uncertainty of $N1$, the smaller number of flights the models are based on and the grouping of similar aircraft types.

A narrow-body and a wide-body aircraft are example compared to each other in Fig. 6.10. The narrow-body B737 in Fig. 6.10a shows values for the medians close to zero. The variations are small. The wide-body B763 in Fig. 6.10b underestimates the measurements in particular in the far range, where the variation is substantially larger for the B737. In contrast, the differences and variations of $\Delta L_{AE,t10}$ in the close range are small.

6.3 Energy correction

Fig. 6.11a presents the difference $\Delta L_{AE,t10}$ for the A320 for all flights. It compares the energy corrected model with the corresponding model without correction. The simulated sound exposure levels for the A320 with the uncorrected model underestimate the measured sound exposure levels for approach and departure by −0.7 dB. In contrast, the model which is corrected for the energy mean deviates less than 0.1 dB for approach and departure (no significant difference from zero).

For the A343 in Fig. 6.11b the uncorrected model underestimates by −0.1 dB for approach and −0.4 dB for departure. The corrected model overestimates the mean values

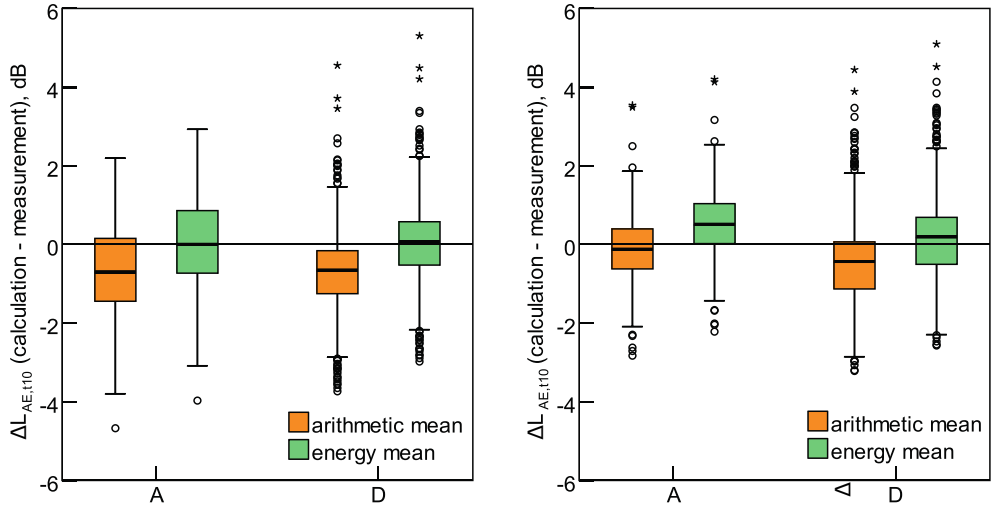

(a) A320_CFM56-5B

(b) A343_CFM56-5C

Figure 6.11: Box-and-whisker plot of $\Delta L_{AE,t10}$ with 3D, for approach (A) and departure (D) for the uncorrected model (arithmetic mean, orange) and the corrected model (energy mean, green).

by 0.5 dB for approach and 0.2 dB for departure. In this case the correction leads to a significant overestimation. In Sec. 6.1.2 it was shown that the events in the far range distribute well around zero, but the close range is overestimated by the corrected model. Therefore, the assumption of the point source could be a reason for the systematic overestimation.

In addition to the two aircraft types shown, the simulations of the 10 524 events for all aircraft noise emission models with FDR data were repeated by using the uncorrected models (3D and 3Dred). The results revealed a mean difference between calculations and measurements of -0.5 dB for $\Delta L_{AE,t10}$ and -0.8 dB for $\Delta L_{AS,max}$. Hence, simulations with the uncorrected models lead to a systematic underestimation of $\Delta L_{AE,t10}$ and $\Delta L_{AS,max}$. This result supports that the energy correction from Sec. 4.4.3 is necessary.

7 Application

7.1 Implementation into a GIS-environment

Within the project sonAIR the aircraft noise emission model was already implemented into a professional aircraft noise simulation program. The core of the program consists of three main modules (Fig. 7.1): aircraft noise emission model, propagation model, and simulation tool. They are all embedded into ESRI ArcGIS, which provides a powerful user interface to view and handle input data, view and process results, and generate noise maps. The implementation of sonAIR was realized by n-sphere AG[1].

The aircraft noise emission models are implemented as look-up tables to improve the calculation time. They provide a flexible interface for the implementation of all model variants and also other spectral aircraft noise emission models: The parameters of the look-up tables and their resolution can be defined via data tables. During the simulation the corresponding sound emission levels are read and interpolated for the specified parameters θ, Ma, and $N1$ using a multivariate interpolation. For other parameters

[1] `http://www.n-sphere.ch/`

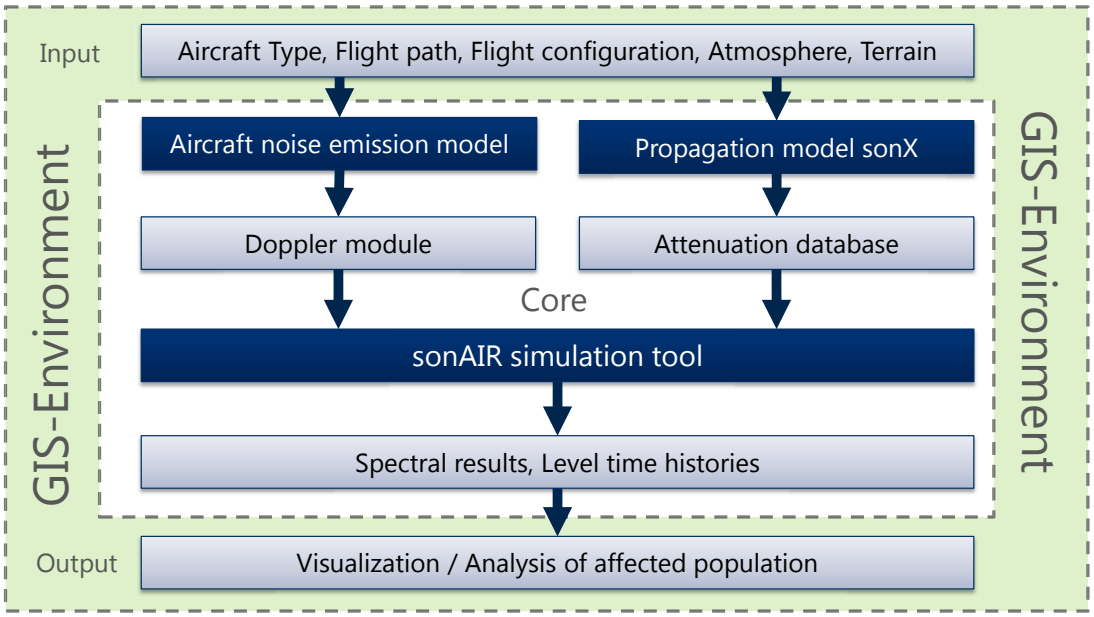

Figure 7.1: Flow chart of the sonAIR implementation in a GIS-environment.

(φ, ρ and aeroplane configuration) the sound emission level of the nearest value is read. Afterward, the Doppler module shifts the frequency and adds the flight effect to the sound emission spectra (Sec. 2.2.4).

The sound propagation calculation follows a hybrid concept: For sources close to the ground, ground effect, barrier effects, and reflections occur and are demanding to a sound propagation calculation. If the source is at high altitudes, the direct sound is dominant and reflections are of minor importance. Barrier effects can be neglected and the ground effect can be simplified. The threshold between simple and sophisticated calculation is defined over the angle-of-sight of a receiver relative to the horizon, including buildings. With an angle-of-sight above 15° only a simplified direct calculation (geometrical divergence and atmospheric absorption) is sufficient. Below the angle-of-sight criterion sonX calculations are needed.

While simplified direct calculations (angle-of-sight $> 15°$) can be calculated fast, each source and receiver combination is calculated during the simulation. In contrast, time-consuming sonX calculations (angle-of-sight $< 15°$) are pre-calculated and stored in an attenuation database (Fig. 7.1). Such an attenuation database has to be generated for every new airport.

To minimize the calculation time and reduce storage capacity, several optimization strategies have been applied. Instead of calculating each source and receiver combination, which can easily sum up to 10^{13} attenuations, a 3D cell grid is calculated for each receiver. The horizontal and vertical resolution of the cell grid increases with distance to the receiver to reduce the number of grid points. In addition, only cells which contain at least one source point, are calculated. If the airport is calculated again (e.g. a year later), the attenuation database only needs updates for new cells.

During the simulation only eight grid points from the current cell grid need to be looked up from the database for each source point close to the ground. These attenuations are then interpolated to account for the true source position inside the cell. With a time-step method the sound emission levels and attenuations are added up to calculate level-time histories for each receiver and flight path (Sec. 2.4). This yields to noise maps of L_{AE} or $L_{AS,max}$ on a receiver grid. These results can be further processed in the GIS-environment, e.g. to generate contours of whole scenarios, calculate the areas inside certain contours, and evaluate the affected population.

Fig. 7.2 depicts an $L_{AS,max}$ noise map of a departure with the A333_TRENT7. Buildings and reflections are not accounted for. From the sound emission the cutback ($N1$-reduction) is clearly visible in the contours. After the cutback, the contours are smooth, as the direct sound dominates these receiver points. Before the cutback and in particular on the runway, where the source is low above ground, propagation effects as foliage attenuation and shielding due to terrain are prominent. For instance, a forest

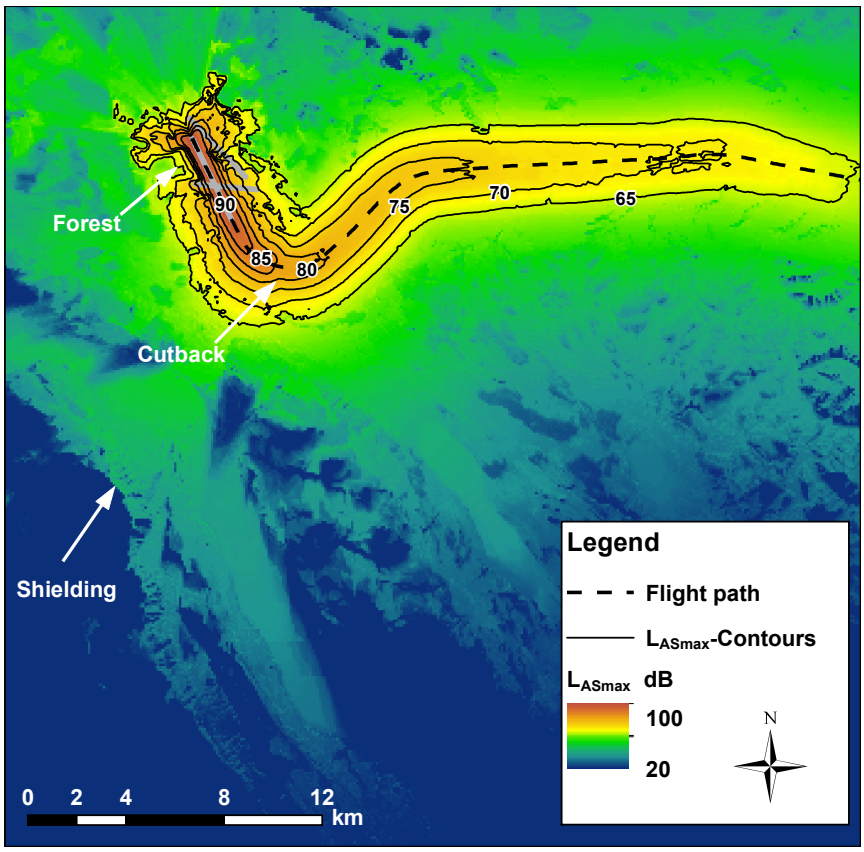

Figure 7.2: $L_{AS,max}$ noise map of the A333_TRENT7 at departure form runway 16, calculated with the aircraft noise emission model implemented as look-up table in the aircraft noise simulation program sonAIR.

close to the runway leads to a strong contraction of the contours to the west of the runway. The shielding effect at a mountain ridge can be found in the noise map as a strong level drop.

An example of an approach of an A333_TRENT7 is depicted in Fig. 7.3. The $L_{AS,max}$ noise map shows the same propagation effects as before, but due to the low source on the 3.2° glide path, the contours are not as smooth to the side of the flight path. The contours also change with the aeroplane configuration, in particular the landing gear deployment and the increase of $N1$ to 55 % widens the contours. In addition, the decreasing aircraft Mach number continuously changes the sound source emission, as seen in Sec. 5.4.

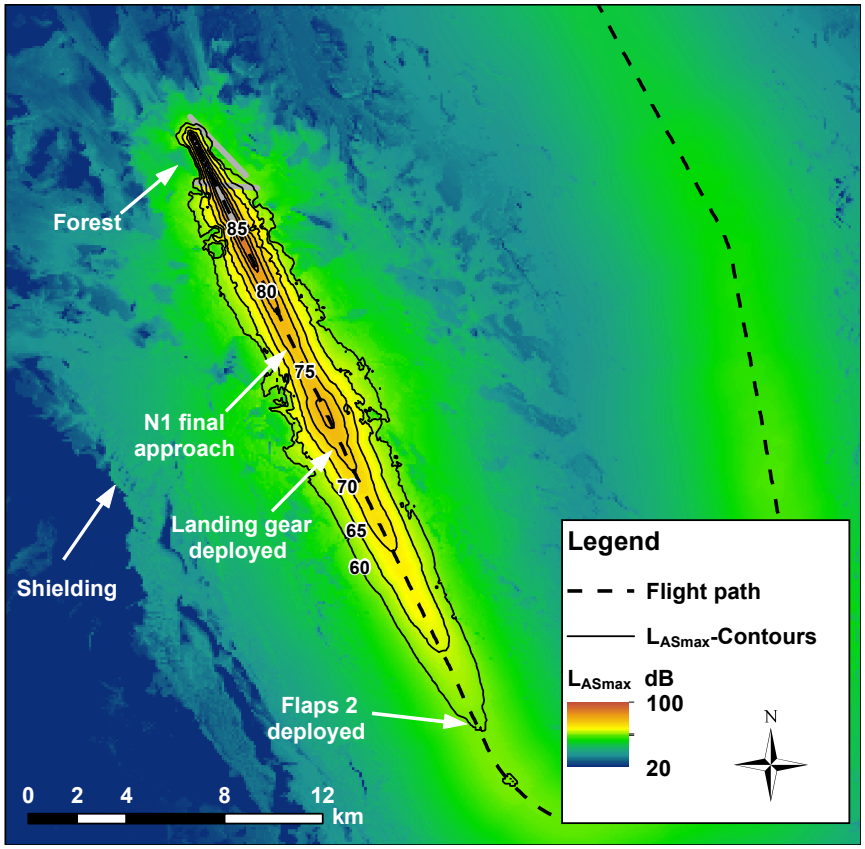

Figure 7.3: $L_{AS,max}$ noise map of the A333_TRENT7 at approach on runway 34, calculated with the aircraft noise emission model implemented as look-up table in the aircraft noise simulation program sonAIR.

7.2 Interface to a full flight simulator

With the scope to optimize and assess flight procedures, it is of interest how accurate a new procedure can be followed by pilots and their aircraft. Such questions can be investigated by a feasibility study in the full flight simulator under different weather and aircraft conditions. Those studies are especially relevant for the air traffic management and operators to examine safety issues or to check the implementation.

A data format was specified in collaboration with Swiss Aviation Training to directly feed the presented aircraft noise emission models with flight data from simulators. In this way, the aircraft noise of new procedures can be assessed in parallel to a feasibility study and prior to an implementation.

An example for the usage of flight simulator data is presented in Fig. 7.4 for an arbitrary airport. Two departures were flown by a licensed pilot in the Swiss A320 full flight simulator. The nominal route is defined as an early left turn after achieving 460 m (1500 ft). At this altitude also the cutback should be performed. Flight A departed with an ATOM of 63 t and flight B departed with an ATOM of 77 t, which corresponds to the maximum take-off mass.

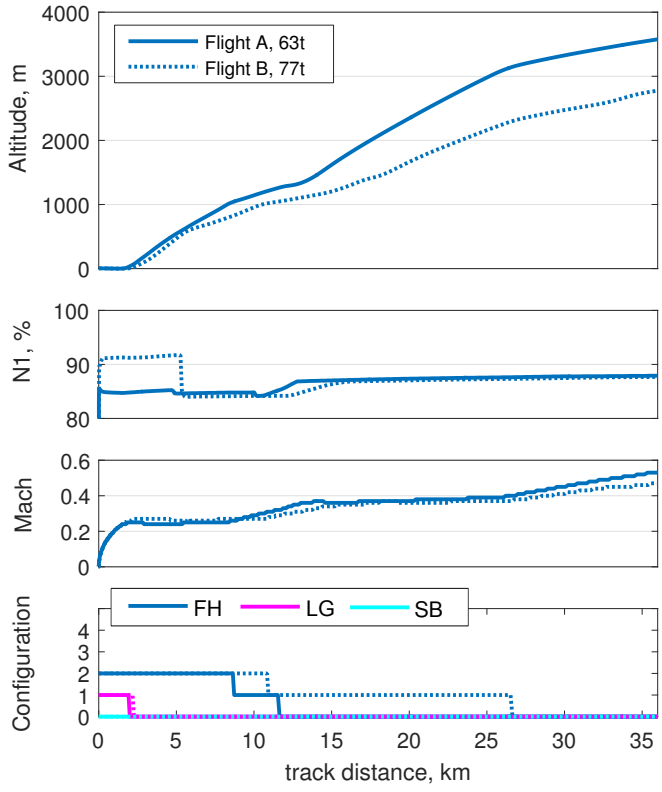

Figure 7.4: Comparison of the simulator data of the A320_CFM56-5B for flight A (63 t) and B (77 t). Cutback and left turn at 460 m (1500 ft).

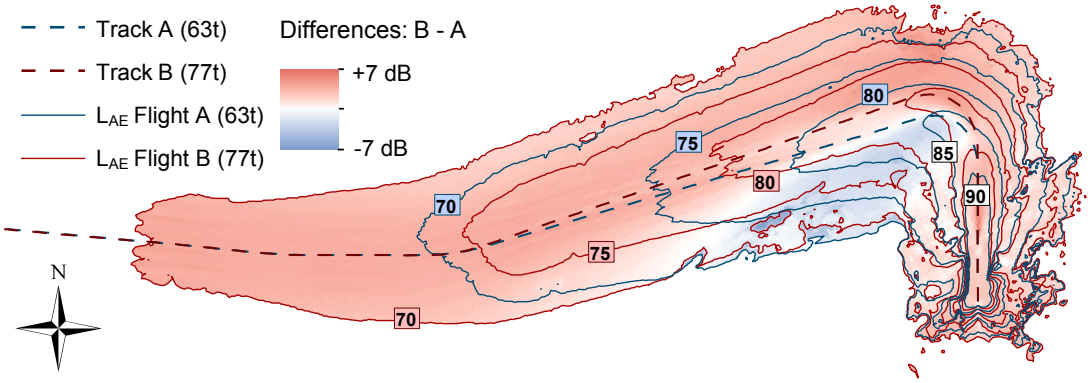

Figure 7.5: Comparison of the L_{AE} of two different departures of the A320_CFM56-5B. Flight A (blue lines) compared to flight B (red lines) with left turn at 460 m (1500 ft). Differences as flight B − A.

Flight B shows a similar height profile to flight A until cutback, approximately at 460 m (Fig. 7.4). The high thrust setting of B at $N1 \approx 91\,\%$ compensates the high mass. At cutback, $N1$ drops to 84 %. For flight A, the initial thrust setting is already reduced to 85 % and the cutback is negligible. Consequently, flight A performs a better climb rate after cutback than B. In addition, the flap retraction is retarded for flight B.

Fig. 7.5 shows the horizontal tracks of both flights and the resulting sound exposure levels. As discussed before, the initial climb segment differs only in the larger $N1$, which yields to a 2 to 3 dB larger sound exposure for flight B than for flight A. Inward of the left turn the exposure is reduced because of the slightly later turn of flight B. At the end of the track, the sound exposure of B is around 4 dB higher compared to A due to the lower altitude, as the flight configurations are similar.

7.3 Example application to approach procedures

In the following example, the advanced regression model for the A320_CFM56-5B is applied within a simulation program that accounts for the sound propagation using sonX (Sec. 3.5), the flight effect, and the Doppler shift. A noise map was calculated on a receiver grid with 150 m spacing in an area of 60 km × 32 km. To highlight the observable effects of the noise emission model, an artificial airport was modeled with a flat grassland terrain and a homogenous atmosphere ($T = 14\,°\mathrm{C}$, $p = 1000\,\mathrm{hPa}$, $RH = 60\,\%$).

In the example in Fig. 7.6 two approach procedures are compared: a Low Drag Low Power (LDLP) approach versus a Continuous Descent Approach (CDA). The noise map shows noise contours as well as the differences $\Delta L_{AS,max}$ between the CDA and the LDLP approach, where positive differences mean that the CDA has larger maximum levels than the LDLP approach. This is the case between 56 to 40 km and on the glide path between 21 and 10 km. To highlight the differences due to the sound emission rather than to different horizontal tracks, both approach procedures were simulated along the same flight path. The differences $\Delta L_{AS,max}$ under the flight path and the flight parameters such as altitude, aircraft Mach number, $N1$, and aeroplane configuration are depicted in Fig. 7.7. Additionally, in Fig. 7.6 and Fig. 7.7, the same distance markers are depicted to connect the resulting $\Delta L_{AS,max}$ noise map with the flight parameters. The markers refer to the flight path distance, where 0 m is at the end of the runway.

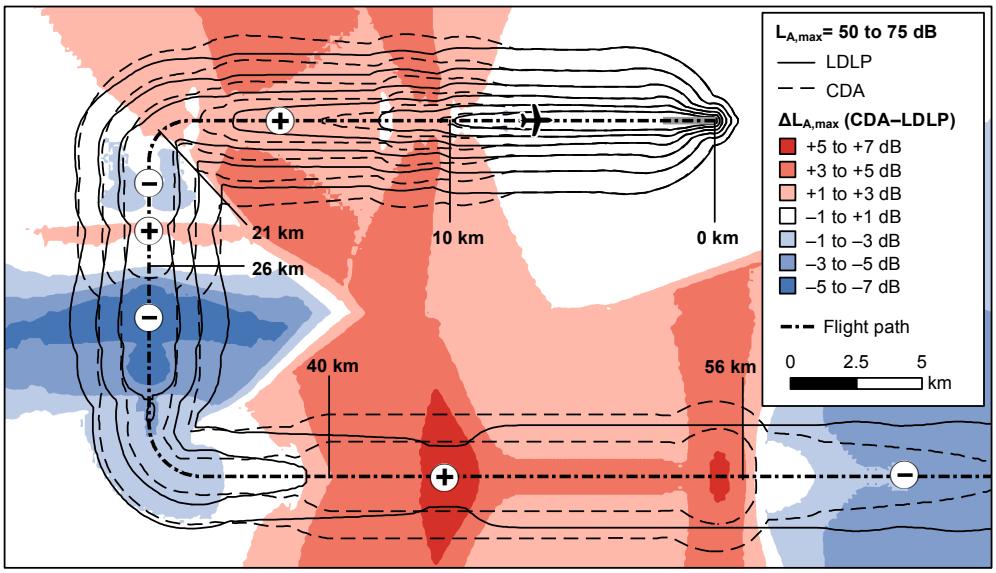

Figure 7.6: Example comparison of a CDA and LDLP approach procedure for the A320 (CFM56-5B). The noise map depicts the differences $\Delta L_{A,max}$ between CDA and LDLP approach. (Color online)

The calculation shows that the flight parameters strongly affect the results and that they need to be considered to compare different noise abatement procedures. For instance, far away from the runway (>56 km), the CDA is quieter than the LDLP because the engines are running in idle. Between 56 to 40 km CDA is louder due to the lower altitude and the higher sound emission by the airframe (Ma) and engines ($N1$). In the subsequent segment (40 to 26 km), the CDA is again quieter than LDLP because of the higher altitude but also the high-lift devices are deployed later. Between 26 to 21 km the differences tend around zero, because the airframe noise (larger Ma) of the CDA is compensated by the engine noise (larger $N1$) of the LDLP approach. While the altitude after 21 km is the same for both approaches on the glide path, the higher aircraft Mach number of the CDA leads again to positive differences.

In the final segment no differences can be found as all flight parameters are the same. It was not the scope of this calculation to systematically evaluate CDA and LDLP, as the results only reflect the specific flight parameters used for this example, but to illustrate the application of the noise emission model.

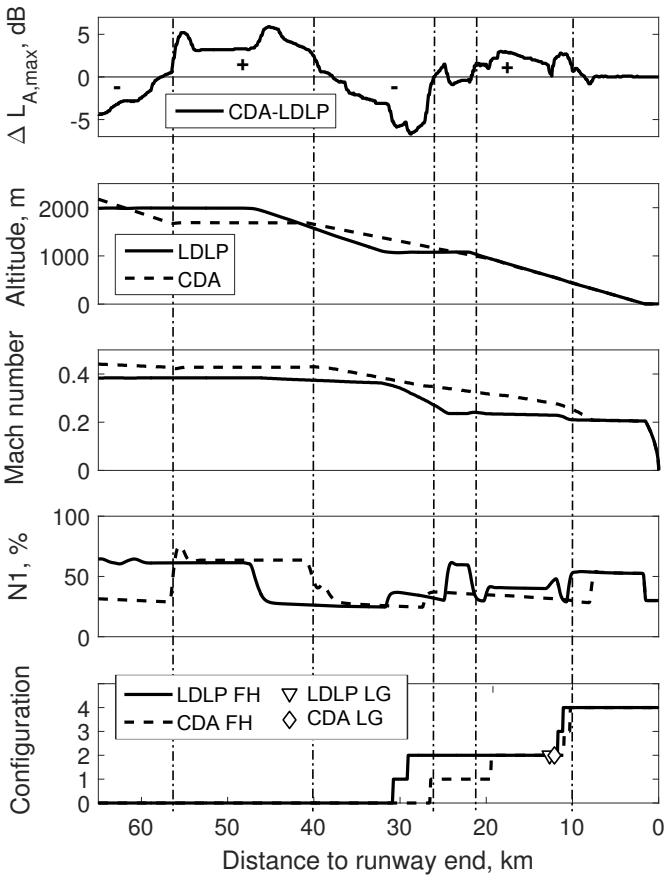

Figure 7.7: $\Delta L_{A,max}$ between CDA and LDLP approach versus flight track distance and corresponding flight parameters of the A320 (CFM56-5B). The vertical distance markers correspond to those of Fig. 7.6.

8 Discussion

The purpose of the present thesis was the development of a general aircraft noise emission model for turbofan-powered aircraft to predict the sound emission level depending on the flight configuration. Further, the separation of airframe and engine noise sources was aimed at. These goals were achieved, as the presented regression model (3D) describes engine and airframe noise separately in function of seven flight parameters and two radiation angles.

The main parameter for engine noise is $N1$, which substitutes the essential parameters of jet and fan noise generation, i.e. jet speed [95], total temperature rise over the fan stage, and mass flow [42]. In addition, $N1$ provides spectral changes as the broadband and tone noise (BPF) of the fan. A quadratic approach between the sound emission level and $N1$ was revealed from an engine run-up test. An advantage over alternative parameters such as thrust is, that it can be measured reliably by sensors or determined from acoustical data as in [86; 87; 92]. Therefore, $N1$ is a suitable parameter to predict engine noise. It provides an analog parameter to the net thrust in the NPD data from Doc. 29/Doc. 9911 [31; 48].

Furthermore, the lateral directivity changes with $N1$ compared to a fixed correction for the lateral directivity in Doc. 29/Doc. 9911. It was shown, that 3D directivity patterns in function of $N1$ are of improved prediction capability compared to 2D models such as FLULA2 [61]. In addition, the influence of the Mach number on the jet noise is considered in the engine noise model, which is not the case for many other aircraft noise programs. Indeed, the mass flow of the engine and thus the fan noise rise with increasing Mach number. Additionally, the airflow that surrounds the jet decreases the sound emission level during take-off. In comparison to the semi-empirical models from Stone et al. [95] for jet noise and Heidmann [42] for fan noise, considerably less flight parameters are needed to precisely reproduce the sound emission level for engine noise.

An advantage of the model – compared to best practice programs such as Doc. 29, Doc. 9911, or FLULA2 – is the separate consideration of airframe and engine noise. This is a fundamental requirement for the development of approach procedures, as airframe noise is the dominant source during approach [51; 91]. Airframe noise was modeled with the base-10 logarithm of Ma and ρ/ρ_0, related to the aeroacoustic theory. Moreover, the effects of the landing gear, flap handle position and speedbrakes were identified and included into the model.

Related to the measurements in real air traffic, the statistical model is based on unbalanced data. In particular, the coefficients determined for the flap handle positions are only valid for specific Mach number and angle of attack ranges. Extrapolations to unknown flight parameters, e.g. for unconventional approach procedures, must be interpreted with care. However, the influence of the flap handle position was observed to be small compared to the landing gear, which can lead to a considerable increase of the sound emission level during approach.

The verifications based on the $L_{AE,t10}$ indicated the capability of the 3D model to simulate highly accurate sound exposure levels. While 3Dred showed similarly good results, 2Dred showed considerably higher variations of $\Delta L_{AE,t10}$. It is therefore recommended to use the advantage of a 3D directivity. For all model variants the mean $L_{AE,t10}$ of the simulation was slightly overestimated. In contrast, $L_{AS,max}$ was underestimated for all model variants with higher variations of $\Delta L_{AS,max}$ than for $\Delta L_{AE,t10}$. This trend might be explained by atmospheric turbulence and temporary tones at the source, which lead to higher variations of the momentary sound pressure level, thus randomly rising the $L_{AS,max}$.

The results of the verification also supported the energy correction of the models. Without applying the energy correction to the models, the $L_{AE,t10}$ would be systematically underestimated. The correction for the energy mean was based on the root-mean-square error from the close range only. The large variations between model and measurement in the far range were neglected, as they do not represent the underlying level variations of the source. Hence, correcting with the total root-mean-square error would have lead to an overestimation of the model predictions.

Where available, it is recommended to use the advanced model for studies on single flight procedures. For instance, by using data from flight mechanical calculations or full flight simulators, which usually provide the required parameters of the model. Nevertheless, the reduced model is similarly applicable, although the effect of changing aeroplane configuration cannot be accounted for. However, at least for airport scenarios and yearly calculations, the reduced model is likely to improve the accuracy of today's noise maps compared to best practice programs due to the following reasons. First, the aircraft Mach number is accounted for, which correlates with the effects of the aeroplane configuration of the airframe and thus is a proxy for the latter. Second, the model is based on measurements up to 20 km from the airport and is thus reliable to a large range of flight parameters.

The applicability of the aircraft noise emission model on a specific airport is currently limited by the available aircraft types, as the effort is large to establish additional aircraft types. The prerequisites to establish the model for new aircraft types are (i) measurements at different locations close to and far from an airport, (ii) back propagation

to the source, and (iii) spectral analysis to determine $N1$ or processing FDR data. It is thus costly to establish an additional aircraft type, but feasible as already demonstrated for 19 aircraft types. Other aircraft noise emission models, which are based on semi-empirical models, also need to be tuned by measurements. For instance, Bertsch [12; 9] had to revisit and update the original constants of the fan model from [42] to account for modern turbofans. In the same way, the coefficients of the semi-empirical airframe models (e.g. [30; 76; 80]) are fitted with wind tunnel experiments and other data.

Furthermore, the separation of airframe and engine noise is limited to the assumption that airframe noise dominates in each 1/3-octave band when the engines are running in idle. In general, the assumption is supported by literature [51; 91]. The validity of this assumption and the resulting separation still needs to be proved, for instance with array measurements such as in [39; 67].

Current research strongly focuses on the optimization of new aircraft concepts, investigating blended wing body aircraft [40] and hybrid wing body aircraft [99] using ANOPP [60] and ANOPP2 [64], or economic and environmental efficiency of new aircraft concepts [13] using PANAM [11]. Predicting new aircraft concepts justifies the high level of detail of the applied semi-empirical models and the number of input parameters. In contrast, the presented aircraft noise emission model is limited to existing aircraft types as it is based on empirical data. However, for these aircraft types the empirical approach accounts for all noise source and parasitic noise such as cavity tones, which is not the case for the aforementioned models.

For the application to auralization of aircraft noise, the model provides sufficient information for broadband noise as it is based on 1/3-octave bands. However, tonal components are included in their respective bands, which is not sufficient for the purpose of auralization. Such components can be extracted from measured narrow band spectra as in [78; 79]. Preferably, further research should focus on generating tonal components artificially based on spectral modeling synthesis, as described by [73] for passenger cars.

In practice, new procedures such as the CDA can be compared to existing procedures and optimized acoustically by means of the presented aircraft noise emission model. Example results showed that the effects of flight parameters on the sound emission at approach are much more important than mere changes in altitude. This is a major advantage to best practice programs (Doc. 9911, FLULA2) which cannot account for those effects [84].

Conclusions and Outlook

An aircraft noise emission model was established for a wide range of relevant aircraft and engine types, which showed the general applicability of the modeling approach. The model describes the sound emission in great detail as spectral three-dimensional directivity patterns in function of flight parameters, separately for airframe and engine noise. The developed aircraft noise emission model fills the gap between existing best practice and high-end models.

Two regression models with different levels of detail and different applicability were derived. The advanced model is suitable to optimize and assess noise abatement procedures in great detail. However, its application is limited by the availability of flight data records to establish the model. In case such data are missing, a reduced model can be established, which will still improve the accuracy of today's noise maps as it includes important flight parameters and is based on extensive measurements covering a wide range of flight configurations.

Overall, a physical behavior of the statistical model was achieved by appropriately choosing and linearizing the model parameters. First, the effects of the model parameters are reasonable, also in regions of extrapolation, as demonstrated in the results section. Second, the verification showed a good agreement of the simulations over the whole range of measured flight events. On this account, moderate extrapolations of the model parameters are approved. However, the models are only verified in their known and documented parameter ranges as long as no further validations are performed.

To further increase the credibility of the model, a validation with independent measurements is required. Compared to the data used for the verification, different airports, measurement geometries, unusual flight configurations, and different weather conditions are of interest. Besides, the methodology to separate airframe and engine noise should be validated, for instance with sophisticated data from array measurements.

An open question to improve and apply the aircraft noise emission model is a correction for the $L_{AS,max}$ to improve its prediction, as the $L_{AS,max}$ was found to be systematically underestimated due to atmospheric turbulence and temporary tones. Another possible improvement of the model could be an extension to correctly reproduce tones, e.g. with the purpose to auralize aircraft noise. Furthermore, it would be desirable to use a similar modeling approach to develop aircraft noise emission models for helicopters,

propeller-driven airplanes or military jets. If and how the approach can be adapted to that purpose needs to be tested (e.g. without separation of airframe and engine noise).

In the future, studies of noise abatement procedures for approach and departure can be accurately calculated and compared to existing procedures with the presented aircraft noise emission model. Such potential should be exploited in the design and decision process by the responsible authorities and stakeholders. In addition, the influence of new procedures is of interest for complex scenarios at different airports. Therefore, it is desired to extend the list of aircraft noise emission models with existing and future aircraft types.

Bibliography

[1] AIP (2016): "Aeronautical Information Publication (AIP) Switzerland", Tech. rep., Skyguide.

[2] Akaike, H. (1998): "Information Theory and an Extension of the Maximum Likelihood Principle", in Parzen, E.; Tanabe, K.; Kitagawa, G. (Eds.), *Selected Papers of Hirotugu Akaike*, Springer, New York, pp. 199–213.

[3] Asensio, C.; Recuero, M.; Pavon, I. (2014): "Citizens perception of the efficacy of airport noise insulation programmes in Spain", *Applied Acoustics*, ISSN 0003-682X, doi: http://dx.doi.org/10.1016/j.apacoust.2014.03.020.

[4] AzB (2008): "Anleitung zur Berechnung von Lärmschutzbereichen", Drucksache 566/08, Bundesrat, Anlage 2.

[5] Babisch, W.; Houthuijs, D.; Pershagen, G.; et al. (2009): "Annoyance due to aircraft noise has increased over the years-Results of the HYENA study", *Environment International*, vol. 35, no. 8, pp. 1169–1176, ISSN 0160-4120.

[6] Barry, T.; Reagan, J. (1978): "FHWA Highway Traffic Noise Prediction Model", Tech. rep., U.S. Department of Transportation.

[7] Basner, M.; Samel, A.; Isermann, U. (2006): "Aircraft noise effects on sleep: Application of the results of a large polysomnographic field study", *Journal of the Acoustical Society of America*, vol. 119, no. 5, pp. 2772–2784.

[8] Basner, M.; Muller, U.; Elmenhorst, E. M. (2011): "Single and combined effects of air, road, and rail traffic noise on sleep and recuperation", *Sleep*, vol. 34, no. 1, pp. 11–23, ISSN 1550-9109 (Electronic) 0161-8105 (Linking).

[9] Bertsch, L. (2013): *Noise Prediction within Conceptual Aircraft Design*, Ph.D. thesis, Technische Universität Carolo-Wilhelmina zu Braunschweig.

[10] Bertsch, L.; Isermann, U. (2013): "Noise prediction toolbox used by the DLR aircraft noise working group", in *42nd International Congress and Exposition on Noise Control Engineering 2013, INTER-NOISE 2013: Noise Control for Quality of Life*, vol. 1, pp. 833–841.

[11] Bertsch, L.; Dobrzynski, W.; Guérin, S. (2010): "Tool Development for Low-Noise Aircraft Design", *Journal of Aircraft*, vol. 47, no. 2, pp. 694–699.

[12] Bertsch, L.; Guérin, S.; Looye, G.; Pott-Pollenske, M. (2011): "The Parametric Aircraft Noise Analysis Module - Status overview and recent applications", in *17th AIAA/CEAS Aeroacoustics Conference 2011 (32nd AIAA Aeroacoustics Conference)*.

[13] Bertsch, L.; Heinze, W.; Lummer, M. (2014): "Application of an aircraft design-to-noise simulation process", in *AIAA AVIATION 2014 -14th AIAA Aviation Technology, Integration, and Operations Conference*.

[14] Blankenship, G. L.; Low, J. K. C.; Watkins, J. A.; Merriman, J. E. (1977): "Effect of Forward Motion on Engine Noise", Tech. Rep. NASA-CR-134954, NASA Lewis Research Center.

[15] Boeing (2016): "Current Market Outlook 2016 - 2035", Tech. rep., Boeing Commercial Airplanes.

[16] Brink, M.; Lercher, P.; Eisenmann, A.; Schierz, C. (2008): "Influence of slope of rise and event order of aircraft noise events on high resolution actimetry parameters", *Somnologie*, vol. 12, pp. 118–128.

[17] Brink, M.; Wirth, K.; Schierz, C.; Thomann, G.; Bauer, G. (2008): "Annoyance responses to stable and changing aircraft noise exposure", *Journal of the Acoustical Society of America*, vol. 124, no. 5, pp. 2930–2941.

[18] Brink, M.; Schreckenberg, D.; Thomann, G.; Basner, M. (2010): "Aircraft noise indexes for effect oriented noise assessment", *Acta Acustica United with Acustica*, vol. 96, pp. 1012–1025.

[19] Bẗikofer, R.; Thomann, G. (2009): "Uncertainty and level adjustments of aircraft noise measurements", in *Proceedings of the 2009 International Congress and Exposition on Noise Control Engineering (INTER-NOISE 2009)*, Institute of Noise Control Engineering, Ottawa, Canada.

[20] Bütikofer, R. (2007): "Concepts of aircraft noise calculations", *Acta Acustica united with Acustica*, vol. 93, no. 2, pp. 253–262.

[21] Bütikofer, R. (2012): "Airport noise", in *Noise Mapping in the EU*, CRC Press, pp. 129–158, ISBN 978-0-415-58509-5, doi:10.1201/b12885-9.

[22] Craven, P.; Wahba, G. (1978): "Smoothing noisy data with spline functions - Estimating the correct degree of smoothing by the method of generalized cross-validation", *Numerische Mathematik*, vol. 31, no. 4, pp. 377–403.

[23] Cremer, L. (1990): "Fresnels Methoden zur Berechnung von Beugungsfeldern", *Acustica*, vol. 72, pp. 1 – 6.

[24] Daigle, G. A.; Embleton, T. F. W.; Piercy, J. E. (1986): "Propagation of sound in the presence of gradients and turbulence near the ground", *Journal of the Acoustical Society of America*, vol. 79, no. 3, pp. 613–627, ISSN 0001-4966.

[25] Defrance, J.; Salomons, E.; Noordhoek, I.; et al. (2007): "Outdoor sound propagation reference model developed in the European harmonoise project", *Acta Acustica united with Acustica*, vol. 93, no. 2, pp. 213–227.

[26] DIN (2004): *Electroacoustics - Sound calibrators (IEC 60942:2003); German version EN 60942:2003*, DIN Deutsches lnstitut für Normung e. V.

[27] DIN (2011): *Measurement and assessment of aircraft sound; Text in German and English DIN 45643:2011-02*, DIN Deutsches lnstitut für Normung e. V.

[28] DIN (2014): *Electroacoustics - Sound level meters - Part 1: Specifications (IEC 61672-1:2013), German version EN 61672-1:2013*, DIN Deutsches lnstitut für Normung e. V.

[29] Dobrzynski, W. (2010): "Almost 40 years of airframe noise research: What did we achieve?", *Journal of Aircraft*, vol. 47, no. 2, pp. 353–367, doi:10.2514/1.44457.

[30] Dobrzynski, W.; Pott-Pollenske, M. (2001): "Slat noise source studies for farfield noise prediction", in *7th AIAA/CEAS Aeroacoustics Conference and Exhibit*.

[31] ECAC (2016): *DOC.29: Report on Standard Method of Computing Noise Contours around Civil Airports, Volume 2: Technical Guide. 4th ed.*, European Civil Aviation Conference (ECAC), Neuilly-sur-Seine, France.

[32] Empa (2013): "Abnahmemessungen Schallschutzhalle Triebwerk-Standläufe", Tech. Rep. 5214.002380, Eidgenössische Materialprüfungs- und Forschungsanstalt (Empa), Abteilung Akustik / Lärmminderung.

[33] Empa (2016): "Dokumentation des sonX Ausbreitungsmodells. Programmversion: sonRAIL V5.0.0 bzw. sonARMS V4.0.0 bzw. sonAIR V2.2.0 (vom 12. September 2016)", Tech. Rep. 5211.00687.100.14, Eidgenössische Materialprüfungs- und Forschungsanstalt (Empa), Abteilung Akustik / Lärmminderung.

[34] Filzmoser, P.; Garrett, R. G.; Reimann, C. (2005): "Multivariate outlier detection in exploration geochemistry", *Computers and Geosciences*, vol. 31, no. 5, pp. 579–587.

[35] Gasco, L.; Asensio, C.; de Arcas, G. (2017): "Communicating airport noise emission data to the general public", *Science of The Total Environment*, ISSN 0048-9697, doi: http://dx.doi.org/10.1016/j.scitotenv.2017.02.063.

[36] Gaumain, C. (1998): "Prediction of Noise in the Vicinity of an Airport: A Simulation Method based on Frequency Dependent Directivity Patterns", Tech. rep., KTH Royal Institute of Technology.

[37] Gjestland, T.; Gelderblom, F. B. (2017): "Prevalence of Noise Induced Annoyance and Its Dependency on Number of Aircraft Movements", *Acta Acustica United with Acustica*, vol. 103, no. 1, pp. 28–33, doi:10.3813/AAA.919030.

[38] Guérin, S.; Michel, U. (2006): "Aero-engine noise investigated from flight tests", in *Collection of Technical Papers - 12th AIAA/CEAS Aeroacoustics Conference*, vol. 2, pp. 827–838.

[39] Guérin, S.; Michel, U.; Siller, H.; Finke, U.; Saueressig, G. (2005): "Airbus A319 database from dedicated flyover measurements to investigate noise abatement procedures", in *Collection of Technical Papers - 11th AIAA/CEAS Aeroacoustics Conference*, vol. 4, pp. 2266–2279.

[40] Guo, Y.; Burley, C. L.; Thomas, R. H. (2014): "On Noise Assessment for Blended Wing Body Aircraft", Portland, OR, 17th AIAA/CEAS Aeroacoustics Conference 2011 (32nd AIAA Aeroacoustics Conference).

[41] Guski, R. (2004): "How to forecast community annoyance in planning noisy facilities", *Noise & Health*, vol. 6, pp. 59–64.

[42] Heidmann, M. F. (1979): "Interim Prediction Method for fan and compressor source noise", Tech. Rep. NASA TM-X-71763, NASA Lewis Research Center.

[43] Heutschi, K. (2004): "SonRoad: New Swiss road traffic noise model", *Acta Acustica United with Acustica*, vol. 90, no. 3, pp. 548–554.

[44] Howe, M. S. (1998): *Acoustics of fluid-structure interactions*, Cambridge monographs on mechanics, Cambridge [etc.] : Cambridge University Press.

[45] ICAO (2006): *Flight Procedures*, vol. 1 of *Procedures for Air Navigation Services: Aircraft Operations. Doc 8168 OPS/611*, International Civil Aviation Organization (ICAO), Montréal, Canada, 5. edn.

[46] ICAO (2007): *Review of Noise Abatement Procedure Research & Development and Implementation Results*, International Civil Aviation Organization (ICAO), Montréal, Canada, preliminary edn.

[47] ICAO (2008): *Guidance on the Balanced Approach to Aircraft Noise Management. Doc 9829 AN/451.*, International Civil Aviation Organization (ICAO), Montréal, Canada, 2. edn.

[48] ICAO (2008): *Recommended Method for Computing Noise Contours Around Airports. Doc 9911.*, International Civil Aviation Organization (ICAO), Montréal, Canada, 1. edn.

[49] IEC (2014): *IEC-61260-1: Electroacoustics - Octave-band and fractional-octave-band filters - Part 1: Specifications*, International Electrotechnical Commission (IEC), Geneva, Switzerland.

[50] Isermann, U. (2011): "Overview on the development of the airport noise modeling standard DIN 45689", in *40th International Congress and Exposition on Noise Control Engineering 2011, INTER-NOISE 2011*, vol. 5, pp. 4425–4430.

[51] Isermann, U. (2013): "Potentials and limits of noise abatement flight procedures", in *42nd International Congress and Exposition on Noise Control Engineering 2013, INTER-NOISE 2013: Noise Control for Quality of Life*, vol. 2, pp. 1081–1088.

[52] Isermann, U.; Schmid, R. (1999): "Bewertung und Berechnung von Fluglärm", Tech. Rep. FE-Nr. L-2/96-50144/96, DLR, Institut für Stömungsmechanik.

[53] Isermann, U.; Vogelsang, B. (2010): "AzB and ECAC Doc.29-Two best-practice European aircraft noise prediction models", *Noise Control Engineering Journal*, vol. 58, no. 4, pp. 455–461.

[54] Isermann, U.; Matschat, K.; Mueller, E. A. (1986): "Prediction of Aircraft Noise around Airports by a Simulation Procedure", in *International Conference on Noise Control Engineering, Progress in Noise Control: Inter-Noise 86.*, vol. 1, pp. 717–722.

[55] ISO (1988): *ISO 1151-1:1988. Flight dynamics – Concepts, quantities and symbols – Part 1: Aircraft motion relative to the air*, International Organisation for Standardization (ISO), Geneva, Switzerland, 4. edn.

[56] ISO (1993): *ISO 9613-1. Acoustics - attenuation of sound during propagation outdoors - Part 1: calculation of the absorption of sound by the atmosphere*, International Organisation for Standardization (ISO), Geneva, Switzerland.

[57] ISO (1996): *ISO 9613-2. Acoustics - attenuation of sound during propagation outdoors - Part 2: general method of calculation*, International Organisation for Standardization (ISO), Geneva, Switzerland.

[58] ISO/IEC (2008): *Evaluation of measurement data - Part 3: Guide to the expression of uncertainty in measurement (GUM:1995)*, JCGM 100:2008, International Organisation for Standardization (ISO) and International Electrotechnical Commission (IEC), Geneva, Switzerland, 1. edn.

[59] Kim, Y.-H. (2010): *Sound Propagation: An Impedance Based Approach*, Wiley, Singapore.

[60] Kontos, K. B.; Janardan, B. A.; Gliebe, P. R. (1996): "Improved NASA-ANOPP Noise Prediction Computer Code for Advanced Subsonic Propulsion Systems. Volume 1: ANOPP Evaluation and Fan Noise Model", Tech. Rep. NASA-CR-195480, NASA Lewis Research Center.

[61] Krebs, W.; Bütikofer, R.; Plüss, S.; Thomann, G. (2004): "Sound source data for aircraft noise simulation", *Acta Acustica united with Acustica*, vol. 90, no. 1, pp. 91–100.

[62] Krebs, W.; Bütikofer, R.; Plüss, S.; Thomann, G. (2006): "Spectral three-dimensional sound directivity models for fixed wing aircraft", *Acta Acustica united with Acustica*, vol. 92, no. 2, pp. 269–277.

[63] Lighthill, M. J. (1952): "On Sound Generated Aerodynamically. I. General Theory", *Proceedings of the Royal Society of London A: Mathematical, Physical and Engineering Sciences*, vol. 211, no. 1107, pp. 564–587.

[64] Lopes, L. V.; Burley, C. L. (2011): "Design of the next generation aircraft noise prediction program: ANOPP2", Portland, OR, 17th AIAA/CEAS Aeroacoustics Conference 2011 (32nd AIAA Aeroacoustics Conference).

[65] Lu, C.; Morrell, P. (2006): "Determination and applications of environmental costs at different sized airports - aircraft noise and engine emissions", *Transportation*, vol. 33, no. 1, pp. 45–61, doi:10.1007/s11116-005-2300-y.

[66] Maekawa, Z.; Rindel, J. H.; Lord, P. (2011): *Environmental and architectural acoustics*, London : Spon Press/Taylor & Francis, 2. edn.

[67] Merino-Martinez, R.; Bertsch, L.; Simons, D. G.; Snellen, M. (2016): "Analysis of landing gear noise during approach", in *22nd AIAA/CEAS Aeroacoustics Conference*, American Institute of Aeronautics and Astronautics, Aeroacoustics Conferences.

[68] Merriman, J.; Good, R.; Low, J.; Yee, P.; Blankenship, G. (1976): "Forward motion and installation effects on engine noise", in *3rd Aeroacoustics Conference*, American Institute of Aeronautics and Astronautics.

[69] Möser, M. (2015): *Technische Akustik*, VDI-Buch, Springer Vieweg, Berlin, Heidelberg, 10. edn.

[70] Neter, J.; Nachtsheim, C. J.; Kutner, M. H. (2004): *Applied linear regression models*, Maidenhead : McGraw Hill, 4. edn.

[71] Parkin, P. H.; Scholes, W. E. (1965): "Horizontal propagation of sound from a jet engine close to ground at Hatfield", *Journal of Sound and Vibration*, vol. 2, no. 4, p. 353ff., ISSN 0022-460X.

[72] Pierce, A. (1991): "Acoustics. An Introduction to its Physical Principles and Applications", *American Institute of Physics, Woodbury.*

[73] Pieren, R.; Bütler, T.; Heutschi, K. (2016): "Auralization of accelerating passenger cars using spectral modeling synthesis", *Applied Sciences (Switzerland)*, vol. 6, no. 1, pp. 1–27, doi:10.3390/app6010005.

[74] Pietrzko, S.; Hofmann, R. F. (1988): "Prediction of A-weighted aircraft noise based on measured directivity patterns", *Applied Acoustics*, vol. 23, no. 1, pp. 29–44.

[75] Plovsing, B.; Svane, C. (1983): "Aircraft Noise Exposure Prediction Model: Guidelines for the Methodology of a Danish Computer Program", Tech. rep., Danish Acoustical Institute.

[76] Pott-Pollenske, M.; Dobrzynski, W.; Buchholz, H.; et al. (2006): "Airframe noise characteristics from flyover measurements and predictions", in *Collection of Technical Papers - 12th AIAA/CEAS Aeroacoustics Conference*, vol. 4, pp. 2069–2082.

[77] Ribner, H. S. (1964): "The Generation of Sound by Turbulent Jets", *Advances in Applied Mechanics*, vol. 8, no. C, pp. 103–182, doi:10.1016/S0065-2156(08)70354-5.

[78] Rietdijk, F. (2017): *Auralisation of airplanes considering sound propagation in a turbulent atmosphere*, Ph.d. dissertation, Chalmers University of Technology, Gothenburg.

[79] Rietdijk, F.; Heutschi, K.; Zellmann, C. (2015): "Determining an Empirical Emission Model for the Auralization of Jet Aircraft", in *Proceedings of the 10th European Conference on Noise Control*, EAA-NAG-ABAV, Maastricht, vol. 31, pp. 781–784.

[80] Rossignol, K. S. (2011): "Empirical prediction of flap tip noise", in *17th AIAA/CEAS Aeroacoustics Conference 2011 (32nd AIAA Aeroacoustics Conference).*

[81] Ruijgrok, G. (2004): *Elements of Aviation Acoustics*, Delft University Press.

[82] SAE (1986): "Procedure for the Calculation of Airplane Noise in the Vicinity of Airports. Aerospace Information Report SAE AIR 1845", Tech. Rep. Aerospace Information Report (AIR) 1845, Society of Automotive Engineers (SAE), Committee A-21 Aircraft Noise.

[83] Schäffer, B.; Thomann, G.; Huber, P.; et al. (2012): "Zurich Aircraft Noise Index: an index for the assessment and analysis of the effects of aircraft noise on the population", *Acta Acustica united with Acustica*, vol. 98, no. 3, pp. 505–519, doi:10.3813/AAA.918533.

[84] Schäffer, B.; Zellmann, C.; Krebs, W.; et al. (2012): "Sound source data for aircraft noise calculations - state of the art and future challenges", in *Proceedings of Euronoise 2012, Ninth European Conference on Noise Control*, Prague, Czech Republic, pp. 589–594.

[85] Schäffer, B.; Plüss, S.; Thomann, G. (2014): "Estimating the model-specific uncertainty of aircraft noise calculations", *Applied Acoustics*, vol. 84, pp. 58–72, doi:10.1016/j.apacoust.2014.01.009.

[86] Schlüter, S. (2015): *Bestimmung der Triebwerksleistung eines überfliegenden Flugzeuges durch Audio Feature Extraction*, Master thesis, TU Berlin.

[87] Schlüter, S.; Becker, S. (2016): "Determination of Aircraft Engine Speed Based on Acoustic Measurements", in *INTER-NOISE 2016 - 45th International Congress on Noise Control Engineering: Towards a Quieter Future*, Hamburg, pp. 778–785.

[88] Schmid, R. (1999): *Physikalische Modellierung der Richtcharakteristik der Schallabstrahlung von Nebenstromtriebwerken*, Ph.D. thesis, Georg-August-Universität Göttingen.

[89] Schwarz, G. (1978): "Estimating the Dimension of a Model", *The Annals of Statistics*, vol. 6, no. 2, pp. 461–464, doi:citeulike-article-id:90008doi:10.2307/2958889.

[90] Simons, D. G.; Snellen, M.; Midden, B. v.; Arntzen, M.; Bergmans, D. H. T. (2015): "Assessment of Noise Level Variations of Aircraft Flyovers Using Acoustic Arrays", *Journal of Aircraft*, vol. 52, no. 5, pp. 1625–1633, doi:10.2514/1.C033020.

[91] Smith, M. J. T. (1989): *Aircraft noise*, Cambridge University Press, Cambridge.

[92] Snellen, M.; Merino-Martinez, R.; Simons, D. G. (2017): "Assessment of noise variability of landing aircraft using phased microphone array", *Journal of Aircraft*, vol. 54, no. 6, pp. 2173–2183, doi:10.2514/1.C033950.

[93] Stone, J. R. (1974): "Interim prediction method for jet noise", Tech. Rep. NASA-TM-X-71618, NASA Lewis Research Center.

[94] Stone, J. R. (1976): "Flight effects on exhaust noise for turbojet and turbofan engines – comparison of experimental data with prediction", Tech. Rep. NASA-TM-X-73552, NASA Lewis Research Center.

[95] Stone, J. R.; Groesbeck, D. E.; Zola, C. L. (1983): "Conventional Profile Coaxial Jet Noise Prediction", *AIAA journal*, vol. 21, no. 3, pp. 336–342.

[96] Tang, S. K. (2010): "On sound transmission loss across a Helmholtz resonator in a low Mach number flow duct", *Journal of the Acoustical Society of America*, vol. 127, no. 6, pp. 3519–3525, doi:10.1121/1.3409481.

[97] Thomann, G. (2007): *Mess- und Berechnungsunsicherheit von Fluglärmbelastungen und ihre Konsequenzen (Uncertainties of Measured and Calculated Aircraft Noise and Consequences in Relation to Noise Limits)*, Ph.d. dissertation, diss. eth nr. 17433, ETH Zurich.

[98] Thomann, G. (2008): "Uncertainties of measured and calculated aircraft noise and consequences in relation to noise limits", in *Proceedings - European Conference on Noise Control*, pp. 1831–1834.

[99] Thomas, R. H.; Burley, C. L.; Olson, E. (2012): "Hybrid wing body aircraft system noise assessment with propulsion airframe aeroacoustic experiments", *International Journal of Aeroacoustics*, vol. 11, no. 3-4, pp. 369–410, doi:10.1260/1475-472X.11.3-4.369.

[100] Thron, T.; Hecht, M. (2010): "The sonRAIL emission model for railway noise in Switzerland", *Acta Acustica united with Acustica*, vol. 96, no. 5, pp. 873–883.

[101] Wittstock, V.; Bethke, C. (2005): "On the uncertainty of sound pressure levels determined by third-octave band analyzers in a hemianechoic room", in *Forum Acusticum Budapest 2005: 4th European Congress on Acustics*, pp. 1301–1306.

[102] Wunderli, J. M.; Rotach, M. W. (2011): "Application of statistical weather data from the numerical weather prediction model COSMO-2 for noise mapping purposes", *Acta Acustica united with Acustica*, vol. 97, no. 3, pp. 403–415, cited By (since 1996):6 Export Date: 7 August 2014.

[103] Wunderli, J. M.; Pieren, R.; Heutschi, K. (2012): "The Swiss shooting sound calculation model sonARMS", *Noise Control Engineering Journal*, vol. 60, no. 3, pp. 224–235.

[104] Zellmann, C.; Wunderli, J. M. (2014): "Influence of the atmospheric stratification on the sound propagation of single flights", in *INTER-NOISE 2014 - 43rd International Congress on Noise Control Engineering: Improving the World Through Noise Control*, Melbourne.

[105] Zellmann, C.; Wunderli, J. M.; Schäffer, B. (2013): "SonAIR - Data acquisition for a next generation aircraft noise simulation model", in *INTER-NOISE 2013 - 42nd International Congress and Exposition on Noise Control Engineering: Noise Control for Quality of Life*, Innsbruck, vol. 1, pp. 842–850.

[106] Zellmann, C.; Wunderli, J. M.; Paschereit, C. O. (2016): "The sonAIR sound model: spectral three-dimensional directivity patterns in dependency of the flight condition", in *INTER-NOISE 2016 - 45th International Congress on Noise Control Engineering: Towards a Quieter Future*, Hamburg, pp. 786–794.

[107] Zellmann, C.; Schäffer, B.; Wunderli, J. M.; Isermann, U.; Paschereit, C. O. (2017): "An Aircraft Noise Emission Model Accounting for Aircraft Flight Parameters", *Journal of Aircraft*, doi:10.2514/1.C034275, accessed September 09, 2017.

[108] Zuur, A.; Ieno, E.; Walker, N.; Saveliev, A.; Smith, G. (2009): *Mixed Effects Models and Extensions in Ecology with R*, Springer New York.

A Appendix

A.1 Initial model

The initial airframe model only reduces for the parameter $Proc$ as the data with $N1 < 40\,\%$ consists solely of approaches.

$$\widehat{L}^i_{e,afm}(f) = \underbrace{\widehat{L}^i_{0,afm}(lMa, l\rho, FH, LG, SB)}_{\text{source terms}} + \underbrace{\Delta\widehat{L}^i_{\theta,afm}(\theta)}_{\text{radiation angle terms}} \tag{A.1}$$

$$\begin{aligned}\widehat{L}^i_{0,afm} = {} & L_{a0} + a_{a1}\cdot lMa + b_{a1}\cdot l\rho \\ & + LG\cdot(c_{a1} + c_{a3}\cdot lMa) \\ & + \sum_{j=1}^{4} FH_j\cdot(d_{a1j} + d_{a2j}\cdot LG) \\ & + SB\cdot(e_{a1} + e_{a2}\cdot LG + e_{a3}\cdot lMa)\end{aligned} \tag{A.2}$$

$$\Delta\widehat{L}^i_{\theta,afm} = k_a\cdot\cos\theta + l_a\cdot\cos 2\theta + m_a\cdot\sin\theta + n_a\cdot\sin 2\theta \tag{A.3}$$

The quadratic behavior of L_e over $N1$ is neglected for the initial engine model to prevent for a negative slope below $40\,\%$, where no more data are given. In Fig. 4.3 a linear approach for $N1 > 40\,\%$ is actually a good approximation for most of the cases, even though the linear extrapolation to idle is not correct in all cases as seen in Sec. 4.2.3.

$$\widehat{L}^i_{e,eng}(f) = \underbrace{\widehat{L}^i_{0,eng}(Ma, N1)}_{\text{source terms}} + \underbrace{\Delta\widehat{L}^i_{\theta,eng}(\theta, N1) + \Delta\widehat{L}^i_{\varphi,eng}(\varphi, N1)}_{\text{radiation angle terms}} \tag{A.4}$$

$$\widehat{L}^i_{0,eng} = L_{e0} + a_{e1}\cdot Ma + b_{e1}\cdot N_1 \tag{A.5}$$

The same change applies for the longitudinal directivity which has only an interaction with $N1$.

$$\Delta\widehat{L}^i_{\theta,eng} = (k_{e,j}\cdot\cos\theta + l_{e,j}\cdot\cos 2\theta + m_{e,j}\cdot\sin\theta + n_{e,j}\cdot\sin 2\theta)\cdot(1 + N1) \tag{A.6}$$

$$\Delta\widehat{L}^i_{\varphi,eng} = (o_{e,j}\cdot\sin\varphi + p_{e,j}\cdot\sin 2\varphi)\cdot(1 + N1) \tag{A.7}$$

A.2 Flight parameters

Table A.1: Engine types and their parameters from the TCDS. From BeSB GmbH Berlin with permission.

Engine type	Z_{Fan}	ω_{max} [rpm]	$N1_{max}$[%]	BPF_{max} [Hz]
BR700-710A	24	7 542	101.5	3 017
CF34-10E	24	6 325	106.2	2 530
CF34-3	28	7 300	98.6	3 407
CF34-8C5	28	7 360	99.5	3 435
CF34-8E	28	7 360	99.5	3 435
CF6-50	38	3 810	111.0	2 413
CF6-80A	38	4 016	117.0	2 543
CF6-80C2	38	3 854	117.5	2 441
CF6-80E	38	3 835	115.5	2 429
CFM56-3	38	5 490	106.0	3 477
CFM56-5A	36	5 100	102.0	3 060
CFM56-5B	36	5 200	104.0	3 120
CFM56-5C	36	4 985	104.2	2 991
CFM56-7B	24	5 382	104.0	2 153
GE90-11	22	2 602	110.5	954
GP7270	24	2 738	111.0	1 095
JT8D-217C	34	8 350	101.6	4 732
JT8D-219	34	8 350	101.6	4 732
LF502	40	7 602	100.0	5 068
LF507	40	7 602	100.0	5 068
PW307	21	11 110	101.0	3 889
PW4060	38	4 012	111.4	2 541
PW4168	34	3 600	101.0	2 040
TAY650-15	22	8 250	98.3	3 025
TAY620-15	22	8 343	99.4	3 059
TFE731-20	30	21 000	100.0	10 553
TRENT5	26	3 900	100.0	1 690
TRENT7	26	3 900	100.0	1 690
TRENT9	24	2 900	100.0	1 160
V2500	22	5 650	100.0	2 072

Table A.2: Data structure of FDR data from the event management system of Swiss International Air Lines.

Name	Description (Unit)	Code
Record	Flight Record	fdr_id
Fleet-Information	Fleet	type
Event Count	Event Count - Array of Reference Events	ref
Counter	Counter (integer)	counter
Quality-Flag	Reliability Flag (1 = okay)	reliability
Eng-type (SAC/DAC)	DAC / SAC Flag (0 = SAC, 1 = DAC, 2 = intermix)	dac
Time at shortest distance	GMT (real) (hrs)	utc
Time	Relative Offset (Seconds (from monitoring site))	reltime
Air Temperature	Air Temperature (outside) (Deg Celsius)	oat
Air Density	Air Density (ambient) ($^{kg}/_{m^3}$)	rho
Air Pressure	Air Pressure (ambient) (hPa (mbar))	p
Radio Altitude	Radio Altitude (fine) (ft)	h_radio
Headwind	Headwind (knots)	hdwind
Crosswind	Crosswind (knots)	crwind
Vertical Wind	Vertical Wind (ft / min)	vwind
Corrected MSL Altitude	Corrected MSL Altitude (corrected trajectory) (feet)	h_msl
Baro-Corrected Altitude	Baro Altitude (baro-corrected) (feet)	h_baro
Geometric Altitude	Geometric Altitude (above MSL) (feet)	h_geom
HATO/HAT	Height AFE (feet)	h_afe
Ground Speed	Ground Speed (knots)	gs
CalibratedAirspeed	Airspeed (calibrated) (knots)	cas
True Airspeed	True Airspeed (TAS) (knots)	tas
Vertical Speed	Vertical Speed (library best available) (ft per min)	vs
Pitch Attitude	Pitch Attitude (Captain's or only) (degrees)	theta
Angle of Attack	Average Angle of Attack (deg)	alpha
Roll Attitude	Roll Attitude (Captain's or only) (degrees)	phi
Heading	Heading (true) (degrees)	psi
Track Angle	Track Angle (true) (degrees)	track
Drift Angle	Drift Angle (deg)	drift
Sideslip Angle	Sideslip Angle (deg)	beta
Corrected Latitude	Latitude (best available) (degrees)	lat
Corrected Longitude	Longitude (best available) (degrees)	lon
3D-Distance	GPS 3D-Distance to Reference (MIN / best available) (m)	min
N1 Average	N1 Average (over all engines) (% of max available)	n1
N2 Average	N2 Average (over all engines) (%)	n2
Thrust (total)	Average Thrust (over all engines) (N)	f
Thrust (relative)	Relative Thrust (over all engines) (%)	f_rel
Thrust Reversers	Thrust Reversers Deployed (0 = deployed)	reverser
Configuration	Flap / Slat Handle Position (configuration)	flaps
Speedbrake Position	Speed Brakes Deployed (1 = deployed)	speedbrake
Gross Weight	Gross Weight (tons)	mass
Landing Gear	Landing Gear Down and Locked (0 = all gear down)	gears

Table A.3: Initial climb: mean parameters, standard deviations σ and number of events from measurements at Zurich airport.

Model name	$\overline{N1}$ [%]	σ_{N1} [%]	$\overline{Ma}$ [-]	σ_{Ma} [-]	$\overline{\rho}$ [kg/m^3]	σ_ρ [kg/m^3]	Number
A319_CFM56-5A	89.1	0.0	0.23	0.005	1.18	0.01	1
A320_CFM56-5A	91.3	1.3	0.24	0.010	1.16	0.02	11
A319_CFM56-5B	87.2	1.6	0.23	0.008	1.15	0.02	19
A320_CFM56-5B	90.8	1.9	0.24	0.009	1.14	0.02	175
A321_CFM56-5B	94.2	1.8	0.26	0.012	1.14	0.02	66
A319_V2500	83.9	1.9	0.24	0.016	1.15	0.02	31
A320_V2500	86.5	2.2	0.25	0.007	1.15	0.02	8
A321_V2500	89.0	2.1	0.25	0.009	1.16	0.01	4
A333_TRENT7	86.7	2.1	0.26	0.009	1.14	0.02	99
A343_CFM56-5C	94.5	2.8	0.25	0.014	1.15	0.02	48
A388_GP7270	90.4	2.9	0.25	0.011	1.15	0.02	5
A388_TRENT9	82.2	1.1	0.26	0.005	1.15	0.02	11
B733_CFM56-3	90.6	1.4	0.25	0.010	1.15	0.02	10
B734_CFM56-3	93.4	0.2	0.28	0.005	1.16	0.01	1
B735_CFM56-3	90.5	1.5	0.24	0.007	1.14	0.03	6
B736_CFM56-7B	88.8	1.4	0.23	0.010	1.16	0.01	5
B737_CFM56-7B	89.3	1.2	0.23	0.006	1.15	0.02	10
B738_CFM56-7B	93.1	1.6	0.25	0.009	1.15	0.02	12
B762_CF6-80C2	101.0	0.8	0.28	0.007	1.15	0.02	8
B763_CF6-80C2	104.1	5.6	0.28	0.009	1.15	0.02	6
B764_CF6-80C2	110.4	0.0	0.29	0.000	1.16	0.00	1
B763_PW4060	95.7	1.7	0.29	0.006	1.14	0.02	2
CRJ9_CF34-8C5	87.8	1.8	0.26	0.013	1.17	0.01	3
E170_CF34-8E	86.3	0.9	0.23	0.006	1.15	0.02	14
E190_CF34-10E	91.0	1.3	0.23	0.008	1.14	0.02	41
F100_TAY650-15	84.2	1.7	0.24	0.011	1.15	0.02	31
FA7X_PW307	83.8	10.9	0.22	0.013	1.12	0.03	5
RJ1H_LF507	89.8	2.3	0.22	0.010	1.14	0.02	106

Table A.4: Final approach: mean parameters, standard deviations σ and number of events from measurements at Zurich airport.

Model name	$\overline{N1}$ [%]	σ_{N1} [%]	$\overline{Ma}$ [-]	σ_{Ma} [-]	$\overline{\rho}$ [kg/m^3]	σ_ρ [kg/m^3]	Number
A319_CFM56-5A	57.4	3.2	0.20	0.007	1.13	0.02	4
A320_CFM56-5A	54.2	1.9	0.21	0.010	1.14	0.01	6
A319_CFM56-5B	48.6	3.9	0.20	0.009	1.14	0.02	17
A320_CFM56-5B	51.3	4.3	0.21	0.008	1.15	0.02	171
A321_CFM56-5B	54.7	4.6	0.22	0.008	1.15	0.02	83
A319_V2500	55.2	5.2	0.21	0.005	1.13	0.01	4
A320_V2500	47.8	5.0	0.21	0.005	1.16	0.01	2
A321_V2500	53.0	2.3	0.21	0.010	1.15	0.02	3
A333_TRENT7	45.2	3.6	0.22	0.006	1.16	0.01	60
A343_CFM56-5C	53.3	7.6	0.22	0.005	1.14	0.01	33
A388_GP7270							0
A388_TRENT9	55.0	0.0	0.22	0.005	1.16	0.01	6
B733_CFM56-3	55.3	3.6	0.21	0.009	1.15	0.02	16
B734_CFM56-3	45.9	1.2	0.20	0.008	1.15	0.00	0
B735_CFM56-3	51.2	4.4	0.21	0.008	1.14	0.01	9
B736_CFM56-7B	51.6	3.0	0.21	0.008	1.15	0.01	5
B737_CFM56-7B	53.9	2.5	0.21	0.006	1.14	0.01	13
B738_CFM56-7B	55.3	3.6	0.23	0.010	1.14	0.01	5
B762_CF6-80C2							0
B763_CF6-80C2	58.5	1.3	0.24	0.001	1.16	0.00	1
B764_CF6-80C2							0
B763_PW4060	56.2	3.2	0.23	0.008	1.16	0.01	10
CRJ9_CF34-8C5	58.1	2.6	0.21	0.007	1.15	0.01	8
E170_CF34-8E	50.1	5.5	0.20	0.009	1.15	0.01	23
E190_CF34-10E	56.5	2.7	0.20	0.007	1.14	0.02	19
F100_TAY650-15	56.2	6.3	0.21	0.010	1.15	0.01	11
FA7X_PW307	51.3	3.1	0.19	0.008	1.14	0.02	5
RJ1H_LF507	57.4	6.3	0.20	0.009	1.14	0.02	114

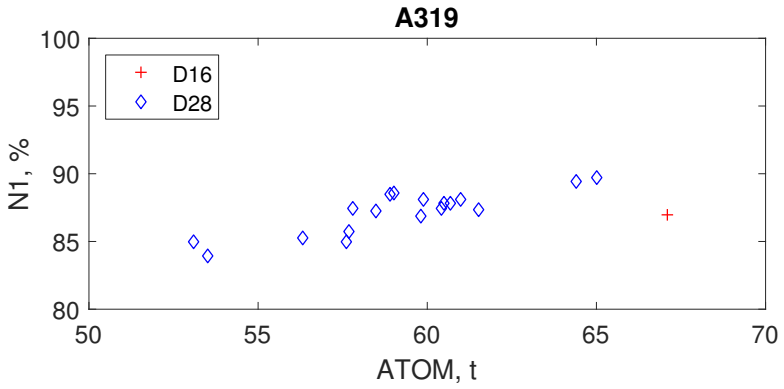

(a) A319

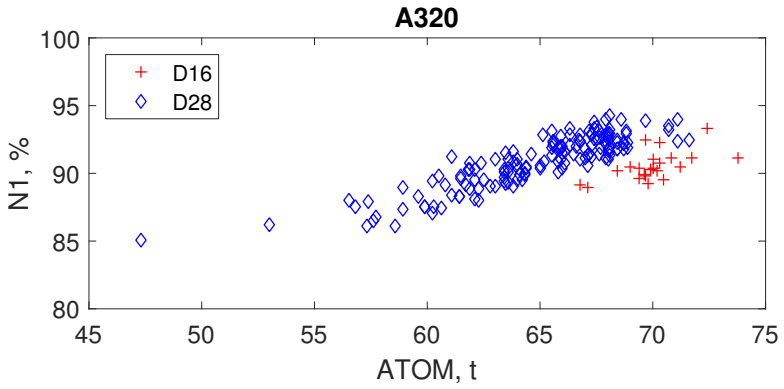

(b) A320

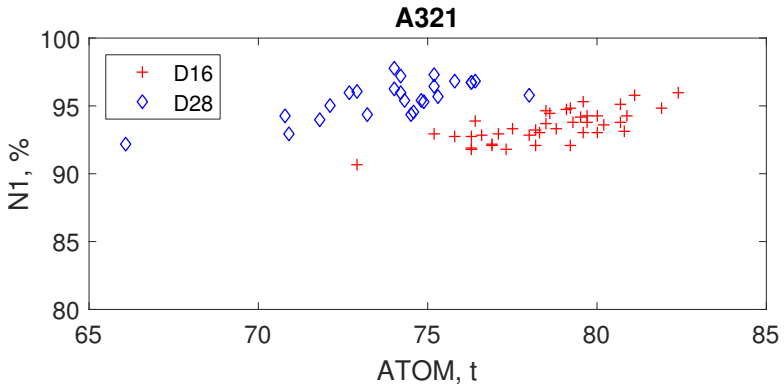

(c) A321

Figure A.1: $N1$ versus ATOM for each aircraft type of the A320-family.

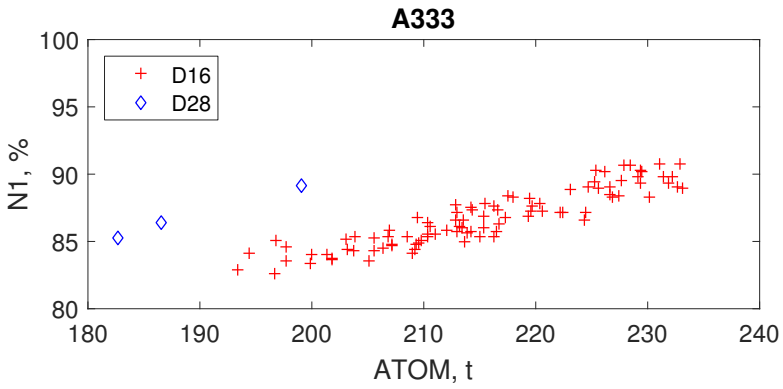

(a) A333

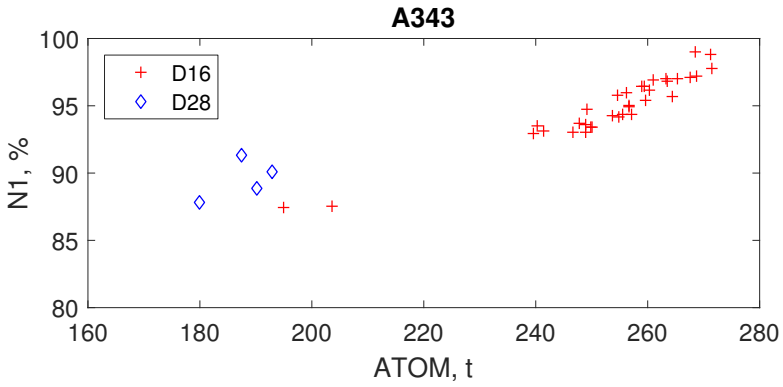

(b) A343

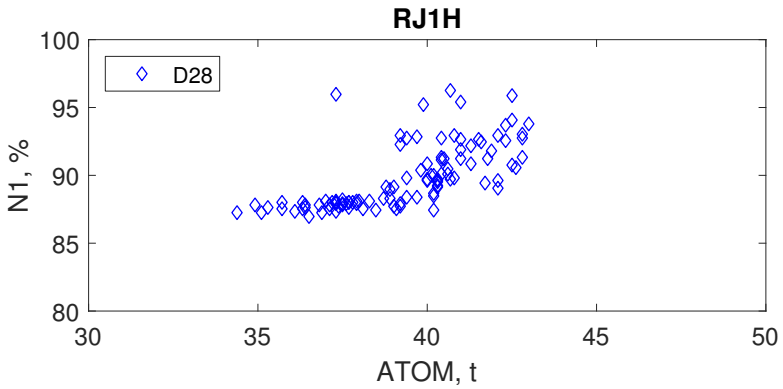

(c) RJ1H

Figure A.2: $N1$ versus ATOM for three different aircraft types with FDR data.

A.3 Model coefficients for the A333_TRENT7

3D Model

Table A.5: Airframe model 3D, Part 1: Model coefficients of the A333_TRENT7 for each mid-frequency f_m. The number of observations N and the term $\widehat{\sigma}^2_{E,afm,CR}$ for the energy correction are provided. V1.0-0436.

f_m	N	$\widehat{\sigma}^2_{E,afm,CR}$	Intercept L_{a0}	lMa a_{a1}	$l\rho$ b_{a1}	$Proc$ a_{a2}	lMa:$Proc$ a_{a3}
25.1	1181775	15.8	1.61E+02	5.57E+01	1.23E+02	−4.31E+00	−8.36E+00
31.6	1180272	14.7	1.58E+02	6.12E+01	1.13E+02	−6.54E+00	−1.07E+01
39.8	1208525	14.2	1.57E+02	6.00E+01	9.06E+01	−7.24E+00	−9.02E+00
50.1	1200809	12.8	1.54E+02	5.24E+01	7.99E+01	−6.58E+00	−6.44E+00
63.1	1198263	12.4	1.54E+02	5.26E+01	6.46E+01	−8.34E+00	−9.03E+00
79.4	1188102	11.9	1.57E+02	5.68E+01	7.20E+01	−7.98E+00	−8.51E+00
100.0	1215056	11.0	1.53E+02	4.89E+01	8.27E+01	−6.37E+00	−7.92E+00
125.9	1201690	9.6	1.57E+02	5.08E+01	8.82E+01	−5.20E+00	−5.26E+00
158.5	1206488	8.5	1.51E+02	4.23E+01	7.71E+01	−2.51E−02	5.82E+00
199.5	1218075	7.7	1.46E+02	3.65E+01	6.45E+01	4.06E+00	1.37E+01
251.2	1235149	6.8	1.46E+02	3.74E+01	6.42E+01	3.70E+00	1.17E+01
316.2	1237104	5.8	1.44E+02	3.64E+01	6.10E+01	2.76E+00	9.73E+00
398.1	1235540	5.3	1.42E+02	3.09E+01	7.35E+01	2.64E+00	9.80E+00
501.2	1226912	4.7	1.49E+02	4.34E+01	7.13E+01	2.73E−01	4.09E+00
631.0	1211575	4.2	1.51E+02	4.41E+01	7.72E+01	−1.08E−01	4.14E+00
794.3	1191238	4.1	1.47E+02	3.65E+01	9.23E+01	3.43E+00	9.13E+00
1000.0	1170815	4.0	1.50E+02	4.52E+01	1.01E+02	5.55E+00	1.18E+01
1258.9	1132839	4.0	1.50E+02	3.87E+01	7.87E+01	2.40E+00	7.29E+00
1584.9	1057370	4.1	1.53E+02	3.40E+01	1.01E+02	2.26E+00	1.07E+01
1995.3	935851	4.0	1.48E+02	3.21E+01	9.34E+01	5.82E+00	1.31E+01
2511.9	776887	4.3	1.47E+02	3.16E+01	4.17E+01	4.44E+00	1.01E+01
3162.3	591439	4.8	1.42E+02	2.61E+01	1.64E+01	8.07E+00	9.83E+00
3981.1	390483	5.5	1.63E+02	4.23E+01	−1.53E+01	−9.31E+00	−8.62E+00
5011.9	201387	5.9	1.46E+02	3.29E+01	−7.74E+01	−1.49E+01	−7.00E−01

Table A.6: Airframe model 3D, Part 2: Model coefficients of the A333_TRENT7 for each mid-frequency f_m. V1.0-0436.

$\cdots$	LG_1	SB_1	$lMa{:}Proc$	$Proc{:}FH\_1$	$Proc{:}FH\_2$	$Proc{:}FH\_3$	$Proc{:}FH\_4$
f_m	c_{a1}	c_{a2}	c_{a3}	d_{a11}	d_{a12}	d_{a13}	d_{a14}
25.1	2.07E+01	−3.55E+00	1.70E+01	5.70E+00	1.78E+00	7.27E+00	9.58E+00
31.6	1.07E+01	−1.74E+00	5.35E+00	4.83E+00	6.23E−01	4.77E+00	8.12E+00
39.8	4.71E+00	−5.63E−01	2.68E+00	1.76E+00	−1.13E+00	1.49E+00	3.90E+00
50.1	9.09E+00	−2.98E−01	1.34E+01	−1.26E+00	−2.74E+00	−9.35E−01	−7.20E−03
63.1	1.16E+01	−2.30E−01	2.07E+01	−3.98E+00	−3.89E+00	−2.41E+00	−1.64E−01
79.4	1.05E+01	−1.30E+00	1.58E+01	−3.10E+00	−1.57E+00	−2.10E−01	2.76E+00
100.0	1.93E+01	−1.47E+00	2.67E+01	−5.79E−01	1.85E+00	2.96E+00	5.33E+00
125.9	2.18E+01	−1.87E+00	2.85E+01	−1.25E+00	1.12E+00	1.57E+00	3.13E+00
158.5	2.59E+01	−1.28E+00	4.00E+01	−1.55E+00	3.38E−01	5.72E−01	−4.85E−01
199.5	2.97E+01	−4.05E−01	4.42E+01	1.34E−02	1.49E+00	1.56E+00	−1.07E+00
251.2	2.84E+01	−5.80E−01	4.07E+01	1.97E+00	3.11E+00	3.29E+00	1.01E+00
316.2	2.39E+01	−8.47E−01	3.05E+01	2.85E+00	3.98E+00	4.14E+00	1.79E+00
398.1	2.09E+01	−1.23E+00	2.74E+01	2.16E+00	3.12E+00	2.98E+00	2.23E+00
501.2	1.77E+01	−1.46E+00	2.08E+01	2.49E+00	3.68E+00	3.40E+00	4.54E+00
631.0	2.27E+01	−1.62E+00	2.98E+01	1.11E+00	2.27E+00	2.14E+00	1.22E+00
794.3	3.00E+01	−1.72E+00	4.06E+01	2.48E+00	3.50E+00	3.27E+00	6.52E−01
1000.0	2.29E+01	−2.59E+00	2.56E+01	3.84E+00	4.97E+00	5.13E+00	5.57E+00
1258.9	2.41E+01	−1.81E+00	3.28E+01	1.16E+00	1.87E+00	2.36E+00	4.05E−01
1584.9	1.92E+01	−1.63E+00	3.31E+01	−2.18E+00	−1.72E+00	−1.49E+00	−4.80E+00
1995.3	1.67E+01	−1.90E+00	2.39E+01	2.21E+00	2.00E+00	1.97E+00	−1.68E−01
2511.9	8.23E+00	−1.93E+00	1.12E+01	3.35E+00	1.20E+00	1.57E+00	−6.70E−02
3162.3	1.48E+00	−1.67E+00	−9.56E−01	8.33E+00	2.73E+00	2.77E+00	8.67E−01
3981.1	−2.30E+01	−1.46E+00	−3.88E+01	4.17E+00	−4.78E+00	−8.07E−01	−2.85E+00
5011.9	−1.87E+01	2.84E−01	−2.73E+01	4.13E+00	−9.87E+00	−7.29E−01	−6.24E+00

Table A.7: Airframe model 3D, Part 3: Model coefficients of the A333_TRENT7 for each mid-frequency f_m. V1.0-0436.

$\cdots$	$FH\_1{:}LG\_1$	$FH\_2{:}LG\_1$	$FH\_3{:}LG\_1$	$FH\_4{:}LG\_1$	$Proc{:}FH\_1$	$Proc{:}FH\_2$	$Proc{:}FH\_3/4$
f_m	d_{a21}	d_{a22}	d_{a23}	d_{a24}	d_{a31}	d_{a32}	d_{a33}, d_{a34}
25.1	−5.47E+00	−1.57E+00	−1.03E+01	−1.25E+01	−1.26E+00	2.00E+00	0.00E+00
31.6	−2.86E+00	3.49E−01	−6.10E+00	−1.01E+01	−3.51E−01	2.32E+00	0.00E+00
39.8	1.07E+00	2.99E+00	−7.80E−01	−3.91E+00	6.29E−01	3.68E+00	0.00E+00
50.1	1.87E+00	3.32E+00	1.30E+00	−7.04E−01	1.62E+00	4.21E+00	0.00E+00
63.1	3.38E+00	4.38E+00	3.35E+00	2.97E−01	2.76E+00	4.37E+00	0.00E+00
79.4	1.60E+00	1.99E+00	1.06E+00	−2.52E+00	2.72E+00	4.44E+00	0.00E+00
100.0	−1.93E+00	−1.32E+00	−1.22E+00	−4.56E+00	1.51E+00	2.98E+00	0.00E+00
125.9	−1.95E+00	−1.01E+00	−2.22E−01	−3.94E+00	1.97E+00	3.01E+00	0.00E+00
158.5	1.13E+00	1.09E+00	1.36E+00	8.86E−01	2.10E+00	3.90E+00	0.00E+00
199.5	−1.38E+00	−1.74E+00	−1.06E+00	1.01E+00	1.63E+00	4.43E+00	0.00E+00
251.2	−3.48E+00	−3.06E+00	−2.05E+00	−2.01E−01	1.05E+00	3.62E+00	0.00E+00
316.2	−4.86E+00	−4.64E+00	−3.97E+00	−2.53E+00	9.45E−01	3.29E+00	0.00E+00
398.1	−3.15E+00	−3.40E+00	−2.88E+00	−3.77E+00	1.24E+00	3.44E+00	0.00E+00
501.2	−2.25E+00	−2.80E+00	−1.95E+00	−4.28E+00	8.37E−01	2.87E+00	0.00E+00
631.0	−2.33E+00	−2.20E+00	−1.17E+00	−1.44E+00	1.58E+00	3.59E+00	0.00E+00
794.3	−3.47E+00	−3.40E+00	−2.16E+00	−9.09E−01	8.63E−01	2.92E+00	0.00E+00
1000.0	−3.78E+00	−3.99E+00	−3.66E+00	−5.48E+00	−3.16E−01	3.01E+00	0.00E+00
1258.9	−1.87E+00	−1.77E+00	−1.51E+00	−5.50E−01	1.16E+00	3.95E+00	0.00E+00
1584.9	1.48E+00	2.10E+00	2.52E+00	4.41E+00	2.78E+00	5.40E+00	0.00E+00
1995.3	−2.46E+00	−9.58E−01	−5.02E−01	−7.78E−02	0.00E+00	3.20E+00	0.00E+00
2511.9	−1.16E+00	−2.95E−01	−9.68E−02	0.00E+00	−1.04E+00	3.38E+00	0.00E+00
3162.3	3.47E−01	−6.23E−01	−5.78E−01	0.00E+00	−6.29E+00	−2.21E−02	0.00E+00
3981.1	0.00E+00	3.18E+00	−1.45E+00	0.00E+00	−1.88E+00	7.91E+00	0.00E+00
5011.9	0.00E+00	6.06E+00	0.00E+00	4.87E+00	0.00E+00	1.89E+01	0.00E+00

Table A.8: Airframe model 3D, Part 4: Model coefficients of the A333_TRENT7 for each mid-frequency f_m. V1.0-0436.

$\cdots$	SB_1	$LG\_1{:}SB\_1$	$lMa{:}SB\_1$	$\cos(\theta)$	$\cos(2\theta)$	$\sin(\theta)$	$\sin(2\theta)$
f_m	e_{a1}	e_{a2}	e_{a3}	k_a	l_a	m_a	n_a
25.1	$1.32E{+}01$	$-1.84E{+}00$	$1.64E{+}01$	$-3.10E{+}00$	$-4.24E{+}00$	$-1.17E{+}01$	$2.40E{+}00$
31.6	$1.64E{+}01$	$-1.14E{+}00$	$2.42E{+}01$	$-1.42E{+}00$	$9.50E{-}01$	$1.10E{+}00$	$5.69E{-}01$
39.8	$1.48E{+}01$	$-4.62E{-}01$	$2.35E{+}01$	$5.11E{-}01$	$2.32E{+}00$	$5.97E{+}00$	$-1.01E{+}00$
50.1	$8.37E{+}00$	$-8.79E{-}01$	$1.22E{+}01$	$8.37E{-}01$	$2.91E{+}00$	$8.21E{+}00$	$-1.36E{+}00$
63.1	$2.41E{+}00$	$-1.43E{+}00$	$2.73E{-}01$	$6.91E{-}01$	$3.02E{+}00$	$9.52E{+}00$	$-1.55E{+}00$
79.4	$2.38E{+}00$	$-1.19E{+}00$	$1.28E{-}01$	$-1.72E{-}01$	$2.18E{+}00$	$7.70E{+}00$	$-1.22E{+}00$
100.0	$-8.07E{-}01$	$-1.06E{+}00$	$-4.91E{+}00$	$-5.09E{-}01$	$1.34E{+}00$	$5.71E{+}00$	$-1.31E{+}00$
125.9	$-6.43E{+}00$	$-1.45E{+}00$	$-1.50E{+}01$	$-8.65E{-}01$	$2.40E{-}01$	$3.20E{+}00$	$-1.24E{+}00$
158.5	$-5.41E{+}00$	$-1.57E{+}00$	$-1.35E{+}01$	$-8.93E{-}01$	$1.00E{+}00$	$5.94E{+}00$	$-1.20E{+}00$
199.5	$-3.45E{+}00$	$-1.53E{+}00$	$-1.03E{+}01$	$-1.03E{+}00$	$9.48E{-}01$	$5.71E{+}00$	$-8.66E{-}01$
251.2	$-4.04E{+}00$	$-1.44E{+}00$	$-1.11E{+}01$	$-1.28E{+}00$	$8.21E{-}01$	$5.40E{+}00$	$-6.49E{-}01$
316.2	$-5.24E{+}00$	$-8.79E{-}01$	$-1.25E{+}01$	$-1.17E{+}00$	$1.14E{+}00$	$7.08E{+}00$	$-7.14E{-}01$
398.1	$-2.79E{+}00$	$-8.25E{-}01$	$-8.19E{+}00$	$-9.12E{-}01$	$1.04E{+}00$	$7.35E{+}00$	$-1.06E{+}00$
501.2	$-2.44E{+}00$	$-1.23E{+}00$	$-8.00E{+}00$	$-1.01E{+}00$	$3.02E{-}01$	$5.10E{+}00$	$-1.08E{+}00$
631.0	$-4.73E{+}00$	$-1.49E{+}00$	$-1.25E{+}01$	$-4.15E{-}01$	$2.93E{-}01$	$4.12E{+}00$	$-1.51E{+}00$
794.3	$-5.09E{+}00$	$-1.76E{+}00$	$-1.34E{+}01$	$2.20E{-}01$	$1.26E{-}01$	$2.92E{+}00$	$-1.84E{+}00$
1000.0	$-6.30E{+}00$	$-1.55E{+}00$	$-1.54E{+}01$	$5.69E{-}01$	$-1.64E{-}01$	$1.87E{+}00$	$-2.04E{+}00$
1258.9	$-8.50E{+}00$	$-1.48E{+}00$	$-1.94E{+}01$	$1.61E{+}00$	$-7.18E{-}01$	$-5.24E{-}01$	$-2.87E{+}00$
1584.9	$-8.04E{+}00$	$-1.11E{+}00$	$-1.77E{+}01$	$2.48E{+}00$	$-1.23E{+}00$	$-1.64E{+}00$	$-3.52E{+}00$
1995.3	$-1.57E{+}01$	$-5.48E{-}01$	$-3.06E{+}01$	$3.16E{+}00$	$-1.53E{+}00$	$-2.65E{+}00$	$-3.77E{+}00$
2511.9	$-2.61E{+}01$	$-3.68E{-}01$	$-4.85E{+}01$	$4.23E{+}00$	$-1.65E{+}00$	$-4.08E{+}00$	$-4.40E{+}00$
3162.3	$-2.54E{+}01$	$-8.76E{-}01$	$-4.66E{+}01$	$5.95E{+}00$	$-2.16E{+}00$	$-6.14E{+}00$	$-6.30E{+}00$
3981.1	$-2.75E{+}01$	$2.64E{-}01$	$-4.94E{+}01$	$1.04E{+}01$	$-5.94E{+}00$	$-1.70E{+}01$	$-9.82E{+}00$
5011.9	$-5.97E{+}01$	$0.00E{+}00$	$-1.01E{+}02$	$1.31E{+}01$	$3.70E{-}01$	$3.15E{+}00$	$-1.01E{+}01$

Table A.9: Engine model 3D, Part 1: Model coefficients of the A333_TRENT7 for each mid-frequency f_m. The number of observations N and the term $\widehat{\sigma}^2_{E,afm,CR}$ for the energy correction are provided. V1.0-0436.

			Intercept	Ma	$N1$	$N1^2$
f_m	N	$\widehat{\sigma}^2_{E,eng,CR}$	L_{e0}	a_{e1}	b_{e1}	b_{e2}
25.1	1181775	15.9	$1.10E{+}02$	$-3.62E{+}01$	$6.63E{-}01$	$-2.98E{-}03$
31.6	1180272	14.7	$9.00E{+}01$	$-3.09E{+}01$	$1.29E{+}00$	$-8.19E{-}03$
39.8	1208525	14.2	$8.87E{+}01$	$-3.58E{+}01$	$1.27E{+}00$	$-7.42E{-}03$
50.1	1200809	12.9	$1.01E{+}02$	$-3.59E{+}01$	$6.98E{-}01$	$-2.69E{-}03$
63.1	1198263	12.4	$1.09E{+}02$	$-3.87E{+}01$	$5.26E{-}01$	$-1.96E{-}03$
79.4	1188102	11.9	$1.11E{+}02$	$-3.50E{+}01$	$6.15E{-}01$	$-3.63E{-}03$
100.0	1215056	11.0	$1.13E{+}02$	$-2.50E{+}01$	$9.31E{-}01$	$-8.17E{-}03$
125.9	1201690	9.5	$1.21E{+}02$	$-2.61E{+}01$	$5.75E{-}01$	$-5.11E{-}03$
158.5	1206488	8.4	$1.28E{+}02$	$-2.69E{+}01$	$-1.23E{-}01$	$2.08E{-}03$
199.5	1218075	7.6	$1.23E{+}02$	$-2.54E{+}01$	$1.85E{-}01$	$-8.92E{-}04$
251.2	1235149	6.7	$1.24E{+}02$	$-2.57E{+}01$	$1.73E{-}01$	$-6.41E{-}04$
316.2	1237104	5.8	$1.26E{+}02$	$-2.63E{+}01$	$1.49E{-}01$	$-5.98E{-}04$
398.1	1235540	5.2	$1.29E{+}02$	$-2.49E{+}01$	$-7.87E{-}02$	$1.50E{-}03$
501.2	1226912	4.6	$1.31E{+}02$	$-2.41E{+}01$	$-4.13E{-}03$	$3.86E{-}04$
631.0	1211575	4.1	$1.34E{+}02$	$-2.30E{+}01$	$-1.27E{-}01$	$1.13E{-}03$
794.3	1191238	4.0	$1.38E{+}02$	$-1.64E{+}01$	$-2.76E{-}01$	$1.94E{-}03$
1000.0	1170815	3.8	$1.42E{+}02$	$-7.70E{+}00$	$-5.58E{-}01$	$4.42E{-}03$
1258.9	1132839	4.0	$1.76E{+}02$	$-6.57E{+}00$	$-1.94E{+}00$	$1.50E{-}02$
1584.9	1057370	4.0	$1.69E{+}02$	$-8.78E{+}00$	$-1.56E{+}00$	$1.17E{-}02$
1995.3	935851	3.9	$1.70E{+}02$	$-5.08E{+}00$	$-1.74E{+}00$	$1.33E{-}02$
2511.9	776887	4.3	$1.71E{+}02$	$-3.31E{+}00$	$-1.77E{+}00$	$1.36E{-}02$
3162.3	591439	4.8	$1.89E{+}02$	$-1.91E{-}01$	$-2.54E{+}00$	$2.05E{-}02$
3981.1	390483	5.4	$1.60E{+}02$	$5.67E{+}00$	$-1.11E{+}00$	$9.26E{-}03$
5011.9	201387	5.9	$1.00E{+}02$	$2.69E{+}01$	$1.12E{+}00$	$-8.60E{-}03$

Table A.10: Engine model 3D, Part 2: Model coefficients of the A333_TRENT7 for each mid-frequency f_m. V1.0-0436.

$\cdots$	$\cos(\theta)$	$\cos(2\theta)$	$\sin(\theta)$	$\sin(2\theta)$	$\sin(\varphi)$	$\sin(2\varphi)$
f_m	$k_{e,1}$	$l_{e,1}$	$m_{e,1}$	$n_{e,1}$	$o_{e,1}$	$p_{e,1}$
25.1	$-3.79E{+}00$	$7.33E{+}00$	$1.70E{+}01$	$1.44E{+}01$	$-3.68E{+}00$	$-4.66E{+}00$
31.6	$2.15E{+}01$	$1.20E{+}01$	$3.81E{+}01$	$-3.51E{+}00$	$4.22E{-}01$	$-8.37E{-}01$
39.8	$2.83E{+}01$	$1.43E{+}01$	$4.17E{+}01$	$-9.92E{+}00$	$-3.06E{+}00$	$4.59E{+}00$
50.1	$2.02E{+}01$	$9.40E{+}00$	$2.69E{+}01$	$-4.63E{+}00$	$-7.54E{+}00$	$6.02E{+}00$
63.1	$1.86E{+}01$	$4.95E{+}00$	$1.77E{+}01$	$-3.24E{+}00$	$-1.16E{+}01$	$7.96E{+}00$
79.4	$1.35E{+}01$	$5.02E{+}00$	$1.74E{+}01$	$-1.61E{+}00$	$-5.77E{+}00$	$2.64E{+}00$
100.0	$7.40E{+}00$	$8.26E{+}00$	$2.01E{+}01$	$1.75E{-}01$	$-2.12E{+}00$	$-2.40E{+}00$
125.9	$5.35E{+}00$	$6.36E{+}00$	$1.32E{+}01$	$8.61E{-}01$	$-8.04E{+}00$	$1.09E{+}00$
158.5	$3.90E{+}00$	$6.52E{-}01$	$1.23E{+}00$	$-2.90E{-}01$	$-1.19E{+}01$	$4.97E{+}00$
199.5	$4.06E{+}00$	$3.28E{+}00$	$5.92E{+}00$	$-2.62E{+}00$	$-1.48E{+}01$	$8.95E{+}00$
251.2	$1.78E{+}00$	$5.08E{+}00$	$8.18E{+}00$	$-2.05E{+}00$	$-1.17E{+}01$	$5.79E{+}00$
316.2	$-2.35E{+}00$	$5.07E{+}00$	$7.15E{+}00$	$1.43E{-}01$	$-7.01E{+}00$	$3.39E{+}00$
398.1	$-4.01E{+}00$	$3.10E{+}00$	$2.55E{+}00$	$3.64E{-}01$	$-9.94E{+}00$	$6.84E{+}00$
501.2	$-7.04E{+}00$	$3.29E{+}00$	$-4.72E{-}01$	$2.44E{+}00$	$-7.38E{+}00$	$4.10E{+}00$
631.0	$-8.27E{+}00$	$-1.18E{-}01$	$-8.18E{+}00$	$2.87E{+}00$	$-8.58E{+}00$	$4.67E{+}00$
794.3	$-8.75E{+}00$	$-4.15E{+}00$	$-1.73E{+}01$	$2.91E{+}00$	$-8.88E{+}00$	$5.02E{+}00$
1000.0	$-1.37E{+}01$	$-8.68E{+}00$	$-2.60E{+}01$	$4.83E{+}00$	$-1.04E{+}01$	$6.76E{+}00$
1258.9	$-1.62E{+}01$	$-3.15E{+}01$	$-8.30E{+}01$	$3.12E{+}00$	$-1.25E{+}01$	$6.11E{+}00$
1584.9	$-1.77E{+}01$	$-2.63E{+}01$	$-7.21E{+}01$	$4.77E{+}00$	$-1.12E{+}01$	$6.44E{+}00$
1995.3	$-1.71E{+}01$	$-2.74E{+}01$	$-7.75E{+}01$	$4.21E{+}00$	$-1.19E{+}01$	$7.15E{+}00$
2511.9	$-2.70E{+}01$	$-2.60E{+}01$	$-8.20E{+}01$	$1.19E{+}01$	$-1.26E{+}01$	$7.74E{+}00$
3162.3	$-2.88E{+}01$	$-3.30E{+}01$	$-1.10E{+}02$	$1.00E{+}01$	$-1.06E{+}01$	$8.06E{+}00$
3981.1	$-2.14E{+}01$	$-1.30E{+}01$	$-6.84E{+}01$	$1.75E{+}00$	$-1.14E{+}01$	$9.00E{+}00$
5011.9	$-1.94E{+}01$	$1.40E{+}01$	$1.16E{+}01$	$-6.29E{-}01$	$-5.88E{+}00$	$3.14E{+}00$

Table A.11: Engine model 3D, Part 3: Model coefficients of the A333_TRENT7 for each mid-frequency f_m. V1.0-0436.

$\cdots$	$\cos(\theta)$:$N1$	$\cos(2\theta)$:$N1$	$\sin(\theta)$:$N1$	$\sin(2\theta)$:$N1$	$\sin(\varphi)$:$N1$	$\sin(2\varphi)$:$N1$
f_m	$k_{e,2}$	$l_{e,2}$	$m_{e,2}$	$n_{e,2}$	$o_{e,2}$	$p_{e,2}$
25.1	$2.95E{-}01$	$-3.42E{-}01$	$-7.85E{-}01$	$-5.25E{-}01$	$-7.17E{-}02$	$1.14E{-}01$
31.6	$-7.14E{-}01$	$-5.39E{-}01$	$-1.61E{+}00$	$2.09E{-}01$	$-1.01E{-}01$	$6.31E{-}02$
39.8	$-1.01E{+}00$	$-5.85E{-}01$	$-1.63E{+}00$	$4.96E{-}01$	$-5.20E{-}02$	$-1.52E{-}03$
50.1	$-6.14E{-}01$	$-3.15E{-}01$	$-8.86E{-}01$	$2.19E{-}01$	$1.47E{-}02$	$-1.74E{-}02$
63.1	$-5.09E{-}01$	$-2.06E{-}01$	$-6.88E{-}01$	$1.19E{-}01$	$6.03E{-}02$	$-3.38E{-}02$
79.4	$-3.86E{-}01$	$-2.95E{-}01$	$-8.84E{-}01$	$1.36E{-}01$	$-6.05E{-}03$	$3.05E{-}02$
100.0	$-1.84E{-}01$	$-6.80E{-}01$	$-1.60E{+}00$	$6.14E{-}02$	$-3.02E{-}02$	$7.37E{-}02$
125.9	$-1.32E{-}01$	$-5.30E{-}01$	$-1.14E{+}00$	$-1.64E{-}02$	$5.69E{-}02$	$2.88E{-}02$
158.5	$-1.37E{-}01$	$-1.18E{-}02$	$-1.56E{-}02$	$5.84E{-}02$	$1.15E{-}01$	$-2.71E{-}02$
199.5	$-2.13E{-}01$	$-1.82E{-}01$	$-4.26E{-}01$	$2.12E{-}01$	$1.47E{-}01$	$-7.27E{-}02$
251.2	$-2.02E{-}01$	$-2.36E{-}01$	$-4.90E{-}01$	$2.76E{-}01$	$1.08E{-}01$	$-3.18E{-}02$
316.2	$2.42E{-}02$	$-3.05E{-}01$	$-4.94E{-}01$	$1.18E{-}01$	$5.69E{-}02$	$-3.68E{-}03$
398.1	$1.15E{-}01$	$-1.78E{-}01$	$-1.65E{-}01$	$7.54E{-}02$	$9.46E{-}02$	$-4.48E{-}02$
501.2	$2.50E{-}01$	$-2.99E{-}01$	$-3.06E{-}01$	$-1.56E{-}02$	$6.61E{-}02$	$-1.11E{-}02$
631.0	$3.46E{-}01$	$-1.38E{-}01$	$-2.15E{-}02$	$-6.92E{-}02$	$7.94E{-}02$	$-1.46E{-}02$
794.3	$4.51E{-}01$	$1.63E{-}02$	$2.43E{-}01$	$-1.19E{-}01$	$8.75E{-}02$	$-2.18E{-}02$
1000.0	$6.65E{-}01$	$2.54E{-}01$	$6.84E{-}01$	$-2.05E{-}01$	$1.10E{-}01$	$-4.92E{-}02$
1258.9	$7.87E{-}01$	$1.18E{+}00$	$2.99E{+}00$	$-1.62E{-}01$	$1.35E{-}01$	$-3.52E{-}02$
1584.9	$9.68E{-}01$	$8.74E{-}01$	$2.36E{+}00$	$-3.37E{-}01$	$1.24E{-}01$	$-4.24E{-}02$
1995.3	$1.03E{+}00$	$9.76E{-}01$	$2.68E{+}00$	$-3.89E{-}01$	$1.33E{-}01$	$-5.02E{-}02$
2511.9	$1.45E{+}00$	$9.01E{-}01$	$2.84E{+}00$	$-7.14E{-}01$	$1.38E{-}01$	$-5.41E{-}02$
3162.3	$1.56E{+}00$	$1.15E{+}00$	$3.96E{+}00$	$-6.89E{-}01$	$1.13E{-}01$	$-5.63E{-}02$
3981.1	$1.37E{+}00$	$1.92E{-}01$	$1.92E{+}00$	$-4.72E{-}01$	$1.15E{-}01$	$-6.55E{-}02$
5011.9	$1.30E{+}00$	$-8.26E{-}01$	$-1.19E{+}00$	$-3.56E{-}01$	$4.49E{-}02$	$6.11E{-}03$

Table A.12: Engine model 3D, Part 4: Model coefficients of the A333_TRENT7 for each mid-frequency f_m. V1.0-0436.

$\cdots$	$\cos(\theta)$:$N1^2$	$\cos(2\theta)$:$N1^2$	$\sin(\theta)$:$N1^2$	$\sin(2\theta)$:$N1^2$
f_m	$k_{e,3}$	$l_{e,3}$	$m_{e,3}$	$n_{e,3}$
25.1	$-4.64E{-}03$	$3.62E{-}03$	$7.87E{-}03$	$4.13E{-}03$
31.6	$3.71E{-}03$	$5.75E{-}03$	$1.55E{-}02$	$-2.05E{-}03$
39.8	$6.30E{-}03$	$6.00E{-}03$	$1.54E{-}02$	$-4.64E{-}03$
50.1	$2.95E{-}03$	$3.55E{-}03$	$8.92E{-}03$	$-2.15E{-}03$
63.1	$1.92E{-}03$	$2.95E{-}03$	$8.31E{-}03$	$-1.02E{-}03$
79.4	$1.49E{-}03$	$4.00E{-}03$	$1.10E{-}02$	$-1.64E{-}03$
100.0	$3.02E{-}04$	$8.00E{-}03$	$1.92E{-}02$	$-1.23E{-}03$
125.9	$2.04E{-}04$	$6.39E{-}03$	$1.48E{-}02$	$-5.19E{-}04$
158.5	$6.37E{-}04$	$1.05E{-}03$	$3.26E{-}03$	$-1.25E{-}03$
199.5	$1.60E{-}03$	$2.55E{-}03$	$7.23E{-}03$	$-2.63E{-}03$
251.2	$1.96E{-}03$	$2.65E{-}03$	$7.17E{-}03$	$-3.46E{-}03$
316.2	$3.58E{-}05$	$3.33E{-}03$	$7.19E{-}03$	$-1.94E{-}03$
398.1	$-6.10E{-}04$	$2.06E{-}03$	$3.97E{-}03$	$-1.55E{-}03$
501.2	$-1.62E{-}03$	$3.36E{-}03$	$5.92E{-}03$	$-8.42E{-}04$
631.0	$-2.48E{-}03$	$2.02E{-}03$	$3.91E{-}03$	$-3.13E{-}04$
794.3	$-3.65E{-}03$	$8.27E{-}04$	$2.20E{-}03$	$2.85E{-}04$
1000.0	$-5.47E{-}03$	$-1.30E{-}03$	$-1.70E{-}03$	$1.06E{-}03$
1258.9	$-6.40E{-}03$	$-8.51E{-}03$	$-1.96E{-}02$	$8.04E{-}04$
1584.9	$-8.21E{-}03$	$-5.66E{-}03$	$-1.39E{-}02$	$2.63E{-}03$
1995.3	$-9.32E{-}03$	$-6.81E{-}03$	$-1.70E{-}02$	$3.55E{-}03$
2511.9	$-1.28E{-}02$	$-6.32E{-}03$	$-1.84E{-}02$	$6.20E{-}03$
3162.3	$-1.36E{-}02$	$-8.64E{-}03$	$-2.85E{-}02$	$6.00E{-}03$
3981.1	$-1.21E{-}02$	$-1.05E{-}03$	$-1.29E{-}02$	$4.45E{-}03$
5011.9	$-1.15E{-}02$	$6.69E{-}03$	$1.14E{-}02$	$3.36E{-}03$

3Dred Model

Table A.13: Airframe model 3Dred, Part 1: Model coefficients of the A333_TRENT7 for each mid-frequency f_m. The number of observations N and the term $\widehat{\sigma}^2_{E,afm,CR}$ for the energy correction are provided. V1.0-0436

f_m	N	$\widehat{\sigma}^2_{E,afm,CR}$	Intercept L_{a0}	lMa a_{a1}	$l\rho$ b_{a1}	$Proc$ a_{a2}	$lMa{:}Proc$ a_{a3}
25.1	1181775	15.8	$1.83E{+}02$	$7.58E{+}01$	$1.93E{+}02$	$-1.32E{+}01$	$-2.46E{+}01$
31.6	1180272	14.7	$1.78E{+}02$	$7.88E{+}01$	$1.89E{+}02$	$-1.23E{+}01$	$-2.28E{+}01$
39.8	1208525	14.2	$1.71E{+}02$	$7.34E{+}01$	$1.68E{+}02$	$-1.35E{+}01$	$-2.49E{+}01$
50.1	1200809	12.8	$1.67E{+}02$	$6.91E{+}01$	$1.43E{+}02$	$-1.49E{+}01$	$-2.76E{+}01$
63.1	1198263	12.4	$1.65E{+}02$	$6.83E{+}01$	$1.24E{+}02$	$-1.60E{+}01$	$-2.94E{+}01$
79.4	1188102	11.9	$1.65E{+}02$	$6.63E{+}01$	$1.17E{+}02$	$-1.56E{+}01$	$-2.87E{+}01$
100.0	1215056	11.0	$1.65E{+}02$	$6.11E{+}01$	$1.11E{+}02$	$-1.56E{+}01$	$-2.85E{+}01$
125.9	1201690	9.6	$1.70E{+}02$	$6.48E{+}01$	$1.28E{+}02$	$-1.61E{+}01$	$-2.92E{+}01$
158.5	1206488	8.5	$1.71E{+}02$	$6.93E{+}01$	$1.20E{+}02$	$-1.73E{+}01$	$-3.13E{+}01$
199.5	1218075	7.7	$1.69E{+}02$	$6.70E{+}01$	$1.07E{+}02$	$-1.73E{+}01$	$-3.16E{+}01$
251.2	1235149	6.8	$1.67E{+}02$	$6.29E{+}01$	$1.02E{+}02$	$-1.73E{+}01$	$-3.14E{+}01$
316.2	1237104	5.8	$1.63E{+}02$	$5.81E{+}01$	$8.66E{+}01$	$-1.71E{+}01$	$-3.10E{+}01$
398.1	1235540	5.3	$1.62E{+}02$	$5.68E{+}01$	$8.89E{+}01$	$-1.68E{+}01$	$-3.04E{+}01$
501.2	1226912	4.7	$1.65E{+}02$	$5.90E{+}01$	$1.06E{+}02$	$-1.63E{+}01$	$-2.96E{+}01$
631.0	1211575	4.2	$1.67E{+}02$	$6.28E{+}01$	$1.17E{+}02$	$-1.57E{+}01$	$-2.88E{+}01$
794.3	1191238	4.1	$1.69E{+}02$	$6.37E{+}01$	$1.30E{+}02$	$-1.41E{+}01$	$-2.59E{+}01$
1000.0	1170815	4.0	$1.68E{+}02$	$6.11E{+}01$	$1.41E{+}02$	$-1.20E{+}01$	$-2.25E{+}01$
1258.9	1132839	4.0	$1.66E{+}02$	$5.79E{+}01$	$1.14E{+}02$	$-1.30E{+}01$	$-2.51E{+}01$
1584.9	1057370	4.1	$1.67E{+}02$	$5.97E{+}01$	$1.22E{+}02$	$-1.18E{+}01$	$-2.23E{+}01$
1995.3	935851	4.0	$1.61E{+}02$	$5.19E{+}01$	$1.04E{+}02$	$-1.01E{+}01$	$-1.95E{+}01$
2511.9	776887	4.3	$1.54E{+}02$	$4.26E{+}01$	$5.34E{+}01$	$-1.01E{+}01$	$-1.98E{+}01$
3162.3	591439	4.8	$1.50E{+}02$	$3.44E{+}01$	$3.71E{+}01$	$-9.05E{+}00$	$-1.81E{+}01$
3981.1	390483	5.5	$1.43E{+}02$	$1.27E{+}01$	$-3.65E{+}00$	$-7.93E{+}00$	$-1.68E{+}01$
5011.9	201387	5.9	$1.26E{+}02$	$4.59E{+}00$	$-5.36E{+}01$	$-1.38E{+}01$	$-2.62E{+}01$

Table A.14: Airframe model 3Dred, Part 2: Model coefficients of the A333_TRENT7 for each mid-frequency f_m. V1.0-0436.

$\cdots$	$\cos(\theta)$	$\cos(2\theta)$	$\sin(\theta)$	$\sin(2\theta)$
f_m	k_a	l_a	m_a	n_a
25.1	$-3.58E{+}00$	$-4.65E{+}00$	$-1.33E{+}01$	$2.23E{+}00$
31.6	$-1.86E{+}00$	$2.20E{-}01$	$-1.27E{+}00$	$5.16E{-}01$
39.8	$1.52E{-}01$	$1.70E{+}00$	$4.07E{+}00$	$-9.70E{-}01$
50.1	$5.47E{-}01$	$2.51E{+}00$	$6.91E{+}00$	$-1.28E{+}00$
63.1	$3.44E{-}01$	$2.70E{+}00$	$8.36E{+}00$	$-1.36E{+}00$
79.4	$-5.14E{-}01$	$2.12E{+}00$	$7.30E{+}00$	$-1.10E{+}00$
100.0	$-8.65E{-}01$	$1.25E{+}00$	$5.25E{+}00$	$-1.30E{+}00$
125.9	$-1.37E{+}00$	$1.90E{-}02$	$2.22E{+}00$	$-1.12E{+}00$
158.5	$-1.39E{+}00$	$7.77E{-}01$	$4.89E{+}00$	$-1.09E{+}00$
199.5	$-1.35E{+}00$	$7.24E{-}01$	$4.80E{+}00$	$-8.28E{-}01$
251.2	$-1.52E{+}00$	$6.28E{-}01$	$4.69E{+}00$	$-6.36E{-}01$
316.2	$-1.32E{+}00$	$9.70E{-}01$	$6.52E{+}00$	$-7.45E{-}01$
398.1	$-1.04E{+}00$	$9.08E{-}01$	$6.92E{+}00$	$-1.09E{+}00$
501.2	$-1.10E{+}00$	$1.43E{-}01$	$4.60E{+}00$	$-1.09E{+}00$
631.0	$-4.79E{-}01$	$1.05E{-}01$	$3.49E{+}00$	$-1.53E{+}00$
794.3	$1.80E{-}01$	$-6.30E{-}02$	$2.29E{+}00$	$-1.90E{+}00$
1000.0	$4.78E{-}01$	$-1.55E{-}01$	$1.71E{+}00$	$-2.04E{+}00$
1258.9	$1.61E{+}00$	$-4.85E{-}01$	$-2.79E{-}01$	$-2.89E{+}00$
1584.9	$2.55E{+}00$	$-7.68E{-}01$	$-8.76E{-}01$	$-3.54E{+}00$
1995.3	$3.21E{+}00$	$-9.17E{-}01$	$-1.42E{+}00$	$-3.75E{+}00$
2511.9	$4.21E{+}00$	$-9.77E{-}01$	$-2.55E{+}00$	$-4.33E{+}00$
3162.3	$5.83E{+}00$	$-1.64E{+}00$	$-4.95E{+}00$	$-6.17E{+}00$
3981.1	$1.03E{+}01$	$-5.51E{+}00$	$-1.59E{+}01$	$-9.59E{+}00$
5011.9	$1.31E{+}01$	$2.41E{-}01$	$2.89E{+}00$	$-1.01E{+}01$

Table A.15: Engine model 3Dred, Part 1: Model coefficients of the A333_TRENT7 for each mid-frequency f_m. The number of observations N and the term $\widehat{\sigma}^2_{E,afm,CR}$ for the energy correction are provided. V1.0-0436.

			Intercept	Ma	$N1$	$N1^2$
f_m	N	$\widehat{\sigma}^2_{E,eng,CR}$	L_{e0}	a_{e1}	b_{e1}	b_{e2}
25.1	1181775	15.9	$1.23E{+}02$	$-4.24E{+}01$	$2.22E{-}01$	$6.56E{-}04$
31.6	1180272	14.7	$9.83E{+}01$	$-3.65E{+}01$	$1.02E{+}00$	$-5.94E{-}03$
39.8	1208525	14.2	$9.36E{+}01$	$-3.86E{+}01$	$1.10E{+}00$	$-6.09E{-}03$
50.1	1200809	12.9	$1.05E{+}02$	$-3.62E{+}01$	$5.46E{-}01$	$-1.48E{-}03$
63.1	1198263	12.4	$1.13E{+}02$	$-3.70E{+}01$	$3.74E{-}01$	$-8.03E{-}04$
79.4	1188102	11.9	$1.15E{+}02$	$-3.63E{+}01$	$4.63E{-}01$	$-2.49E{-}03$
100.0	1215056	11.0	$1.19E{+}02$	$-2.98E{+}01$	$7.40E{-}01$	$-6.67E{-}03$
125.9	1201690	9.5	$1.31E{+}02$	$-3.03E{+}01$	$2.07E{-}01$	$-2.16E{-}03$
158.5	1206488	8.4	$1.39E{+}02$	$-3.17E{+}01$	$-5.18E{-}01$	$5.28E{-}03$
199.5	1218075	7.6	$1.32E{+}02$	$-3.12E{+}01$	$-8.56E{-}02$	$1.23E{-}03$
251.2	1235149	6.7	$1.33E{+}02$	$-3.22E{+}01$	$-8.54E{-}02$	$1.36E{-}03$
316.2	1237104	5.8	$1.35E{+}02$	$-3.49E{+}01$	$-1.01E{-}01$	$1.37E{-}03$
398.1	1235540	5.2	$1.38E{+}02$	$-3.46E{+}01$	$-3.21E{-}01$	$3.43E{-}03$
501.2	1226912	4.6	$1.39E{+}02$	$-3.07E{+}01$	$-2.35E{-}01$	$2.13E{-}03$
631.0	1211575	4.1	$1.43E{+}02$	$-2.92E{+}01$	$-4.01E{-}01$	$3.16E{-}03$
794.3	1191238	4.0	$1.48E{+}02$	$-2.37E{+}01$	$-5.73E{-}01$	$4.16E{-}03$
1000.0	1170815	3.8	$1.50E{+}02$	$-1.17E{+}01$	$-8.43E{-}01$	$6.49E{-}03$
1258.9	1132839	4.0	$1.85E{+}02$	$-9.07E{+}00$	$-2.24E{+}00$	$1.72E{-}02$
1584.9	1057370	4.0	$1.75E{+}02$	$-1.08E{+}01$	$-1.77E{+}00$	$1.33E{-}02$
1995.3	935851	3.9	$1.75E{+}02$	$-7.19E{+}00$	$-1.89E{+}00$	$1.45E{-}02$
2511.9	776887	4.3	$1.73E{+}02$	$-3.52E{+}00$	$-1.82E{+}00$	$1.39E{-}02$
3162.3	591439	4.8	$1.90E{+}02$	$1.74E{+}00$	$-2.57E{+}00$	$2.06E{-}02$
3981.1	390483	5.4	$1.62E{+}02$	$8.67E{+}00$	$-1.18E{+}00$	$9.63E{-}03$
5011.9	201387	5.9	$9.97E{+}01$	$2.86E{+}01$	$1.13E{+}00$	$-8.79E{-}03$

Table A.16: Engine model 3Dred, Part 2: Model coefficients of the A333_TRENT7 for each mid-frequency f_m. V1.0-0436.

$\cdots$	$\cos(\theta)$	$\cos(2\theta)$	$\sin(\theta)$	$\sin(2\theta)$	$\sin(\varphi)$	$\sin(2\varphi)$
f_m	$k_{e,1}$	$l_{e,1}$	$m_{e,1}$	$n_{e,1}$	$o_{e,1}$	$p_{e,1}$
25.1	$-5.55E{+}00$	$3.20E{+}00$	$4.36E{+}00$	$1.73E{+}01$	$-4.78E{+}00$	$-5.94E{+}00$
31.6	$2.04E{+}01$	$9.22E{+}00$	$3.01E{+}01$	$-1.18E{+}00$	$-1.38E{-}01$	$-1.60E{+}00$
39.8	$2.77E{+}01$	$1.25E{+}01$	$3.66E{+}01$	$-8.54E{+}00$	$-3.26E{+}00$	$3.97E{+}00$
50.1	$1.94E{+}01$	$7.99E{+}00$	$2.24E{+}01$	$-3.82E{+}00$	$-8.20E{+}00$	$5.43E{+}00$
63.1	$1.74E{+}01$	$3.87E{+}00$	$1.33E{+}01$	$-2.48E{+}00$	$-1.26E{+}01$	$7.56E{+}00$
79.4	$1.29E{+}01$	$3.98E{+}00$	$1.35E{+}01$	$-8.44E{-}01$	$-6.74E{+}00$	$2.27E{+}00$
100.0	$6.68E{+}00$	$7.44E{+}00$	$1.65E{+}01$	$1.41E{+}00$	$-3.85E{+}00$	$-2.65E{+}00$
125.9	$3.36E{+}00$	$3.66E{+}00$	$3.79E{+}00$	$2.89E{+}00$	$-1.07E{+}01$	$7.71E{-}01$
158.5	$1.88E{+}00$	$-2.70E{+}00$	$-9.34E{+}00$	$1.65E{+}00$	$-1.45E{+}01$	$4.57E{+}00$
199.5	$2.79E{+}00$	$1.18E{+}00$	$-9.93E{-}01$	$-1.32E{+}00$	$-1.68E{+}01$	$8.87E{+}00$
251.2	$6.49E{-}01$	$3.20E{+}00$	$1.55E{+}00$	$-1.10E{+}00$	$-1.35E{+}01$	$5.90E{+}00$
316.2	$-3.90E{+}00$	$3.64E{+}00$	$1.31E{+}00$	$1.35E{+}00$	$-8.66E{+}00$	$3.51E{+}00$
398.1	$-5.93E{+}00$	$1.91E{+}00$	$-2.75E{+}00$	$1.72E{+}00$	$-1.16E{+}01$	$6.92E{+}00$
501.2	$-9.04E{+}00$	$2.01E{+}00$	$-6.51E{+}00$	$3.85E{+}00$	$-8.67E{+}00$	$4.04E{+}00$
631.0	$-1.06E{+}01$	$-1.77E{+}00$	$-1.56E{+}01$	$4.30E{+}00$	$-1.04E{+}01$	$4.62E{+}00$
794.3	$-1.14E{+}01$	$-5.81E{+}00$	$-2.49E{+}01$	$4.49E{+}00$	$-1.11E{+}01$	$5.05E{+}00$
1000.0	$-1.60E{+}01$	$-1.09E{+}01$	$-3.46E{+}01$	$6.15E{+}00$	$-1.23E{+}01$	$6.63E{+}00$
1258.9	$-1.80E{+}01$	$-3.44E{+}01$	$-9.30E{+}01$	$3.90E{+}00$	$-1.44E{+}01$	$5.90E{+}00$
1584.9	$-1.92E{+}01$	$-2.80E{+}01$	$-7.86E{+}01$	$5.44E{+}00$	$-1.27E{+}01$	$6.20E{+}00$
1995.3	$-1.79E{+}01$	$-2.85E{+}01$	$-8.20E{+}01$	$4.56E{+}00$	$-1.34E{+}01$	$7.00E{+}00$
2511.9	$-2.71E{+}01$	$-2.62E{+}01$	$-8.35E{+}01$	$1.19E{+}01$	$-1.34E{+}01$	$7.68E{+}00$
3162.3	$-2.90E{+}01$	$-3.38E{+}01$	$-1.12E{+}02$	$1.04E{+}01$	$-1.07E{+}01$	$7.99E{+}00$
3981.1	$-2.15E{+}01$	$-1.45E{+}01$	$-7.23E{+}01$	$1.95E{+}00$	$-1.13E{+}01$	$8.77E{+}00$
5011.9	$-2.01E{+}01$	$1.41E{+}01$	$1.21E{+}01$	$-3.34E{-}01$	$-6.01E{+}00$	$3.48E{+}00$

Table A.17: Engine model 3Dred, Part 3: Model coefficients of the A333_TRENT7 for each mid-frequency f_m. V1.0-0436.

$\cdots$	$\cos(\theta)$:$N1$	$\cos(2\theta)$:$N1$	$\sin(\theta)$:$N1$	$\sin(2\theta)$:$N1$	$\sin(\varphi)$:$N1$	$\sin(2\varphi)$:$N1$
f_m	$k_{e,2}$	$l_{e,2}$	$m_{e,2}$	$n_{e,2}$	$o_{e,2}$	$p_{e,2}$
25.1	$3.84E{-}01$	$-1.57E{-}01$	$-2.24E{-}01$	$-6.37E{-}01$	$-5.89E{-}02$	$1.33E{-}01$
31.6	$-6.62E{-}01$	$-4.18E{-}01$	$-1.26E{+}00$	$1.24E{-}01$	$-9.44E{-}02$	$7.62E{-}02$
39.8	$-9.72E{-}01$	$-5.08E{-}01$	$-1.41E{+}00$	$4.45E{-}01$	$-4.92E{-}02$	$6.99E{-}03$
50.1	$-5.78E{-}01$	$-2.52E{-}01$	$-6.90E{-}01$	$1.88E{-}01$	$2.40E{-}02$	$-1.17E{-}02$
63.1	$-4.54E{-}01$	$-1.61E{-}01$	$-5.10E{-}01$	$8.63E{-}02$	$7.46E{-}02$	$-3.22E{-}02$
79.4	$-3.55E{-}01$	$-2.54E{-}01$	$-7.27E{-}01$	$1.06E{-}01$	$4.76E{-}03$	$3.55E{-}02$
100.0	$-1.45E{-}01$	$-6.44E{-}01$	$-1.44E{+}00$	$1.54E{-}02$	$-1.15E{-}02$	$8.03E{-}02$
125.9	$-4.01E{-}02$	$-4.10E{-}01$	$-7.18E{-}01$	$-9.66E{-}02$	$8.92E{-}02$	$3.47E{-}02$
158.5	$-4.86E{-}02$	$1.37E{-}01$	$4.56E{-}01$	$-1.63E{-}02$	$1.47E{-}01$	$-2.07E{-}02$
199.5	$-1.58E{-}01$	$-9.13E{-}02$	$-1.27E{-}01$	$1.65E{-}01$	$1.70E{-}01$	$-6.92E{-}02$
251.2	$-1.56E{-}01$	$-1.57E{-}01$	$-2.13E{-}01$	$2.44E{-}01$	$1.28E{-}01$	$-2.98E{-}02$
316.2	$8.72E{-}02$	$-2.40E{-}01$	$-2.38E{-}01$	$7.55E{-}02$	$7.54E{-}02$	$-1.12E{-}03$
398.1	$1.91E{-}01$	$-1.20E{-}01$	$7.64E{-}02$	$2.62E{-}02$	$1.14E{-}01$	$-4.18E{-}02$
501.2	$3.27E{-}01$	$-2.43E{-}01$	$-5.48E{-}02$	$-6.63E{-}02$	$8.12E{-}02$	$-7.94E{-}03$
631.0	$4.35E{-}01$	$-6.81E{-}02$	$2.81E{-}01$	$-1.21E{-}01$	$1.01E{-}01$	$-1.14E{-}02$
794.3	$5.56E{-}01$	$8.96E{-}02$	$5.61E{-}01$	$-1.77E{-}01$	$1.14E{-}01$	$-1.89E{-}02$
1000.0	$7.57E{-}01$	$3.44E{-}01$	$1.02E{+}00$	$-2.54E{-}01$	$1.33E{-}01$	$-4.64E{-}02$
1258.9	$8.60E{-}01$	$1.29E{+}00$	$3.37E{+}00$	$-1.93E{-}01$	$1.58E{-}01$	$-3.22E{-}02$
1584.9	$1.03E{+}00$	$9.35E{-}01$	$2.61E{+}00$	$-3.66E{-}01$	$1.42E{-}01$	$-3.92E{-}02$
1995.3	$1.07E{+}00$	$1.02E{+}00$	$2.85E{+}00$	$-4.07E{-}01$	$1.50E{-}01$	$-4.82E{-}02$
2511.9	$1.46E{+}00$	$9.04E{-}01$	$2.89E{+}00$	$-7.20E{-}01$	$1.48E{-}01$	$-5.33E{-}02$
3162.3	$1.57E{+}00$	$1.18E{+}00$	$4.03E{+}00$	$-7.05E{-}01$	$1.14E{-}01$	$-5.54E{-}02$
3981.1	$1.37E{+}00$	$2.38E{-}01$	$2.04E{+}00$	$-4.80E{-}01$	$1.15E{-}01$	$-6.31E{-}02$
5011.9	$1.33E{+}00$	$-8.28E{-}01$	$-1.21E{+}00$	$-3.67E{-}01$	$4.84E{-}02$	$1.77E{-}03$

Table A.18: Engine model 3Dred, Part 4: Model coefficients of the A333_TRENT7 for each mid-frequency f_m. V1.0-0436.

$\cdots$ f_m	$\cos(\theta)$:$N1^2$ $k_{e,3}$	$\cos(2\theta)$:$N1^2$ $l_{e,3}$	$\sin(\theta)$:$N1^2$ $m_{e,3}$	$\sin(2\theta)$:$N1^2$ $n_{e,3}$
25.1	$-5.48E{-}03$	$1.98E{-}03$	$3.00E{-}03$	$4.98E{-}03$
31.6	$3.21E{-}03$	$4.68E{-}03$	$1.25E{-}02$	$-1.42E{-}03$
39.8	$5.95E{-}03$	$5.33E{-}03$	$1.35E{-}02$	$-4.25E{-}03$
50.1	$2.61E{-}03$	$2.99E{-}03$	$7.23E{-}03$	$-1.90E{-}03$
63.1	$1.42E{-}03$	$2.58E{-}03$	$6.86E{-}03$	$-7.38E{-}04$
79.4	$1.18E{-}03$	$3.66E{-}03$	$9.77E{-}03$	$-1.40E{-}03$
100.0	$-8.02E{-}05$	$7.69E{-}03$	$1.79E{-}02$	$-8.82E{-}04$
125.9	$-6.25E{-}04$	$5.37E{-}03$	$1.12E{-}02$	$1.13E{-}04$
158.5	$-1.37E{-}04$	$-2.27E{-}04$	$-7.57E{-}04$	$-6.75E{-}04$
199.5	$1.13E{-}03$	$1.80E{-}03$	$4.77E{-}03$	$-2.29E{-}03$
251.2	$1.56E{-}03$	$2.00E{-}03$	$4.94E{-}03$	$-3.25E{-}03$
316.2	$-4.66E{-}04$	$2.78E{-}03$	$5.10E{-}03$	$-1.64E{-}03$
398.1	$-1.20E{-}03$	$1.56E{-}03$	$1.97E{-}03$	$-1.20E{-}03$
501.2	$-2.21E{-}03$	$2.91E{-}03$	$3.96E{-}03$	$-4.90E{-}04$
631.0	$-3.16E{-}03$	$1.47E{-}03$	$1.59E{-}03$	$4.60E{-}05$
794.3	$-4.47E{-}03$	$2.40E{-}04$	$-2.59E{-}04$	$7.02E{-}04$
1000.0	$-6.20E{-}03$	$-2.00E{-}03$	$-4.24E{-}03$	$1.42E{-}03$
1258.9	$-6.98E{-}03$	$-9.33E{-}03$	$-2.25E{-}02$	$1.03E{-}03$
1584.9	$-8.76E{-}03$	$-6.11E{-}03$	$-1.58E{-}02$	$2.87E{-}03$
1995.3	$-9.68E{-}03$	$-7.11E{-}03$	$-1.83E{-}02$	$3.71E{-}03$
2511.9	$-1.30E{-}02$	$-6.33E{-}03$	$-1.87E{-}02$	$6.27E{-}03$
3162.3	$-1.37E{-}02$	$-8.79E{-}03$	$-2.90E{-}02$	$6.13E{-}03$
3981.1	$-1.21E{-}02$	$-1.36E{-}03$	$-1.37E{-}02$	$4.51E{-}03$
5011.9	$-1.17E{-}02$	$6.68E{-}03$	$1.16E{-}02$	$3.47E{-}03$

A.4 Parameter ranges for the established models

Table A.19: Parameter ranges (minimum to maximum) of the continuous flight parameters on which the aircraft noise emission models were established and verified. These parameter ranges should not be exceeded for a model prediction. However, regression models with multiple dimensions naturally extrapolate for some combinations of the data ranges. $N1$ values marked with * were estimated for approach in far range with 30 %.

Model name	Proc	$N1$ [%]	Ma [-]	ρ [kg/m^3]
A319_CFM56-5B	A	26 - 65	0.18 - 0.35	1.02 - 1.19
	D	67 - 91	0.20 - 0.45	0.88 - 1.19
A320_CFM56-5B	A	23 - 69	0.18 - 0.35	1.04 - 1.19
	D	71 - 97	0.19 - 0.47	0.89 - 1.20
A321_CFM56-5B	A	28 - 71	0.19 - 0.34	1.03 - 1.20
	D	70 - 98	0.20 - 0.47	0.92 - 1.21
A32X_CFM56-5A	A	30* - 63	0.18 - 0.31	1.05 - 1.17
	D	83 - 97	0.20 - 0.41	0.96 - 1.19
A32X_V2500	A	30* - 70	0.18 - 0.34	1.04 - 1.18
	D	77 - 97	0.17 - 0.45	0.89 - 1.19
A333_TRENT7	A	25 - 66	0.20 - 0.36	1.02 - 1.20
	D	61 - 92	0.22 - 0.48	0.93 - 1.21
A343_CFM56-5C	A	25 - 84	0.20 - 0.37	1.01 - 1.20
	D	87 - 99	0.21 - 0.45	0.96 - 1.20
A388_GP7270	A	30* - 30	0.21 - 0.32	1.06 - 1.15
	D	88 - 106	0.23 - 0.48	0.89 - 1.18
A388_TRENT9	A	30* - 55	0.20 - 0.36	1.04 - 1.19
	D	81 - 94	0.24 - 0.48	0.96 - 1.19
B737_CFM56-3	A	30* - 66	0.18 - 0.34	1.04 - 1.18
	D	73 - 100	0.19 - 0.43	0.90 - 1.19
B737_CFM56-7B	A	30* - 66	0.18 - 0.32	1.01 - 1.17
	D	74 - 104	0.19 - 0.48	0.86 - 1.19
B763_PW4060	A	30* - 64	0.19 - 0.35	1.03 - 1.18
	D	89 - 102	0.23 - 0.44	0.92 - 1.17
B76X_CF6-80C2	A	30* - 62	0.21 - 0.39	1.02 - 1.18
	D	82 - 110	0.26 - 0.44	0.90 - 1.19
CRJ9_CF34-8C5	A	30* - 66	0.19 - 0.35	1.03 - 1.17
	D	75 - 96	0.23 - 0.40	0.99 - 1.18
E170_CF34-8E	A	30* - 67	0.16 - 0.36	1.05 - 1.18
	D	59 - 95	0.15 - 0.38	0.98 - 1.18
E190_CF34-10E	A	30* - 67	0.18 - 0.35	1.02 - 1.18
	D	79 - 99	0.19 - 0.44	0.86 - 1.19
F100_TAY650-15	A	30* - 75	0.18 - 0.38	1.02 - 1.18
	D	70 - 91	0.14 - 0.45	0.95 - 1.18
FA7X_PW307	A	30* - 62	0.16 - 0.38	1.04 - 1.16
	D	64 - 92	0.20 - 0.43	0.84 - 1.18
RJ1H_LF507	A	32 - 83	0.17 - 0.41	0.84 - 1.18
	D	77 - 96	0.18 - 0.43	0.70 - 1.19

Table A.20: Parameter ranges (minimum to maximum) of the categorical (FH and LG) and continuous flight parameters (Ma, α) on which the advanced aircraft noise emission models were established and verified. These parameter ranges should not be exceeded for a model prediction. The angle of attack (α) is provided as additional information but is no model parameter.

			Approach		Departure	
Model name	FH	LG	Ma [-]	α [°]	Ma [-]	α [°]
A319_CFM56-5B	0	0	-	-	0.27 - 0.45	1.5 - 6.9
	0	1	-	-	-	-
	1	0	0.28 - 0.35	4.7 - 7.6	0.22 - 0.36	2.3 - 7.2
	1	1	0.29 - 0.34	4.7 - 7.4	-	-
	2	0	0.21 - 0.33	1.4 - 8.6	0.20 - 0.28	3.1 - 8.8
	2	1	0.21 - 0.31	1.8 - 8.6	0.22 - 0.26	4.6 - 9.4
	3	0	0.21 - 0.30	1.4 - 8.3	-	-
	3	1	0.20 - 0.28	2.2 - 8.6	-	-
	4	0	0.22 - 0.28	−2.1 - 4.0	-	-
	4	1	0.18 - 0.27	−1.2 - 7.7	-	-
A320_CFM56-5B	0	0	0.30 - 0.34	3.8 - 6.4	0.29 - 0.47	1.5 - 6.6
	0	1	-	-	-	-
	1	0	0.30 - 0.35	3.8 - 8.6	0.23 - 0.38	1.7 - 8.2
	1	1	0.33 - 0.33	4.9 - 4.9	-	-
	2	0	0.24 - 0.33	0.7 - 8.8	0.19 - 0.32	2.2 - 9.9
	2	1	0.24 - 0.33	0.7 - 7.2	0.22 - 0.26	3.5 - 12.2
	3	0	0.22 - 0.31	0.7 - 7.3	0.24 - 0.25	4.1 - 7.2
	3	1	0.21 - 0.30	0.1 - 8.5	0.25 - 0.25	5.5 - 8.6
	4	0	0.20 - 0.27	−1.3 - 6.5	-	-
	4	1	0.18 - 0.29	−1.8 - 8.4	-	-
A321_CFM56-5B	0	0	-	-	0.30 - 0.47	1.7 - 6.4
	0	1	-	-	-	-
	1	0	0.31 - 0.34	5.8 - 8.0	0.24 - 0.39	1.1 - 7.8
	1	1	-	-	-	-
	2	0	0.25 - 0.34	0.1 - 7.1	0.20 - 0.32	2.1 - 8.4
	2	1	0.24 - 0.32	1.7 - 6.2	0.23 - 0.28	3.5 - 9.0
	3	0	0.22 - 0.31	−0.9 - 6.1	-	-
	3	1	0.24 - 0.29	−0.9 - 6.2	-	-
	4	0	0.19 - 0.29	−1.9 - 5.2	-	-
	4	1	0.19 - 0.28	−1.1 - 7.4	-	-
A333_TRENT7	0	0	0.29 - 0.29	5.1 - 5.9	0.25 - 0.48	2.7 - 8.7
	0	1	0.21 - 0.28	4.4 - 6.5	-	-
	1	0	0.29 - 0.36	5.6 - 9.5	0.24 - 0.41	4.0 - 9.4
	1	1	0.28 - 0.34	6.1 - 9.4	-	-
	2	0	0.26 - 0.34	2.3 - 9.9	0.22 - 0.33	2.8 - 10.9
	2	1	0.24 - 0.34	2.4 - 8.8	0.23 - 0.28	4.9 - 10.7
	3	0	0.23 - 0.30	1.3 - 6.8	-	-
	3	1	0.22 - 0.30	1.5 - 7.8	-	-
	4	0	0.20 - 0.22	4.4 - 6.7	-	-
	4	1	0.20 - 0.29	0.8 - 8.4	-	-
A343_CFM56-5C	0	0	0.29 - 0.29	1.6 - 2.8	0.26 - 0.45	1.3 - 9.2
	0	1	0.23 - 0.27	2.0 - 6.2	-	-
	1	0	0.30 - 0.37	6.1 - 9.5	0.23 - 0.42	1.4 - 9.7
	1	1	-	-	-	-
	2	0	0.26 - 0.34	0.4 - 9.4	0.21 - 0.34	2.2 - 10.5
	2	1	0.24 - 0.32	1.1 - 5.2	0.21 - 0.27	5.5 - 10.2
	3	0	0.23 - 0.30	0.9 - 5.5	-	-
	3	1	0.20 - 0.30	1.4 - 7.6	-	-
	4	0	0.22 - 0.28	0.0 - 7.1	-	-
	4	1	0.20 - 0.29	0.9 - 12.1	-	-
RJ1H_LF507	0	0	0.24 - 0.41	−4.8 - 11.8	0.18 - 0.43	−0.8 - 16.5
	0	1	0.17 - 0.34	−8.8 - 11.6	0.19 - 0.24	2.2 - 14.8

FH was not available for this type.

Table A.21: Parameter ranges (minimum to maximum) of the categorical (SB and LG) and continuous flight parameters (Ma, α) on which the advanced aircraft noise emission models were established and verified. These parameter ranges should not be exceeded for a model prediction. The angle of attack (α) is provided as additional information but is no model parameter.

			Approach		Departure	
Model name	SB	LG	Ma [-]	α [°]	Ma [-]	α [°]
A319_CFM56-5B	0	0	0.21 - 0.35	−2.1 - 8.6	0.20 - 0.45	1.5 - 8.8
	0	1	0.18 - 0.34	−1.2 - 8.6	0.22 - 0.26	4.6 - 9.4
	1	0	0.25 - 0.35	3.9 - 7.6	-	-
	1	1	0.27 - 0.33	3.0 - 7.6	-	-
A320_CFM56-5B	0	0	0.20 - 0.35	−1.3 - 7.5	0.19 - 0.47	1.5 - 9.9
	0	1	0.18 - 0.33	−1.8 - 8.5	0.22 - 0.26	3.5 - 12.2
	1	0	0.22 - 0.35	0.7 - 8.8	-	-
	1	1	0.27 - 0.31	2.9 - 7.2	-	-
A321_CFM56-5B	0	0	0.19 - 0.34	−1.9 - 8.0	0.20 - 0.47	1.1 - 8.4
	0	1	0.19 - 0.32	−1.1 - 7.4	0.23 - 0.28	3.5 - 9.0
	1	0	0.25 - 0.34	−0.6 - 6.6	-	-
	1	1	0.28 - 0.28	2.6 - 2.9	-	-
A333_TRENT7	0	0	0.20 - 0.36	1.3 - 9.9	0.22 - 0.48	2.7 - 10.9
	0	1	0.20 - 0.33	0.8 - 9.2	0.23 - 0.28	4.9 - 10.7
	1	0	0.25 - 0.36	2.3 - 9.7	-	-
	1	1	0.23 - 0.34	1.8 - 9.4	-	-
A343_CFM56-5C	0	0	0.22 - 0.35	0.0 - 9.3	0.21 - 0.45	1.3 - 10.5
	0	1	0.20 - 0.32	0.9 - 12.1	0.21 - 0.27	5.5 - 10.2
	1	0	0.24 - 0.37	0.7 - 9.5	-	-
	1	1	0.24 - 0.32	1.4 - 7.1	-	-
RJ1H_LF507	0	0	0.24 - 0.37	−4.8 - 11.8	0.18 - 0.43	−0.8 - 16.5
	0	1	0.17 - 0.34	−8.8 - 11.6	0.19 - 0.24	2.2 - 14.8
	1	0	0.26 - 0.41	−4.5 - 10.1	-	-
	1	1	0.17 - 0.31	−8.8 - 10.9	-	-

A.5 Model performance for aircraft types with FDR data

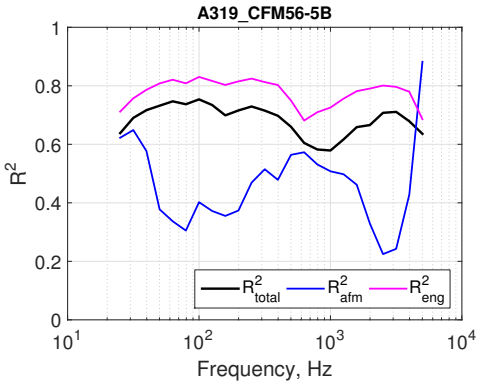

(a) Coefficient of determination (3D)

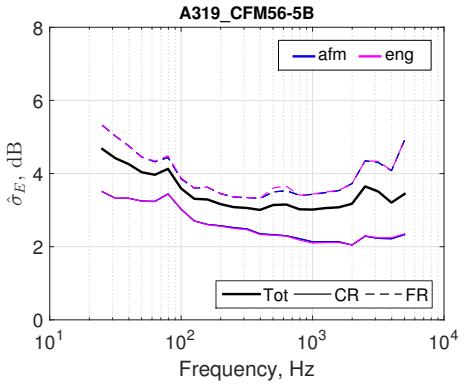

(b) Root-mean-square error (3D)

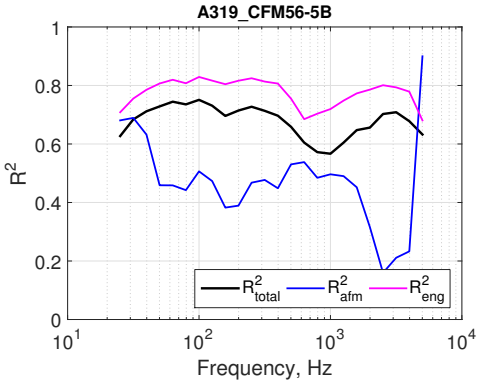

(c) Coefficient of determination (3Dred)

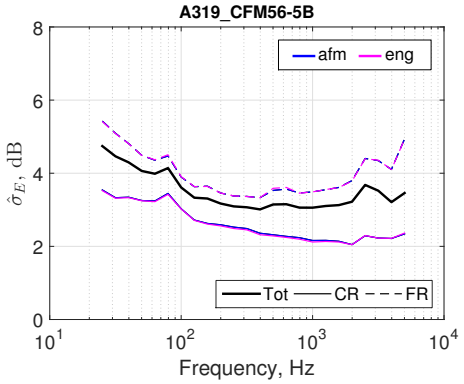

(d) Root-mean-square error (3Dred)

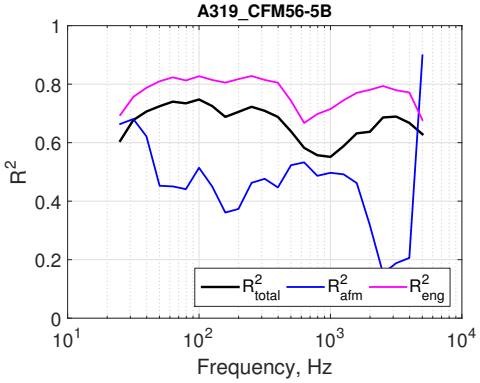

(e) Coefficient of determination (2Dred)

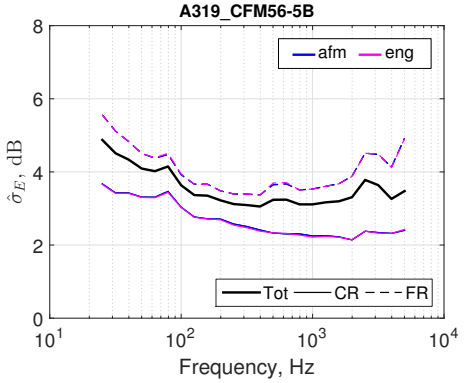

(f) Root-mean-square error (2Dred)

Figure A.3: Model performance of the A319_CFM56-5B, model attributes for variants 3D, 3Dred and 2Dred

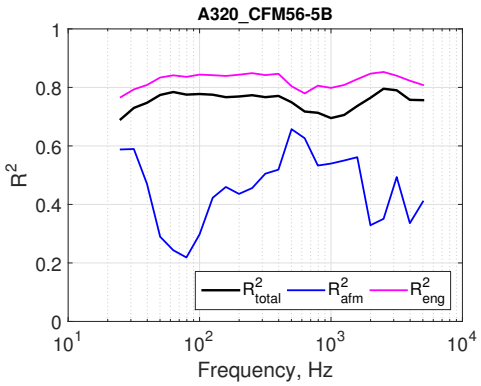

(a) Coefficient of determination (3D)

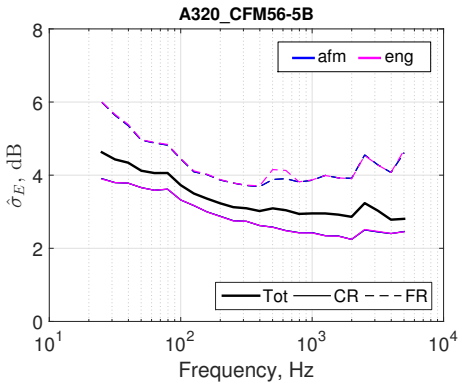

(b) Root-mean-square error (3D)

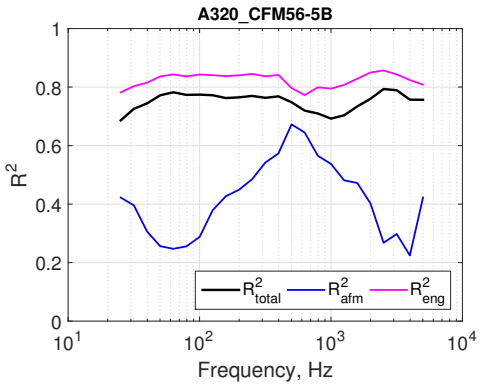

(c) Coefficient of determination (3Dred)

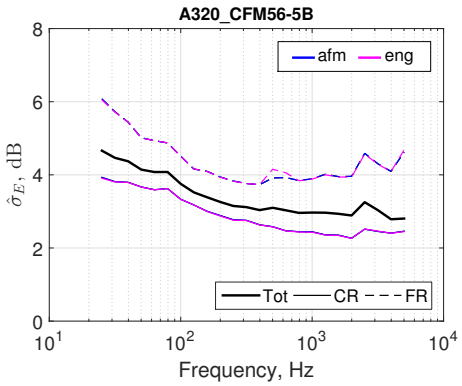

(d) Root-mean-square error (3Dred)

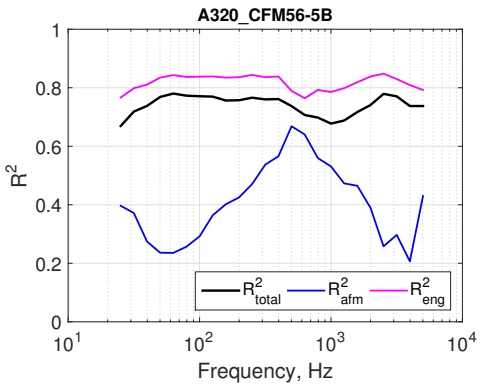

(e) Coefficient of determination (2Dred)

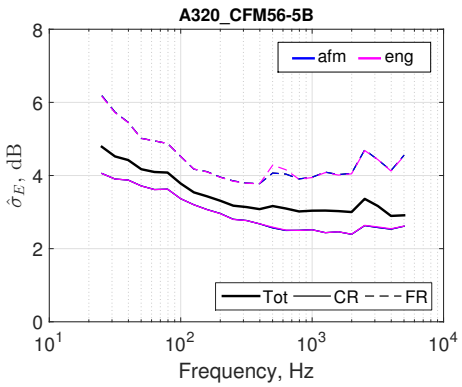

(f) Root-mean-square error (2Dred)

Figure A.4: Model performance of the A320_CFM56-5B, model attributes for variants 3D, 3Dred and 2Dred

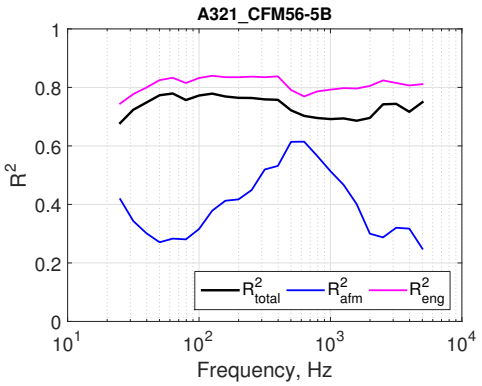

(a) Coefficient of determination (3D)

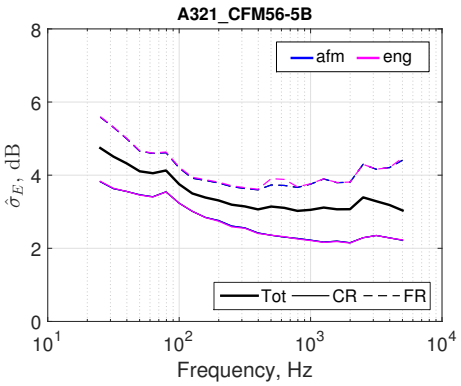

(b) Root-mean-square error (3D)

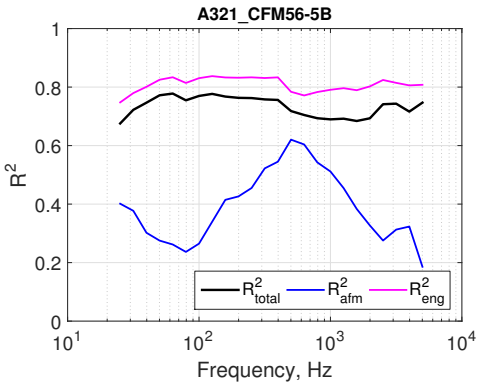

(c) Coefficient of determination (3Dred)

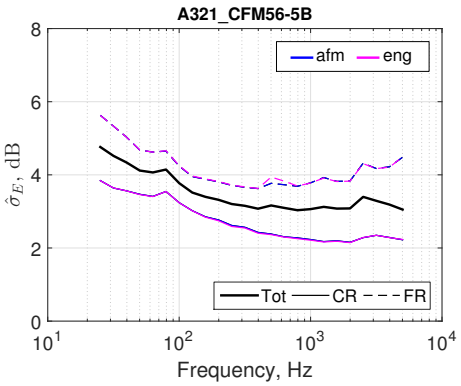

(d) Root-mean-square error (3Dred)

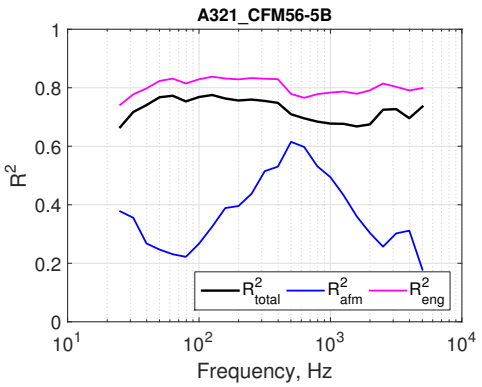

(e) Coefficient of determination (2Dred)

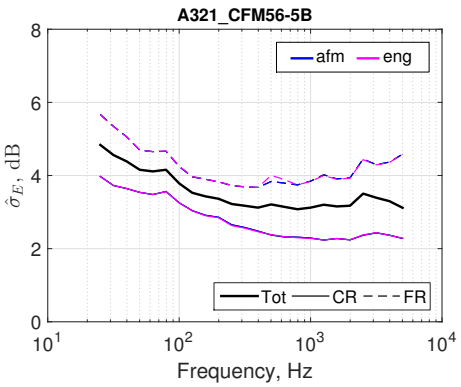

(f) Root-mean-square error (2Dred)

Figure A.5: Model performance of the A321_CFM56-5B, model attributes for variants 3D, 3Dred and 2Dred

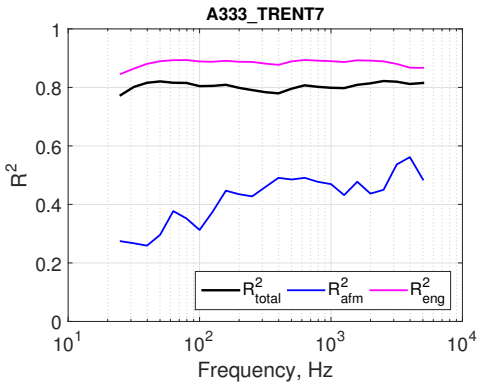

(a) Coefficient of determination (3D)

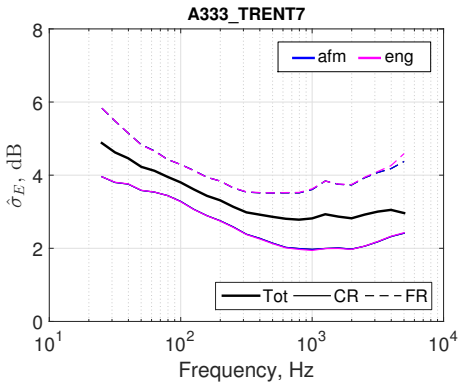

(b) Root-mean-square error (3D)

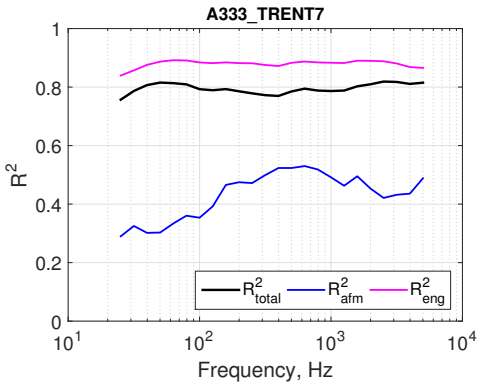

(c) Coefficient of determination (3Dred)

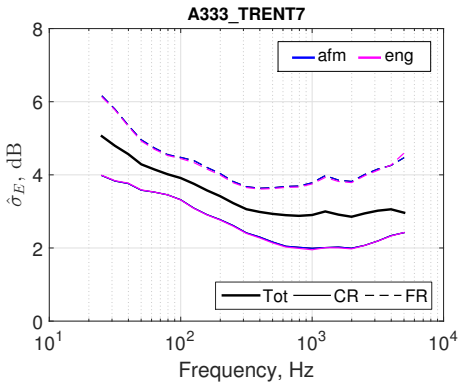

(d) Root-mean-square error (3Dred)

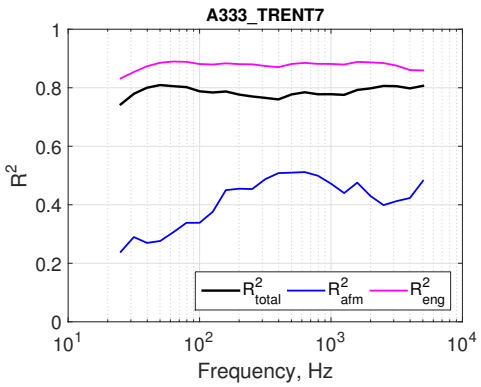

(e) Coefficient of determination (2Dred)

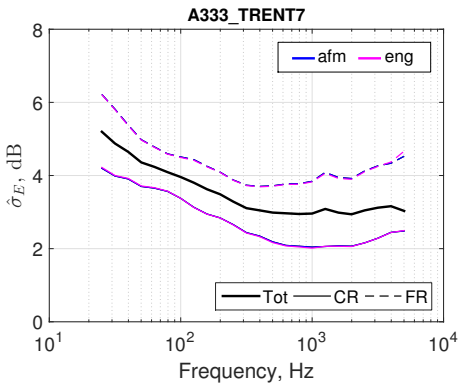

(f) Root-mean-square error (2Dred)

Figure A.6: Model performance of the A333_CFM56-5B, model attributes for variants 3D, 3Dred and 2Dred

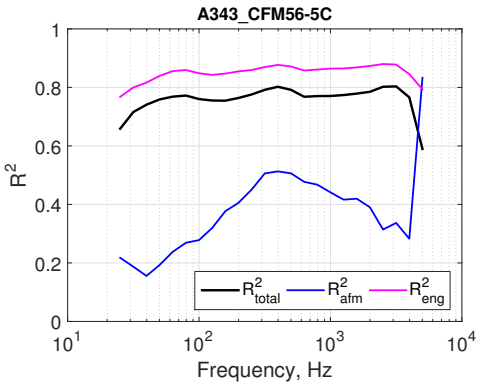

(a) Coefficient of determination (3D)

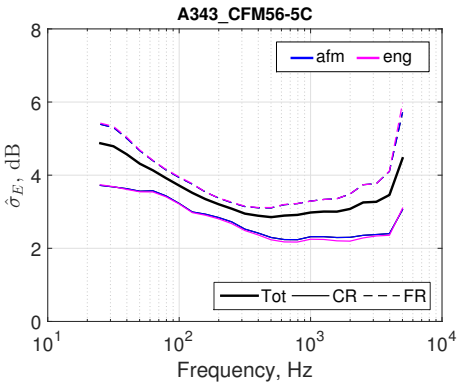

(b) Root-mean-square error (3D)

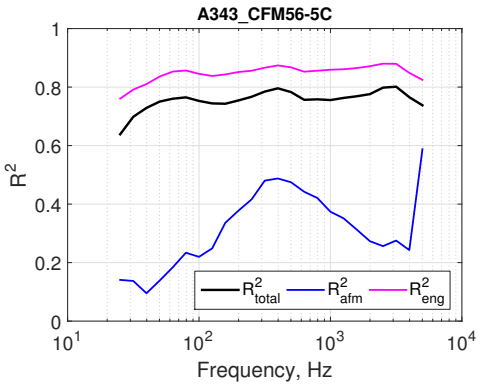

(c) Coefficient of determination (3Dred)

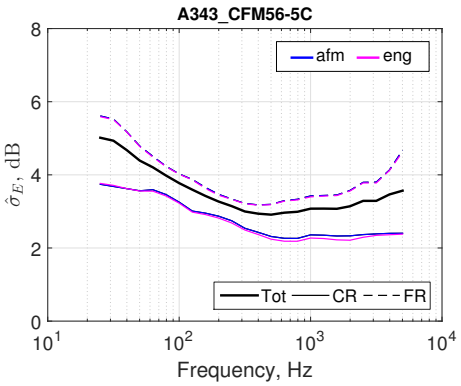

(d) Root-mean-square error (3Dred)

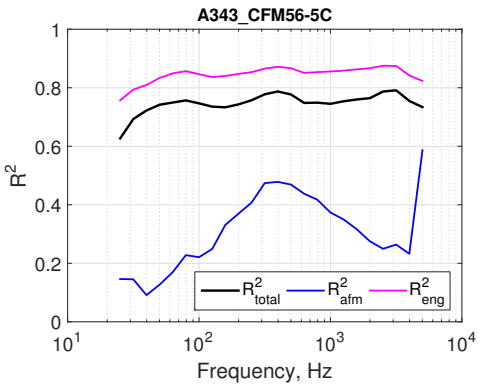

(e) Coefficient of determination (2Dred)

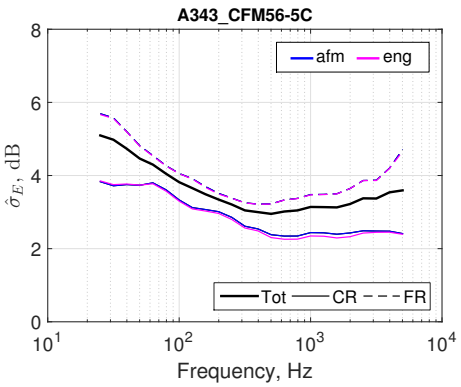

(f) Root-mean-square error (2Dred)

Figure A.7: Model performance of the A343_CFM56-5B, model attributes for variants 3D, 3Dred and 2Dred

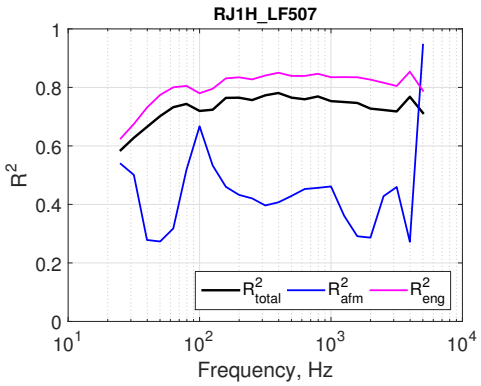

(a) Coefficient of determination 3D

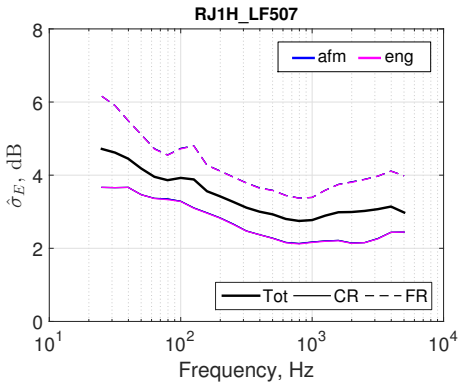

(b) Root-mean-square error 3D

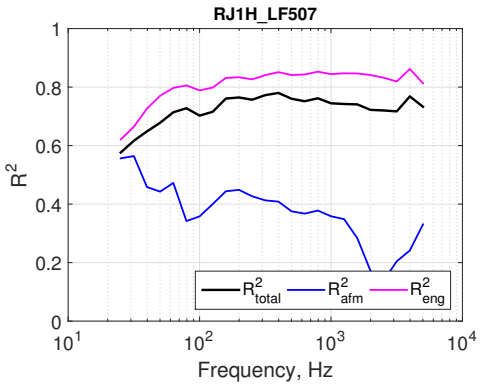

(c) Coefficient of determination 3Dred

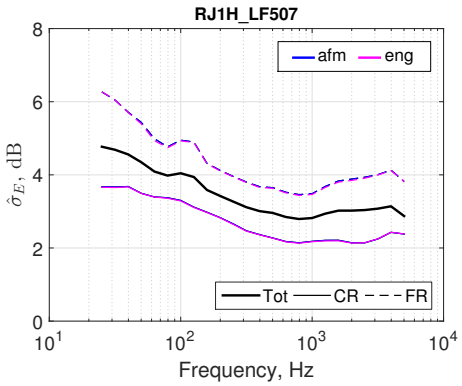

(d) Root-mean-square error 3Dred

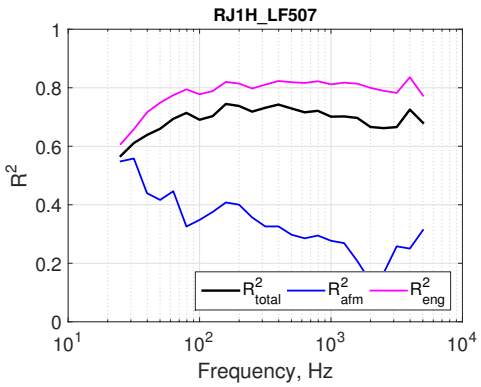

(e) Coefficient of determination 2Dred

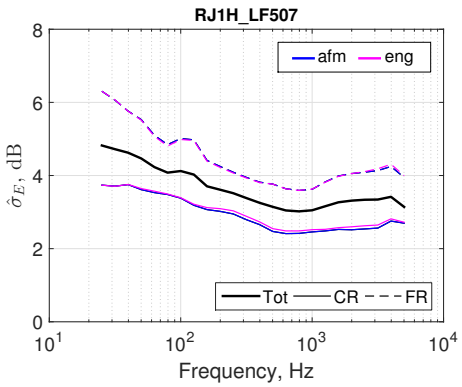

(f) Root-mean-square error 2Dred

Figure A.8: Model performance of the RJ1H_CFM56-5B, model attributes for variants 3D, 3Dred and 2Dred

A.6 Model performance for aircraft types without FDR data

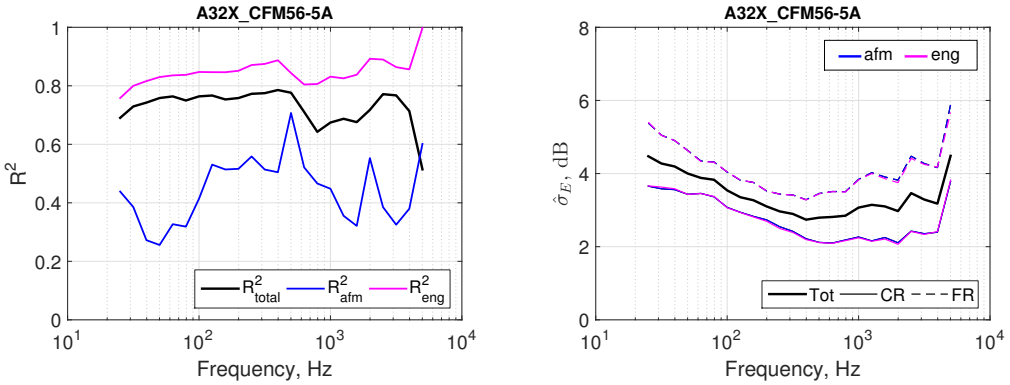

(a) Coefficient of determination (b) Root-mean-square error

Figure A.9: Model performance of the A32X_CFM56-5A, 3Dred model

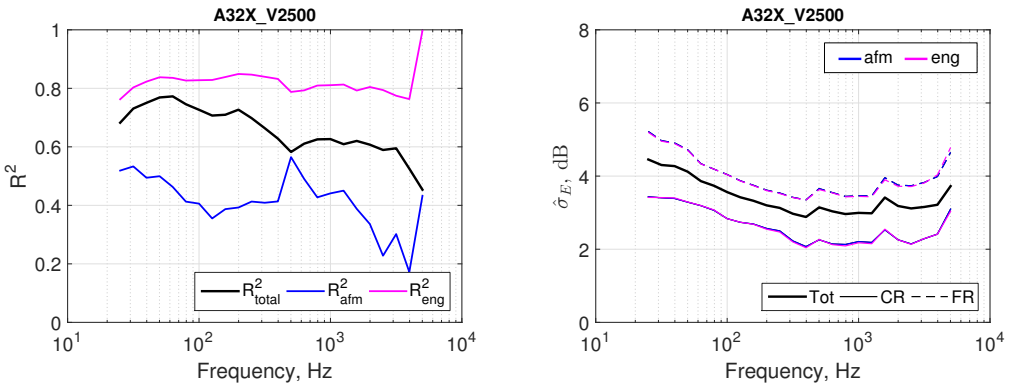

(a) Coefficient of determination (b) Root-mean-square error

Figure A.10: Model performance of the A32X_V2500, 3Dred model

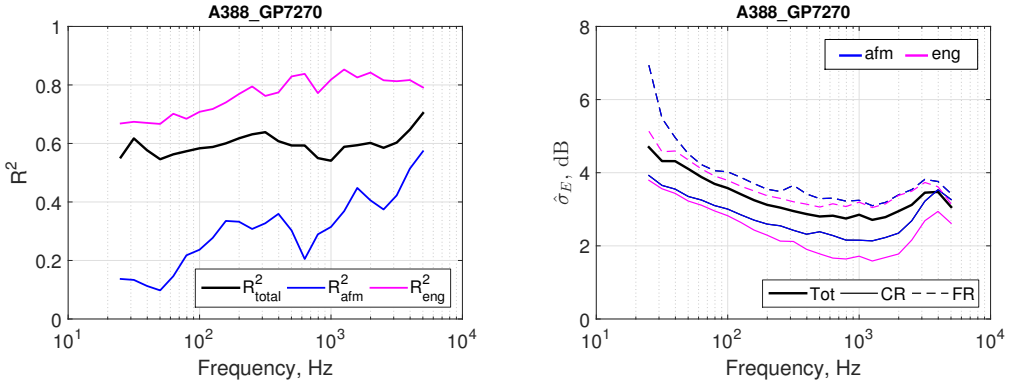

(a) Coefficient of determination (b) Root-mean-square error

Figure A.11: Model performance of the A388_GP7270, 3Dred model

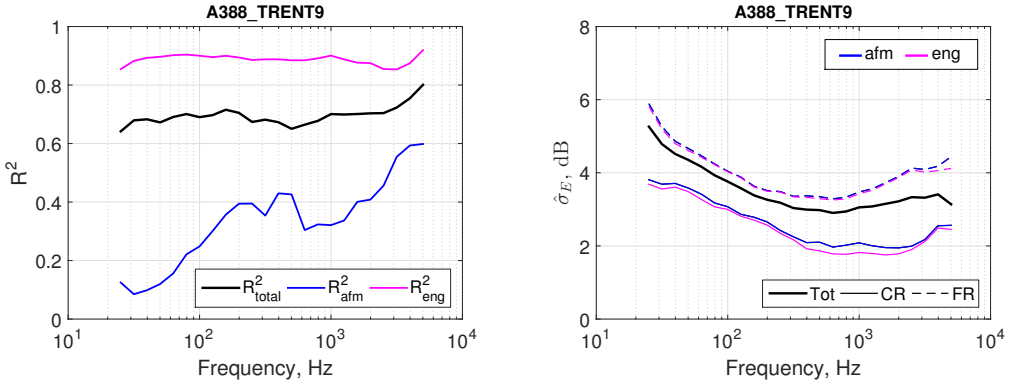

(a) Coefficient of determination (b) Root-mean-square error

Figure A.12: Model performance of the A388_TRENT9, 3Dred model

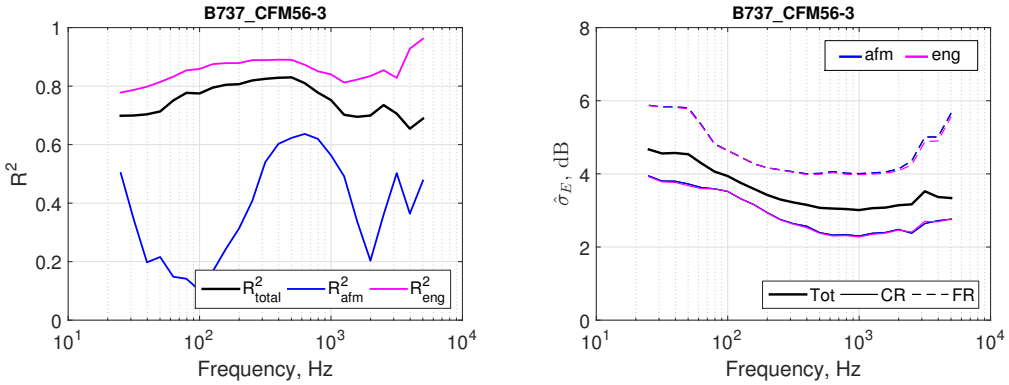

(a) Coefficient of determination (b) Root-mean-square error

Figure A.13: Model performance of the B737_CFM56-3, 3Dred model

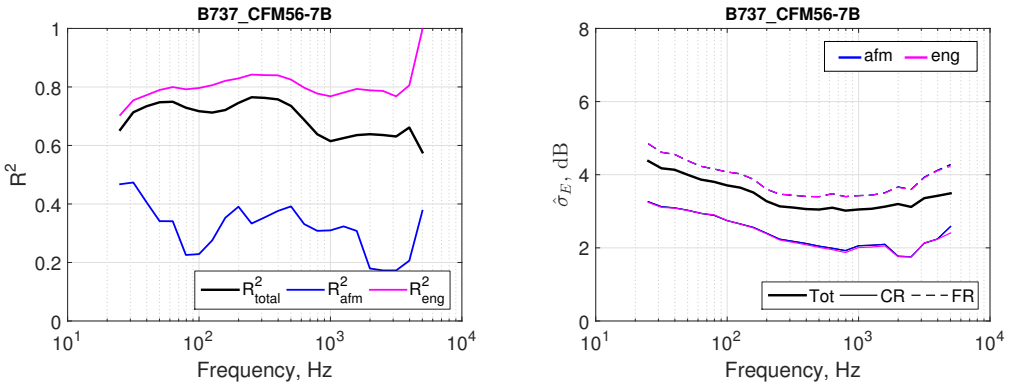

(a) Coefficient of determination (b) Root-mean-square error

Figure A.14: Model performance of the B737_CFM56-7B, 3Dred model

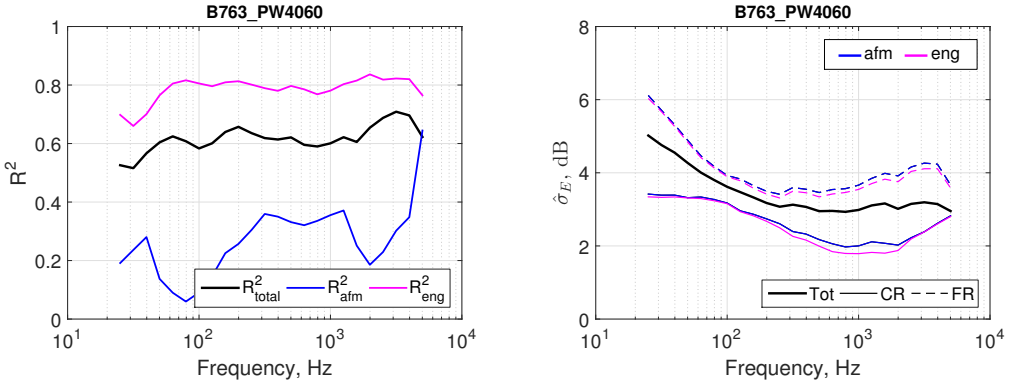

(a) Coefficient of determination (b) Root-mean-square error

Figure A.15: Model performance of the B763_PW4060, 3Dred model

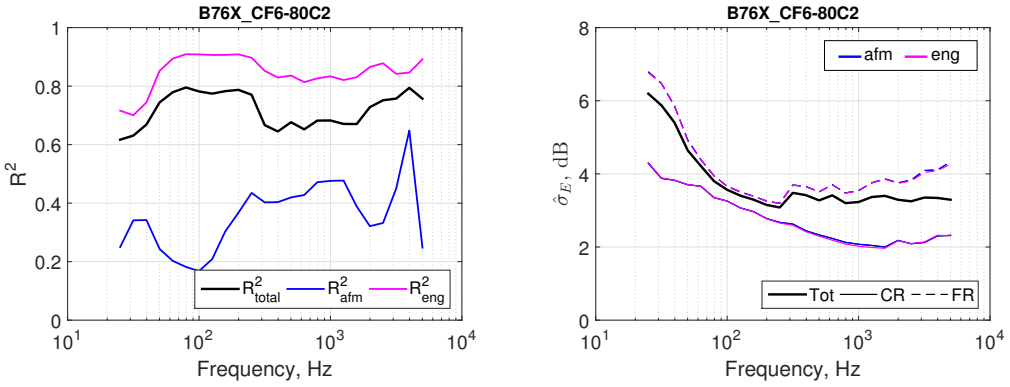

(a) Coefficient of determination (b) Root-mean-square error

Figure A.16: Model performance of the B76X_CF6-80C2, 3Dred model

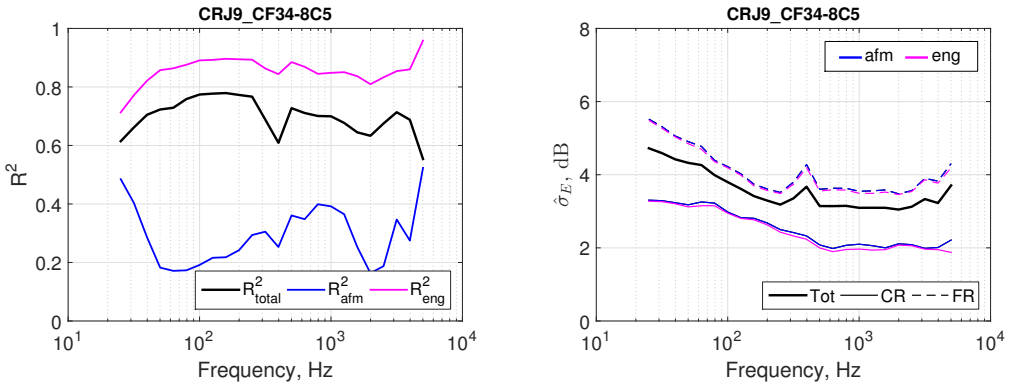

(a) Coefficient of determination (b) Root-mean-square error

Figure A.17: Model performance of the CRJ9_CF34-8C5, 3Dred model

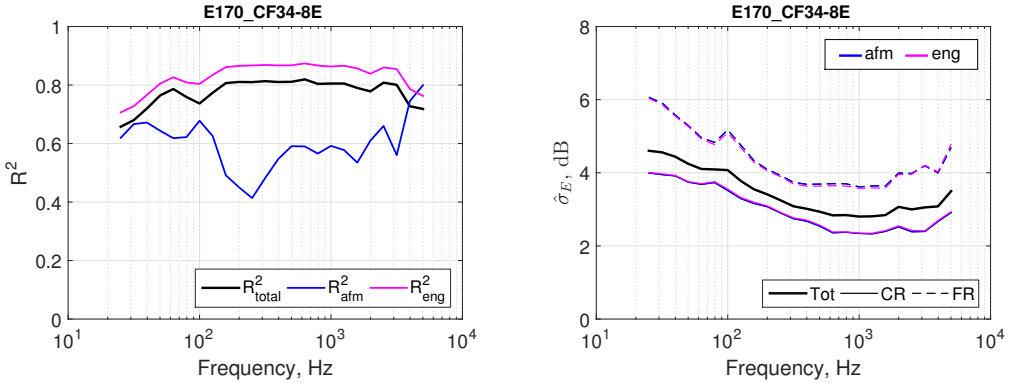

(a) Coefficient of determination (b) Root-mean-square error

Figure A.18: Model performance of the E170_CF34-8E, 3Dred model

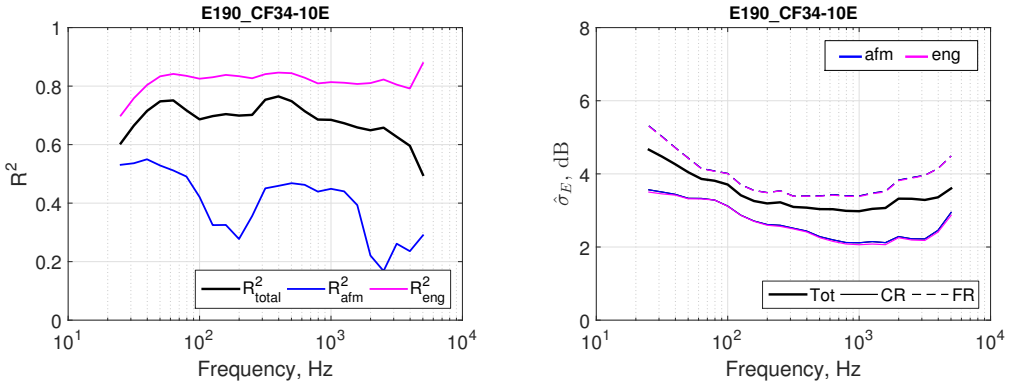

(a) Coefficient of determination (b) Root-mean-square error

Figure A.19: Model performance of the E190_CF34-10E, 3Dred model

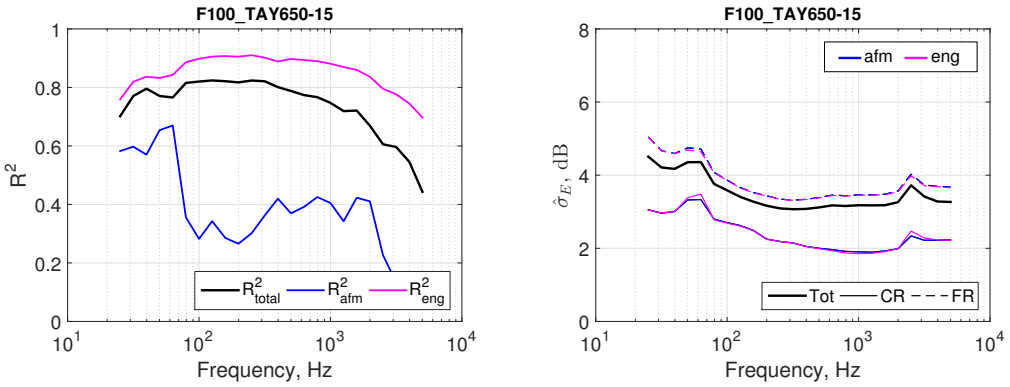

(a) Coefficient of determination (b) Root-mean-square error

Figure A.20: Model performance of the F100_TAY650-15, 3Dred model

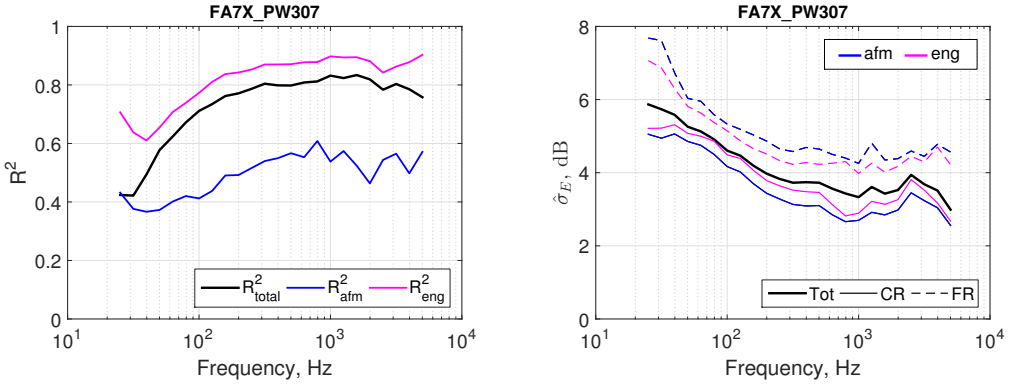

(a) Coefficient of determination (b) Root-mean-square error

Figure A.21: Model performance of the FA7X_PW307, 3Dred model

A.7 Effects of the parameters

The effects are presented for the total sound emission level at the source (left side, red) as well as for the total sound pressure level at a receiver (right side, blue). The former represents the energetic sum of all predicted frequency bands of the regression models applying the Doppler and flight effect, as these effects occur at the source. The latter represents the propagated sound to a receiver at a fix distance of 304.8 m. The receiver level is additionally corrected for:

- A-filter
- direct sound propagation
  - geometrical divergence
  - atmospheric absorption (T=15 °C, p=1013.25 hPa, H=70 %)
  - mean ground effect

A320_CFM56-5B

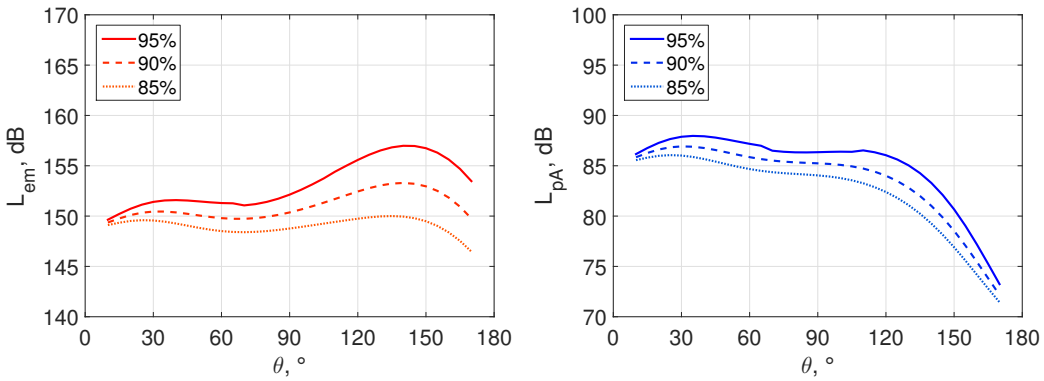

(a) Level at source (d=1 m) (b) Level at receiver (d=304.8 m)

Figure A.22: Relationship of (a) $\widehat{L}_{\overline{em}}$ and (b) L_{pA} to the polar angle for different $N1$ settings at take-off for the A320_CFM56-5B. Predicted with 3Dred model at φ=0°, Ma=0.24, ρ=1.15 $^{kg}/_{m^3}$.

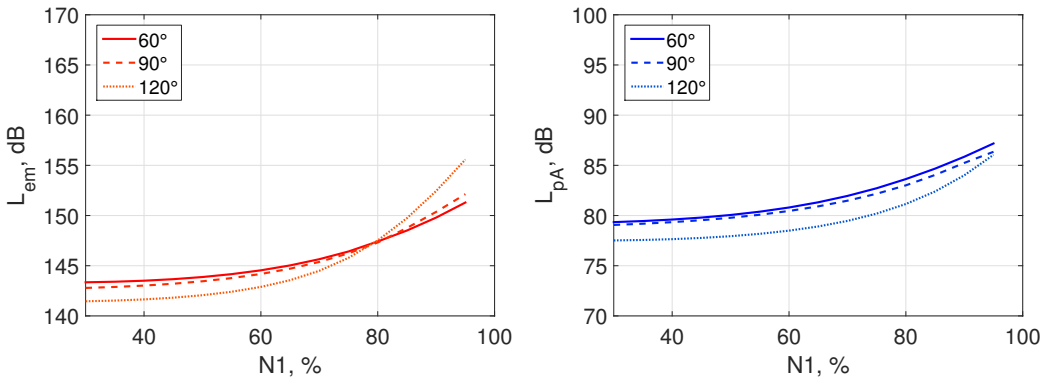

(a) Level at source (d=1 m) (b) Level at receiver (d=304.8 m)

Figure A.23: Relationship of (a) $\widehat{L}_{\overline{em}}$ and (b) L_{pA} to $N1$ for different polar angles at departure for the A320_CFM56-5B. Predicted with 3Dred model at φ=0°, Ma=0.24, ρ=1.15 $^{\mathrm{kg}}/_{\mathrm{m}^3}$.

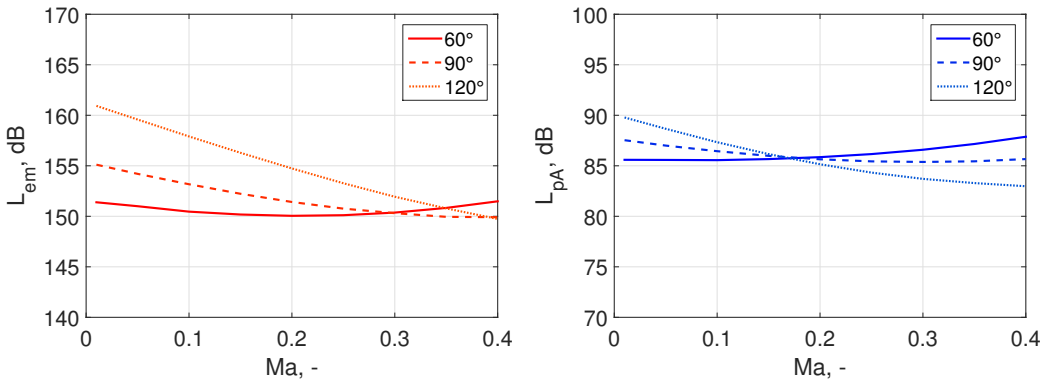

(a) Level at source (d=1 m) (b) Level at receiver (d=304.8 m)

Figure A.24: Relationship of (a) $\widehat{L}_{\overline{em}}$ and (b) L_{pA} to the Mach number for different polar angles at departure for the A320_CFM56-5B. Predicted with 3Dred model at φ=0°, $N1$=92 %, ρ=1.1 $^{\mathrm{kg}}/_{\mathrm{m}^3}$.

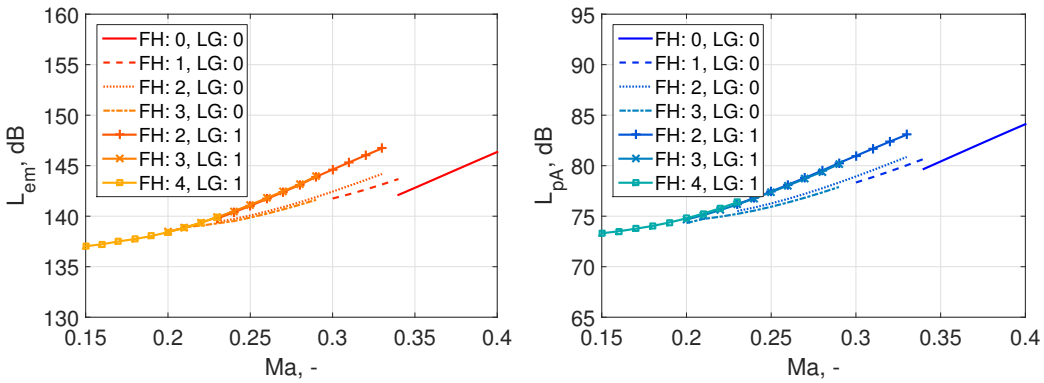

(a) Level at source (d=1 m) (b) Level at receiver (d=304.8 m)

Figure A.25: Relationship of (a) $\widehat{L_{\overline{em}}}$ and (b) L_{pA} to the Mach number for different aeroplane configurations (FH: flap handle, LG: landing gear) at approach for the A320_CFM56-5B. Predicted with 3D model at θ=90°, φ=0°, $N1$=30 %, ρ=1.1 $^{\mathrm{kg}}/_{\mathrm{m}^3}$.

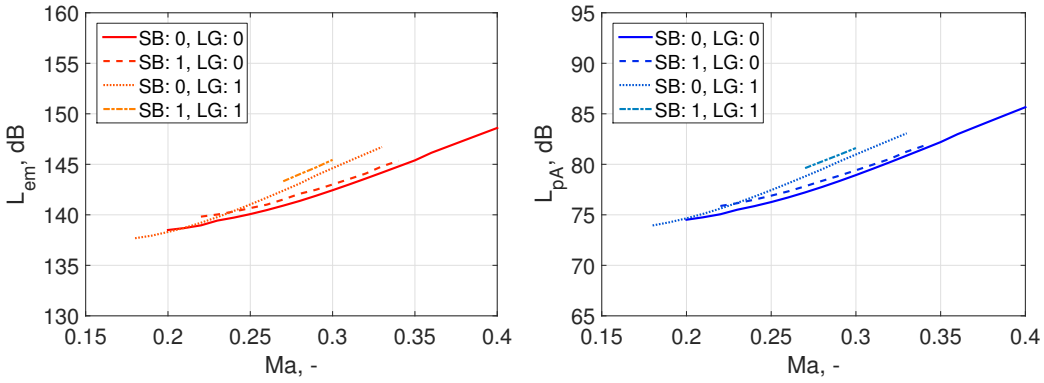

(a) Level at source (d=1 m) (b) Level at receiver (d=304.8 m)

Figure A.26: Relationship of (a) $\widehat{L_{\overline{em}}}$ and (b) L_{pA} to the Mach number for different aeroplane configurations (SB: speedbrakes, LG: landing gear) at approach for the A320_CFM56-5B. Predicted with 3D model at θ=90°, φ=0°, $N1$=30 %, ρ=1.1 $^{\mathrm{kg}}/_{\mathrm{m}^3}$, FH=2.

A343_CFM56-5C

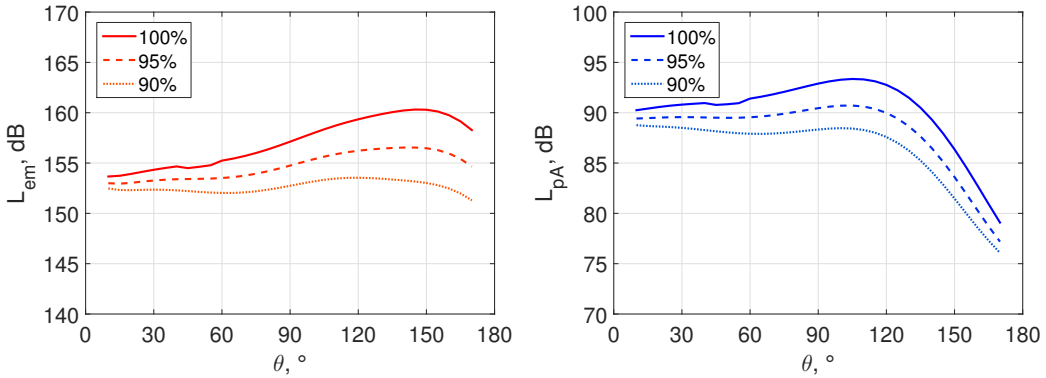

(a) Level at source (d=1 m) (b) Level at receiver (d=304.8 m)

Figure A.27: Relationship of (a) $\widehat{L}_{\overline{em}}$ and (b) L_{pA} to the polar angle for different $N1$ settings at take-off for the A343_CFM56-5C. Predicted with 3Dred model at φ=0°, Ma=0.26, ρ=1.15 kg/m³.

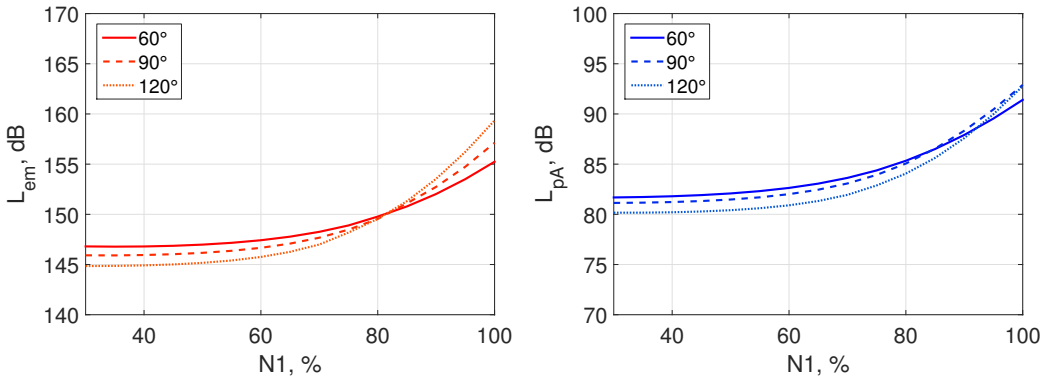

(a) Level at source (d=1 m) (b) Level at receiver (d=304.8 m)

Figure A.28: Relationship of (a) $\widehat{L}_{\overline{em}}$ and (b) L_{pA} to $N1$ for different polar angles at departure for the A343_CFM56-5C. Predicted with 3Dred model at φ=0°, Ma=0.26, ρ=1.15 kg/m³.

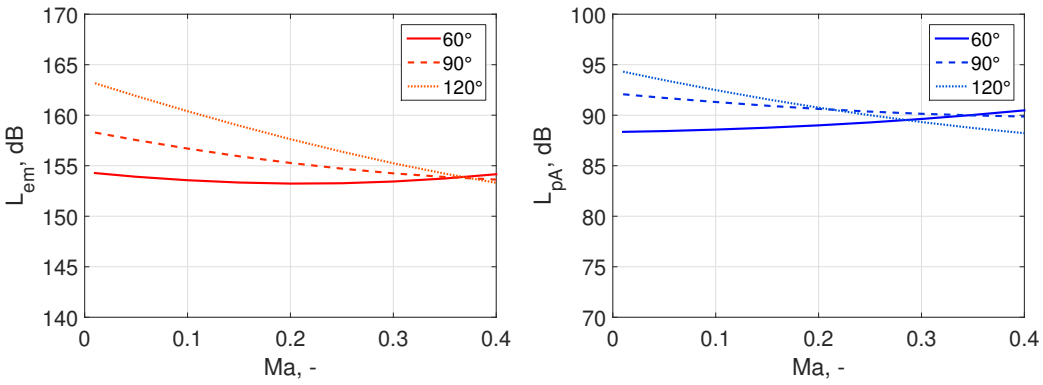

(a) Level at source (d=1 m) (b) Level at receiver (d=304.8 m)

Figure A.29: Relationship of (a) $\widehat{L_{\overline{em}}}$ and (b) L_{pA} to the Mach number for different polar angles at departure for the A343_CFM56-5C. Predicted with 3Dred model at φ=0°, $N1$=95 %, ρ=1.1 kg/m³.

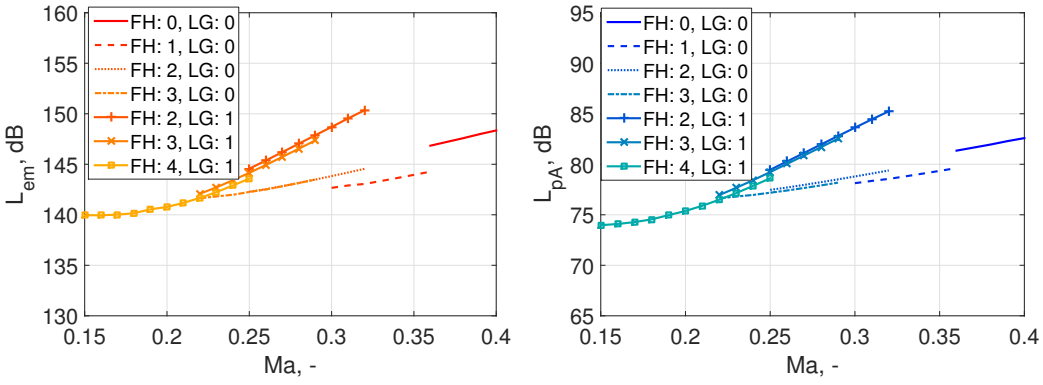

(a) Level at source (d=1 m) (b) Level at receiver (d=304.8 m)

Figure A.30: Relationship of (a) $\widehat{L_{\overline{em}}}$ and (b) L_{pA} to the Mach number for different aeroplane configurations (FH: flap handle, LG: landing gear) at approach for the A343_CFM56-5C. Predicted with 3D model at θ=90°, φ=0°, $N1$=30 %, ρ=1.1 kg/m³.

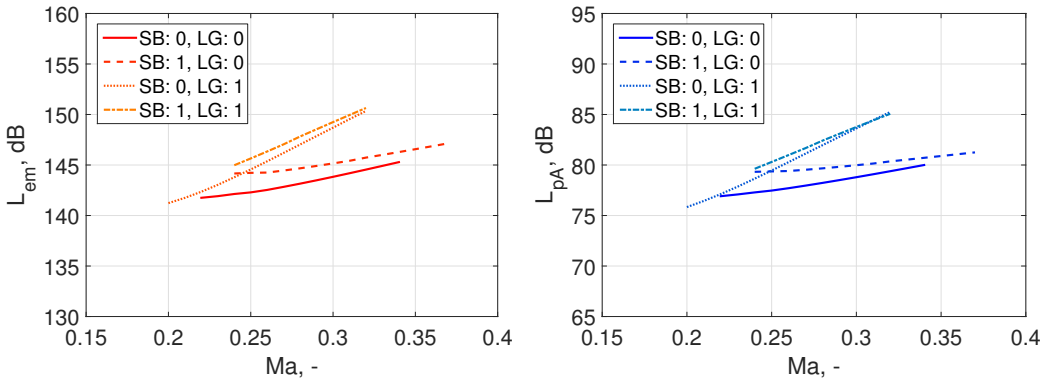

(a) Level at source (d=1 m) (b) Level at receiver (d=304.8 m)

Figure A.31: Relationship of (a) $\widehat{L_{\overline{em}}}$ and (b) L_{pA} to the Mach number for different aeroplane configurations (SB: speedbrakes, LG: landing gear) at approach for the A343_CFM56-5C. Predicted with 3D model at θ=90°, φ=0°, $N1$=30 %, ρ=1.1 kg/m³, FH=2.

RJ1H_LF507

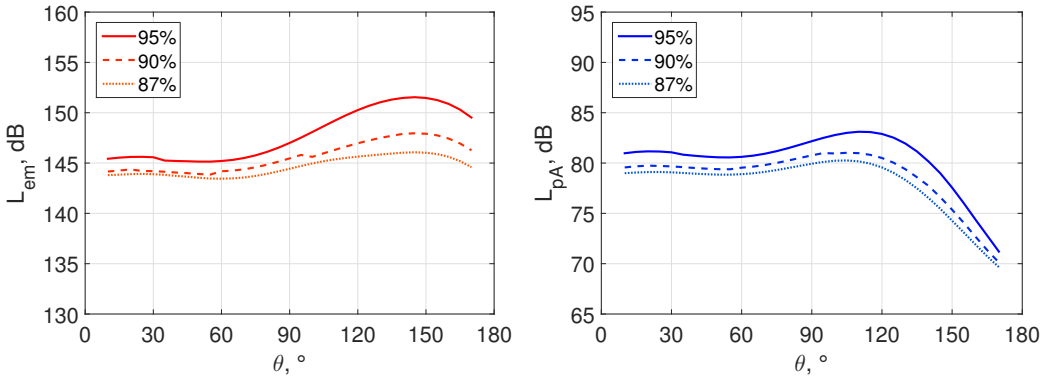

(a) Level at source (d=1 m) (b) Level at receiver (d=304.8 m)

Figure A.32: Relationship of (a) $\widehat{L}_{\overline{em}}$ and (b) L_{pA} to the polar angle for different $N1$ settings at take-off for the RJ1H_LF507. Predicted with 3Dred model at φ=0°, Ma=0.22, ρ=1.15 kg/m³.

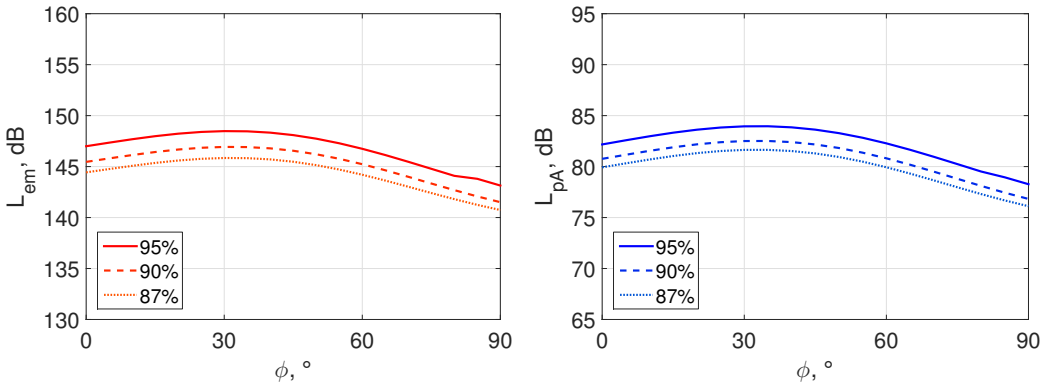

(a) Level at source (d=1 m) (b) Level at receiver (d=304.8 m)

Figure A.33: Relationship of (a) $\widehat{L}_{\overline{em}}$ and (b) L_{pA} to the azimuth angle for different $N1$ settings at take-off for the RJ1H_LF507. Predicted with 3Dred model at θ=90°, Ma=0.22, ρ=1.15 kg/m³.

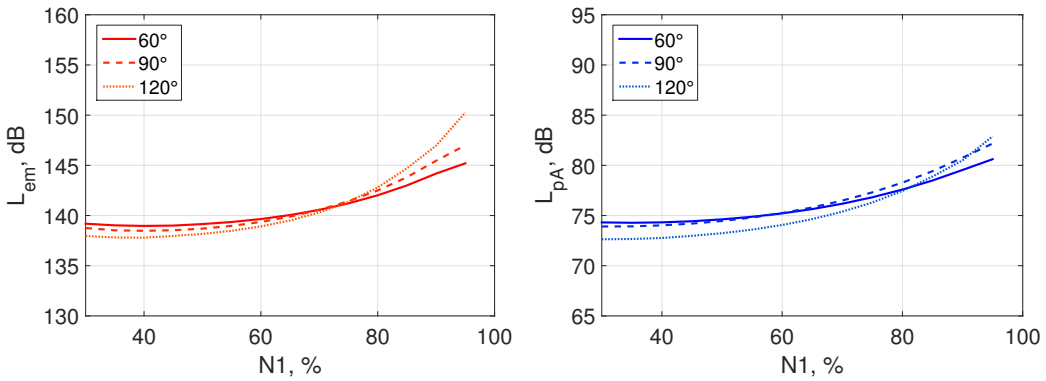

(a) Level at source (d=1 m) (b) Level at receiver (d=304.8 m)

Figure A.34: Relationship of (a) $\widehat{L}_{\overline{em}}$ and (b) L_{pA} to $N1$ for different polar angles at departure for the RJ1H_LF507. Predicted with 3Dred model at φ=0°, Ma=0.22, ρ=1.15 $^{\mathrm{kg}}/_{\mathrm{m}^3}$.

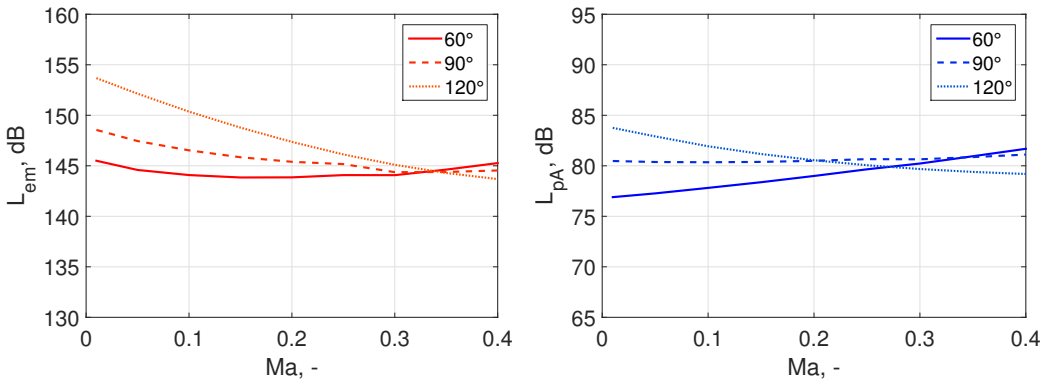

(a) Level at source (d=1 m) (b) Level at receiver (d=304.8 m)

Figure A.35: Relationship of (a) $\widehat{L}_{\overline{em}}$ and (b) L_{pA} to the Mach number for different polar angles at departure for the RJ1H_LF507. Predicted with 3Dred model at φ=0°, $N1$=90 %, ρ=1.1 $^{\mathrm{kg}}/_{\mathrm{m}^3}$.

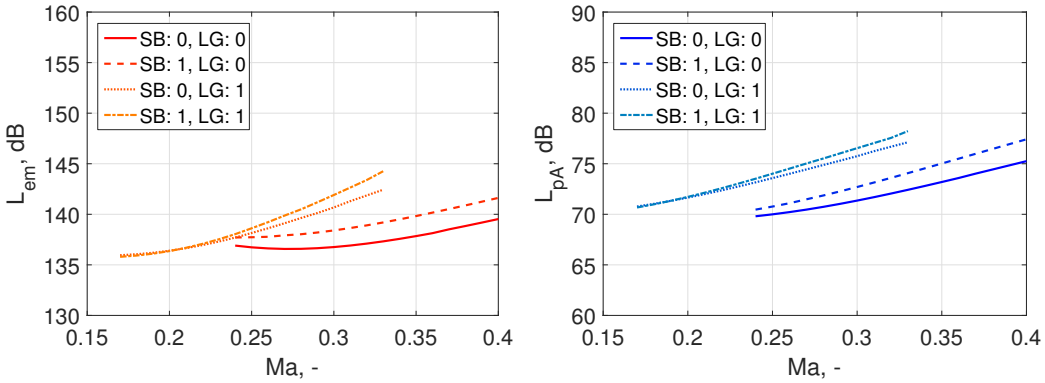

(a) Level at source (d=1 m) (b) Level at receiver (d=304.8 m)

Figure A.36: Relationship of (a) $\widehat{L}_{\overline{em}}$ and (b) L_{pA} to the Mach number for different aeroplane configurations (SB: speedbrakes, LG: landing gear) at approach for the RJ1H_LF507. The dashed black line shows an example parameter setting during approach on the glide path. Predicted with 3D model at θ=90°, φ=0°, $N1$=30 %, ρ=1.1 $^{\mathrm{kg}}/_{\mathrm{m}^3}$.

A.8 Level-time histories for 1/3-octave bands

The following level-time histories are the detailed results of the examples in Fig. 5.21 of Sec. 5.6.

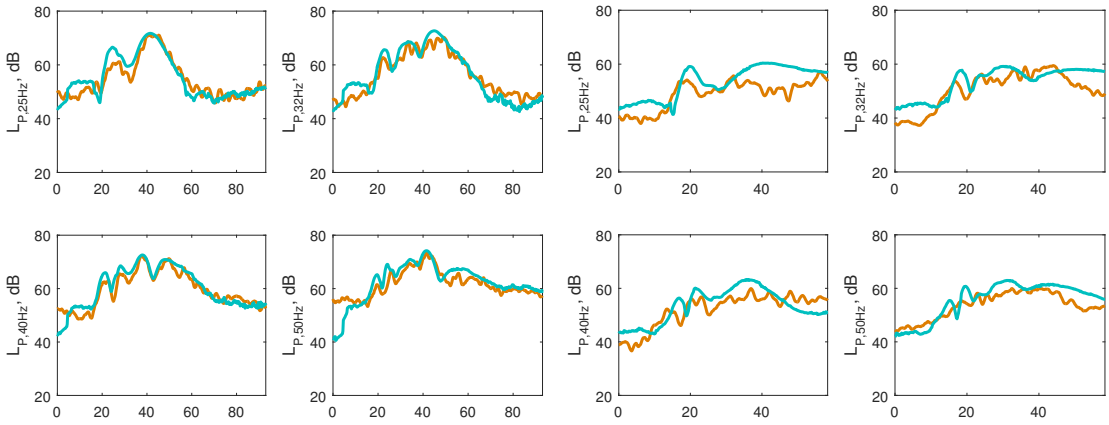

(a) Microphone 5 (b) Microphone 7

Figure A.37: Simulation and measurement of a departing A320_CFM56B at two different locations. Low frequencies 25-50 Hz.

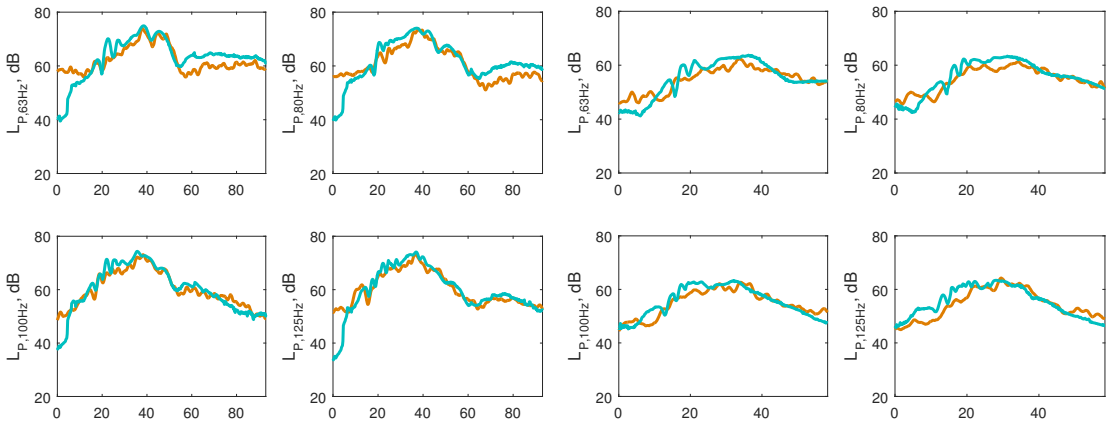

(a) Microphone 5 (b) Microphone 7

Figure A.38: Simulation and measurement of a departing A320_CFM56B at two different locations. Low frequencies 63-125 Hz.

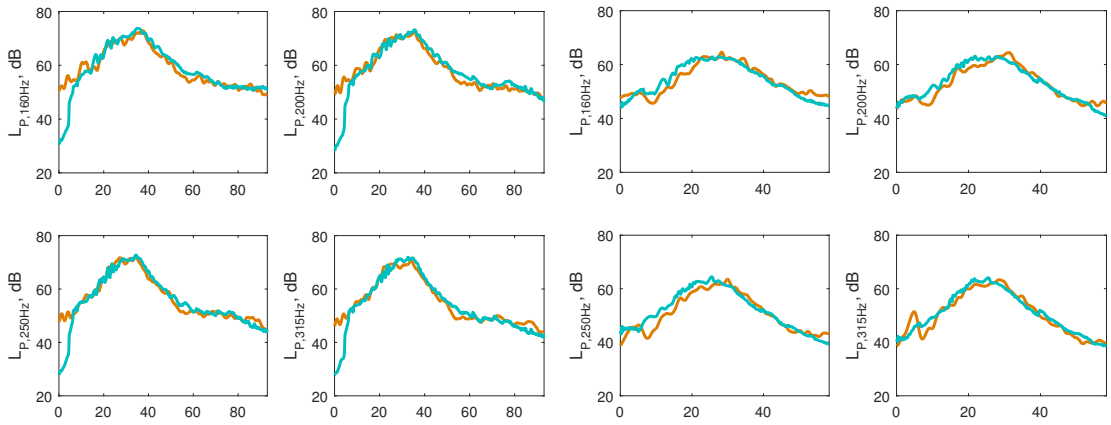

(a) Microphone 5 (b) Microphone 7

Figure A.39: Simulation and measurement of a departing A320_CFM56B at two different locations. Mid frequencies 160-315 Hz.

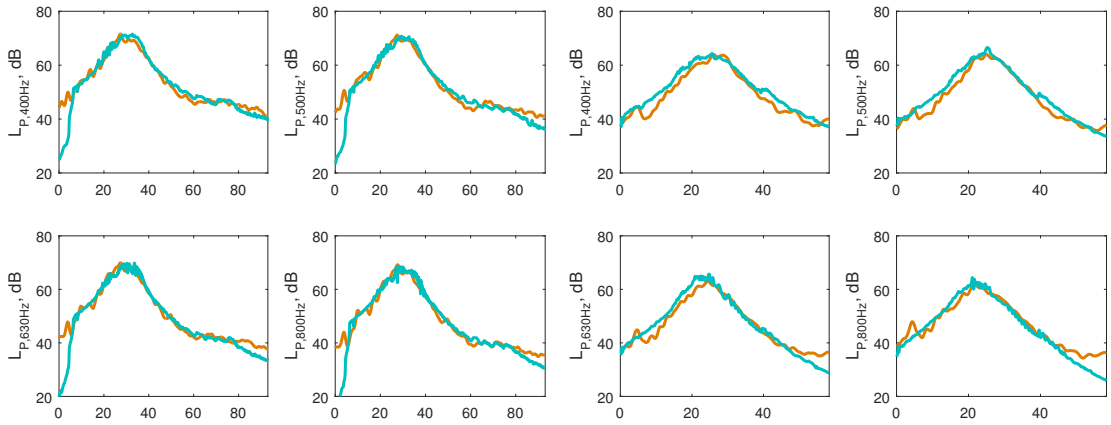

(a) Microphone 5 (b) Microphone 7

Figure A.40: Simulation and measurement of a departing A320_CFM56B at two different locations. Mid frequencies 400-800 Hz.

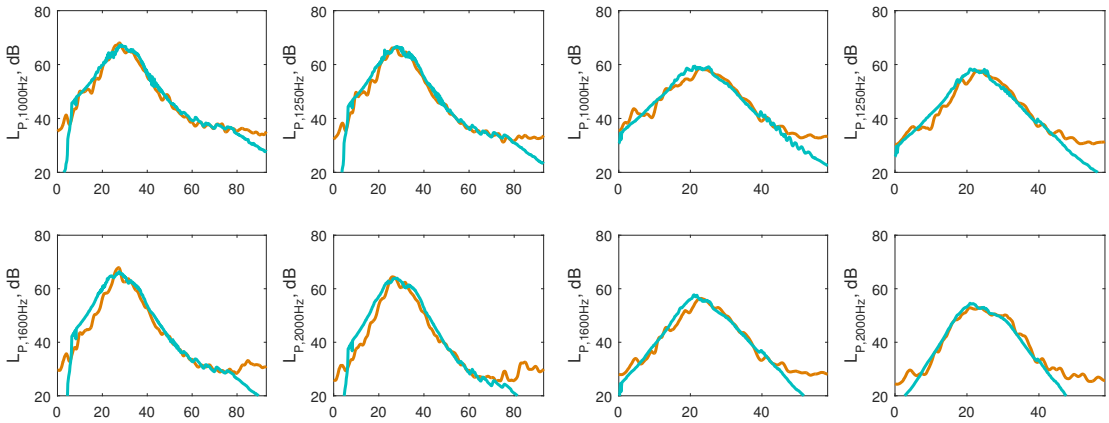

(a) Microphone 5 (b) Microphone 7

Figure A.41: Simulation and measurement of a departing A320_CFM56B at two different locations. High frequencies 1-2 kHz.

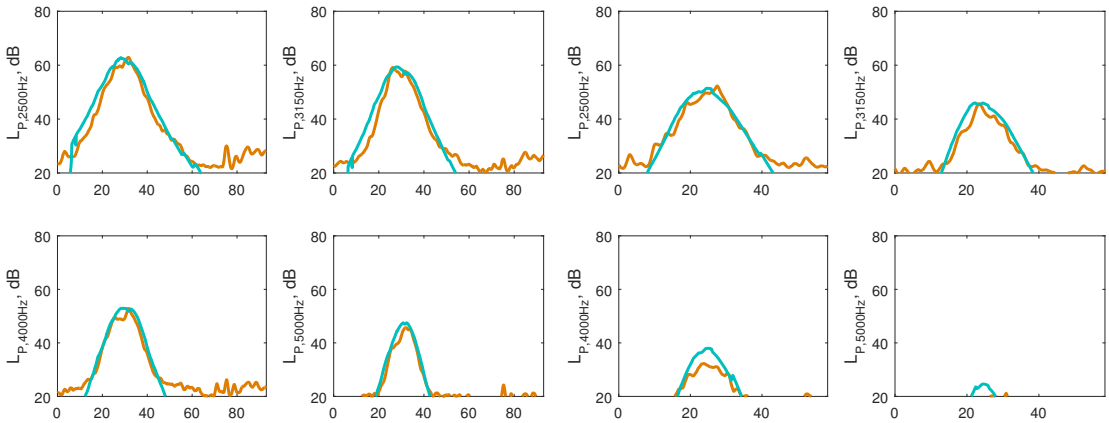

(a) Microphone 5 (b) Microphone 7

Figure A.42: Simulation and measurement of a departing A320_CFM56B at two different locations. High frequencies 2.5-5 kHz.

Two additional simulations for an approach are shown in Fig. A.43. Microphone 4 corresponds to a flight configuration at the beginning of the glide path, which is at $Ma \approx 0.3$ in idle power Fig. A.43a. Flaps 2 are already deployed and speedbrakes are used partly. During the overflight of microphone 2, the aircraft prepares the final approach by deploying the landing gear and flaps while reducing to landing airspeed Fig. A.43b. Again, the level-time histories for both examples agree very well. The measurements show a higher variability which are caused by atmospheric turbulence or background noise.

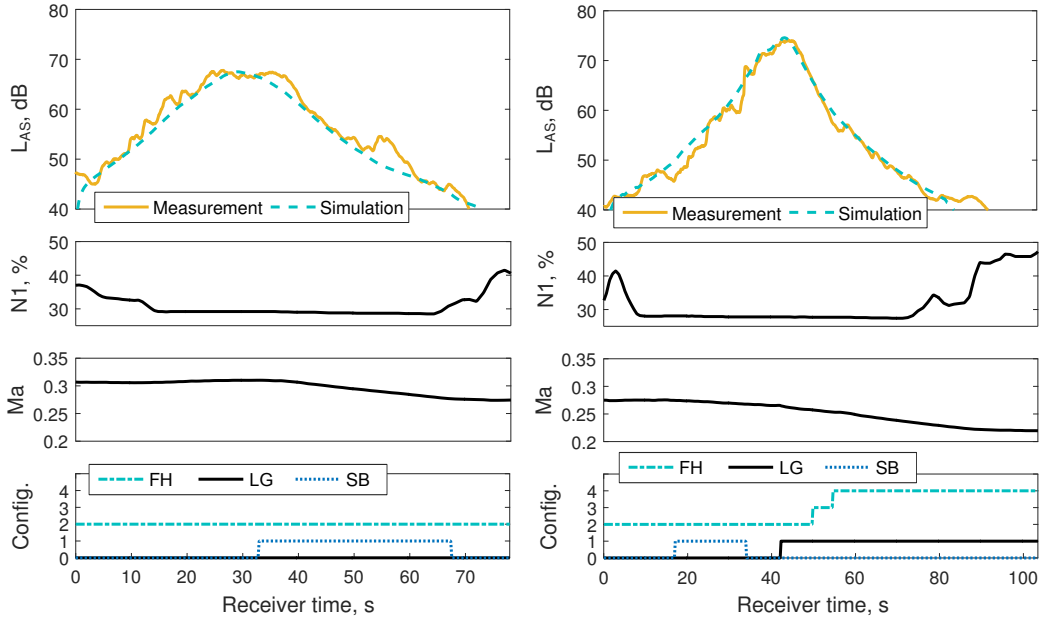

(a) Microphone 4: Idle at begin of the glide path(b) Microphone 2: Preparation to final approach

Figure A.43: Level-time histories for an approaching A320_CFM56B at two different locations in the far range. Model: 3D.

A.9 Verification

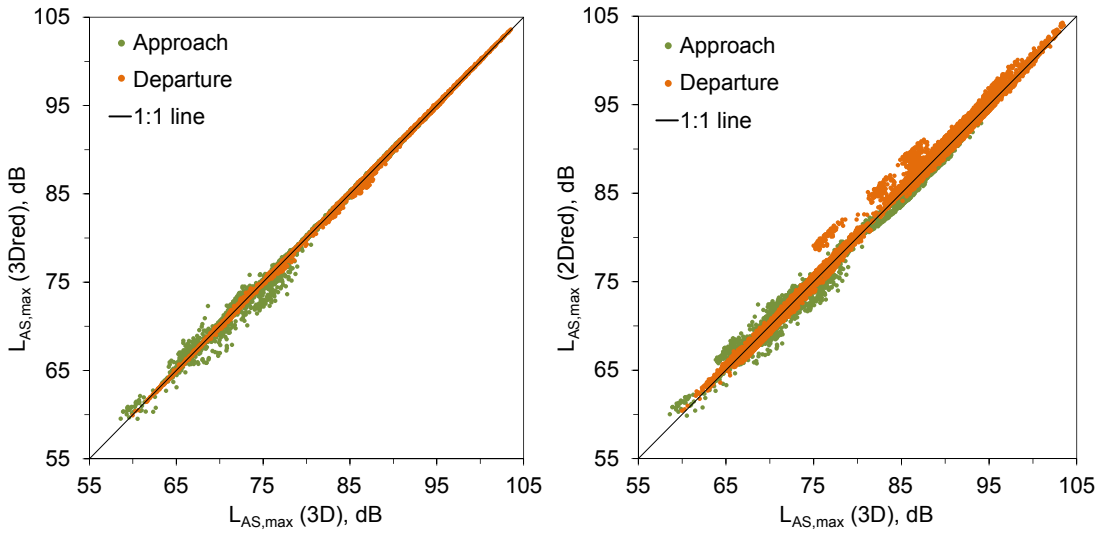

(a) 3Dred versus 3D (b) 2Dred versus 3D

Figure A.44: Scatter plot based on $L_{AS,max}$ to compare the model variants with each other.

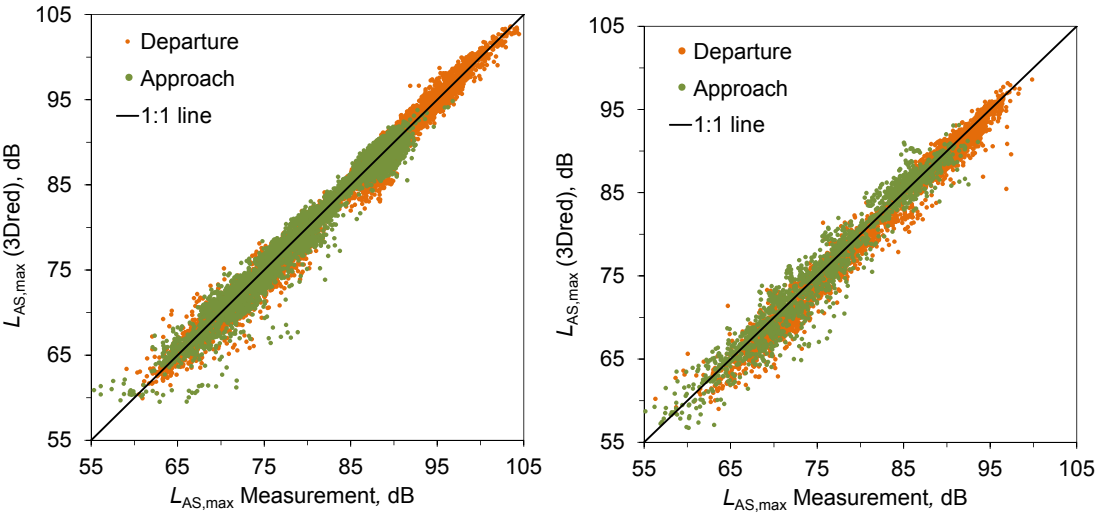

(a) Types with FDR data (b) Types without FDR data

Figure A.45: Comparison based on $L_{AS,max}$ of the 3Dred variant with measurements.

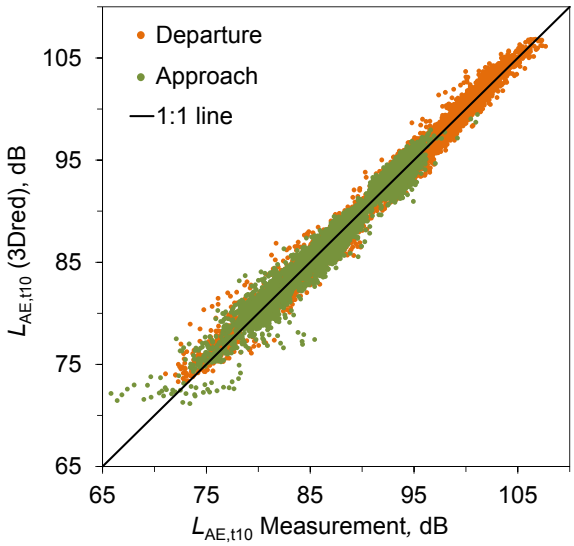

Figure A.46: Comparison of the 3Dred variant with measurements including all aircraft types with FDR data (10 524 events).

Table A.22: Level differences $\Delta L_{AE,t10}$ and $\Delta L_{AS,max}$ (calculation minus measurement) of all types with FDR data for 3D and 3Dred. Mean values and standard deviations (in brackets) are given for each model based on N events.

			3D		3Dred	
Model name	Proc.	N	$\Delta L_{AE,t10}$ [dB]	$\Delta L_{AS,max}$ [dB]	$\Delta L_{AE,t10}$ [dB]	$\Delta L_{AS,max}$ [dB]
A319_CFM56-5B	A	164	+0.0 (±1.0)	−0.1 (±1.4)	+0.0 (±1.1)	−0.2 (±1.4)
	D	358	−0.2 (±0.9)	−0.9 (±1.2)	−0.1 (±0.8)	−0.8 (±1.2)
A320_CFM56-5B	A	1 288	+0.0 (±1.1)	−0.2 (±1.5)	+0.0 (±1.1)	−0.2 (±1.5)
	D	1 884	+0.0 (±0.9)	−0.4 (±1.1)	+0.1 (±0.9)	−0.4 (±1.1)
A321_CFM56-5B	A	670	+0.0 (±1.1)	−0.2 (±1.5)	+0.1 (±1.1)	−0.2 (±1.6)
	D	1 015	+0.1 (±0.8)	−0.5 (±1.1)	+0.1 (±0.8)	−0.5 (±1.1)
A333_CFM56-B	A	602	+0.3 (±0.8)	+0.0 (±1.2)	+0.3 (±1.0)	+0.0 (±1.3)
	D	1 110	+0.2 (±0.8)	+0.0 (±1.1)	+0.2 (±0.8)	+0.0 (±1.2)
A343_TRENT7	A	560	+0.5 (±0.8)	+0.5 (±1.1)	+0.5 (±1.1)	+0.4 (±1.2)
	D	618	+0.2 (±1.1)	−0.2 (±1.3)	+0.2 (±1.1)	−0.2 (±1.3)
RJ1H_LF507	A	947	+0.1 (±1.2)	−0.2 (±1.7)	+0.1 (±1.2)	−0.3 (±1.7)
	D	1 308	+0.2 (±0.8)	−0.1 (±1.1)	+0.2 (±0.9)	−0.1 (±1.1)

Table A.23: Level differences $\Delta L_{AE,t10}$ and $\Delta L_{AS,max}$ (calculation minus measurement) of all types with FDR data for 2Dred. Mean values and standard deviations (in brackets) are given for each model based on N events.

			2Dred	
Model name	Proc.	N	$\Delta L_{AE,t10}$ [dB]	$\Delta L_{AS,max}$ [dB]
A319_CFM56-5B	A	164	−0.2 (±1.2)	−0.3 (±1.5)
	D	358	−0.1 (±1.0)	−0.8 (±1.3)
A320_CFM56-5B	A	1 288	−0.2 (±1.3)	−0.4 (±1.6)
	D	1 884	+0.1 (±1.1)	−0.3 (±1.3)
A321_CFM56-5B	A	670	−0.2 (±1.3)	−0.4 (±1.7)
	D	1 015	+0.1 (±0.9)	−0.4 (±1.2)
A333_CFM56-B	A	602	+0.1 (±1.1)	−0.2 (±1.4)
	D	1 110	+0.4 (±1.0)	+0.2 (±1.3)
A343_TRENT7	A	560	+0.4 (±1.3)	+0.3 (±1.3)
	D	618	+0.3 (±1.1)	−0.1 (±1.4)
RJ1H_LF507	A	947	−0.1 (±1.5)	−0.5 (±1.9)
	D	1 308	+0.9 (±1.7)	+0.6 (±1.9)

Table A.24: Level differences $\Delta L_{AE,t10}$ and $\Delta L_{AS,max}$ (calulation minus measurement) of all types without FDR data for the model 3Dred. Mean values and standard deviations (in brackets) are given for each model based on N events.

			3Dred	
Model name	Proc.	N	$\Delta L_{AE,t10}$ [dB]	$\Delta L_{AS,max}$ [dB]
A32X_CFM56-5A	A	79	+0.0 (±0.7)	−0.1 (±1.0)
	D	159	−0.1 (±1.0)	−0.6 (±1.3)
A32X_V2500	A	116	+1.2 (±1.8)	+1.1 (±2.2)
	D	558	−0.2 (±1.0)	−0.7 (±1.4)
A388_GP7270	A	7	+1.0 (±1.9)	+0.2 (±2.5)
	D	85	+0.5 (±1.1)	+0.2 (±1.3)
A388_TRENT9	A	53	−0.3 (±1.3)	−0.9 (±1.6)
	D	144	−0.1 (±1.3)	−0.4 (±1.7)
B737_CFM56-3	A	214	−0.1 (±1.0)	−0.4 (±1.3)
	D	224	+0.1 (±0.9)	−0.4 (±1.1)
B737_CFM56-7B	A	191	+0.0 (±1.2)	−0.2 (±1.6)
	D	658	−0.2 (±1.1)	−0.9 (±1.4)
B763_PW4060	A	152	−0.4 (±1.3)	−0.5 (±1.6)
	D	27	−0.8 (±1.4)	−1.5 (±2.0)
B76X_CF6-80C2	A	190	+0.3 (±2.0)	+0.0 (±2.6)
	D	112	−0.1 (±1.1)	−0.4 (±1.3)
CRJ9_CF34-8C5	A	96	+0.0 (±1.2)	−0.1 (±1.5)
	D	107	−0.1 (±0.9)	−0.8 (±1.4)
E170_CF34-8E	A	152	+0.2 (±1.0)	+0.2 (±1.3)
	D	162	+0.1 (±1.2)	−0.4 (±1.3)
E190_CF34-10E	A	223	+0.0 (±1.0)	−0.3 (±1.5)
	D	662	+0.1 (±0.9)	−0.6 (±1.2)
F100_TAY650-15	A	207	+0.6 (±1.8)	+0.3 (±2.3)
	D	614	−0.4 (±1.0)	−1.2 (±1.2)
FA7X_PW307	A	43	+1.3 (±2.0)	+0.8 (±2.5)
	D	43	+0.0 (±2.0)	−0.4 (±1.8)